Taylor Bubble Rise in Circular Tubes: Steady-States and Linear Stability Analysis

Habib Adebisi Abubakar

Matar Fluids Group
Department of Chemical Engineering and Chemical Technology
Imperial College London

A dissertation submitted in part fulfilment of the requirements for the degree of
Doctor of Philosophy in Chemical Engineering and the Diploma of Imperial College London
February, 2019

Declaration

This dissertation is a description of the work carried out by the author in the Department of Chemical Engineering, Imperial College London, under the supervision of Prof. Omar K. Matar. Except where acknowledged, the content is the original work of the author and no portion of it has been submitted in support of an application for a degree at any other university. The copyright of this thesis rests with the author and is made available under a Creative Commons Attribution Non-Commercial No Derivatives licence. Researchers are free to copy, distribute or transmit the thesis on the condition that they attribute it, that they do not use it for commercial purposes and that they do not alter, transform or build upon it. For any reuse or redistribution, researchers must make clear to others the licence terms of this work

Abstract

Slug flow is one of the flow regimes that is encountered in two-phase gas-liquid flows in pipes. The flow regime is of great interest in many applications such as hydrocarbons production in oil wells and their transportation in pipelines, conventional and nuclear power generation plants, heat and mass transfer operations between gas and liquid in chemical reactors, among many others. Slug flow in vertical tubes is characterised by periodic rise of large bullet-shaped bubbles known as Taylor bubbles separated by pockets of liquids, known as liquid slugs. While numerous studies have been carried out in the areas of estimation of steady state hydrodynamics features of a single Taylor bubble rising in liquids, not much has been done in understanding some of the transitions featuring in this flow.

This dissertation focuses on studying the transitions encountered in the dynamics of a rising Taylor bubble. A particular attention is given to the understanding of the mechanism governing the transition of the bubble from symmetric to asymmetric shape in downward liquid flow. This involves three basic steps; computing the steady state solution, examining the stability of the steady state solution and carrying out energy analysis on the stability results.

For different flow conditions, characterised by dimensionless Eötvös number (Eo), inverse viscosity number (Nf) and centreline liquid velocity Froude number (U_m), we compute the steady state solution of a rising two-dimensional axisymmetric Taylor bubble. The linear stability of the steady state solutions to three-dimensional infinitesimal perturbations are then investigated. The analysis enable us to determine the region in the dimensionless parameters space at which a Taylor bubble transitioned from symmetric to asymmetric shape.

To understand the mechanism that govern the instability, we carried out energy budget analysis to isolate the most dominant energy term that drives the instability. The analysis showed that the mechanism that drives the instability is different depending on whether the effect of surface tension can be neglected or not. For region of negligible surface tension effect, the instability originates from inside the bubble and the dominant source of energy that drives the instability is the bubble pressure, while for region where surface tension has strong effect, the instability originates from the liquid phase and the dominant source of energy that drives the instability is the tangential stress.

Acknowledgements

I would like to express my sincere thank you to my supervisor, Professor Omar K. Matar. His support, patience, encouragement and guidance are simply super amazing. The opportunities to attend numerous trainings and to present my work at different fora are gestures that I deeply appreciate. In his world, all a student need to do is to ask for anything and indeed, from my experiences and that of many others, it is always granted. Many a times, it is I who would asked myself if what I was seeking of him is not too much. For all that and many more, I am very grateful.

I must also express my appreciation to Dr David Fabre and his then PhD student, Paul Bonnefis, both of Institute of Fluid Mechanics, Toulouse, France for their help in understanding the open-source finite element package used for the dissertation work. My two weeks stay in Toulouse was a turning point in my research work. Indeed, I very much appreciate the fruitful discussions we had and the suggestions given.

I am also indebted to a number of research associates in the group. I appreciate the help of Dr Alexander Wray. His mastery of mathematics often awes me. At the inception of my PhD, whenever I ran into mathematical trench, all I needed to do was to raise my head, he was sitting right opposite my desk. Of course it was not too long that he had to move on, the assistance I got while he was around helped me a great deal. To Dr Edward Smith, I say big thanks. Edward was the shoulder upon which I laid whenever it comes to computational and programming help. He patiently guided me to transit from Window platform to Unix, without which this research would not have been accomplished within the time frame it was done. Indeed, I am also grateful to many other research associates in the group, past and present, who I had the privilege of interacting with on many issues; Dr Zhizhao Che, Dr Zhihua Xie, Dr Lyes Kahouadji, Dr Aditya Karnik, Dr Jason Stafford, Dr Lachlan Mason and Dr Mirco Magnini. You guys are marvellous.

I would not forget the help of Dr Arnoldo Badillo, formerly of The Paul Scherrer Institute, Switzerland. Our collaboration on the use of diffuse interface method for numerical simulation of my research work was the beginning of my venturing into Unix platform and a great eye opening in deeper understanding of the physics of my problem. Arnoldo comments and ques-

tions on issues are always thought provoking.

To my fellow PhD colleagues in the group, past and present, my friends in the college and back home in Nigeria who are too numerous to mention, I am very grateful for the show of love and understanding. You guys are family. I specially thank Dr Ayo Rufai, who will always pop in from his desk in RODH 338 to check on me at my desk in RODH 149 to know how things are going and whether progress have been made. To Wasiu Hamzat and Ismaila Omeiza Ibrahim, your frequent calls asking how things are going even up to the last day of me writing-up this thesis are enormously appreciated.

I appreciate the Undergraduate students and MSc student who I had the privilege of working with on my research. I particularly acknowledged Mohammed Fazel, Kushagra Kohli and Liam Sheppard whose collaborative work led to great improvement on the modelling of my work.

To my sponsor, Federal Government of Nigeria, under the Presidential Special Scholarship Scheme for Innovations and Developments (PRESSID), through the Petroleum Technology Development Fund (PTDF), I thank you for the scholarship opportunity and to Ahmadu Bello University (ABU), Zaria I appreciate the fellowship given to me to undertake this study.

Finally, and *most importantly*, my forever thank you goes to my *parents and siblings*. You guys are the strongest pillar of support I have. Your encouragements, prayers and understanding during the course of my research and writing were the greatest source of energy which kept me going till the end. During my PhD, we had a number of occasions in the family which I ought to attend but could not. Thank you all for the understanding. It meant a great deal to me.

To my *Olori*, I deeply appreciate your understanding beyond anything you can possibly imagined.

Alhamdullilah.

Contents

Declaration i

Abstract i

Acknowledgements iii

1 Introduction 1

1.1 Two-phase gas-liquid flows 1

1.2 Taylor bubble 3

1.3 Motivations 5

1.4 Aim and objectives 8

1.5 Thesis outlines 9

2 Literature review 11

2.1 Dimensionless groups 11

2.2 Dynamics of a rising Taylor bubble 12

2.2.1 Rise velocity 12

2.2.2 Film thickness 16

2.2.3 Wake length 18

2.3 Stability of a rising Taylor bubble 20

2.3.1 Taylor bubble in downward liquid flow 21

2.3.2 Taylor bubble in turbulent field 24

2.4 Summary 26

3 Computational development **28**

3.1 Problem description 29

3.2 Governing equations and non-dimensionalisation 30

3.3 Weak formulations 34

3.4 Galerkin finite element approximation 37

3.5 Interface deformation 40

3.5.1 Interface capturing methods 41

3.5.2 Interface tracking methods 43

3.5.3 Mesh deformation 45

3.6 Curvature 46

3.6.1 Curvature linearisation 47

3.6.2 Curvature computation and approximation 50

3.7 Bubble pressure 54

3.8 Shape functions 55

3.9 Summary 59

4 Steady state numerical simulations **60**

4.1 Steady state model description 61

4.2 Steady state model solution 69

4.3 Steady state model validation 71

4.4 Steady state characterisations in stagnant liquids 76

4.4.1 Qualitative analysis of steady state shapes and flow field 77

4.4.2 Hydrodynamic features of the nose region 83

4.4.3 Hydrodynamic features of the film region 88

4.4.4 Hydrodynamic features at the wall and interface 92

4.4.5 Hydrodynamic features of bottom region 98

4.5 Steady state characterisations in flowing liquids 103

4.5.1 Bubble rise velocity in upward liquid flow 104

4.5.2 Qualitative and quantitative analysis of steady state shapes and flow field in flowing liquids 105

4.6 Steady state numerical simulations challenges . . . 109
4.7 Summary . . . 110

5 Linear stability and energy budget analyses 111

5.1 Linear stability model formulation . . . 112
5.2 Linear stability model solution . . . 123
5.3 Linear stability model validation . . . 124
5.4 Stability analysis of steady state solutions . . . 128
5.4.1 Growth rate . . . 128
5.4.2 Asymmetric bubble shapes . . . 131
5.4.3 Instability map . . . 135
5.5 Energy budget analysis . . . 137
5.5.1 Energy balance model . . . 137
5.5.2 Energy analysis of linear stability results . . . 141
5.6 Summary . . . 145

6 Conclusions and future work 147

6.1 Conclusions . . . 147
6.2 Future work . . . 150
6.2.1 Wake instability and breakup of bubble . . . 150
6.2.2 Three-dimensional numerical simulations of Taylor bubble . . . 150

References 151

A Computational development operators 163

A.1 Axisymmetric surface tensor products and operators . . . 163

B Steady state simulations results in flowing liquid 166

B.1 Additional bubble shapes in stagnant liquids . . . 166
B.2 Steady state mean curvature . . . 168
B.3 Bubble shapes in flowing liquids . . . 172

C Stability analysis model and results **177**

C.1 Model development 177

C.2 Maximum growth rate results 180

C.3 Energy analysis 182

List of Tables

4.1 Dimensionless parameters corresponding to the properties of the fluid used for validation. 72

4.2 Number and length of the edge of triangle elements at different sections of the domain boundary used in mesh generation. 73

4.3 Definition of notations depicted in Figure 4.7. 77

5.1 Bubble rise velocity at the onset of transition to asymmetric Taylor bubble: effect of inverse viscosity and Eötvös numbers. 136

5.2 Balance of energy distribution among the different energy terms in (5.64) for $Nf = 80$, $Eo = 140$ and mode, $m = 1$. 141

List of Figures

1.1 Flow patterns in gas-liquid flows in vertical pipes. Reproduced from [52] 1

1.2 Geometrical sections around a Taylor bubble. Adapted from [64] 3

1.3 Taylor bubble shapes in a (a) stangant ($\bar{U}_L = 0$) and (b) downward flowing liquid ($\bar{U}_L = -0.08$), with $Nf = 71,428.57$ and $Eo = 888.89$. Reproduced from [34] . 6

1.4 Wake flow patterns behind Taylor bubbles rising through stagnant liquids in a 55 mm pipe: (a) laminar ($Nf = 420$), (b) transitional ($Nf = 520$) and (c) turbulent ($Nf = 11000$). Reproduced from [19] 7

1.5 Taylor bubble shapes when it rises through a stagnant liquid in a 290 mm pipe in which the liquid ahead is (a) quiescent (no breakup observed) (b) disturbed (breakup observed). Reproduced from [94] 8

2.1 Regions showing the limits of the signficance of dimensionless quantities on hydrodynamics of a rising Taylor bubble in stagnant liquid. Reproduced from [114]. 14

2.2 Effect of Nf or Re_b on equilibrium film thickness. Adapted from [64]. 18

2.3 CFD simulation of Taylor bubble rise in a stagnant liquid in pipes of diameter (a) 400 mm (b) 500 mm (c) 400 mm. Adapted from [29]. 26

3.1 Depiction of a Taylor bubble rising through a stagnant liquid. 30

3.2 Two dimensional triangulated domain with linear approximations on subdomain, thereby having three nodes. 38

3.3 Interface representation on (a) Eulerian mesh (b) Lagrangian mesh. In Lagrangian representation, the interface coincides with the computational mesh unlike in Eulerian representation. Adapted from [3] 41

3.4 Interface parametrisation for cubic spline interpolation. 51

3.5 Triangular finite element with (a) P_2 (b) P_1 approximations 56

3.6 Triangular finite element with P_1^+ approximation 56

3.7 Triangular finite element with (a) P_2^+ (b) P_{-1} approximations 57

3.8 Triangular finite element with P_1 approximation showing the local coordinates of the three nodes. 58

4.1 Axisymmetric 2D domain. 61

4.2 Mesh structure around Taylor bubble 72

4.3 Flow structure around the steady state topology in a moving frame of reference showing the five different positions at which measurements were taken for validation. 73

4.4 Velocity profiles ahead of the bubble, (a) axial velocity component along the tube axis (position 1) and (b) axial and radial velocity components at $\frac{z}{D} = 0.111$ ahead of the bubble nose (position 2); Numerical results (solid lines) compared to experimental PIV measurements (symbols) of [17]. 74

4.5 Velocity profiles in the film regions, (a) axial and radial velcity components in the developing film at $\frac{z}{D} = 0.504$ below the bubble nose (position 3) and (b) axial velocity component in the fully developed film (position 4); Numerical results (solid lines) compared to experimental PIV measurements (symbols) of Bugg and Saad [17]. 74

4.6 Axial and radial components of velocity at distance $\frac{z}{D} = 0.20$ below the bubble bottom (position 5); Numerical results (solid lines) compared to experimental PIV measurements (symbols) of Bugg and saad [17]. 75

4.7 Schematic representation of the main hydrodynamic features of Taylor bubble discussed in the thesis. All features are dimensionless and are based on the characteristic scales stated in section 3.2 76

4.8 Effect of Nf on steady state bubble shape and the surrounding flow field for $Eo = 220$ and $U_m = 0$; showing streamlines and vector field superimposed on velocity magnitude pseudocolour plot on the right and left sides of the symmetry axis, respectively. 78

4.9 Effect of Eo on steady state bubble shape and the surrounding flow field at $Nf = 100$ and $U_m = 0$; showing streamlines and vector field superimposed on velocity magnitude pseudocolour plot on the right and left sides of the symmetry axis, respectively. 79

4.10 Effect of variation of Nf on steady state Taylor bubble shapes at low Eötvös numbers (a) $Eo = 20$ (b) $Eo = 10$; showing streamlines and vector field superimposed on velocity magnitude pseudocolour plot on the right and left sides of the symmetry axis, respectively. 80

4.11 Steady state bubble shapes and surrounding flow fields; effect of inverse viscosity and Eötvös numbers. 82

4.12 Effect of Nf and Eo on steady state bubble rise velocity in stagnant liquids. Comparison between numerical results (coloured marker symbols) and analytical prediction of equation (2.8) (coloured continuous line). 83

4.13 Typical radial velocity profile (coloured blue) along the interface (coloured red). 84

4.14 Frontal radius of Taylor bubble: influence of inverse viscosity and Eötvös numbers 85

4.15 Normalised frontal radius; showing convergence towards a constant value of 0.815 when $Nf \geq 80$ 86

4.16 Normalised bubble showing (a) full bubble shape (b) nose region with a plot of normalised frontal radius limit (continuous black line): effect of Nf at $Eo = 220$ 87

4.17 Developing length ahead of Taylor bubble nose: influence of inverse viscosity and Eötvös numbers 87

4.18 Developing length below the bubble nose: influence of inverse viscosity and Eötvös numbers 89

4.19 Equilibrium film thickness: Comparison between numerical simulations (coloured markers) and theoretical prediction using (4.32) and (2.8) (coloured continuous solid line) for different inverse viscosity and Eötvös numbers. 90

4.20 Axial velocity profile in the fully developed film: effect of Eötvös number at (a) $Nf = 40$ (b) $Nf = 100$ (c) $Nf = 160$. Comparison between numerical simulations (coloured markers) and theoretical predictions of (4.34) (coloured solid lines) 92

4.21 Axial velocity profile in the fully developed film: effect of inverse viscosity number at (a) $Eo = 20$ (b) $Eo = 140$ (c) $Eo = 260$. Comparison between numerical simulations (coloured markers) and theoretical predictions of (4.34) (coloured solid lines) 92

4.22 Shear stress at wall boundary: Numerical effects of inverse viscosity number at (a) $Eo = 20$ (b) $Eo = 140$ (c) $Eo = 260$ (broken lines) compared to theoretical prediction of (4.38) in the developed film (solid lines) 94

4.23 Shear stress at wall boundary: Numerical effects of Eötvös number at (a) $Nf = 40$ (b) $Nf = 100$ (c) $Nf = 160$ (broken lines) compared to theoretical prediction of (4.38) in the developed film (solid lines) 94

4.24 Maximum wall shear stress: effects of inverse viscosity and Eötvös numbers. . . 95

4.25 Normal stress (solid lines) and total pressure (broken lines) at the interface: effect of inverse viscosity number at (a) $Eo = 20$ (b) $Eo = 140$ (c) $Eo = 260$ . . 96

4.26 Normal stress (solid lines) and total pressure (broken lines) at the interface: effect of Eötvös number at (a) $Nf = 40$ (b) $Nf = 100$ (c) $Nf = 160$ 96

4.27 Taylor bubble (a) shape and (b) mesh structure for $Nf = 160$ and $Eo = 300$. . 97

4.28 Enlarged view of Taylor bubble (a) bottom and (b) tail tip mesh structures for $Nf = 160$ and $Eo = 300$. 97

4.29 Maximum interface normal stress: effects of inverse viscosity and Eötvös numbers. 98

4.30 Taylor bubble bottom radius of curvature: influence of inverse viscosity and Eötvös numbers 99

4.31 Bottom deformation: influence of Eötvös number for $Nf = 160$ 99

4.32 Bottom deformation: influence of inverse viscosity number for $Eo = 300$ 100

4.33 Wake length: influence of inverse viscosity and Eötvös numbers 100

4.34 Effect of inverse viscosity and Eötvös numbers on (a) radial (b) axial, location of the vortex eye with reference to bubble bottom. 101

4.35 Taylor bubble bottom: influence of inverse viscosity and Eötvös numbers, showing region in the parameters space where bubble bottom takes concave or convex shape and whether or not the shape is associated with a wake. 102

4.36 Bottom length: influence of inverse viscosity and Eötvös numbers 103

4.37 Effect of imposed upward liquid flow on bubble rise velocity for varying inverse viscosity numbers. Comparison between numerical result (coloured markers), theoretical prediction using (4.43) and (4.44) (black solid line) and theoretical prediction using (2.8) and (4.44) (coloured dashed line). 104

4.38 Effect of inverse viscosity and Eötvös numbers on (a) C_1 (b) C_0. 105

4.39 Effect of U_m on steady state bubble shape and the surrounding flow field at $Nf = 80$ and $Eo = 140$; showing streamlines and vector field superimposed on velocity magnitude pseudocolour plot on the right and left side of the symmetry axis. 106

4.40 Effect of U_m on steady state bubble rise velocity at $Eo = 140$ and different Nf. 107

4.41 Effect of U_m on steady state modified interface normal stress (4.41) at $Nf = 80$ and $Eo = 140$. 107

4.42 Effect of U_m on steady state modified interface normal stress at $Nf = 80$ and $Eo = 140$. 108

5.1 Spherical bubble in stagnant liquid. 124

5.2 Comparison between amplification rate from analytical solution of equation (5.46) (coloured continuous solid line) and numerical global linear stability analysis (coloured markers), for modes m = 2, 3, 4 and 5. 127

5.3 Comparison between oscillation frequency from analytical solution of equation (5.46) (coloured continuous solid line) and numerical global linear stability analysis (coloured markers), for modes m = 2, 3, 4 and 5. 127

5.4 Largest growth rate for $Nf = 80$ as a function of tube center liquid velocity at (a) $Eo = 20$ (b) $Eo = 180$ (c) $Eo = 300$: showing results for $m = 1, 2$ and 3. . . 128

5.5 Largest growth rate for $Nf = 80$ as a function of Eötvös number at (a) $U_m = -0.20$ (b) $U_m = -0.55$: showing results for $m = 1, 2$ and 3. 129

5.6 Largest growth rate for $Nf = 100$ as a function of tube center liquid velocity at (a) $Eo = 20$ (b) $Eo = 180$ (c) $Eo = 300$: showing results for $m = 1, 2$ and 3. . . 129

5.7 Largest growth rate for $Nf = 60$ as a function of tube center liquid velocity at (a) $Eo = 20$ (b) $Eo = 180$ (c) $Eo = 300$: showing results for $m = 1, 2$ and 3. . . 129

5.8 Largest growth rate for $Nf = 40$ as a function of tube center liquid velocity at (a) $Eo = 180$ (b) $Eo = 300$: showing results for $m = 1, 2$ and 3. 131

5.9 Deformed bubble shape for $Nf = 100$ and $Eo = 220$ at (a) $U_m = -0.25$ (b) $U_m = -0.40$ (c) $U_m = -0.55$ when $m = 1$. 132

5.10 Deformed bubble shape for $Nf = 100$ and $Eo = 220$ at $U_m = -0.55$ when $m = 2$. 132

5.11 Deformed bubble shape for $Nf = 80$ and $U_m = -0.50$ at (a) $Eo = 100$ (b) $Eo = 180$ (c) $Eo = 260$ when $m = 1$. 133

5.12 Deformed bubble shape for $Nf = 80$ and $U_m = -0.50$ at $Eo = 260$ when $m = 2$. 133

5.13 Deformed bubble shape for $Eo = 300$ and $U_m = -0.45$ at (a) $Nf = 60$ (b) $Nf = 80$ (c) $Nf = 100$ when $m = 1$. 134

5.14 Deformed bubble shape for $Eo = 300$ and $U_m = -0.45$ at (a) $Nf = 60$ (b) $Nf = 80$ (c) $Nf = 100$ when $m = 2$. 134

5.15 Instability showing the onset of transition to asymmetric bubble shape in downward liquid flow for (a) $Nf = 40$ (b) $Nf = 60$ (c) $Nf = 80$ (c) $Nf = 100$ (e) $Nf = 120$. 135

5.16 Energy analysis for $Nf = 80$ as a function of tube center liquid velocity at (a) $Eo = 20$ (b) $Eo = 180$ (c) $Eo = 300$ when $m = 1$. The point where β_R first become positive, marking the onset of asymmetric bubble is indicated by the black vertical dashed lines. 141

5.17 Distribution of tangential energy for $Nf = 80$ as a function of tube center liquid velocity at (a) $Eo = 20$ (b) $Eo = 180$ (c) $Eo = 300$ when $m = 1$. The point where β_R first become positive, marking the onset of asymmetric bubble is indicated by the black vertical dashed lines. 143

5.18 Energy distribution of component energy terms in equation (a) (5.64) (b) (5.66) for $Nf = 80$, $U_m = -0.20$ and $m = 1$ as a function of Eötvös number, showing a switch in the role of TAN_{strs} from destabilising to stabilising energy term in open interval $(60, 100)$. 144

5.19 Energy distribution of component energy terms in equation (a) (5.64) (b) (5.66) for $Eo = 300$, $U_m = -0.25$ and $m = 1$ as a function of inverse viscosity number, showing a trend in the role of TAN_{pb} from stabilising to destabilising energy term as Nf is decreased. 144

6.1 Isosurface of Taylor bubble coloured with the magnitude of the velocity at different computational time steps compared with the experimental steady shape of Rana *et al* [98] 151

B.1 Steady state bubble shapes and surrounding flow fields; effect of inverse viscosity and Eötvös numbers. 167

B.2 Steady state bubble shapes and surrounding flow fields; effect of inverse viscosity and Eötvös numbers. 168

B.3 Mean curvature of the bubble interface as a functions of Nf and Eo, $Eo = 10 - 40$. 169

B.4 Mean curvature of the bubble interface as a functions of Nf and Eo, $Eo = 50 - 140$. 170

B.5 Mean curvature of the bubble interface as a functions of Nf and Eo, $Eo = 180 - 300$. 171

B.6 Steady state bubble shapes and flow field; effect of centreline liquid velocity Froude number and Eötvös number for $Nf = 100$. 173

B.7 Steady state bubble shapes and flow field; effect of centreline liquid velocity Froude number and Eötvös number for $Nf = 80$. 174

B.8 Steady state bubble shapes and flow field; effect of centreline liquid velocity Froude number and Eötvös number for $Nf = 60$. 175

B.9 Steady state bubble shapes and flow field; effect of centreline liquid velocity Froude number and Eötvös number for $Nf = 40$. 176

C.1 Maximum growth rate as a function of liquid centreline Froude number; effect of Nf and Eo, showing modes, $m = 1, 2$ and 3. 181

C.2 Energy contribution of the different energy terms in (5.64) for mode, $m = 1$; effect of inverse viscosity and Eötvös numbers. 183

C.3 Energy contribution of the different energy terms in (5.66) for mode, $m = 1$; effect of inverse viscosity and Eötvös numbers. 184

Chapter 1

Introduction

1.1 Two-phase gas-liquid flows

Two-phase gas-liquid flow refers to the interactive flow of gas and liquid, as a result of which the interface between the two phases is influenced by their motion. Because of the deformable nature of the interface and the compressible nature of the gas phase, two-phase gas-liquid flows are considered the most complex of the four types of two-phase flows; gas-liquid, gas-solid, liquid-liquid, and liquid-solid [52]. Depending on the flow rates and fluid properties of the phases, and the geometry and orientation of the flowing channel, different classes of interface distribution, termed flow regimes or patterns, can be defined.

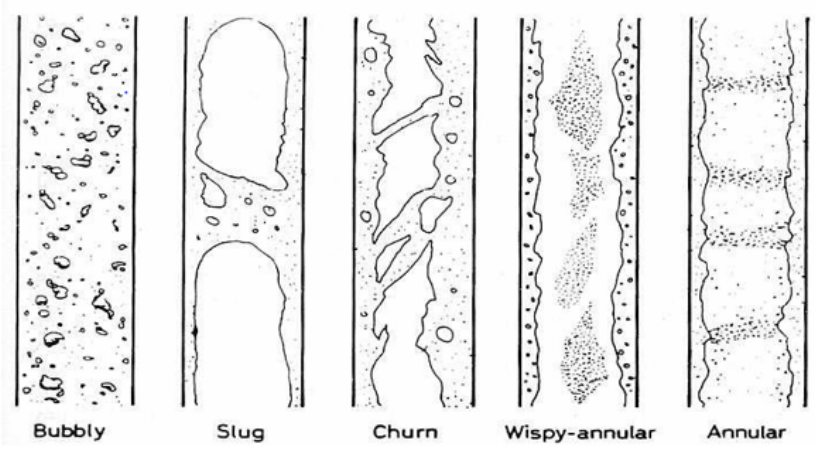


Figure 1.1: Flow patterns in gas-liquid flows in vertical pipes. Reproduced from [52]

In vertical flow of gas and liquid through pipes, increasing the gas phase flow rate, at constant liquid phase flow rate, results in the following flow regimes: bubbly flow, slug or plug flow, churn flow and annular flow, shown in Figure 1.1.

The *bubbly flow* occurs at relatively low gas flow rate. It is a regime of continuous liquid phase with small bubbles dispersed in it. At a much higher gas flow rate, the flow pattern changes to *slug flow*. This regime features periodic-like flow of large bullet-shaped bubbles separated by regions containing liquid which may have dispersed smaller bubbles. These large bubbles are known as *Taylor bubbles*. Slug flow typically involves the downward flow of the liquid phase in the form of a falling film on the outside of the Taylor bubbles. However, the net flow of both liquid and gas can be upward. On further increase in the gas flow rate, there is a transition to *churn flow* pattern. Churn flow is an unstable flow regime that is characterised, particularly in wide tubes, by an upward and downward oscillatory motion of the liquid phase. In narrow pipes, churn flow regime may not be noticed. At extremely high gas flow rate, the flow becomes annular. In this regime, there is a core of gas, usually with small liquid droplets entrained, and a liquid film, sometime with gas bubbles entrained, that flows on the wall of the pipe.

Among the different flow patterns, slug flow has attracted a lot of attention in the literature. It occurs over a wide range of flow conditions and has find applications in numerous processes, both on large and small scales. It is encountered in hydrocarbons production in oil wells and their transportation in pipelines, emergency cooling of nuclear reactors, heat and mass transfer operations between gas and liquid in chemical reactors, boiling and condensation in liquid-vapour systems of thermal power plants and in steam production in geothermal power plants [35, 70, 107]. For examples, in the oil and gas production, slug flow occurs in vertical pipes that connect oil wells to remote wellhead platforms. In the operation of this process, slug flow is undesirable as it leads to pressure and velocity fluctuations at the outlet of the risers, which in a severe case could lead to platform trips and plant shutdown [49]. In addition to the aforementioned processes, slug flow has also find applications in microfluidic systems

such as the cooling of electronics [68], geological systems such as the study of the dynamics of large bubble rise during volcanic eruption [20, 89] and physiological systems such as the understanding of blood flow physics in blood vessels [58, 96].

1.2 Taylor bubble

Of interest to this research is the understanding of the behaviour of a single Taylor bubble in stagnant and flowing liquids. This simplified form is considered as a paradigm for the slug flow in vertical pipes [94] because of the near-periodicity of the gas-liquid flows in the regime [70].

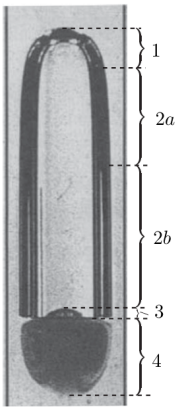


Figure 1.2: Geometrical sections around a Taylor bubble. Adapted from [64]

A Taylor bubble rising through a liquid parametrised by the dimensionless inverse viscosity number, Nf, Eötvös number, Eo and Froude number, Fr define as,

$$Nf = \frac{\rho \left(gD^3\right)^{\frac{1}{2}}}{\mu} \tag{1.1}$$

$$Eo = \frac{\rho g D^2}{\gamma} \tag{1.2}$$

and

$$Fr = \frac{u}{\sqrt{gD}} \tag{1.3}$$

respectively, is generally conferred with topological (or geometrical) symmetry and can be sectioned into four distinct regions [64] as shown in Figure 1.2 with each region having specific

features used for its characterisation.

In equations (1.1)-(1.3), ρ, μ and u denote the density, kinematic viscosity and velocity of the liquid, respectively; D is the tube diameter; and g is the acceleration due to gravity. Also, it is assumed that the viscosity and density of the gas phase are negligibly small when compared to that of the liquid phase. For definiteness, in flowing liquid, we denote the Froude number that is based on mean and maximum liquid velocity as $\bar{U}_L$ and U_m, respectively.

Nose region : This is region 1 in Figure 1.2. It is nearly hemispherical and is characterised by its frontal radius of curvature, the magnitude of the axial component of velocity at its tip, which is the bubble rise velocity, the maximum distance ahead of the bubble nose where the bubble impact is felt and the velocity profile ahead of it.

Body region : This is region 2 in Figure 1.2. It is nearly tubular and is surrounded by a thin liquid film which can be divided into developing and fully developed film parts, labelled, in Figure 1.2, $2a$ and $2b$, respectively. The characteristic features of this region are the length of the developing film part, the thickness of the film in the fully developed part, the wall shear stress in the film region and the velocity profile in the fully developed film part.

Bottom region : This is region 3 in Figure 1.2. It is characterised by its shapes, which could be concave or convex and the radius of curvature computed along the axis of symmetry.

Wake region : This is region 4 in Figure 1.2. If present, it is a recirculation zone behind the bubble and its basic features are the wake length, wake volume, the nature of the flow pattern in this region, which could be be laminar, transitional or turbulent, the maximum distance below the bubble bottom where the bubble impact is felt and the location of the vortex center.

We note that in the Taylor bubble literature, it is common to include the wake region under the bottom region, in which case, it is possible to then distinguish between a bottom region with/without a wake.

Because of the numerous applications of the slug flow, a great amount of research have been done to understand the hydrodynamics of a Taylor bubble as it pertains to its different regions. While extensive experimental [17, 19, 38, 45, 64, 76, 79, 82, 94, 98, 114] and a number of theoretical studies [15, 25, 30, 33, 41] have been carried out on some of the features highlighted for all the aforementioned topological regions, there are still much more to be understood, particularly in the area of systematically studying the influence of the dimensionless parameters on the dynamics of the bubble and in the area of providing deep insight into the flow field around and within the bubble. In these areas, numerical simulations have proven to be an efficient and cost effective means, and in recent years, there have been a number of computational studies that have attempted to address them. It is worthy of note that a large number of these numerical studies are based on axisymmetric assumption [17, 58, 66, 70, 71, 107] with only a few focusing on full three-dimensional simulation [3, 63, 107]. The reason for this is not far-fetched, three-dimensional simulations are computationally very expensive.

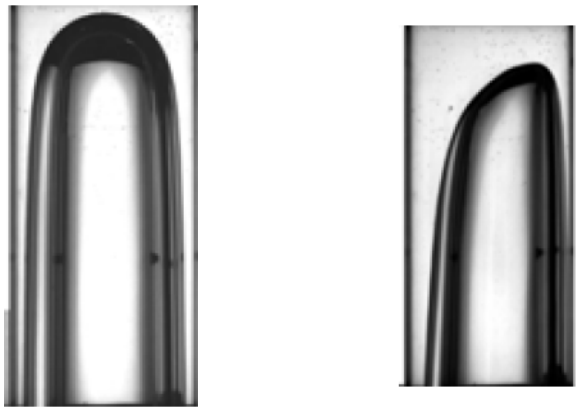
Although, the axisymmetric assumption for a Taylor bubble is generally valid for wide ranges of the dimensionless parameters and flow conditions, experimental evidences have shown that there are instances where transitions are observed, making it difficult to know whether the simulated axisymmetric bubble itself is genuinely stable or it is just a numerical artefact.

1.3 Motivations

Here we highlight some of the transitions that have been observed experimentally in the dynamics of a rising Taylor bubble in stagnant and flowing liquids. For these transitions, experiments are generally limited in the range of parameters investigated and the few numerical and/or theoretical studies that have been carried out are based on very simplifying assumptions and have not been successful in correctly predicting experimental observations.

Asymmetric Taylor bubble in downward liquid flow

The shape of the nose of a rising Taylor bubble plays an important role in determining the rise velocity of the bubble, a very important feature in the hydrodynamic of the bubble because of its significant in developing predictive models for the flow regime [70]. In a downward flowing liquid, the symmetric nature of a rising Taylor bubble shape is lost when the liquid flow velocity exceeds some critical values. This transition to asymmetric bubble shape, shown in Figure 1.3, has been confirmed by experiments in both laminar and turbulent flow conditions [34, 38, 45, 72, 79, 92].



(a) (b)

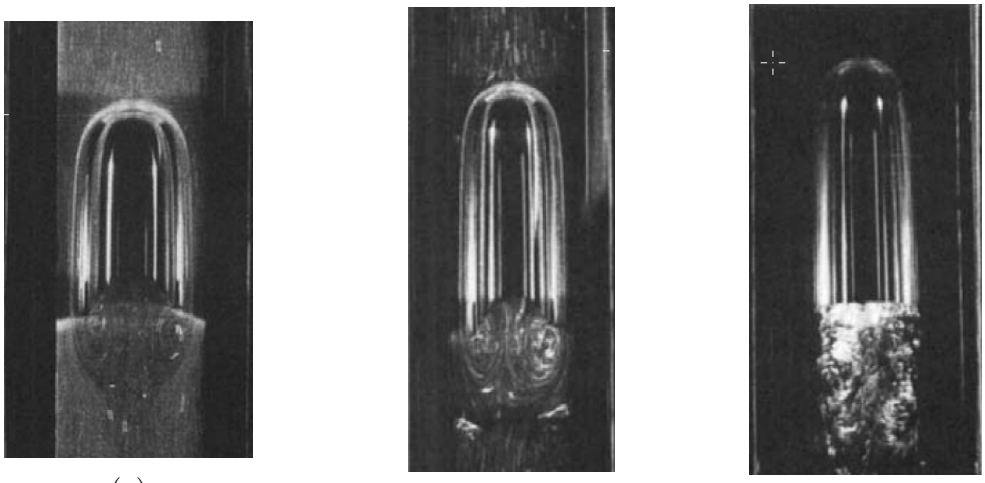
Figure 1.3: Taylor bubble shapes in a (a) stangant ($\bar{U}_L = 0$) and (b) downward flowing liquid ($\bar{U}_L = -0.08$), with $Nf = 71,428.57$ and $Eo = 888.89$. Reproduced from [34]

Because of the transition associated with this flow, it is very important to examine the stability of any axisymmetric numerical simulations of Taylor bubble to confirm their genuineness. In addition, a systematic approach to the role of the dimensionless parameters characterising the flow on the onset of the instability need to be investigated in order to fully understand the mechanism governing this transition.

Taylor bubble wake instability

The wake of a Taylor bubble is a region of intense mixing and its study is important to the understanding of the mechanism governing the interaction and coalescence between Taylor

bubbles [76, 107], and the stability of a trailing bubble [2, 10, 29, 55, 94]. The flow structure in the wake of a Taylor bubble in both stagnant and flowing liquids can either be laminar, transitional or turbulent. Experimentally, it is suggested that the nature of the flow pattern depends only on the inverse viscosity number in stagnant liquids and only on the Reynolds number, defined based on the magnitude of average liquid velocity far ahead of the bubble when viewed in a frame of reference that moves with the bubble, in flowing liquids [19, 82]. This assertion would only be true in sufficient large tubes and for liquid of very low viscosity for which Eo and Nf are large, respectively, leaving several questions unanswered. What impact would a general values of Eo and Nf have on the onset of transitions between the different flow patterns? Is there a limit to the Eo values beyond which the transitions depend only on Nf in stagnant liquids or Re in flowing liquids? Could there be any relationship between the onset of the transitions and the breakup of small bubbles from the bottom of the parent Taylor bubbles?



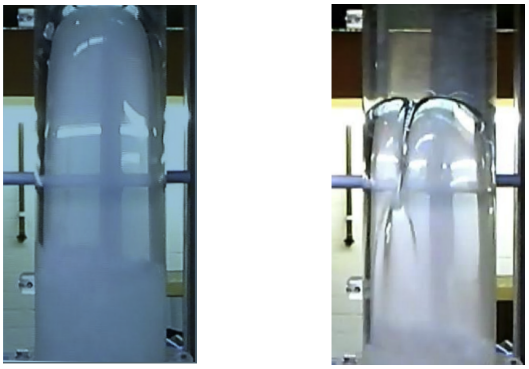
(a) (b) (c)

Figure 1.4: Wake flow patterns behind Taylor bubbles rising through stagnant liquids in a 55 mm pipe: (a) laminar ($Nf = 420$), (b) transitional ($Nf = 520$) and (c) turbulent ($Nf = 11000$). Reproduced from [19]

Taylor bubble breakup in turbulent field

Considering the numerous problems the fluctuating effect associated with the intermittent arrival of slugs has on process plant equipment in the oil and gas industry, a means of completely avoiding the slug flow would significantly reduce the cost of production. Recent experimental

[94] and numerical studies [2, 29] have shown that a single Taylor bubble rising through a quiescent stagnant liquid of low viscosity in *large-diameter* tubes, such that the flow due to the bubble motion is turbulent, rises smoothly and maintains its axisymmetric topology. However, when this bubble rises through a stagnant liquid already disturbed by the turbulent wake left behind by another Taylor bubble that had previously risen, it experiences breakup. The implication of this is that a Taylor bubble rising in tubes with such sizes is unstable to the presence of sufficiently large perturbations, thus Taylor bubble maybe stable when its stability analysis is examined using linear theory but unstable using nonlinear theory. What is the lower limit of pipe size as dictated by Eo above which this instability will occur and what role does the viscosity of the fluid plays as captured by Nf?



(a) (b)

Figure 1.5: Taylor bubble shapes when it rises through a stagnant liquid in a 290 mm pipe in which the liquid ahead is (a) quiescent (no breakup observed) (b) disturbed (breakup observed). Reproduced from [94]

1.4 Aim and objectives

The aim of this research is to examine the stability of an axisymmetric Taylor bubble rising in stagnant and flowing liquids, particularly focussing on studying the transition from symmetric to asymmetric Taylor bubble shape in downward liquid flows under laminar flow condition. The restriction of the study to this particular problem and the flow condition is due to the range of values of the dimensionless parameters examined during the research.

To achieve the research aim, the study is divided into four parts:

1. Develop a mathematical model for a steadily rising Taylor bubble in liquids.

2. Numerically solve the model derived in (1) for different ranges of parameters that characterise the model.

3. Derive a linear stability model for the same problem and use the model to examine the stability of the steady state solutions obtained in (2).

4. Carry out energy budget analysis on the results obtained in (3) and use the result of the analysis to single out the most dominant mechanism that drives the instability observed in (3).

1.5 Thesis outlines

The thesis is structured as follows.

Chapter 2 covers the review of existing studies on a Taylor bubble rising in stagnant and flowing Newtonian liquids, specifically focusing on studies carried out on some of the features of the geometrical regions around a Taylor bubble mentioned in section (1.2) and on studies related to the stability problems described in section (1.3).

Chapter 3 describes the fundamental of finite element method which is the computational method utilised for finding approximate numerical solution to the steady state and the linear stability models. This chapter lays the foundation for chapters (4) and (5) with attention given to how the flow field unknowns, velocity and pressure, and interface unknowns, curvature and interface positions are approximated.

Chapter 4 addresses the first two objectives set out in section (1.4). The derivation and solution of steady state model based on Finite Element Method is addressed and the results of the characterisation of the four topological regions around a Taylor bubble is also covered.

Chapter 5 covers the last two objectives set out in section (1.4); that is the derivation of linear stability and energy budget analyses models and the discussion of the results from both

analyses.

Chapter 6 provides the summary of the entire work, the challenges faced and gives idea on what the future study would be.

Chapter 2

Literature review

It is evident from previous studies [45, 79] that the starting point for the understanding of the two-phase slug flow regime is the study of the behaviour of single Taylor bubble rising through liquids. In this chapter, we briefly review some of the experimental, analytical and numerical studies that have been carried out on the hydrodynamics of a steadily rising Taylor bubble and the transitions encountered.

We begin in section 2.1 highlighting the different dimensionless groups use in characterising the forces that act on a rising Taylor bubble. Section 2.2 discuses the hydrodynamics of Taylor bubble, focusing on rise velocity, film thickness and the wake length, each representing one of the features used in characterising the nose, body and wake topological regions, respectively . This is then followed in section 2.3 with a review of the studies carried out on the stability of Taylor bubbles. Finally, in section 2.4, a summary of the chapter is given.

2.1 Dimensionless groups

The behaviour of a Taylor bubble is governed by the interaction of the different forces that act on it. These forces include gravitational, interfacial, viscous and inertia forces, characterised by the acceleration due to gravity (g), surface tension (γ), viscosity (μ) and liquid velocity

(u), respectively. The relative magnitudes of these forces, defined in terms of a number of dimensionless groups, are used in describing the behaviour of a rising Taylor bubble in liquids. In the previous chapter, we have encountered the inverse viscosity number (Nf), Eötvös number (Eo) and the Froude number (Fr). A few of other commonly used dimensionless groups are the Reynolds number (Re), Morton number (Mo), Archimedes number (Ar) and Poiseuille number (Ps). They are related to the three aforementioned groups as follow:

$$Re = FrNf \tag{2.1}$$

$$Mo = Eo^3 Nf^{-4} \tag{2.2}$$

$$Ar = Nf^2 \tag{2.3}$$

$$Ps = FrNf^{-1} \tag{2.4}$$

More explicitly we can distinguish Reynolds number that is based on the average liquid velocity and the bubble rise velocity

$$Re_b = U_b Nf \tag{2.5}$$

$$Re_L = \bar{U}_L Nf \tag{2.6}$$

Here U_b denotes the Froude number that is based on the bubble rise velocity or simply put, it represents the dimensionless bubble rise velocity.

2.2 Dynamics of a rising Taylor bubble

2.2.1 Rise velocity

The problem of determining the rise velocity of a Taylor bubble rising in a stagnant liquid has been extensively studied by several authors and has been shown that for sufficient long bubbles of several tube diameters in length, the bubble rise velocity is independent of the bubble length [45, 69, 79, 92]. Neglecting the effect of surface tension and assuming an inviscid flow around

the bubble nose, [30] and [28] independently show that the rise velocity of the bubble is given by:

$$u_b = C_0\sqrt{gD} \tag{2.7}$$

Where u_b denotes dimensional bubble rise velocity; g and D, as earlier defined in the previous chapter, represent the acceleration due to gravity and the diameter of the tube through which the bubble rises, respectively. C_0 is a dimensionless proportionality constant.
It can be implied from (2.7), that under the stated assumption, the Froude number based on the bubble rise velocity is a constant. While [30] arrived at a value of 0.351 for U_b, using three terms in the series expansion for the stream function obtained in their solution, [28] reported a value of 0.328, using one term in the series expansion of the same solution. This value is however not unique but depends on the choice of point at which the solution is evaluated and it approaches a value of 0.36 as the point of evaluation gets closer to the bubble nose [15]. This assertion has been confirmed by experimental measurements as the reported range is 0.33-0.36 [24, 43, 79, 92].

Using three dimensionless groups, [114] used a large pool of experimental data generated using different liquids to produce a graphical correlation, Figure 2.1 , depicting regimes where the effect of surface tension, inertia, viscous or combinations of these forces on a bubble rising in stagnant liquid can be neglected. It was established that beyond $Eo > 70$ and $Mo > 3 \times 10^5$, a region now known as inertia regime, surface tension and viscosity have no significant effect on the rise velocity of the bubble. Although later numerical simulations have shown that the limit of surface tension is indeed greater than $Eo = 70$, it can be deduced that the analytical solutions of [30] and [28] correspond to inertia regime.

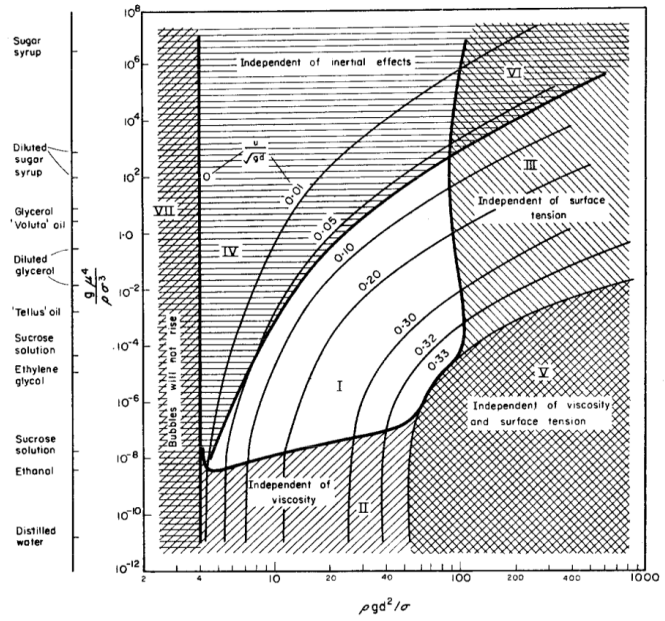


Figure 2.1: Regions showing the limits of the signficance of dimensionless quantities on hydrodynamics of a rising Taylor bubble in stagnant liquid. Reproduced from [114].

Experimental, theoretical and numerical studies [15, 43, 58, 66, 78, 116] have provided further insights on the role of surface tension and viscosity on the rise velocity in both inertia and non-inertia regimes. The rise velocity is a unique function of the radius of curvature at the bubble nose and is dependent on viscosity and surface tension in as much as they change the radius of curvature. Within the limits in which the radius of curvature changes, the effect of both viscosity and surface tension is to reduce the bubble rise velocity. Below we show the correlations of [111], recently modified by [63] to account for the effect of pipe inclinations, and [112] for the prediction of the effect of Eo and Nf on bubble rise velocity,

$$U_b = \frac{0.34\left[1+(14.793/Eo)^{3.06}\right]^{-0.58}}{\left[1+\left(Nf\left[31.08\left(1+(29.868/Eo)^{1.96}\right)^{0.49}\right]^{-1}\right)^{\Theta}\right]^{-1.0295\Theta^{-1}}} \tag{2.8}$$

where

$$\Theta = -1.45\left[1+(24.867\ Eo)^{9.93}\right]^{0.094}$$

and

$$U_b = 0.345\left(1-e^{\frac{-0.01Nf}{0.345}}\right)\left(1-e^{\frac{(3.37-Eo)}{\Upsilon}}\right) \tag{2.9}$$

where

$$\Upsilon = \begin{cases} 25 & \text{if} \quad Nf < 18; \\ 69Nf^{-0.35} & \text{if} \quad 18 < Nf < 250; \\ 10 & \text{if} \quad Nf > 250. \end{cases}$$

respectively.

For a Taylor bubble rising in a flowing liquid in inertia-controlled regime, [79] presented pioneering work from a series of experimental data carried out in a tube of diameter 25.4 mm and proposed a correlation that relates the bubble rise velocity to the mean liquid velocity, which in dimensionless form is given as

$$U_b = C_1 \bar{U}_L + C_0 \tag{2.10}$$

Where C_0 and C_1 are dimensionless constants; $\bar{U}_L$, as earlier defined, denotes Froude number based on mean liquid velocity.

C_0 has a value of 0.35, equivalent to dimensionless bubble rise velocity in a stagnant liquid while the value of C_1 depends on the velocity profile in the liquid into which the bubble is rising and has been shown to equal the ratio of the maximum to mean liquid velocity of the velocity profile [11, 24, 25, 79]. For turbulent flow, $C_1 \approx 1.2$ and it increases with decrease in Reynolds number based on mean liquid velocity, approaching a value of 1.9 at $Re_L = 100$ [79].

Equation (2.10) indicates that the bubble rise velocity in a flowing liquid is a combination of its rise velocity in stagnant liquid and a contribution due to the flowing liquid ahead of the bubble. For upward flowing liquid, the topology of a rising Taylor bubble is similar to what is observed in a stagnant liquid; the bubble is bullet-shaped and axisymmetric [66, 79]. However, for downward flow of liquid, there are situations where Taylor bubble undergoes a change in shape, most often becoming wedge-shaped in an attempt to bypass the fast moving liquid at the tube axis [45, 79].

A theoretical analysis for determining the effect of liquid velocity profile on the rise velocity and shape of Taylor bubble was carried out by [25], neglecting the effect of surface tension.

Specifically, upward liquid flow was considered and analytical expression for computing the rise velocity and radius of curvature at the nose was presented. The analytical solution was later extended by [11] to account for the effect of surface tension. In both studies, the liquid motion far upstream of the bubble was assumed to have a prescribed vorticity, whereas the liquid motion due to the bubble was taken to be inviscid and irrotational. Both studies give support to (2.10).

Numerical simulations are used to complement experimental and theoretical studies. Foremost among the numerical simulations of a rising Taylor bubble was by [69, 70]. The shape of a Taylor bubble, its rise velocity and the velocity profile in the liquid around it was determined by solving the incompressible Navier-Stokes equations using finite volume under the assumption of axial symmetry based on volume of fluid. Since then, a number of numerical simulations in stagnant and flowing liquids have been carried out to compute rise velocity using different discretisation strategies (finite-difference, finite-element and finite-volume), domain spatial configurations (two-dimensional, two-dimensional-axisymentric and three-dimensional) and interface deformation types (interface capturing, interface tracking) [3, 17, 36, 37, 58, 63, 66].

2.2.2 Film thickness

As a Taylor bubble rises through liquid, it displaces the immediate liquid ahead of it, which flows downward as a thin film through the annular space between the interface and the wall of the pipe. As the liquid film flows down the annulus, it accelerates, the boundary layer grows, becoming thicker until a point is reached at which the boundary layer becomes fully developed. Beyond this point, the film is entirely supported by the wall shear stress and the film thickness remains constant. This constant film thickness region, represented as ($2b$) in Figure 1.2, continues until the film approaches the bottom of the bubble.

When the liquid film flowing down a surface is thin, the local curvature of the surface can be neglected and the behaviour of the liquid film can be taken to be the same as that of a liquid falling down a plane surface [59, 64]. The liquid film around a Taylor bubble rising in

liquids with low viscosity can be considered to be thin and on that basis, [43], theoretically derived (2.11) that relates the dimensionless film thickness in the fully developed region around a Taylor bubble, Δ_f, to the bubble rise velocity, under the assumption that the flow is laminar.

$$U_b = \frac{4}{3} N f \Delta_f^3 \tag{2.11}$$

Equation (2.11) was later extended by [15] to account for the effect of viscosity by relaxing the thin film assumption to give

$$U_b = \frac{4}{3\left(1 - 2\Delta_f\right)} N f \Delta_f^3 \tag{2.12}$$

which is identical to the relation derived by [9] and whose solution for film thickness can be written as [15, 64]

$$\Delta_f = \frac{-1 + \sqrt{1+N}}{N} \tag{2.13a}$$

$$N = \left[\frac{16}{9U_b^2} N f^2\right]^{\frac{1}{3}} \tag{2.13b}$$

It is noteworthy that the length scale used in non-dimensionalising the film thicknss is the tube diameter. In addition, we note that equations (2.13a) and (2.13b) represent the generalised dimensionless forms of equations (16) and (17) in [15], respectively. The dimensionless form of equation (17) in [15] can be obtained from (2.13b) by substituting $U_b = 0.35$. Neglecting the idea of constant U_b assumed by [15], [64] solves a cubic equation derived from (2.12) for film thickness to give (2.14), which the author termed cubic brown model.

$$\Delta_f = \frac{1}{2} \frac{\sqrt[3]{\left(9w + \sqrt{12w^3 + 81w^2}\right)^2} - \sqrt[3]{12w}}{\sqrt[3]{18\left(9w + \sqrt{12w^3 + 81w^2}\right)}} \tag{2.14a}$$

$$w = 6\frac{U_b}{Nf} \tag{2.14b}$$

Equations (2.13) and (2.14) have the advantage that when used together with (2.8) or (2.9), they can be used to account for the effect of Eo and Nf on film thickness.

A number of theoretically models derived for thin falling films on surfaces that are not necessarily related to Taylor bubble can be used to estimate the fully developed film thickness around Taylor bubble for both laminar and turbulent flows. Details of these models and their performances in film thickness prediction are available in [64]. While there exist a number of theoretical models that can be used to estimate the equilibrium thickness of the falling film around a Taylor bubble rising in both stagnant and flowing liquids, there are only a few experiments [64, 81] and numerical simulations [4, 58] that have been carried out to systematically obtain quantitative data. Figure 2.2 shows the effect of Nf on the equilibrium film thickness.

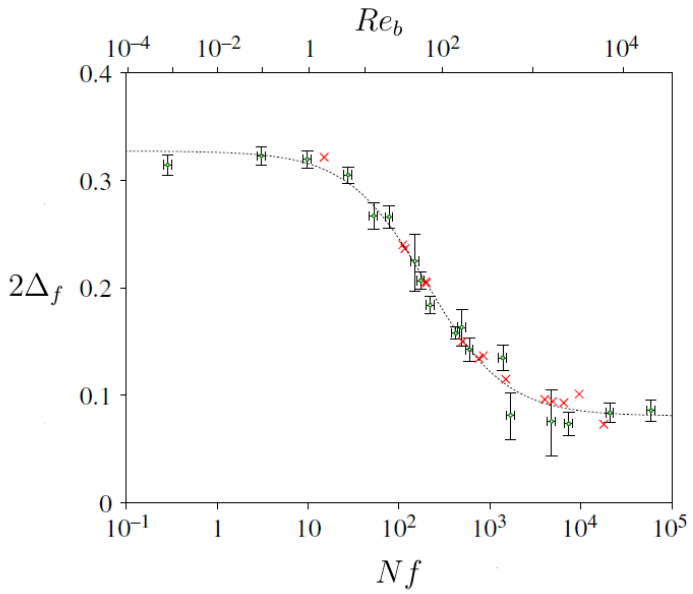


Figure 2.2: Effect of Nf or Re_b on equilibrium film thickness. Adapted from [64].

2.2.3 Wake length

The wake is characteristically a region of intense mixing, the understanding of which is very crucial to the modelling of the slug flow regime [35]. Because the rise velocity of a Taylor bubble depends on the velocity profile of the liquid ahead of it, and since the slug flow regime involves a train of Taylor bubbles, the nature of the flow in the wake region of a leading Taylor bubble plays an important role in understanding the behaviour of a trailing bubble, in explaining the interaction and coalescence mechanisms between two successive Taylor bubbles [82, 90, 107] and in the stability of a trailing bubble [2, 10, 29, 55, 94].

Early studies on the flow of the wake region were conducted by [76]. Through measurement of the velocity profiles at various distances behind a Taylor bubble, it was postulated that the flow pattern in the wake of a leading bubble disturbs the dynamics of the trailing Taylor bubble. This was later observed by [73], who utilised a relatively simplistic visualization technique to demonstrate how separated liquid flow exists at the rear end of a Taylor bubble.

Systematic photographic study of the flow in the wake of individual Taylor bubbles rising through stagnant liquids was carried out by [19] in tubes of 19 mm and 52 mm diameters. Their study covered a wide range of viscosities (10^{-3} to $10^{-1} N s m^{-2}$) which correspond to the regime where inertia is dominant. Since, in the inertia regime, the dimensionless bubble rise velocity in a stagnant liquid is a constant and the effect of surface tension on the dynamics of the bubble is negligible, it was postulated that the wake flow pattern is determined by Nf, and can be classified into three distinct patterns; laminar, transitional and turbulent flow patterns.

Laminar wake regime : This regime is defined for values of $Nf < 500$. Under this condition, the wake region is axisymmetric and closed, consisting of an internal toroidal vortex.

Transitional wake regime : This regime is defined for values of $500 < Nf < 1500$. For this range, a closed wake region still exists but is no longer axisymmetric, now consisting of a vortex ring that oscillates at higher frequencies with increasing Nf.

Turbulent wake regime : This regime is defined for values of $Nf > 1500$. Here, the wake does not have clearly defined boundaries but with visible recirculation regions which disappear as the Nf is increased, giving rise to the emergence of turbulent eddies.

In addition to classification of the flow patterns, the following relationships are proposed for the dimensionless wake length and wake volume :

$$L_w = 0.30 + 1.22 \times 10^{-3} Nf \qquad 100 < Nf < 800 \tag{2.15}$$

$$V_w = 7.5 \times 10^{-4} Nf \qquad 100 < Nf < 500 \tag{2.16}$$

Extending the characterisation to a rising Taylor bubble in an upward flowing liquid, [91] proposed that the emerging profile from the wake of the bubble develops so as to restore the original profile in the liquid far ahead of the bubble, be it laminar or turbulent. If we let V_L be the average liquid velocity far ahead of the bubble in a frame of reference that moves with the velocity of bubble rising in upward flowing liquid with average velocity U_L, then $V_L = (C_1 - 1)\,\bar{U}_L + U_b$.

$$Re_{V_L} = (C_1 - 1)\,Re_L + Re_b, \tag{2.17}$$

Defining a Reynolds number based on V_L, Re_{V_L} as in (2.17), the limits for the characterisation of the wake flow pattern are expressed as

Laminar wake regime : wake is closed and axisymmetric with internal toroidal vortex.

$$Re_{V_L} < 175 \tag{2.18}$$

Transitional wake regime : wake is closed but not axisymmetric, with internal toroidal vortex observed.

$$175 < Re_{V_L} < 525 \tag{2.19}$$

Turbulent wake regime : wake is open and perfectly mixed.

$$Re_{V_L} > 525 \tag{2.20}$$

and have been validated experimentally by [82] for a Taylor bubble rising in a stagnant and flowing liquid. In 2.17, Re_L and Re_b, as previously defined, denote Reynolds numbers based on average liquid velocity and bubble rise velocity, respectively.

2.3 Stability of a rising Taylor bubble

While a lot of experimental, theoretical and numerical investigations have been carried out in predicting the shape, rise velocity and velocity field around a rising Taylor bubble in a motionless

or flowing liquid, not much has been done in the area of systematically studying some of the transitions observed in the dynamics of a rising Taylor bubble. One of such transitions is the change from axisymmetric to asymmetric wake flow patterns reviewed in the previous section. In this section, we review the existing studies on the loss of axial symmetry of Taylor bubble shape in downward liquid flow and the breakup of Taylor bubble in a turbulent field.

2.3.1 Taylor bubble in downward liquid flow

A Taylor bubble rising in a stagnant and upward flowing liquid, as earlier stated is generally axisymmetric and rises with a constant velocity in inertia dominated regime. This is not always the case in downward liquid flow. In the experiment conducted by [45] in tubes of diameter 25.4 mm, 19.05 mm and 12.7 mm using air and water, it was observed that the axial stability of Taylor bubble was lost as the downward liquid flow was increased beyond a limit. The bubble nose become distorted, and in an attempt to avoid the fast moving fluid at the centre of the tubes, the bubble had to move closer to the wall of the tube [79], rising much faster than it would have been if it were symmetric [72, 92].

Extensive investigation was first carried out by [72] in tubes of diameters 101.6 mm, 140 mm and 260 mm and it was confirmed that the behaviour of Taylor bubble in downward liquid flow is very much different from that in upward liquid flows. It was stated that a stable Taylor bubble in downward liquid flow can only be observed in tubes where surface tension effect is very large (i.e small diameter tubes defined by low Eo values) and the absolute value of the downward velocity at which a bubble lost its stability decreases with increase in tube diameter.

Motivated by the aforementioned observations, [65] carried out linear stability analysis to establish the condition at which the symmetry of a Taylor bubble shape breaks with respect to the axis in downward liquid flow. In their analysis, effect of surface tension was neglected and a potential flow around the bubble nose was assumed. Using one-term approximation from the series expansion for the stream function solution of [25] as a base flow, they demon-

strated that an axisymmetric Taylor bubble rising in a liquid with laminar velocity profile, subjected to irrotational perturbations becomes unstable when the downward flowing velocity equals $-0.13\sqrt{gD}$. The reason given for this occurrence is that the relative velocity between the bubble and the liquid decreases with increasing downward flow, leading to the bubble nose becoming flattened. Both conditions have a destabilizing effect as the stabilisation associated with the convective flow of liquid around the bubble nose is reduced.

Two dimensional numerical experiment was carried out by [39] to determine the stability of a plane Taylor bubble rising in a flowing liquid with laminar velocity profile and to quantify the effect of surface tension. For a fixed value of surface tension parameter, increasing downward velocity of flow has the same effect as observed by [65]. For the range of surface tension parameter studied $57.14 \leq Eo \leq 400$, it was shown that surface tension has stabilisation effect on the loss of axial symmetry by increasing the value of the downward velocity at which the transition occurs. The numerical simulations also confirms the observation that asymmetric bubbles rise much faster than their symmetric counterparts for the same liquid velocity profile far upstream of the bubble nose. In addition, unlike symmetric bubbles, the dynamics of asymmetric bubbles is very sensitive to surface tension parameter.

Following on the numerical simulation of [39], [34] performed experimental investigations in tubes of diameters 20, 40 and 80 mm. Both instances of Taylor bubble rising against laminar and turbulent flowing liquids were investigated. Complemented by numerical simulations using the boundary element method of [48], they showed that the curvature radius at the nose of the bubble plays a key role in the stability of Taylor bubble and that the onset of instability is dependent on the surface tension parameters. By neglecting surface tension, [65] overestimate the onset of instability. It was also argued that the correct bifurcation parameter that governs the transition to asymmetry bubble is the vorticity to radius ratio along the axis of symmetry and the dependency of its critical value at the onset of transition on surface tension is

$$\Pi = -\left(30Eo^{-1} + 0.06\right) \pm 0.07 \tag{2.21}$$

which is independent of whether the flow is laminar or turbulent. In (2.21), Π denotes the vorticity to radius ratio evaluated along the axis of symmetry far ahead of the bubble in a frame of reference moving with the bubble velocity. Given the dimensionless velocity profile for velocity far upstream of the bubble in laminar flow and turbulent flow as

$$u_z = U_m \left[1 - 4r^2\right] \tag{2.22}$$

and

$$u_z = U_m \left[1 - 4\xi r^2 - 2^{2n} \left(1 - \xi\right) r^{2n}\right], \tag{2.23}$$

the expressions for the vorticity in axisymmetric flow are

$$vorticity = -8U_m r \tag{2.24}$$

and

$$vorticity = -2U_m r \left[4\xi + 2^{2n} n \left(1 - \xi\right) r^{2(n-1)}\right] \tag{2.25}$$

and therefore, the vorticity-radius ratios evaluated at the axis of symmetry are

$$\Pi = -8U_m \tag{2.26}$$

and

$$\Pi = -8\xi U_m, \tag{2.27}$$

respectively. Equations (2.23) represents the Pai approximation for turbulent velocity [11, 25] and ξ and n are parameters that are dependent on the Reynolds number of the turbulent flow. From (2.26) it is clear that for laminar flow there is no clear cut difference between vorticity-radius ratio and tube-center velocity as a bifurcation parameter other than the factor -8. Also, (2.26) and (2.27) indicate that the parameter ξ is what distinguishes the bifurcation parameter for laminar and turbulent flow and responsible for the unifying nature of vorticity-radius as a bifurcation parameter.

2.3.2 Taylor bubble in turbulent field

Slug flow, as earlier stated and shown in Figure 1.1, is one of the flow regimes that is observed when gas and liquid flow together in vertical pipes and is characterised by intermittent flow of Taylor bubbles and liquid slugs. For gas-liquid flows in sufficiently *large diameter* pipes, say greater than 100 mm, using liquid of low viscosity, Taylor bubbles are not observed and hence the conventional slug flow regime is absent. What is seen is a direct transition from bubbly flow to churn flow [1, 84–86]. This suggests that Taylor bubbles are unstable under such conditions.

To gain insights into the limiting conditions for the existence of slug flow in vertical pipes, [55] examine the stability of single Taylor bubble in pipes of $12.7 - 356\ mm$ diameters in stagnant liquid when the flow field ahead of the bubble is quiescent and disturbed. It was observed that insofar as the liquid into which the bubble rises is quiescent, the bubble remains stable for all the pipe diameters. However, when a bubble rises into a disturbed field created either by the wake of a previous Taylor bubble that has risen, by convective cells due to temperature gradient in the liquid or by pressure pulsation due to expansion and contraction of the bubble as it rises, the bubble experienced breakup. Although, no explicit detail was given on the nature of the flow in the study, studies [72, 94] have shown that flow due to a rising Taylor bubble in low viscosity liquid in large diameter pipes is generally turbulent.

Similar observations to that of [55] were made by [94]. Taylor bubbles were found to be stable in pipes of diameters 121 and 290 mm, and flows in both pipes were confirmed to be turbulent. For two consecutive bubbles, they found that a settling time of $\sim 50\ s$, corresponding to a separation distance of about 30 m, is required for the attenuation of the turbulent eddies left behind by the wake of the leading bubble in order to observe a stable trailing bubble in the 290 mm pipe. Whenever the settling time is less than $50\ s$, the trailing bubble breaks up. It is evident that it is the encountering of turbulent eddies that triggers bubble breakup. The possibility therefore exist, that breakup of Taylor bubble could be observed in pipes with diameter that are smaller than $100\ mm$ if the bubble encountered turbulence in such pipes, or to have a stable Taylor bubble in much larger pipes if the viscosity of the fluid is large enough

as to suppress turbulence. The former postulation is corroborated by the recent experimental study of [38] in downward liquid flow in pipe of 44 mm, in which it was reported that gas part was ripped off from Taylor bubble nose and dispersed as small bubbles into the wake when it encountered turbulent eddies that propagated downward from the pipe inlet.

Theoretical investigations into the existence of maximum size beyond which a bubble rising in liquid is unstable have been reported [10, 24, 44]. Of particular interest is the study of [10] where it is estimated that the maximum pipe diameter that can sustain a stable Taylor bubble is 460 mm. Although the limit has not been reported to be experimentally confirmed, numerical investigation carried out by [29], shown in Figure 2.3, shows that it is possible to obtain a stable Taylor bubble in pipe of 500 mm if the liquid is quiescent and it breaks up in smaller diameter tube, just as observed in experimental studies, when it encounters turbulence generated by the wake of a previous bubble that has risen. It is clear that the theoretical study of [10] has not been able to accurately predict the critical conditions for the non-existent of slug flow regime or for a single Taylor bubble breakup. This could possibly be because the analysis was based on potential flow assumption and the effect of surface tension was neglected. Moreover, the predicted 460 mm was based on the assumption that the estimated initial disturbance magnitude that corresponds to the maximum spherical-cap bubble observed by [109] quoted in [10], which was 150 mm, in a large tank of water, holds for a Taylor bubble rising a stagnant liquid for air-water system.

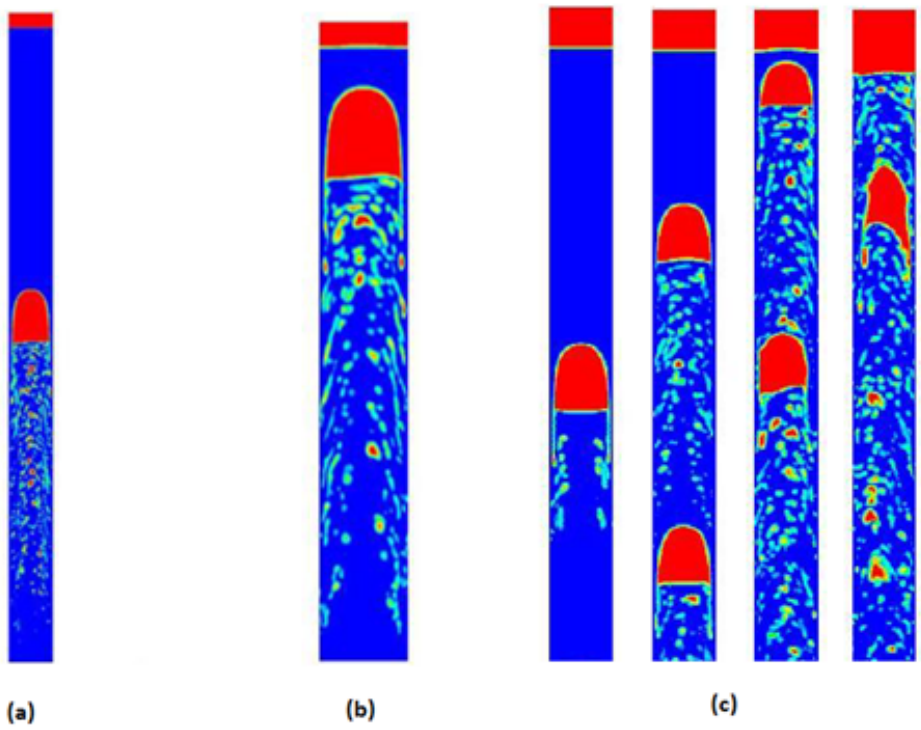


Figure 2.3: CFD simulation of Taylor bubble rise in a stagnant liquid in pipes of diameter (a) 400 mm (b) 500 mm (c) 400 mm. Adapted from [29].

2.4 Summary

We have reviewed some of the existing studies on Taylor bubble steady state features and Taylor bubble stability in stagnant and flowing liquids. Features such as bubble rise velocity, equilibrium film thickness and wake length, which are key in defining the dynamics of the nose, film and wake regions, respectively, were considered. Existing studies have shown that a lot has been done, experimentally, theoretically and numerically in the area of systematic study of bubble rise velocity, particularly in the inertia dominated regime. However, much more need to be done for the equilibrium film thickness and wake length. For stability of Taylor bubbles, it is clear that numerical study remains the viable option towards understanding the mechanism governing the various transitions reviewed, since experimentation of the wide parameter space is very expensive and theoretical investigation requires making simplifying assumptions. It is also evident that the few theoretically studies that have been carried out have not been able to

correctly predict the experimental results that have been reported for transition from symmetric to asymmetric Taylor bubble shape in downward liquid flow and the breakup of Taylor bubble in turbulent field. Therefore, it is desirable that an analysis of the stability of a Taylor bubble using the full equations of motion be carried out. Although, the existing studies on Taylor bubble, particularly the stability of Taylor bubble, focussed largely on inertia regime, there is need for investigation of the parameter space where both viscous and surface tension effects are important.

Chapter 3

Computational development

In chapter (1), we outlined the objectives of the research which essentially involve developing and numerical solving the mathematical models that describe, a steadily rising Taylor bubble in liquids and a Taylor bubble that has its steady state solution perturbed. These models are generally coupled, partial differential equations that govern the evolution of velocity components and pressure, and can be solved using different numerical methods. In addition to flow field variables, velocity and pressure, we have the interface between the fluid phases as an unknown. We mentioned in passing in the previous chapters that our numerical method of choice is finite element method. This choice is based on the capability of the method to handle complex deforming domain and the ease with which the steady state and linear stability analysis computations can be seamlessly handled within the same framework.

The finite element method is an *element-wise* application of the classical variational and weighted-residual methods. It is based on the idea that a given domain can be viewed as an assemblage of simple geometric shapes, called *finite elements*, around which the solution of a differential equation can be approximated in a *weak* sense [99].

In this chapter, the description of the problem to be solved is given in section (3.1) and the governing equations and boundary conditions are presented in section (3.2). Section (3.3) de-

scribes the derivation of the *weak-form* of the governing equations, which is the first step in the solution of the governing equations using finite element method. This is immediately followed by descriptions of the approximations of the variables of the problem, which are the flow field variables, velocity and pressure, covered in section (3.4) and the interface variables, which are interface positions and curvature, covered in sections (3.5) and (3.6), respectively. Finally, the interpolation functions used for all the variables are described in section (3.8) and a summary of the entire chapter given in (3.9).

3.1 Problem description

Taylor bubble of constant volume V_b characterise by length L_b rising at a constant velocity of magnitude U_b through an incompressible fluid of density ρ, viscosity μ and constant interfacial tension γ in a vertical pipe of radius R is considered and assumed to be axisymmetric. This assumption, as stated in chapter (1), is generally true for a wide range of dimensionless parameters and flow conditions in stagnant and flowing liquids. For conditions where the assumption is invalid, it is expected that the steady state solution for the bubble, addressed in chapter 4, should be unstable to the addition of small perturbations when its stability, which is the focus of chapter 5, is examined. In addition, it is also assumed that the density, ρ_g, and viscosity, μ_g, of the gas phase (the bubble) are very small compared to those of the liquid. By these assumptions, the dynamics in the gas phase is approximated to a constant pressure P_b and the influence of the gas phase is therefore restricted to the interface between the liquid and the gas phase Γ_b . As a result, only the flow fields in the liquid phase and the bubble pressure are determined. This concept of constant bubble pressure in the gas phase is relatively common in the literature [6, 40, 110, 115] and have been shown to reasonably describe the dynamics of Taylor bubbles [36, 58, 66].

A typical rising Taylor bubble is depicted in Figure 3.1. Cylindrical co-ordinates system is adopted, so that the coordinates along and perpendicular to the axis of symmetry are z and r, respectively, with the origin of z chosen at the nose of the bubble. The positive sense for the

spatial coordinates, r and z are taken to be right and downward, respectively.

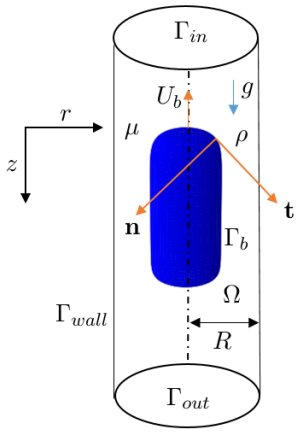


Figure 3.1: Depiction of a Taylor bubble rising through a stagnant liquid.

The problem therefore is to find the rise velocity, U_b, pressure, P_b and shape of a Taylor bubble as it rises through a liquid of density ρ, viscosity, μ and interface tension γ in a pipe of diameter $D = 2R$ so that its volume, V_b, remains constant and then to examine whether the solution is stable to the addition of small disturbance to the shape and the flow fields around it.

3.2 Governing equations and non-dimensionalisation

The motion of a fluid is govern by the global mass, momentum and energy conservations laws. For an isothermal flow, where the effects of temperature can be neglected, the motion of an incompressible Newtonian fluid in a domain $\Omega(t)$ with boundary $\Gamma(t)$ is govern by the time dependent Navier-Stokes and continuity equations. These equations, as mentioned in the introductory part of this chapter, comprise a set of coupled, nonlinear, partial differential equations that relates the velocity components and pressure of the fluid. If length, velocity and pressure variables in these equations are non-dimensionalised by the characteristic length, velocity and pressure scales, taken to be D, $\sqrt{gD}$ and ρgD, respectively, the equations in a frame translated with the velocity $\mathbf{u}_b$ of the bubble nose can be written compactly in dimensionless forms as:

$$\frac{\partial \mathbf{u}}{\partial t} + (\mathbf{u} \cdot \nabla)\,\mathbf{u} - \nabla \cdot \mathbf{T} = \mathbf{0} \qquad \text{in} \qquad \Omega(t) \tag{3.1}$$

$$\nabla \cdot \mathbf{u} = 0 \qquad \text{in} \qquad \Omega(t) \tag{3.2}$$

Here Ω denotes the domain of interest, $\mathbf{u}$ is the velocity vector of the fluid in the moving frame of reference, $\frac{\partial}{\partial t}$ is partial derivative with respect to time, $\mathbf{T}$ is the stress tensor and ∇ is the gradient operator which for cylindrical coordinates system, (r, θ, z), is

$$\nabla = \mathbf{i}_r \frac{\partial}{\partial r} + \mathbf{i}_\theta \frac{1}{r} \frac{\partial}{\partial \theta} + \mathbf{i}_z \frac{\partial}{\partial z} \tag{3.3}$$

In equation (3.3), $\mathbf{i}_r$, $\mathbf{i}_\theta$ and $\mathbf{i}_z$ are the unit vectors in the radial, azimuthal and axial directions, respectively. The constitutive equations that relate the variables of the governing equations to the stress tensor are

$$\mathbf{T}(\mathbf{u}, p) = -p\mathbf{I} + 2Nf^{-1}\mathbf{E}(\mathbf{u}) \tag{3.4}$$

$$\mathbf{E}(\mathbf{u}) = \frac{1}{2}\left[\nabla(\mathbf{u}) + \nabla(\mathbf{u})^T\right] \tag{3.5}$$

$$\mathbf{E}(\mathbf{u}) = \begin{bmatrix} \frac{\partial u_r}{\partial r} & \frac{1}{2}\left(\frac{1}{r}\frac{\partial u_r}{\partial \theta} - \frac{u_\theta}{r} + \frac{\partial u_\theta}{\partial r}\right) & \frac{1}{2}\left(\frac{\partial u_r}{\partial z} + \frac{\partial u_z}{\partial r}\right) \\ \frac{1}{2}\left(\frac{1}{r}\frac{\partial u_r}{\partial \theta} - \frac{u_\theta}{r} + \frac{\partial u_\theta}{\partial r}\right) & \frac{u_r}{r} + \frac{1}{r}\frac{\partial u_\theta}{\partial \theta} & \frac{1}{2}\left(\frac{\partial u_\theta}{\partial z} + \frac{1}{r}\frac{\partial u_z}{\partial \theta}\right) \\ \frac{1}{2}\left(\frac{\partial u_r}{\partial z} + \frac{\partial u_z}{\partial r}\right) & \frac{1}{2}\left(\frac{\partial u_\theta}{\partial z} + \frac{1}{r}\frac{\partial u_z}{\partial \theta}\right) & \frac{\partial u_z}{\partial z} \end{bmatrix} \tag{3.6}$$

where p represents the dynamic pressure, $\mathbf{I}$ is the unit tensor, Nf, as mentioned in section (1.2), is the dimensionless inverse viscosity number, $\mathbf{E}$ is the rate of deformation tensor and $(.)^T$ is the transpose operator; u_r, u_θ and u_z are the components of the velocity vector $\mathbf{u}$ in the radial, azimuthal and axial directions, respectively.

To make the problem represented by the system of equations $(3.1 - 3.6)$ well posed and the solution unique, appropriate boundary conditions have to be given at the boundary of the domain, Γ, which can be divided into Γ_{in}, Γ_{out}, Γ_{wall} and Γ_b as shown in Figure 3.1 . The subscripts *in*, *out*, *wall* and *b* stand for the inlet, outlet, wall and bubble boundaries, respectively. At the wall, no-slip and no-penetration boundary conditions are imposed

$$\mathbf{u} = -\mathbf{u}_b \quad \text{on} \quad \Gamma_{\text{wall}} \tag{3.7}$$

At the inlet, prescribed values are specified for the velocity components, which for the stagnant liquid are zeros and for flowing liquid, only the axial component is non zero.

$$\mathbf{u} = \mathbf{u}_{in} - \mathbf{u}_b \quad \text{on} \quad \Gamma_{\text{in}} \tag{3.8}$$

Boundary conditions of the types at the wall and inlet where the values of the primary variables are specified are called *Dirichlet*, or *essential* boundary conditions. At the outlet of the domain, we imposed a zero traction condition, also known as outlet condition,

$$\mathbf{n} \cdot \mathbf{T} = \mathbf{0} \quad \text{on} \quad \Gamma_{\text{out}} \tag{3.9}$$

As an alternative to equation (3.9), the following conditions can be used

$$\mathbf{n} \cdot \mathbf{T} \cdot \mathbf{n} = 0 \tag{3.10a}$$

$$(\mathbf{I} - \mathbf{n} \otimes \mathbf{n}) \cdot \mathbf{u} = \mathbf{0} \tag{3.10b}$$

Here $\otimes$ denotes tensor product, $\mathbf{n}$ is the unit normal vector to the boundary and $(\mathbf{I} - \mathbf{n} \otimes \mathbf{n})$ is an operator that extracts the tangential component of a vector.
Equations (3.10a) and (3.10b) enforced that the normal stress, which is the sum of pressure and viscous stress, and the tangential projection of the velocity at the outlet boundary are zeros, respectively. These conditions are particularly useful on a boundary where it is certain that the flow is fully developed, which holds for the problem under consideration. Finally, at the interface between the gas and the liquid phases,

$$\mathbf{n} \cdot \mathbf{T} \cdot \mathbf{n} + P_b - z - Eo^{-1}\kappa = 0 \tag{3.11}$$

$$\mathbf{n} \cdot \mathbf{T} \times \mathbf{n} = \mathbf{0} \tag{3.12}$$

$$\frac{d\mathbf{r}_b}{dt} \cdot \mathbf{n} - \mathbf{u} \cdot \mathbf{n} = 0 \tag{3.13}$$

where κ is the curvature of the interface, $\mathbf{r}_b(t)$ represents the position vector of all the points

on the portion of the boundary that corresponds to the interface, Γ_b, z is the axial component of the spatial coordinates and Eo is the dimensionless Eötvös number, defined earlier in chapter (1).

The interface equations (3.11), (3.12) and (3.13) are the normal stress, tangential stress and kinematic boundary conditions. It should be noted that gravity appears in (3.11) as z because the hydrostatic component of the pressure has been subtracted from the total pressure, leaving only the hydrodynamic part. A close look at the system of equations $(3.1 - 3.13)$, shows that the system is similar to what would be obtained for free surface flow; the only difference being that in place of ambient pressure, P_a, we have bubble pressure, P_b, in equation (3.11). Hence, existing methods reported in the literature for solving free surface flow can be adapted to solve the problem.

In order to determine the dimensionless bubble pressure, the constraint that the dimensionless bubble volume, V_b, remains constant is imposed.

$$V_b + \frac{1}{3}\oint_{\Gamma_b} [\mathbf{r}_b \cdot \mathbf{n}]\, d\Gamma_b = 0 \tag{3.14}$$

In arriving at equation (3.14), we have made used of the Gauss' theorem which states that for any vector $\mathbf{a}$ in a closed domain,

$$\int \nabla \cdot \mathbf{a} dV = \oint \mathbf{a} \cdot \mathbf{n} dS \tag{3.15}$$

It should be noted that in equations $(3.11) - (3.14))$, the orientation of the unit tangent on the boundaries is such that the domain occupied by the liquid is on its left as we navigates around the boundary in anticlockwise direction and the unit normal points outward.

3.3 Weak formulations

In the previous section, we stated the governing equations for the problem along with the boundary conditions. These equations describe the continuous form of the problem. General solutions to problems formulated in this manner are rarely possible for situations of interest in science and engineering. To solve the system of partial differential equations $(3.1 - 3.2)$ under the boundary conditions $(3.7 - 3.14)$ using finite element method, the equations have to be transformed into their *weak forms*, the dependent variables in the equations approximated using suitable basis functions and the domain divided into subdomains around which the approximated variables are defined. The final result is a set of algebraic relations among the unknown parameters of the approximations, known as *finite element models* of the equations.

In this section, the transformation of the governing equations into their weak forms is described. This basically involves three steps; multiplying the governing equations for each variables with their corresponding *test functions* and integrating over the domain, integrating by part to reduce the order of integration and finally, incorporating the boundary conditions into the resulting relations. Before proceeding to derive the weak forms of the equations, it is important to define the necessary functional spaces to which the solution and test functions must belong [51].

1. The $L^2(\Omega)$ space: This is a space of functions $f(\mathbf{r})$ defined in Ω that are square integrable over Ω

$$L^2(\Omega) = \left\{ f(\mathbf{r}) \,|\, \int_\Omega \left(f(\mathbf{r})\right)^2 d\Omega < \infty \right\} \tag{3.16}$$

2. The $L_0^2(\Omega)$ subspace: This is a subspace of $L^2(\Omega)$ defined in Ω such that for functions defined in $L^2(\Omega)$, the following equation is satisfied

$$L_0^2(\Omega) = \left\{ f | f \in L^2(\Omega) \text{ and } \int_\Omega f(\mathbf{r}) = 0 \right\} \tag{3.17}$$

3. The Sobolev space $H^1(\Omega)$: This is a space of functions $f(r,z)$ defined in Ω such that both the function and all its first partial derivatives are in $L^2(\Omega)$

$$H^1(\Omega) = \left\{ f(r,z) \,|\, \int_\Omega \left[f^2 + \left(\frac{\partial f}{\partial r}\right)^2 + \left(\frac{\partial f}{\partial z}\right)^2 \right] d\Omega < \infty \right\} \tag{3.18}$$

4. The Sobolev subspace $H_0^1(\Omega)$: This is a subspace of the Sobolev space $H^1(\Omega)$ for which the functions defined in space H^1 vanish on the portions of the boundary of Ω where *Dirichilet* boundary conditions are imposed (i.e $\Gamma_D = \Gamma_{in} + \Gamma_{wall}$).

$$H_0^1(\Omega) = \left\{ f | f \in H^1(\Omega) \text{ and } f(\mathbf{r}) = \mathbf{0} \text{ if } \mathbf{r} \in \Gamma_D \right\} \tag{3.19}$$

Let $\mathbf{\Phi} \in H_0^1$ and $\varphi \in L_0^2$ be the test functions corresponding to $\mathbf{u} \in H^1$ and $\mathrm{p} \in L^2$, respectively. Next we take the inner product of equation (3.1) with $\mathbf{\Phi}$, multiply equation (3.2) with φ and integrate the equations over the domain.

$$\int_\Omega \left\{ \frac{\partial \mathbf{u}}{\partial t} \cdot \mathbf{\Phi} + [(\mathbf{u} \cdot \nabla)\,\mathbf{u}] \cdot \mathbf{\Phi} - [\nabla \cdot \mathbf{T}] \cdot \mathbf{\Phi} \right\} d\Omega = 0 \tag{3.20}$$

$$\int_\Omega \{(\nabla . \mathbf{u})\,\varphi\}\, d\Omega = 0 \tag{3.21}$$

Equations (3.20) and (3.21) are the weighted residual forms of the momentum and continuity equations, respectively. Integrating the last term on the left side of (3.20) by part,

$$\int_\Omega \{[\nabla \cdot \mathbf{T}] \cdot \mathbf{\Phi}\}\, d\Omega = \int_\Gamma \{\mathbf{n} \cdot \mathbf{T} \cdot \mathbf{\Phi}\}\, d\Gamma_b - \int_\Omega \{\mathbf{T} : \nabla(\mathbf{u})\}\, d\Omega \tag{3.22}$$

where

$$\Gamma = \Gamma_b + \Gamma_{in} + \Gamma_{wall} + \Gamma_{out}$$

Enforcing the outlet boundary condition (3.9) and taking into consideration that $\mathbf{\Phi} \in H_0^1$, hence $\mathbf{\Phi}$ are zero where *essential* boundary conditions are imposed, we are left with

$$\Gamma = \Gamma_b$$

Making use of (3.4), equation (3.20) becomes

$$\int_{\Omega}\left\{\frac{\partial \mathbf{u}}{\partial t}\cdot\mathbf{\Phi}+\left[\left(\mathbf{u}\cdot\nabla\right)\mathbf{u}\right]\cdot\mathbf{\Phi}+2Nf^{-1}\mathbf{E}\left(\mathbf{u}\right):\mathbf{E}\left(\mathbf{\Phi}\right)-p\left(\nabla.\,\mathbf{\Phi}\right)\right\}d\Omega-\int_{\Gamma_b}\left\{\mathbf{n}\cdot\mathbf{T}\cdot\mathbf{\Phi}\right\}d\Gamma_b=0 \tag{3.23}$$

The traction term in the last term on the left hand side of (3.23) can be decomposed into its normal and tangential components [93]

$$\mathbf{n}\cdot\mathbf{T}=\left[\mathbf{n}\cdot\mathbf{T}\cdot\mathbf{n}\right]\mathbf{n}+\mathbf{n}\times\left[\mathbf{n}\cdot\mathbf{T}\times\mathbf{n}\right] \tag{3.24}$$

thereby allowing the incorporation of normal stress condition (3.11) and tangential stress condition (3.12) into (3.23) to give

$$\begin{aligned}&\int_{\Omega}\left\{\frac{\partial \mathbf{u}}{\partial t}\cdot\mathbf{\Phi}+\left[\left(\mathbf{u}\cdot\nabla\right)\mathbf{u}\right]\cdot\mathbf{\Phi}+2Nf^{-1}\mathbf{E}\left(\mathbf{u}\right):\mathbf{E}\left(\mathbf{\Phi}\right)-p\left(\nabla.\,\mathbf{\Phi}\right)\right\}d\Omega\\&-\int_{\Gamma_b}\left\{\left[Eo^{-1}\kappa+\mathrm{z}-\mathrm{P_b}\right]\mathbf{n}\cdot\mathbf{\Phi}\right\}d\Gamma_b=0\end{aligned} \tag{3.25}$$

Using the gradient operator (3.3) and deformation rate relation (3.6), the weak form of the momentum equation for the velocity components and continuity equation in cylindrical coordinates system are :

momentum: radial component

$$\begin{aligned}&\int_{\Omega}\left\{\frac{\partial u_r}{\partial t}\Phi_r+\left[u_r\frac{\partial u_r}{\partial r}+\frac{u_\theta}{r}\frac{\partial u_r}{\partial \theta}-\frac{{u_\theta}^2}{r}+u_z\frac{\partial u_r}{\partial z}\right]\Phi_r+Nf^{-1}\left[2\frac{\partial u_r}{\partial r}\frac{\partial \Phi_r}{\partial r}\right.\right.\\&+2\frac{\Phi_r}{r}\left(\frac{1}{r}\frac{\partial u_\theta}{\partial \theta}+\frac{u_r}{r}\right)+\frac{1}{r}\frac{\partial \Phi_r}{\partial \theta}\left(\frac{1}{r}\frac{\partial u_r}{\partial \theta}-\frac{u_\theta}{r}+\frac{\partial u_\theta}{\partial r}\right)+\frac{\partial \Phi_r}{\partial z}\left(\frac{\partial u_r}{\partial z}+\frac{\partial u_z}{\partial r}\right)\Big]\\&\left.-p\left(\frac{\partial \Phi_r}{\partial r}+\frac{\Phi_r}{r}\right)\right\}d\Omega-\int_{\Gamma_b}\left\{\left[Eo^{-1}\kappa+\mathrm{z}-\mathrm{P_b}\right]n_r\Phi_r\right\}d\Gamma_b=0\end{aligned} \tag{3.26}$$

momentum: azimuthal component

$$\begin{aligned}\int_\Omega \Bigg\{ & \frac{\partial u_\theta}{\partial t}\Phi_\theta + \left[u_r\frac{\partial u_\theta}{\partial r} + \frac{u_\theta}{r}\frac{\partial u_\theta}{\partial \theta} + \frac{u_r u_\theta}{r} + u_z\frac{\partial u_\theta}{\partial z}\right]\Phi_\theta + Nf^{-1}\left[2\frac{1}{r}\frac{\partial \Phi_\theta}{\partial \theta}\left(\frac{1}{r}\frac{\partial u_\theta}{\partial \theta} + \frac{u_r}{r}\right)\right. \\ & \left. + \left(\frac{\partial \Phi_\theta}{\partial r} - \frac{\Phi_\theta}{r}\right)\left(\frac{1}{r}\frac{\partial u_r}{\partial \theta} - \frac{u_\theta}{r} + \frac{\partial u_\theta}{\partial r}\right) + \frac{\partial \Phi_\theta}{\partial z}\left(\frac{\partial u_\theta}{\partial z} + \frac{1}{r}\frac{\partial u_z}{\partial \theta}\right)\right] - p\left(\frac{1}{r}\frac{\partial \Phi_\theta}{\partial \theta}\right)\Bigg\} d\Omega \\ & - \int_{\Gamma_b}\left\{\left[Eo^{-1}\kappa + \mathrm{z} - \mathrm{P_b}\right] n_\theta \Phi_\theta\right\} d\Gamma_b = 0\end{aligned} \tag{3.27}$$

momentum: axial component

$$\begin{aligned}\int_\Omega \Bigg\{ & \frac{\partial u_z}{\partial t}\Phi_z + \left[u_r\frac{\partial u_z}{\partial r} + \frac{u_\theta}{r}\frac{\partial u_z}{\partial \theta} + u_z\frac{\partial u_z}{\partial z}\right]\Phi_z \\ & + Nf^{-1}\left[2\frac{\partial u_z}{\partial z}\frac{\partial \Phi_z}{\partial z} + \frac{\partial \Phi_z}{\partial r}\left(\frac{\partial u_r}{\partial z} + \frac{\partial u_z}{\partial r}\right) + \frac{1}{r}\frac{\partial \Phi_z}{\partial \theta}\left(\frac{\partial u_\theta}{\partial z} + \frac{1}{r}\frac{\partial u_z}{\partial \theta}\right)\right] - p\left(\frac{\partial \Phi_z}{\partial z}\right)\Bigg\} d\Omega \\ & - \int_{\Gamma_b}\left\{\left[Eo^{-1}\kappa + \mathrm{z} - \mathrm{P_b}\right] n_z \Phi_z\right\} d\Gamma_b = 0\end{aligned} \tag{3.28}$$

continuity

$$\int_\Omega \left\{\left[\frac{\partial u_r}{\partial r} + \frac{u_r}{r} + \frac{1}{r}\frac{\partial u_\theta}{\partial \theta} + \frac{\partial u_z}{\partial z}\right]\varphi\right\} d\Omega = 0 \tag{3.29}$$

3.4 Galerkin finite element approximation

In the previous section, we derived the weak form of the governing equations in the continuous domain. Let us divide the domain, Ω into smaller subsets known as *finite element*, so that each element occupies a sub-domain Ω^e with boundary Γ^e. The discretised domain is therefore an assemblage of n_e finite elements that make up the domain.

$$\int_{\Omega^h}\{\cdot\}\, d\Omega^h = \sum_{k=1}^{ne}\int_{\Omega_k^e}\{\cdot\}\, d\Omega_k^e \tag{3.30}$$

$$\int_{\Gamma^h}\{\cdot\}\, d\Gamma^h = \sum_{k=1}^{ne}\int_{\Gamma_k^e}\{\cdot\}\, d\Gamma_k^e \tag{3.31}$$

Where Ω^h represents the discretised domain with boundary Γ^h; ne is the number of elements in the discretised domain.

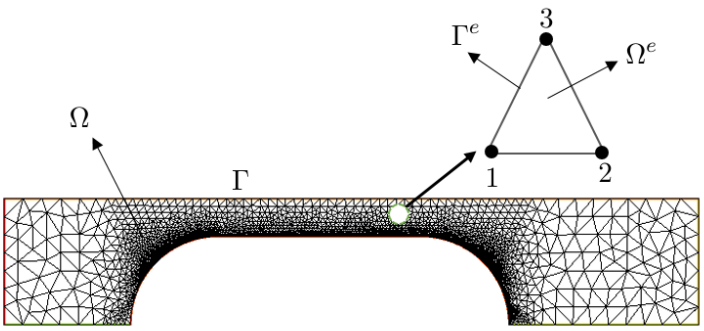


Figure 3.2: Two dimensional triangulated domain with linear approximations on subdomain, thereby having three nodes.

The geometry of the finite element could be a triangle or quadrilateral in two-dimensional domain and in three-dimensional domain, it could be a tetrahedral or hexahedral. On each element, the unknown variables of the problem, known as *trial functions*, are approximated as a linear combination of unknown parameters and piecewise polynomial functions known as *basis* (or *shape*) *functions*. In addition, the test functions corresponding to each variables are set to equal the basis functions used in approximating the variables. Depending on the geometry of an element and the order of polynomial used in approximating the unknown variable on the element, n_v number of nodes/unknown parameters can be associated with the element as shown in Figure 3.2. Thus, on each element, the trial and test functions are approximated as

$$\mathrm{u_r}\left(\mathbf{x},\mathrm{t}\right) = \sum_{k=1}^{n_v} \psi^k\left(\mathbf{x}\right) v_r^k\left(t\right) = \mathbf{\Psi}^T \mathbf{v}_r \tag{3.32a}$$

$$\mathrm{u}_\theta\left(\mathbf{x},t\right) = \sum_{k=1}^{n_v} \psi^k\left(\mathbf{x}\right) v_\theta^k\left(t\right) = \mathbf{\Psi}^T \mathbf{v}_\theta \tag{3.32b}$$

$$\mathrm{u}_z\left(\mathbf{x},t\right) = \sum_{k=1}^{n_v} \psi^k\left(\mathbf{x}\right) v_z^k\left(t\right) = \mathbf{\Psi}^T \mathbf{v}_z \tag{3.32c}$$

$$\mathrm{p}\left(\mathbf{x},t\right) = \sum_{l=1}^{n_p} \lambda^l\left(\mathbf{x}\right) \mathfrak{p}^l\left(t\right) = \mathbf{\Lambda}^T \mathbf{p} \tag{3.32d}$$

$$\Phi_r = \psi^k, \quad \Phi_\theta = \psi^k, \quad \Phi_z = \psi^k \quad \forall \quad k = 1, \cdots, n_v; \quad \varphi = \lambda^l \quad \forall \quad l = 1, \cdots, n_p \tag{3.33}$$

In equations (3.32) and (3.33), ψ and λ are the shape functions for the velocity components and pressure, respectively; n_v and n_p are the number of nodes for the velocity components and pressure, respectively, and $v_j \ \forall \ j = r,\ \theta,\ z$ and $\mathfrak{p}$ are the corresponding unknown nodal parameters of the velocity components and pressure. $\mathbf{v}_i \ \forall \ i = r,\ \theta\ z$ and $\mathbf{p}$ are column vectors of the unknown nodal parameters for the velocity components and pressure, respectively; and $\mathbf{\Psi}$ and $\mathbf{\Lambda}$ are the column vectors of the shape functions for the velocity components and pressure, respectively.

It is seen that the shape functions for the velocity components are the same but differ from that of the pressure. This is to avoid having an overconstrained system of discrete equations. In fact, the shape function used for pressure must be atleast one order lower than that of the velocity field [99].

Using equations (3.32) and (3.33), we can derive, for example, the finite element model for the continuity equation by writing the weak form of it (3.29) over an element and substituting (3.32) and (3.33) to get

$$\left[\int_{\Omega^e}\left\{\mathbf{\Lambda}\left(\frac{\partial\mathbf{\Psi}^T}{\partial r}+\frac{\mathbf{\Psi}^T}{r}\right)\right\}d\Omega^e\right]\mathbf{v}_r+\left[\int_{\Omega^e}\left\{\mathbf{\Lambda}\frac{1}{r}\frac{\partial\mathbf{\Psi}^T}{\partial\theta}\right\}d\Omega^e\right]\mathbf{v}_\theta+\left[\int_{\Omega^e}\left\{\mathbf{\Lambda}\frac{\partial\mathbf{\Psi}^T}{\partial z}\right\}d\Omega^e\right]\mathbf{v}_z=\mathbf{0} \tag{3.34}$$

which can be compactly written as

$$\mathbf{Q}^T\mathbf{v}=\mathbf{0} \tag{3.35}$$

where $\mathbf{v}=\begin{bmatrix}\mathbf{v}_r\\ \mathbf{v}_\theta\\ \mathbf{v}_z\end{bmatrix}$ and $\mathbf{Q}=\begin{bmatrix}\mathbf{Q}_r\\ \mathbf{Q}_\theta\\ \mathbf{Q}_z\end{bmatrix}$. $\mathbf{Q}_i \quad \forall\ i = r,\ \theta\ z$ are the coefficient matrices for the velocity components given by

$$\mathbf{Q}_r=\int_{\Omega^e}\left\{\mathbf{\Lambda}\left(\frac{\partial\mathbf{\Psi}^T}{\partial r}+\frac{\mathbf{\Psi}^T}{r}\right)\right\}d\Omega^e; \tag{3.36}$$

$$\mathbf{Q}_\theta=\int_{\Omega^e}\left\{\mathbf{\Lambda}\frac{1}{r}\frac{\partial\mathbf{\Psi}^T}{\partial\theta}\right\}d\Omega^e; \tag{3.37}$$

$$\mathbf{Q}_z = \int_{\Omega^e} \left\{ \mathbf{\Lambda} \frac{\partial \mathbf{\Psi}^T}{\partial z} \right\} d\Omega^e \tag{3.38}$$

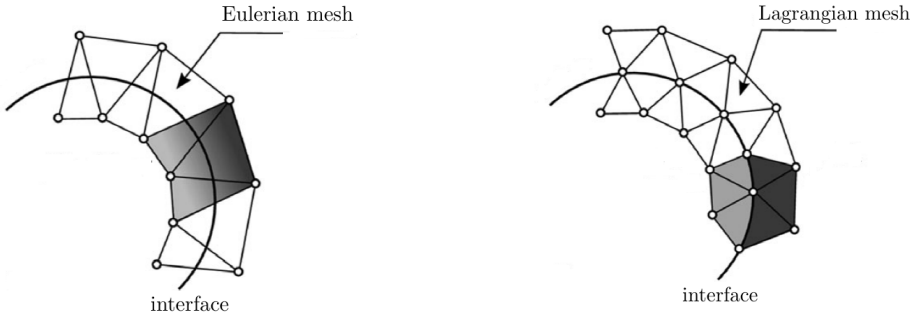
From the coefficient matrix generated for each element, the global coefficient matrix for the discretised domain is built by assembling, which is based on certain rules, most important of which are that the primary variables of the problem must be continuous and the boundary terms must balance at elements common nodes and boundaries, respectively. For this purpose we utilised a finite element package FreeFem++ [50]. Freefem++ makes easy the building of coefficient matrix from the weak form and has different inbuilt solvers that can be used to solve the resulting algebraic linear system of equations or eigenvalue problems.

Finite element equations similar to (3.35) can be derived for the velocity components from their weak form of momentum equations. However, we shall differ further discussion on this till chapters (4) and (5) where we shall focus on the steady and unsteady forms of the equations, respectively. In the meantime, there are two variables, κ and P_b in the weak form of the momentum equation (3.25) that are implicitly related to interface location, an additional unknown of the problem, whose approximation has not been discussed. In the following sections, the approximation of expressions that allow the determination the interface location, curvature and bubble pressure are discussed.

3.5 Interface deformation

In addition to the flow variables, the shape of the domain constitutes additional unknown. Specifically, the interface location has to be determined as part of the solutions. For this, the different approaches for determining the interface locations can be broadly classified into two; the interface capturing and the interface tracking methods [32]. In interface capturing methods, also known as fixed (or Eulerian) mesh methods, the interface location is not explicitly being determined as part of the solution methods, rather it is implicitly determined from a scalar characteristic function use in distinguishing the fluid phases. On the other hand, the interface tracking methods, also known as moving (or Lagrangian) mesh methods, the interface

is explicitly tracked during the solution process.



(a) (b)

Figure 3.3: Interface representation on (a) Eulerian mesh (b) Lagrangian mesh. In Lagrangian representation, the interface coincides with the computational mesh unlike in Eulerian representation. Adapted from [3]

3.5.1 Interface capturing methods

Methods under this category includes the volume-of-fluids (VOF), level-set, front tracking and phase field methods. Depending on the method, the scalar characteristic function use in distinguishing the fluid phases may be described for example by a discontinuous Heaviside function or a signed-distance function and the equation that govern its motion is the standard advection equation:

$$\frac{\partial \chi}{\partial t} + (\mathbf{u} \cdot \nabla)\, \chi = 0 \quad \text{in} \quad \Omega \tag{3.39}$$

where χ is the scalar function use in characterising the fluid phases.

One major advantage of the interface capturing methods is there inherent capability to account for large change in the topology of the interface, including breakage. However, they are faced with challenges such as mass conservation, handling of variable discontinuity across the interface and the imposition of boundary conditions along the interface [32]. In the following subsection, we briefly discuss two commonly used interface capturing methods for simulation of two-phase flows.

Volume of fluid method

The volume of fluid method uses the volume fraction of the fluid phases in the fixed background mesh as the characteristic function. It was first introduced by [53]. Mesh cells that are completely filled by one of the fluid phase is assigned a value of 0 or 1 while those that are intersected by the interface takes a value between 0 and 1 depending on the proportion of the fluid phases that occupies the cell. From the volume fraction information, the interface between the phases is then reconstructed using different approaches such as Simple Linear Interface Calculation (SLIC) and Piecewise Linear Interface Calculation (PLIC).

Level set method

In the level set method, introduced by [87] and further developed by [105], the characteristic function use in distinguishing between the two phases is a smooth level-set function. The interface is assigned an arbitrary level set value, most commonly 0, and the different phases are identified by the signed distance from the interface level set value.

$$\Gamma_b(t) = \{\mathbf{r} \in \Omega \mid \chi(\mathbf{r}, t) = 0\} \tag{3.40}$$

$$\chi(\mathbf{r}, 0) = \begin{cases} d(\Gamma_b, \mathbf{r}) & \mathbf{r} \in \Omega_l \\ 0 & \mathbf{r} \in \Gamma_b \\ -d(\Gamma_b, \mathbf{r}) & \mathbf{r} \in \Omega_g \end{cases} \tag{3.41}$$

Here, $d(\Gamma_b, \mathbf{r})$ is a distance function that compute the magnitude of the distance between points in the domain with position vector $\mathbf{r}$ and the interface, Γ_b, location, $\mathbf{r}_b$; Ω_l and Ω_g are the liquid and gas portion of the domain.

In order to guarantee the conservation of mass in the fluid phases, the level set function must remain a signed distance function, a property that is usually lost with time during the advection of the level set using (3.39). It is therefore essential that the level set is periodically reinitialised and for this purpose, a number of reinitialisation techniques have been proposed in the literature to recover this property [32].

3.5.2 Interface tracking methods

These methods are based on Lagrangian viewpoint and involve explicitly resolution of the interface using the computational mesh. Since the interface coincides with the mesh nodes as shown in Figure 3.3, they offer a better way to accurately follow the deformation of the boundary of a domain by moving the position of the mesh nodes in a Lagrangian fashion using the local velocity. In addition, because the interface is boundary resolved, the imposition of boundary conditions at the interface is direct and simplified. The equations that govern the motions of the mesh nodes is

$$\frac{\partial \mathbf{r}_m}{\partial t} = \mathbf{u}\left(\mathbf{x}, t\right) \tag{3.42}$$

Here, $\mathbf{r}_m$ is the position vector of the mesh nodes. When all mesh nodes in the domain are moved using the local velocity, the method is said to be *Fully Lagrangian*. This approach is simple and has been used in numerical simulation of a number of problems. However, even for situations where the boundary displacement is significantly very small, the method may suffer from unnecessary mesh distortion when the flow field in the interior of the domain exhibit a large amount of circulation or shear [32]. Hence, constant remeshing have to be carried out with respect to the new interface.

To mitigate the problem with fully Lagrangian technique, another class of Lagrangian methods called an *Arbitrary Lagrangian-Eulerian* (ALE) method treats only a fraction of the nodes, usually those on the interface, in a Lagrangian manner. The interior node are then move arbitrarily to preserve the mesh quality. This methhod drastically reduce the rate at which the mesh get deteriorated making it very attractive as a method for solving interfacial and free surface problems. Occasionally, however, like in fully Lagrangian method, there is always the need to carry out remeshing.

Our numerical method for interface deformation is based on interface tracking and we make use of a variant of equation (3.42) in deforming the interface. Equation (3.42) implies that the mesh velocity, $\mathbf{u}_m$ at every nodal points in the domain (including the interface) moves with the

fluid velocity.

$$\mathbf{u}_m = \mathbf{u} \tag{3.43}$$

Because the interface is boundary resolved, the mesh motion at the interface must be such that the kinematic boundary condition (3.13) is satisfied. In terms of the mesh velocity, (3.13) can be written as

$$\mathbf{u}_m \cdot \mathbf{n} = \mathbf{u} \cdot \mathbf{n} \tag{3.44}$$

Equation (3.44) implies that any choice of $\mathbf{u}_m$ that satisfies the kinematic boundary condition is valid for the interface deformation and that the tangential component of the fluid velocity does not contribute to the interface deformation . As a result, we chose the interface velocity to be of the form

$$\mathbf{u}_m = (\mathbf{u} \cdot \mathbf{n})\,\mathbf{n} \tag{3.45}$$

This means that the interface is propagated in a direction that is normal to it with magnitude that equals the normal velocity on the interface. If we let δt be a step size, which for unsteady problem is the time step-size but in the context of steady state covered in chapter (4), it is referred to as pseudo-time step-size, the deformation of the interface, $\mathbf{x}$, is

$$\mathbf{x} = \delta t\,(\mathbf{u} \cdot \mathbf{n})\,\mathbf{n} \tag{3.46}$$

if we let the magnitude of the deformation be h, so that the deformation is of the form

$$\mathbf{x} = h\mathbf{n} \tag{3.47}$$

then, the equation that govern interface deformation magnitude in the normal direction becomes

$$h = \delta t\,(\mathbf{u} \cdot \mathbf{n}) \tag{3.48}$$

Equation (3.48) is the additional relations that allows the interface deformation to be determined. We note that equation (3.48) can be derived directly from the kinematic boundary condition by approximating the time derivative of the interface position vector with a first

order finite difference. Equation (3.48) is therfore coupled has a boundary problem to the momentum equations and it holds only on the interface. The weak form of the equation and the Galerkin finite element approximation for the deformation magnitude are written as

$$\int_{\Gamma_b}^{e} \{h\xi - \delta t \left(\mathbf{u} \cdot \mathbf{n}\right) \xi\} \, d\Gamma_b = 0 \tag{3.49a}$$

$$h = \sum_{k=1}^{n_h} \eta_k \left(\mathbf{r}_b\right) \hbar_k \left(t\right) = \boldsymbol{\eta}^T \mathbf{h} \tag{3.49b}$$

$$\xi = \eta \tag{3.49c}$$

Where ξ, η and n_h are the test function, shape function and the number of nodes for interface deformation magnitude, respectively; $\hbar_k \; \forall \; k = 1, \cdots, n_h$ are the nodal unknown parameters for the interface deformation magnitude; $\boldsymbol{\eta}$ and $\mathbf{h}$ are the column vectors of the shape functions and unknown parameters for the interface deformation magnitude, respectively.

3.5.3 Mesh deformation

The derived relation for the interface deformation (3.48) dictates the magnitude of the deformation of the mesh nodes located on the interface. For all other nodes in the domain, the size of their deformations are adapted to that of the interface in a way that ensures that the mesh quality does not degrade very fast by assuming that the computational mesh is an elastic body whose interior deform in reaction to the boundary deformation. This assumption form the basis of Elastic Mesh Update Method [57] of treating interior nodes. In this method, the linear elasticity equation is solved for the mesh deformation subject to the boundary conditions that equals the desired deformation on the boundaries.

$$\nabla \cdot \boldsymbol{\sigma} \left(\boldsymbol{\phi}\right) = 0 \quad \text{in} \quad \Omega \tag{3.50a}$$

$$\boldsymbol{\sigma} \left(\boldsymbol{\phi}\right) = \lambda_m \left(\nabla \cdot \boldsymbol{\phi}\right) \mathbf{I} + 2\mu_m \mathbf{E} \left(\boldsymbol{\phi}\right) \tag{3.50b}$$

$$\mathbf{D} \left(\boldsymbol{\phi}\right) = \frac{1}{2} \left[\nabla \left(\boldsymbol{\phi}\right) + \nabla \left(\boldsymbol{\phi}\right)^T\right] \tag{3.50c}$$

Here $\boldsymbol{\sigma}$ is the stress tensor for the elastic domain; $\mathbf{D}(\boldsymbol{\phi})$ is the strain tensor; $\boldsymbol{\phi}$ is the domain deformation vector. λ_m and μ_m are two constants that describe the elastic properties of the domain.

The boundary conditions are

$$\boldsymbol{\phi} = h\mathbf{n} \quad \text{on} \quad \Gamma_b \tag{3.51a}$$

$$\boldsymbol{\phi} = \mathbf{0} \quad \text{on} \quad \Gamma_{wall},\ \Gamma_{in} \text{ and } \Gamma_{out} \tag{3.51b}$$

Following [42], we use

$$\lambda_m = \mu_m = 1$$

From the calculated domain deformation using (3.50), position vector of all the mesh nodes can be updated by

$$\mathbf{r}^{j+1} = \mathbf{r}^j + \boldsymbol{\phi} \tag{3.52}$$

3.6 Curvature

In two phase gas-liquid flows, curvature of the interface is a secondary variable which as shown in section (3.3) enters the momentum equation via the normal stress balance. To numerically compute the curvature of an interface, the precise location of the interface, which is not known apriori in two phase flow, has to be specified. While it is possible to numerically approximate the curvature of the unknown surface with that of the currently known interface location in iterative sense, for numerically stability of the solution, it has to be treated implicitly [42, 104]. In this section, we shall first derive an expression that relates the curvature of the unknown interface to that of the currently known interface by linearisation. Subsequently, we shall describe how to compute the curvature of a known interface using cubic spline interpolation and approximate it using Laplace-Beltrami operator.

3.6.1 Curvature linearisation

For a three-dimensional axisymmetric surface, the interface location in any $r-z$ plane is sufficient for computing the curvature of the surface. Consider that the interface in any r-z plane is spanned by a curve with the coordinates of any point on the curve being (r, z) . In addition, let the interface be parametrised by length of arc s so that the position vector of any point on the interface is given as

$$\mathbf{r} = r(s)\mathbf{i}_r + z(s)\mathbf{i}_z \tag{3.53}$$

The total curvature at any given point on the interface is defined as

$$\kappa = -\nabla_s \cdot \mathbf{n} \tag{3.54}$$

where $r\,(s)$ and $z\,(s)$ are the radial and axial coordinates of the points on the interface, respectively; $\mathbf{n}$ still remains the unit normal to the interface and ∇_s is the surface tangential gradient operator which is given as

$$\nabla_s = (\mathbf{I} - \mathbf{n} \otimes \mathbf{n})\,\nabla \tag{3.55}$$

For a three-dimensional axisymmetric surface, (3.55) simplifies to

$$\nabla_s = t_r \frac{d}{ds}\mathbf{i}_r + \frac{1}{r}\frac{\partial}{\partial\theta}\mathbf{i}_\theta + t_z \frac{d}{ds}\mathbf{i}_z \tag{3.56}$$

and equation (3.54) becomes

$$\kappa = -\left(\mathbf{t} \cdot \frac{d\mathbf{n}}{ds} + \frac{n_r}{r}\right) \tag{3.57}$$

where $\mathbf{t}$ is the unit tangent vector to the interface with components t_r, t_θ and t_z in the radial, azimuthal and axial directions, respectively; $\frac{d}{ds} = (\mathbf{t} \cdot \nabla)$ is an operator that denotes derivative in the tangential direction; n_r is the radial component of the unit normal vector, $\mathbf{n}$.

Let us imagine that the unknown interface location (onwards from here referred to as deformed interface) can be expressed as a summation of the current interface location (also onwards from here referred to as undeformed interface) and a very small deformation . We also assume that

the deformed interface does not necessarily have to be axisymmetric in order that the expression that would be derived for change in curvature due to the addition of the small deformation can be used in stability analysis in chapter (5). Thus, the deformed interface can be written as

$$\mathbf{r} = \mathbf{r}^0 + \mathbf{x} \tag{3.58}$$

where $\mathbf{r}^0 = r^0\mathbf{i}_r + \theta^0\mathbf{i}_\theta + z^0\mathbf{i}_z$ and $\mathbf{r} = r\mathbf{i}_r + \theta\mathbf{i}_\theta + z\mathbf{i}_z$ are the undeformed and deformed interface position vectors, respectively; $\mathbf{x} = x_r\mathbf{i}_r + x_\theta\mathbf{i}_\theta + x_z\mathbf{i}_z$, as mentioned in the previous section, is the interface deformation vector and is taken to be very small in magnitude.

Linearisation of the unit normal to, and elemental arc length on, the deformed interface about the undeformed interface give [60, 97, 113]

$$\mathbf{n} = \mathbf{n}^0 - \mathbf{n}^0 \times \nabla_s \times \mathbf{x} \tag{3.59}$$

$$ds = \left(1 + \mathbf{t}^0 \cdot \frac{d\mathbf{x}}{ds}\right) ds^0 \tag{3.60}$$

$$\frac{d}{ds} = \left(1 - \mathbf{t}^0 \cdot \frac{d\mathbf{x}}{ds}\right) \frac{d}{ds^0} \tag{3.61}$$

On further simplification of (3.59)

$$\mathbf{n} = \mathbf{n}^0 - \mathbf{t}^0 \left(\mathbf{n}^0 \cdot \frac{d\mathbf{x}}{ds^0}\right) - \frac{\mathbf{n}^0}{r^0} \cdot \frac{\partial \mathbf{x}}{\partial \theta^0}\mathbf{i}_\theta \tag{3.62}$$

Substituting (3.62) together with (3.58) and (3.61) into (3.57), the linearised curvature neglecting all terms of nonlinear in x gives

$$\kappa = \kappa^0 + \kappa^1 \tag{3.63}$$

with

$$\kappa^0 = -\left(\mathbf{t}^0 \cdot \frac{d\mathbf{n}^0}{ds} + \frac{n_r^0}{r^0}\right) \tag{3.64}$$

$$\kappa^1 = \frac{1}{r^0}\frac{d}{ds^0}\left[r^0\left(\mathbf{n}^0 \cdot \frac{d\mathbf{x}}{ds^0}\right)\right] + 2\left(\mathbf{t}^0 \cdot \frac{d\mathbf{x}}{ds^0}\right)\left(\mathbf{t}^0 \cdot \frac{d\mathbf{n}^0}{ds^0}\right) + \frac{\mathbf{n}^0}{r^{0\,2}} \cdot \frac{\partial^2 \mathbf{x}}{\partial \theta^{0\,2}} + \frac{x_r n_r^0}{r^{0\,2}} - \frac{d\mathbf{n}^0}{ds^0} \cdot \frac{d\mathbf{x}}{ds^0} \tag{3.65}$$

When (3.65) is further simplified by allowing the deformation vector to be of the form

$$\mathbf{x} = h\mathbf{n}^0 \tag{3.66}$$

it results in

$$\kappa^1 = \frac{1}{r^0}\frac{d}{ds^0}\left(r^0\frac{dh}{ds^0}\right) + h\left[{\kappa^0}_a^2 + {\kappa^0}_b^2 + \frac{1}{r^{0\,2}}\frac{\partial^2 h}{\partial\theta^{0\,2}}\right] \tag{3.67}$$

which is the same as the expression derived for curvature perturbation in [22], albeit through a different and longer route. In arriving at (3.67), we have used the following Frenet-Serret relations

$$\frac{d\mathbf{t}}{ds} = \kappa\mathbf{n} \tag{3.68a}$$

$$\frac{d\mathbf{n}}{ds} = -\kappa\mathbf{t} \tag{3.68b}$$

Equation (3.65) and (3.67) are the expressions for curvature deformation and can be used for an axisymmetric deformation by setting the term containing derivative with respect to the azimuthal coordinate to zero to have

$$\kappa^1 = \frac{1}{r^0}\frac{d}{ds^0}\left(r^0\frac{dh}{ds^0}\right) + h\left[{\kappa^0}_a^2 + {\kappa^0}_b^2\right] \tag{3.69}$$

In equations (3.59)-(3.67), $\mathbf{n}^0$ is the unit normal vector to the undeformed interface and n_r^0, n_θ^0 and n_z^0 are its component in the radial, azimuthal and axial directions, respectively; $\mathbf{t}^0$ is the unit tangent vector to the undeformed interface with components t_r^0, t_θ^0 and t_z^0 in the radial, azimuthal and axial directions, respectively; ds and ds^0 are the elemental arc length for the deformed and undeformed interfaces, respectively; κ^0 is the curvature of the undeformed surface and κ^1 is the addition to the undeformed interface curvature (also referred to as curvature perturbation in the context of linear stability analysis) due to linearisation of the deformed interface about the undeformed interface; h is the magnitude of the interface deformation in the direction normal to the undeformed interface. ${\kappa^0}_a$ and ${\kappa^0}_b$ are the two principal curvatures of the undeformed interface (3.64) corresponding to the curvature in the $r-z$ and $r-\theta$ planes,

respectively, define as

$$\kappa^0{}_a = \mathbf{t}^0 \cdot \frac{d\mathbf{n}^0}{ds} \tag{3.70a}$$

$$\kappa^0{}_b = \frac{n_r^0}{r^0} \tag{3.70b}$$

For brevity, the superscript "0" used in denoting terms corresponding to the undeformed interface will be suppressed onward. These terms should be taken to be defined on the undeformed interface except where it is otherwise stated .

3.6.2 Curvature computation and approximation

In the last subsection, we have described how the curvature, an unknown in the problem when treated implicitly, can be expressed in terms of the curvature of the undeformed interface and the magnitude of the deformation to the interface. In this subsection, we discuss how the curvature of the undeformed interface is computed numerically using cubic spline and can be approximated using Laplace-Beltrami operator.

cubic spline interpolation of curvature

In terms of the tangent vector to the interface, equation (3.70a) can be written as

$$\kappa_a = -\frac{z\left(s\right)' r\left(s\right)'' - r\left(s\right)' z\left(s\right)''}{\left(r\left(s\right)'^2 + z\left(s\right)'^2\right)^{\frac{3}{2}}} \tag{3.71}$$

and the unit normal and tangent as

$$n_r = -t_r = \frac{r\left(s\right)'}{\left(r\left(s\right)'^2 + z\left(s\right)'^2\right)^{\frac{1}{2}}} \tag{3.72a}$$

$$n_z = t_z = \frac{z\left(s\right)'}{\left(r\left(s\right)'^2 + z\left(s\right)'^2\right)^{\frac{1}{2}}} \tag{3.72b}$$

where the prime and double primes indicate first and second derivatives with respect to the arc length, respectively.

Compared to (3.70a), equation (3.71) provides a much easier means of numerically computing the curvature of a curve provided the derivatives of the spatial coordinates with respect to the arc length, denoted by upper prime, can be calculated up to second order. Let us imagine that the curve that describe the interface is spanned by $(n_d + 1)$ data points with coordinates $(r_i(s_i), z_i(s_i))\ \forall\ i = 0, 1, \cdots, n_d$. Each data point corresponds to the position vector, $\mathbf{r}_i = r_i\mathbf{i}_r + z_i\mathbf{i}_z\ \forall\ i = 0, 1, \cdots, n_d$, of the node of elements that have one of their edges fitted with the interface Γ_b. The idea is to compute the derivatives of the spatial coordinates from a cubic polynomial function fitted between each two adjacent points on the curve using cubic spline. Cubic spline enforced that the first and second derivative of the polynomial (known as spline) are continuous at all but end points. At the first and last points, appropriate boundary conditions are specified to form a closed system of equations.

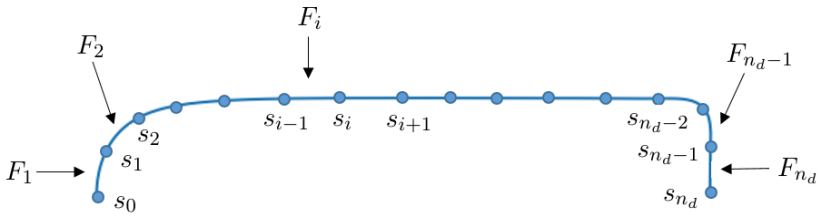


Figure 3.4: Interface parametrisation for cubic spline interpolation.

For any interval $[\mathbf{r}_{i-1}, \mathbf{r}_i]$, we can define two cubic splines, one for each of the spatial coordinates, as a function of the arc length. If we let $q(s)$ be a dummy variable that could be $r(s)$ or $z(s)$, the cubic spline $F_i(s)$ between the interval $[q_{i-1}, q_i]$ corresponding to $[s_{i-1}, s_i]$ shown in Figure 3.4 is [26, 46]

$$F_i(s) = -\frac{1}{6}\left[\frac{(s-s_i)^3 + a_i^2(s-s_i)}{a_i}\right]q''_{i-1} + \frac{1}{6}\left[\frac{(s-s_{i-1})^3 - a_i^2(s-s_{i-1})}{a_i}\right]q''_i + \left[\frac{(s-s_{i-1})q_i - (s-s_i)q_{i-1}}{a_i}\right] \qquad \forall\ i{=}1, 2, \cdots, n_d \tag{3.73}$$

where a_i is differential length of arc define as

$$a_i = s_i - s_{i-1} \qquad \forall\, i = 1, 2, \cdots, n_d \tag{3.74}$$

Taking the first derivative of the cubic spline function with respect to s

$$F_i^{'}(s) = -\frac{1}{6}\left[\frac{3\left(s - s_i\right)^2 + a_i^2}{a_i}\right] q_{i-1}^{''} + \frac{1}{6}\left[\frac{3\left(s - s_{i-1}\right)^2 - a_i^2}{a_i}\right] q_i^{''} + \left[\frac{\left(q_i - q_{i-1}\right)}{a_i}\right] \tag{3.75}$$

and enforcing the continuity of the first derivative at the interior nodes

$$F_i\left(s_i\right)^{'} = F_{i+1}\left(s_i\right)^{'} \qquad \forall\, i = 1, 2, \cdots, n_d - 1. \tag{3.76}$$

we have $n_d - 1$ equations for the interior nodes

$$a_i q_{i-1}^{''} + 2\left(a_i + a_{i+1}\right) q_i^{''} + a_{i+1} q_{i+1}^{''} = 6\frac{\left(q_{i+1} - q_i\right)}{a_{i+1}} - 6\frac{\left(q_i - q_{i-1}\right)}{a_i} \qquad \forall\, i = 1, 2, \cdots, n_d - 1 \tag{3.77}$$

The first derivative of the spatial coordinates with respect to s are the tangents to the interface and are known quantities at the end nodes for an axisymmetric interface. Fixing the values at the first and last nodes using the first and last cubic splines, we have from (3.75) two additional equations

$$2a_1 q_0^{''} + a_1 q_1^{''} = 6\frac{\left(q_1 - q_0\right)}{a_1} - 6F_1^{'}\left(s_0\right) \tag{3.78}$$

$$a_{n_d} q_{n_d-1}^{''} + 2a_{n_d} q_{n_d}^{''} = 6F_{n_d}^{'}\left(s_{n_d}\right) - 6\frac{\left(q_{n_d} - q_{n_d-1}\right)}{a_{n_d}} \tag{3.79}$$

Equations (3.77)-(3.79) constitute an algebraic system of equations in the second derivatives of the spatial coordinates with respect to the arc length.

For all the nodal points on the interface, the system of equations gives (3.80).

$$\begin{bmatrix} 2a_1 & a_1 & 0 & 0 & \dots & 0 & 0 \\ a_1 & 2(a_1+a_2) & a_2 & 0 & \dots & 0 & 0 \\ 0 & a_2 & 2(a_2+a_3) & a_3 & \dots & 0 & 0 \\ \vdots & \vdots & \vdots & \ddots & \dots & \vdots & \vdots \\ 0 & 0 & \dots & a_{n_d-2} & 2(a_{n_d-2}+a_{n_d-1}) & a_{n_d-1} & 0 \\ 0 & 0 & \dots & 0 & a_{n_d-1} & 2(a_{n_d-1}+a_{n_d}) & a_{n_d} \\ 0 & 0 & \dots & 0 & 0 & a_{n_d} & 2a_{n_d} \end{bmatrix} \begin{bmatrix} q_0'' \\ q_1'' \\ q_2'' \\ \vdots \\ q_{n_d-2}'' \\ q_{n_d-1}'' \\ q_{n_d}'' \end{bmatrix}$$

$$= 6 \begin{bmatrix} b_1 - F_0(s_0)' \\ b_2 - b_1 \\ b_3 - b_2 \\ \vdots \\ b_{n_d-1} - b_{n_d-2} \\ b_{n_d} - b_{n_d-1} \\ F_{n_d}(s_{n_d})' - b_{n_d} \end{bmatrix} \tag{3.80}$$

with

$$b_i = \frac{q_i - q_{i-1}}{a_i} \tag{3.81}$$

Solving (3.80), yields the second derivative at the interface nodal points from which the first derivative for the radial and axial coordinates are calculated using (3.75) and the curvature using (3.71). For the radial and axial components of the tangent vector, we fixed $F_0(s_0)' = 1, \quad F_{n_d}(s_{n_d})' = -1$ and $F_0(s_0)' = 0, \quad F_{n_d}(s_{n_d})' = 0$, respectively.

Laplace-Beltrami operator

As alternatives to direct computation of the curvature of a surface using (3.71) and (3.70b), two approaches that have find great applications in finite element simulation of two-phase flows are

the Continuum Surface Force and Laplace-Beltrami techniques. The former first introduced by [13] is commonly used in techniques that are based on interface capturing and involves the replacement of the curvature term on the interface in the weak formulation by a localised volume force smoothed by a finite-width approximated Dirac delta function to restrict the force to region around the vicinity of the interface. The Laplace-Beltrami technique on the other hand is greatly utilised in methods that are based on interface tracking techniques. The technique basically involve replacing the curvature in the weak form by the Laplace-Beltrami operator and then using integration by part to reduce the order of derivative on the spatial coordinates. Since its introduction into finite element methods by [31], it has been used in a number of two phase flow simulations [7, 42]. The Laplace-Beltrami operator is given as

$$\nabla_s \cdot \nabla_s (\mathbf{r}) = \kappa \mathbf{n} \tag{3.82}$$

which makes it easier to naturally incorporates it into the weak form of the momentum equation (3.25)

$$\int_{\Gamma_b} \left\{ Eo^{-1} \kappa \mathbf{n} \cdot \mathbf{\Phi} \right\} d\Gamma_b = \int_{\Gamma_b} \left\{ Eo^{-1} \nabla_s \cdot \nabla_s (\mathbf{r}) \cdot \mathbf{\Phi} \right\} d\Gamma_b \tag{3.83}$$

For a closed surface, integrating by part yields

$$\int_{\Gamma_b} \left\{ Eo^{-1} \kappa \mathbf{n} \cdot \mathbf{\Phi} \right\} d\Gamma_b = - \int_{\Gamma_b} \left\{ Eo^{-1} \nabla_s (\mathbf{r}) : \nabla_s (\mathbf{\Phi}) \right\} d\Gamma_b \tag{3.84}$$

For an open boundary, effect of the boundary end condition must be taken into consideration in the integration by part. Details of how this can be handled is available in [7, 32, 47] . In our numerical method, we use (3.84) to approximate the curvature of the undeformed interface and (3.54) for evaluating the principal curvatures for use in (3.65) or (3.67).

3.7 Bubble pressure

The bubble pressure, as stated in section (3.1), is the variables that accounts for the dynamics in the gas phase. It enters the weak form of the momentum equation, just like curvature,

through the normal stress balance condition on the interface and its value is determined by the relationship between the unknown interface location and bubble volume (3.14). Since the bubble volume must remain the same before and after deformation, equation (3.14) is used to derived an expression that relates bubble volume to other variables of the problem. From equations (3.46) and (3.58),

$$\mathbf{r}^{j+1} = \mathbf{r}^{j} + \delta t \left(\mathbf{u} \cdot \mathbf{n}\right) \mathbf{n} \tag{3.85}$$

Substituting (3.85) into (3.14)

$$V_b^{j+1} + \frac{1}{3} \oint_{\Gamma_b} \mathbf{r}^{j} \cdot \mathbf{n} d\Gamma_b + \frac{1}{3} \oint_{\Gamma_b} \delta t \left(\mathbf{u} \cdot \mathbf{n}\right) d\Gamma_b = 0 \tag{3.86}$$

which simplifies to

$$V_b^{j+1} - V_b^{j} + \frac{1}{3} \oint_{\Gamma_b} \delta t \left(\mathbf{u} \cdot \mathbf{n}\right) d\Gamma_b = 0 \tag{3.87}$$

Equation (3.87) relates the volume of the bubble to the flow field in the liquid phase and when it is compared with (3.25), it can be deduced that the bubble pressure is a Lagrange multiplier that enforces that the net flux across the interface is zero.

3.8 Shape functions

In the previous sections, we have shown how the unknown variables of the problems are approximated by expressing them as a linear combination of their shape (or interpolation) functions and an unknown parameters. We stated that the shape functions are generally polynomial functions and in order to avoid having an overconstrained discrete system, the interpolation functions used for velocity components must be higher than that of pressure. Furthermore, pressure need not be a continuous function across elements because it is not a primary variable of the weak forms of continuity (3.21) and momentum (3.25) equations [99]. The reason being that pressure appears in the weak forms as a Lagrange multiplier that enforces the divergence free constraint on the velocity field . This restriction on the choice of shape functions for the

velocity-pressure combinations for finite element approximations of problems with constraints is captured in *Ladyzhenskaya-Babuska-Brezzi* (LBB) condition (also known as *inf-sup* condition).

Here we state some few finite elements combinations that have been proven to satisfy the LBB condition . Because our steady state numerical simulations are going be axisymmetric and the three-dimensional stability analysis will be shown in chapter (5) to also reduce to 2D, we shall restrict the finite elements combinations to 2-D. Specifically, triangular 2-D finite elements, which is the geometry of elements that are available within FreeFem++, the finite element package used for this study.

$\mathbf{P_2 - P_1}$: The velocity field is approximated with continuous piecewise quadratic finite element P_2 and the pressure is approximated using continuous piecewise linear finite element P_1 [108]. This finite element is known as the lowest-order Taylor-Hood element



(a) (b)

Figure 3.5: Triangular finite element with (a) P_2 (b) P_1 approximations

$\mathbf{P_1^+ - P_1}$ The velocity is approximated with piecewise linear continuous plus bubble finite element P_1^+ , and the pressure is approximated with continuous piecewise linear finite element P_1 [5]. This finite element is known as the mini element.

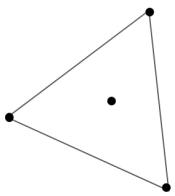
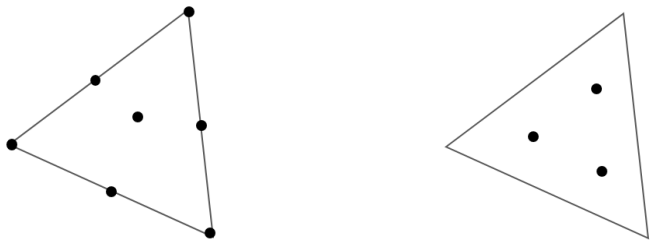


Figure 3.6: Triangular finite element with P_1^+ approximation

$\mathbf{P_2^+ - P_{-1}}$ The velocity is approximated with continuous piecewise quadratic plus bubble finite element P_2^+, and the pressure is approximated with discontinuous piecewise linear finite element P_{-1} [67], known as Crouzeix-Raviart element.



(a) (b)

Figure 3.7: Triangular finite element with (a) P_2^+ (b) P_{-1} approximations

Other finite elements that satisfy the *LBB* conditions include higher-order Taylor-Hood element (e.g $P_3 - P_1$) [14], $P_2 - P_0$ and $P_2 - (P_1 + P_0)$ [8]. For our steady state numerical simulations and linear stability analysis, we use the lowest-order Taylor-Hood elements. In addition, following [7], we approximate the interface deformation using continuous piecewise quadratic element. We note that, the steady state simulations were done in two stages to speed up computation; first using the mini element for velocity-pressure approximation and continuous piecewise linear element for interface deformation, and then in the second stage using the lowest order Taylor-Hood element for velocity-pressure approximation and continuous piecewise quadratic element for interface deformation.

For completeness, we show below the polynomial expressions for the three shape functions on a triangular finite element with a linear interpolation field [51] using pressure field as an example. Further details on the expressions for shape functions for other finite element approximations can be found in [88].

$$\lambda^1(r,z) = \frac{1}{2A}\left[z_2 r_3 - z_3 r_2 + (r_2 - r_3)z + (z_3 - z_2)r\right] \tag{3.88a}$$

$$\lambda^2(r,z) = \frac{1}{2A}\left[z_3 r_1 - z_1 r_3 + (r_3 - r_1)z + (z_1 - z_3)r\right] \tag{3.88b}$$

$$\lambda^3(r,z) = \frac{1}{2A}\left[z_1 r_2 - z_2 r_1 + (r_1 - r_2)z + (z_2 - z_1)r\right] \tag{3.88c}$$

where $(r_i, z_i) \quad \forall\, i = 1, 2, 3.$ are the spatial coordinates of the nodes of the triangle, Figure 3.8; A is the area of the triangular element given by

$$2A = (z_2 r_3 - z_3 r_2) + (z_3 r_1 - z_1 r_3) + (z_1 r_2 - z_2 r_1) \tag{3.89}$$

so that on each element, equation (3.32d) gives

$$p\,(r, z) = \lambda^1\,(r, z)\,\mathfrak{p}^1 + \lambda^2\,(r, z)\,\mathfrak{p}^2 + \lambda^3\,(r, z)\,\mathfrak{p}^2 \tag{3.90}$$

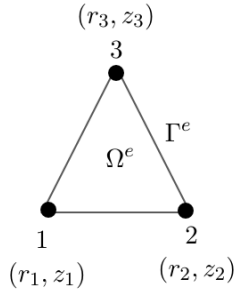


Figure 3.8: Triangular finite element with P_1 approximation showing the local coordinates of the three nodes.

Two properties of shape functions that can be deduced from equation (3.88) are

$$\sum_{i=1}^{n_p=3} \lambda^i = 1 \tag{3.91a}$$

$$\lambda^i\,(r_j, z_j) = \delta_{ij} \tag{3.91b}$$

where δ_{ij} is the Kronecker delta. Thus

$$p\,(r_i, z_i) = \mathfrak{p}^i \quad \forall\, i = 1, 2, 3. \tag{3.92}$$

3.9 Summary

This chapter covers the foundation for the steady state numerical simulations and linear stability analysis discuss in the following chapters. The continuous and Galerkin weak form of the governing equations together with the boundary conditions were presented. The weak form enables us to reduce the order of differentiability requirement on the continuous variables and to naturally enforce the stress boundary conditions. Furthermore, the finite element approximations for velocity, pressure and interface deformation were discussed. Using the finite element approximations for the velocity and pressure, we derived the finite element model for the continuity equations. In addition, we show that although the curvature is also implicitly an unknown of the problem, it can be related to the interface deformation via linearisation. Also, using the interface deformation, we derived a relation between the bubble volume and net flux across the interface, which is the equation needed to determine the bubble pressure simultaneously along with the flow field. Finally, we discussed the interpolation function we selected for velocity, pressure and interface deformation.

Chapter 4

Steady state numerical simulations

In the previous chapter, we have given the general overview of how the weak forms of the equations that govern the rise of a three-dimensional axisymmetric Taylor in a Newtonian liquid are developed and the variables of the problem approximated using Galerkin finite element. This chapter focuses on the derivation and the numerical solutions of a two-dimensional axisymmetric steady state model for the problem and on studying the effect of the three dimensionless parameters, Nf, Eo and U_m on the dynamics of a two-dimensional axisymmetric Taylor bubble.

We begin in section 4.1 by deriving *consistent penalty* Galerkin finite element steady state model for a rising Taylor bubble and then a description of the numerical solution strategy implemented for the model within FreeFem++ is given in section 4.2. In section 4.3, the validation carried out for the model is presented. This is followed in sections 4.4 and 4.5 with the steady state results for the features, listed in section 1.2, characterising the topological regions around Taylor bubble, in stagnant and flowing liquids, respectively. Finally, a summary is provided for the chapter in section 4.7.

4.1 Steady state model description

Let us begin by writing the steady state versions of the weak forms of the continuity (3.21) and momentum (3.25) equations derived in the previous chapter:

$$\int_{\Omega^0} \{\varepsilon p\varphi + (\nabla . \mathbf{u})\,\varphi\}\, d\Omega^0 = 0 \tag{4.1}$$

$$\int_{\Omega^0} \left\{[(\mathbf{u}\cdot\nabla)\,\mathbf{u}]\cdot\mathbf{\Phi} + 2Nf^{-1}\mathbf{E}\,(\mathbf{u}) : \mathbf{E}\,(\mathbf{\Phi}) - p\,(\nabla .\, \mathbf{\Phi})\right\} d\Omega^0 - \int_{\Gamma_b^0} \left\{\left[Eo^{-1}\kappa + z - P_b\right]\mathbf{n}\cdot\mathbf{\Phi}\right\} d\Gamma_b^0 = 0 \tag{4.2}$$

where Ω^0 represents the two-dimensional axisymmetric domain with Γ_b^0 being the portion of its boundary corresponding to the interface depicted in Figure 4.1.

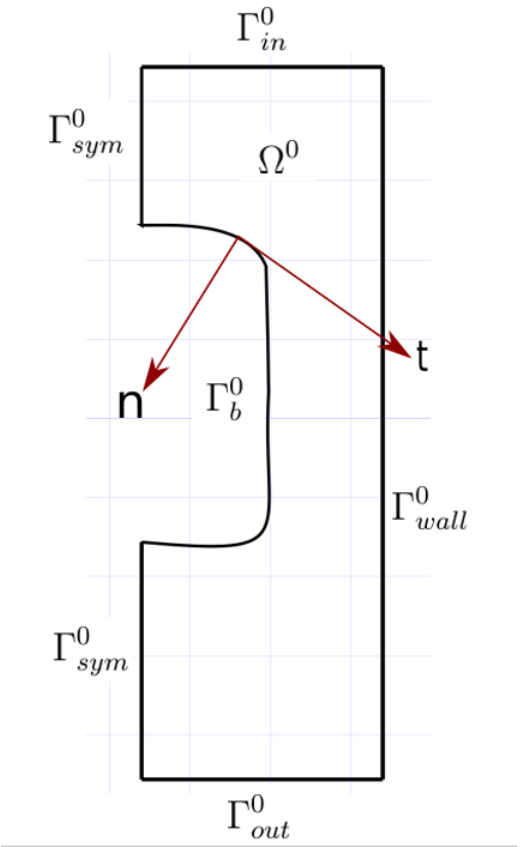


Figure 4.1: Axisymmetric 2D domain.

We note the addition of a new term in (4.1) when it is compared with (3.21). This new weak form of continuity equation is derived from a penalised continuous continuity equation written as

$$\varepsilon p = -\nabla . \mathbf{u} \tag{4.3}$$

where ε is called the *penalty parameter* and the smaller its value, the more exactly the incompressibility constraint is satisfied.

This method of including the incompressibility constraint in the formulation is known as the *consistent penalty function method*, and the model derived using it is termed *consistent penalty finite element model* [99]. The penalty function method allows us to reformulate a problem with constraints as one without constraints. Computationally, this method has the advantage that it prevents the presence of zeroes on the diagonal of the global coefficient matrix that would have resulted from the absence of pressure in the continuity equation, thereby avoiding the difficulties associated with solvers, particularly iterative solvers, used in solving the final discrete linear system of equations derived from weak form of governing equations.

The weak form of the momentum equation is non-linear in velocity and interface position due to the presence of convective term and the implicit treatment of curvature, respectively. For this reason, we solve the equations using Newton's method. First, we shall linearise the variables in the equations about a known solution and then present the penalty finite element models for the linearised equations. We stress that the finite element model can be written for the nonlinear equation and thereafter linearised. We, however, prefer the former approach as it gives a clearer perspective as to how the various component expressions used in building the global coefficient matrix (4.23) are obtained.

Let $\mathbf{u}^0$, p^0 and P_b^0 denote the approximately known solutions to the flow field variables and bubble pressure, respectively, on the currently known domain with interface location and curvature $\mathbf{r}^0$ and κ^0, respectively, then the unknown solution to the variables can be approximated

as

$$\mathbf{u} = \mathbf{u}^0 + \mathbf{u}^1 \tag{4.4a}$$

$$\mathbf{r} = \mathbf{r}^0 + \mathbf{x} \tag{4.4b}$$

$$p = p^0 + p^1 \tag{4.4c}$$

$$\kappa = \kappa^0 + \kappa^1 \tag{4.4d}$$

$$P_b = P_b^0 + P_b^1 \tag{4.4e}$$

where $\mathbf{u}^1$, p^1 and P_b^1 represent increment in the flow field variables and bubble pressure, respectively; $\mathbf{x}$ remains interface deformation and κ^1 is the increment in the interface curvature. Substituting (4.4) into (4.1) and (4.2), and neglecting all terms that are nonlinear in the increment variables (quadratic and higher order terms), we have

$$\int_{\Omega^0} \left\{ -\varepsilon p^1 \varphi - \left(\nabla . \mathbf{u}^1\right) \varphi \right\} d\Omega^0 = \int_{\Omega^0} \left\{ \left(\nabla . \mathbf{u}^0\right) \varphi \right\} d\Omega^0 \tag{4.5}$$

$$\begin{aligned} &\int_{\Omega^0} \left\{ \left[\left(\mathbf{u}^0 \cdot \nabla\right) \mathbf{u}^1 + \left(\mathbf{u}^1 \cdot \nabla\right) \mathbf{u}^0 \right] \cdot \mathbf{\Phi} + 2Nf^{-1} \mathbf{E}\left(\mathbf{u}^1\right) : \mathbf{E}\left(\mathbf{\Phi}\right) - p^1 \left(\nabla . \mathbf{\Phi}\right) \right\} d\Omega^0 \\ &- \int_{\Gamma_b^0} \left\{ \left[Eo^{-1} \kappa^1 - P_b^1 \right] \mathbf{n} \cdot \mathbf{\Phi} \right\} d\Gamma_b^0 = \\ &\quad - \int_{\Omega^0} \left\{ \left[\left(\mathbf{u}^0 \cdot \nabla\right) \mathbf{u}^0 \right] \cdot \mathbf{\Phi} + 2Nf^{-1} \mathbf{E}\left(\mathbf{u}^0\right) : \mathbf{E}\left(\mathbf{\Phi}\right) - p^0 \left(\nabla . \mathbf{\Phi}\right) \right\} d\Omega^0 \\ &\quad + \int_{\Gamma_b^0} \left\{ \left[Eo^{-1} \kappa^0 + z - P_b^0 \right] \mathbf{n} \cdot \mathbf{\Phi} \right\} d\Gamma_b^0 \end{aligned} \tag{4.6}$$

It should be noted that in (4.5) we have taken into consideration that $\varphi \in L_0^2$. Substituting for κ^1 using (3.69) and using Laplace-Beltrami operator (3.84) to approximate κ^0, equation (4.6)

becomes

$$\begin{aligned}
&\int_{\Omega^0} \left\{ \left[\left(\mathbf{u}^0 \cdot \nabla \right) \mathbf{u}^1 + \left(\mathbf{u}^1 \cdot \nabla \right) \mathbf{u}^0 \right] \cdot \mathbf{\Phi} \right\} d\Omega^0 + \int_{\Omega^0} 2Nf^{-1} \left\{ \mathbf{E}\left(\mathbf{u}^1 \right) : \mathbf{E}\left(\mathbf{\Phi} \right) \right\} d\Omega^0 \\
&- \int_{\Omega^0} p^1 \left\{ (\nabla . \mathbf{\Phi}) \right\} d\Omega^0 - \int_{\Gamma_b^0} Eo^{-1} \left\{ -\frac{dh}{ds} \left[\mathbf{n} \cdot \frac{d\mathbf{\Phi}}{ds} - \kappa_a \left(\mathbf{t} \cdot \mathbf{\Phi} \right) \right] + h \left[\kappa_a^2 + \kappa_b^2 \right] \mathbf{n} \cdot \mathbf{\Phi} \right\} d\Gamma_b^0 \\
&+ \int_{\Gamma_b^0} P_b^1 \left\{ \mathbf{n} \cdot \mathbf{\Phi} \right\} d\Gamma_b^0 = - \int_{\Omega^0} \left\{ \left[\left(\mathbf{u}^0 \cdot \nabla \right) \mathbf{u}^0 \right] \cdot \mathbf{\Phi} + 2\mathrm{Nf}^{-1} \mathbf{E}\left(\mathbf{u}^0 \right) : \mathbf{E}\left(\mathbf{\Phi} \right) - p^0 \left(\nabla . \mathbf{\Phi} \right) \right\} d\Omega^0 \\
&- \int_{\Gamma_b^0} \left\{ Eo^{-1} \left(\mathbf{t} \cdot \frac{d\mathbf{\Phi}}{ds} + \frac{\Phi_r}{r} \right) \right\} d\Gamma_b^0 + \int_{\Gamma_b^0} \left\{ \left[z - P_b^0 \right] \mathbf{n} \cdot \mathbf{\Phi} \right\} d\Gamma_b^0
\end{aligned} \tag{4.7}$$

To arrived at (4.7), we have carried out integration by part on κ^1, made use of Frenet-Serret relations (3.68) and simplified the surface gradient terms in (3.84) using (3.56), after substitutions. The goal is to solve for the increment in the flow field variables, bubble pressure and interface deformation magnitude, $\mathbf{u}^1$, p^1, P_b^1 and h, respectively.

Expanding the linearised weak forms of continuity (4.5) and momentum (4.7) equations using (3.3) and (3.6) as done in section 3.3 and then following the same procedures as described in section 3.4 for obtaining finite element models, we have the following compactly written equations as the consistent penalty finite element models for the linearised continuity and velocity components momentum equations, respectively:

continuity equation.

$$- \begin{bmatrix} \mathbf{Q}_r & \mathbf{Q}_z \end{bmatrix} \begin{bmatrix} \mathbf{v}_r^1 \\ \mathbf{v}_z^1 \end{bmatrix} - \mathbf{Q}_p \mathbf{p}^1 = \mathbf{f}^c \tag{4.8}$$

momentum equations

$$\begin{bmatrix} \mathbf{C}_{r,r} & \mathbf{C}_{r,z} \\ \mathbf{C}_{z,r} & \mathbf{C}_{z,z} \end{bmatrix} \begin{bmatrix} \mathbf{v}_r^1 \\ \mathbf{v}_z^1 \end{bmatrix} + \begin{bmatrix} \mathbf{K}_{r,r} & \mathbf{K}_{r,z} \\ \mathbf{K}_{z,r} & \mathbf{K}_{z,z} \end{bmatrix} \begin{bmatrix} \mathbf{v}_r^1 \\ \mathbf{v}_z^1 \end{bmatrix} - \begin{bmatrix} \mathbf{Q}_r^T \\ \mathbf{Q}_z^T \end{bmatrix} \mathbf{p}^1 - \begin{bmatrix} \mathbf{M}_{r,h} \\ \mathbf{M}_{z,h} \end{bmatrix} \mathbf{h} + \begin{bmatrix} \mathbf{m}_{r,P_b} \\ \mathbf{m}_{z,P_b} \end{bmatrix} P_b^1 = \begin{bmatrix} \mathbf{f}_r^m \\ \mathbf{f}_z^m \end{bmatrix} \tag{4.9}$$

where $\mathbf{v}_i^1 \ \forall \ i = r, z$, $\mathbf{p}^1$ and $\mathbf{h}$ are vectors of unknown nodal parameters for linearised velocity components increments, pressure increment and interface deformation magnitude, respectively; P_b^1 is the increment in linearised unknown bubble pressure; $\mathbf{Q}_i \ \forall \ i = r, z$ are coefficient matrices of the velocity components in the continuity equation and are as already defined in (3.36) and

(3.38), respectively. $\mathbf{Q}_p$ is coefficient matrix of pressure nodal parameters in the linearised, penalised continuity equation, define as

$$\mathbf{Q}_p = \int_{\Omega^{0,e}} \left\{ \varepsilon \mathbf{\Lambda} \mathbf{\Lambda}^T \right\} d\Omega^{0,e} \tag{4.10}$$

and $\mathbf{f}^c$ is a vector of the right hand side of the same equation, given as

$$\mathbf{f}^c = \int_{\Omega^{0,e}} \left\{ \left(\nabla . \, \mathbf{u}^0 \right) \mathbf{\Lambda} \right\} d\Omega^{0,e} \tag{4.11}$$

$\mathbf{C}_{i,j}$ and $\mathbf{K}_{i,j}$ $\forall$ $i, j = r, z$ are coefficient matrices of the velocity components in the convective and viscous terms of the momentum equations of the velocity components. They are given as

convective coefficient matrices

$$\mathbf{C}_{i,i} = \int_{\Omega^{0,e}} \left\{ \mathbf{\Psi} \left[\left(\mathbf{u}^0 \cdot \nabla \right) \mathbf{\Psi}^T + \delta_{r,i} \mathbf{\Psi}^T \frac{\partial u_r^0}{\partial r} + \delta_{z,i} \mathbf{\Psi}^T \frac{\partial u_z^0}{\partial z} \right] \right\} d\Omega^{0,e} \; \forall \; i = r, z \tag{4.12a}$$

$$\mathbf{C}_{r,z} = \int_{\Omega^{0,e}} \left\{ \mathbf{\Psi} \mathbf{\Psi}^T \frac{\partial u_r^0}{\partial z} \right\} d\Omega^{0,e} \tag{4.12b}$$

$$\mathbf{C}_{z,r} = \int_{\Omega^{0,e}} \left\{ \mathbf{\Psi} \mathbf{\Psi}^T \frac{\partial u_z^0}{\partial r} \right\} d\Omega^{0,e} \tag{4.12c}$$

viscous coefficient matrices

$$\mathbf{K}_{i,i} = \int_{\Omega^{0,e}} Nf^{-1} \left\{ 2 \frac{\partial \mathbf{\Psi}}{\partial i} \frac{\partial \mathbf{\Psi}^T}{\partial i} + 2 \delta_{r,i} \frac{\mathbf{\Psi} \mathbf{\Psi}^T}{r^2} + \delta_{r,i} \frac{\partial \mathbf{\Psi}}{\partial z} \frac{\partial \mathbf{\Psi}^T}{\partial z} + \delta_{z,i} \frac{\partial \mathbf{\Psi}}{\partial r} \frac{\partial \mathbf{\Psi}^T}{\partial r} \right\} d\Omega^{0,e} \; \forall \; i = r, z \tag{4.13a}$$

$$\mathbf{K}_{r,z} = \int_{\Omega^{0,e}} Nf^{-1} \left\{ \frac{\partial \mathbf{\Psi}}{\partial z} \frac{\partial \mathbf{\Psi}^T}{\partial r} \right\} d\Omega^{0,e} \tag{4.13b}$$

$$\mathbf{K}_{z,r} = \int_{\Omega^{0,e}} Nf^{-1} \left\{ \frac{\partial \mathbf{\Psi}}{\partial r} \frac{\partial \mathbf{\Psi}^T}{\partial z} \right\} d\Omega^{0,e} \tag{4.13c}$$

$\mathbf{M}_{i,h}$ and $\mathbf{m}_{i,P_b}$ $\forall$ $i = r, z$ are coefficient matrices and vectors of interface deformation and bubble pressure, respectively in the momentum equations of the velocity components, define as

$$\mathbf{M}_{i,h} = \int_{\Gamma_b^{0,e}} Eo^{-1} \left\{ - \left[n_i \frac{d\mathbf{\Psi}}{ds} - \kappa_a \left(t_i \mathbf{\Psi} \right) \right] \frac{d\boldsymbol{\eta}^T}{ds} + n_i \left[\kappa_a^2 + \kappa_b^2 \right] \mathbf{\Psi} \boldsymbol{\eta}^T \right\} d\Gamma_b^{0,e} \quad \forall \quad i = r, z \tag{4.14}$$

$$\mathbf{m}_{P_b,i} = \int_{\Gamma_b^{0,e}} \{n_i \boldsymbol{\Psi}\}\, d\Gamma_b^{0,e} \quad \forall \quad i = r, z \tag{4.15}$$

$\mathbf{f}_i^m \quad \forall \quad i = r, z$ are vectors of the right hand side of momentum equations of velocity components. They are given as

$$\begin{aligned}\mathbf{f}_r^m = &- \int_{\Omega^{0,e}} \left\{ \left[\left(\mathbf{u}^0 \cdot \nabla \right) u_r^0 \right] \boldsymbol{\Psi} + Nf^{-1} \left[2\frac{\partial \boldsymbol{\Psi}}{\partial r}\frac{\partial u_r^0}{\partial r} + 2\frac{\boldsymbol{\Psi} u_r^0}{r^2} + \frac{\partial \boldsymbol{\Psi}}{\partial z}\frac{\partial u_r^0}{\partial z} + \frac{\partial \boldsymbol{\Psi}}{\partial z}\frac{\partial u_z^0}{\partial r} \right] \right. \\ &\left. - p^0 \left(\frac{\partial \boldsymbol{\Psi}}{\partial r} + \frac{\boldsymbol{\Psi}}{r} \right) \right\} d\Omega^{0,e} - \int_{\Gamma_b^{0,e}} \left\{ Eo^{-1} \left(t_r \frac{d\boldsymbol{\Psi}}{ds} + \frac{\boldsymbol{\Psi}}{r} \right) \right\} d\Gamma_b^{0,e} + \int_{\Gamma_b^{0,e}} \left\{ \left[z - P_b^0 \right] n_r \ \boldsymbol{\Psi} \right\} d\Gamma_b^{0,e}\end{aligned} \tag{4.16}$$

$$\begin{aligned}\mathbf{f}_z^m = &- \int_{\Omega^{0,e}} \left\{ \left[\left(\mathbf{u}^0 \cdot \nabla \right) u_z^0 \right] \boldsymbol{\Psi} + Nf^{-1} \left[2\frac{\partial \boldsymbol{\Psi}}{\partial z}\frac{\partial u_z^0}{\partial z} + \frac{\partial \boldsymbol{\Psi}}{\partial r}\frac{\partial u_z^0}{\partial r} + \frac{\partial \boldsymbol{\Psi}}{\partial r}\frac{\partial u_r^0}{\partial z} \right] \right. \\ &\left. - p^0 \left(\frac{\partial \boldsymbol{\Psi}}{\partial z} \right) \right\} d\Omega^{0,e} - \int_{\Gamma_b^{0,e}} \left\{ Eo^{-1} \left(t_z \frac{d\boldsymbol{\Psi}}{ds} \right) \right\} d\Gamma_b^{0,e} + \int_{\Gamma_b^{0,e}} \left\{ \left[z - P_b^0 \right] n_z \ \boldsymbol{\Psi} \right\} d\Gamma_b^{0,e}\end{aligned} \tag{4.17}$$

In addition to the finite element models for the linearised momentum and continuity equations, we have models derived from the linearisation of the interface deformation magnitude (3.49) and bubble volume (3.87) equations discussed in sections (3.5) and (3.7), respectively.

interface deformation equation

$$\mathbf{X}_h \mathbf{h} - \begin{bmatrix} \mathbf{X}_r & \mathbf{X}_z \end{bmatrix} \begin{bmatrix} \mathbf{v}_r^1 \\ \mathbf{v}_z^1 \end{bmatrix} = \mathbf{f}^h \tag{4.18}$$

bubble volume equation

$$\begin{bmatrix} \mathbf{b}_r^T & \mathbf{b}_z^T \end{bmatrix} \begin{bmatrix} \mathbf{v}_r^1 \\ \mathbf{v}_z^1 \end{bmatrix} = f^b \tag{4.19}$$

$\mathbf{X}_i$ and $\mathbf{b}_i \ \forall \ i = r, z$ are coefficient matrices and vectors of velocity components in the interface deformation and bubble volume equations, respectively. $\mathbf{X}_h$ is the coefficient matrix of interface deformation vector in interface deformation equation. $\mathbf{f}^d$ and f^v are vector and constant of the right hand side of the linearised deformation and bubble volume equations, respectively. The matrices, vectors and constant are given by

interface deformation equation matrices and vector

$$\mathbf{X}_i = \int_{\Gamma_b^{0,e}} \delta t n_i \left\{ \boldsymbol{\eta} \boldsymbol{\Psi}^T \right\} d\Gamma_b^{0,e} \quad \forall\, i = r, z \tag{4.20a}$$

$$\mathbf{X}_h = \int_{\Gamma_b^{0,e}} \left\{ \boldsymbol{\eta} \boldsymbol{\eta}^T \right\} d\Gamma_b^{0,e} \tag{4.20b}$$

$$\mathbf{f}^h = \int_{\Gamma_b^{0,e}} \left\{ \delta t \left(\mathbf{u}^0 \cdot \mathbf{n} \right) \boldsymbol{\eta} \right\} d\Gamma_b^{0,e} \tag{4.20c}$$

bubble volume equation vectors and constant

$$\mathbf{b}_i = \mathbf{m}_{i,P_b} = \int_{\Gamma_b^{0,e}} n_i \left\{ \boldsymbol{\Psi} \right\} d\Gamma_b^{0,e} \quad \forall\, i = r, z \tag{4.21a}$$

$$f^b = - \int_{\Gamma_b^{0,e}} \left\{ \left(\mathbf{u}^0 \cdot \mathbf{n} \right) \right\} d\Gamma_b^{0,e} - 3 \frac{\Delta V_b}{\delta t} \tag{4.21b}$$

The linearised finite element model equations (4.8), (4.9), (4.18) and (4.19) are combined and compactly written as

$$\mathbf{A}\mathbf{w} = \mathbf{f} \tag{4.22}$$

with

$$\mathbf{A} = \begin{bmatrix} (\mathbf{C}_{r,r} + \mathbf{K}_{r,r}) & (\mathbf{C}_{r,z} + \mathbf{K}_{r,z}) & -\mathbf{Q}_r^T & -\mathbf{M}_{r,h} & \mathbf{b}_r \\ (\mathbf{C}_{z,r} + \mathbf{K}_{z,r}) & (\mathbf{C}_{z,z} + \mathbf{K}_{z,z}) & -\mathbf{Q}_z^T & -\mathbf{M}_{z,h} & \mathbf{b}_z \\ -\mathbf{Q}_r & -\mathbf{Q}_z & -\mathbf{Q}_p & 0 & 0 \\ -\mathbf{X}_r & -\mathbf{X}_z & 0 & \mathbf{X}_h & 0 \\ \mathbf{b}_r^T & \mathbf{b}_z^T & 0 & 0 & 0 \end{bmatrix}, \quad \mathbf{w} = \begin{bmatrix} \mathbf{v}_r^1 \\ \mathbf{v}_z^1 \\ \mathbf{p}^1 \\ \mathbf{h} \\ P_b^1 \end{bmatrix} \quad \text{and} \quad \mathbf{f} = \begin{bmatrix} \mathbf{f}_r^m \\ \mathbf{f}_z^m \\ \mathbf{f}^c \\ \mathbf{f}^h \\ f^b \end{bmatrix} \tag{4.23}$$

Equation (4.22) is solved for the *increment* in the variables of the problem. In the next section, a detailed description of the numerical simulations of the steady state model is described. Before proceeding to the next section, we make note of the following:

The presence of a new boundary, Γ_{sym} along the axis of symmetry. The boundary conditions

imposed along this boundary are

$$\mathbf{u} \cdot \mathbf{n} = 0 \tag{4.24a}$$

$$\mathbf{n} \cdot \mathbf{T} \cdot \mathbf{t} = 0 \tag{4.24b}$$

The principal curvatures, κ_a and κ_b, the unit normals, n_r and n_z and the unit tangents t_r and t_z are finite element functions and approximated using P_1 finite elements after the computation of their values using (3.71) and (3.72).

To avoid numerical problem, we replace the zero in the last diagonal term of the coefficient matrix of (4.22) with constant $b_b = \varepsilon$. The diagonal term is zero because of the absence of the variable P_b in the volume constraint equation (4.19) and the replacement of the zero with the constant is equivalent to penalisation of (4.19) by adding a new term εP_b^1 to its right hand side in a way similar to penalisation of continuity equation (4.8).

At steady state, the normal velocity and deformation magnitude on the interface are

$$\mathbf{u}^s \cdot \mathbf{n} \approx 0 \tag{4.25a}$$

$$\int_{\Gamma_b^0} \left\{h^s \xi\right\} d\Gamma_b^0 = \int_{\Gamma_b^0} \left\{\delta t \left(\mathbf{u}^s \cdot \mathbf{n}\right) \xi\right\} d\Gamma_b^0 \approx 0. \tag{4.25b}$$

and the two weak forms of the governing equations reduce to

$$\int_{\Omega^0} \left\{\varepsilon p^s \varphi + \left(\nabla . \mathbf{u}^s\right) \varphi\right\} d\Omega^0 = 0 \tag{4.26a}$$

$$\begin{aligned} &\int_{\Omega^0} \left\{\left[\left(\mathbf{u}^s \cdot \nabla\right) \mathbf{u}^s\right] \cdot \mathbf{\Phi} + 2Nf^{-1} \mathbf{E}\left(\mathbf{u}^s\right) : \mathbf{E}\left(\mathbf{\Phi}\right) - p^s \left(\nabla . \mathbf{\Phi}\right)\right\} d\Omega^0 \\ &- \int_{\Gamma_b^0} \left\{\left[Eo^{-1} \kappa^s + z^s - P_b^s\right] \mathbf{n} \cdot \mathbf{\Phi}\right\} d\Gamma_b^0 = 0 \end{aligned} \tag{4.26b}$$

where the superscript s is used to denote the converge steady state solutions of the variables.

In (4.12) and (4.13), $\delta_{i,j}\ \forall\ i,j = r,z.$ remains Kronecker delta and ε in b_b above remains penalty parameter. ε is assigned a value of 10^{-8}.

4.2 Steady state model solution

The numerical solution of the model of a steadily rising Taylor bubble for a given Nf, Eo and U_m implemented within FreeFem++ begins by providing initial guess for the bubble rise velocity, U_b, the flow field variables, $(\mathbf{u}, p)$ and position vector of the interface, $\mathbf{r}_i = r_i\mathbf{i}_r + z_i\mathbf{i}_z \ \forall \ i = 0, 1, \cdots, n_d$. For the first simulation carried out, $Nf = 40$, $Eo = 60$, U_b was initially taken to be 0.35 and the Taylor bubble interface position was assumed to be described by a quarter-circle top, cylindrical body and a quarter-circle bottom. The initial guess for the flow field was then obtained by solving the Stokes equation in the domain formed by the assumed bubble interface. For subsequent simulations, the previous steady state solutions for the condition closest to the new condition was used as initial guess. With known initial guess, the solution proceed in three stages: curvature computation, variables solution and domain deformation.

Curvature computation : This is the first stage of the numerical solution. It is used for the computation of the unit normals, unit tangents and the principal curvatures of the interface. The system of equations (3.80) is solved, (3.75) utilised to compute tangent vector, after which the unit normals and tangents are computed using (3.72) and finally the principal curvatures are calculated using (3.70b) and (3.71).

Variables solution : It is the second stage and is divided into two parts. The first part is used for solving the Galerkin weak form of the steady state model described in the previous section using newton method. It begins by building global matrix $\mathbf{A}$ and vector $\mathbf{f}$ of (4.23). The system of equations (4.22) is solved using MUltifrontal Massively Parallel sparse direct Solver (MUMPS) for the increment in the variables (4.27a), the solution to the variables (4.27b) and the initial guess for the flow field and bubble pressure updated (4.27c). This step captured in (4.27) is repeated until the L_2 norm of the increment, err_n

is less than newton iteration tolerance, $tol_n = 10^{-15}$ (4.27d).

$$\mathbf{w} = \mathbf{A}^{-1}\mathbf{f} \tag{4.27a}$$

$$\begin{bmatrix} \mathbf{u}_r \\ \mathbf{u}_z \\ \mathbf{p} \\ P_b \end{bmatrix} = \begin{bmatrix} \mathbf{u}_r^0 \\ \mathbf{u}_z^0 \\ \mathbf{p}^0 \\ P_b^0 \end{bmatrix} + \begin{bmatrix} \mathbf{v}_r^1 \\ \mathbf{v}_z^1 \\ \mathbf{p}^1 \\ P_b^1 \end{bmatrix} \tag{4.27b}$$

$$\begin{bmatrix} \mathbf{u}_r^0 \\ \mathbf{u}_z^0 \\ \mathbf{p}^0 \\ P_b^0 \end{bmatrix} = \begin{bmatrix} \mathbf{u}_r \\ \mathbf{u}_z \\ \mathbf{p} \\ P_b \end{bmatrix} \tag{4.27c}$$

$$err_n = \|\mathbf{w}\|_2 < tol_n \tag{4.27d}$$

In the second part, the rise velocity of the bubble is estimated from the velocity field solution computed in the first part. The velocity field computed is converted from a moving frame of reference to a fixed frame (4.28a) and the value of the axial velocity at the nose of the bubble is extracted and set as the new bubble velocity (4.28b). This step is summarised as

$$\mathbf{u}^{fixed} = \mathbf{u} + \mathbf{u}_b = u_r\mathbf{i}_r + (u_z - U_b)\,\mathbf{i}_z \tag{4.28a}$$

$$U_b = -u_z^{fixed}(0,0) \tag{4.28b}$$

During the entire simulation, we ensure that the nose of the bubble remain fixed at the origin of the domain.

Domain deformation : This is the last stage in the numerical solution. At this stage the mesh deformation, $\boldsymbol{\phi}$ is computed by solving the linear elasticity equation (3.50) under the boundary condition (3.51) using the interface deformation h calculated in (4.27a) and thereafter the domain is updated using (3.52). In addition to boundary conditions specified in (3.51), we also imposed the following conditions along the symmetry axis,

Γ_{sym}.

$$\boldsymbol{\phi} \cdot \mathbf{n} = 0 \tag{4.29a}$$

$$\mathbf{n} \cdot \boldsymbol{\sigma} \cdot \mathbf{t} = 0 \tag{4.29b}$$

where $\boldsymbol{\sigma}$ is the linear elasticity stress tensor defined in section 3.5.3. We note that it is at this stage that it is determined whether the numerical solution have to be terminated or not. Prior to the solving the linear elasticity equation just described, the L_2 norm of the normal velocity at the interface, err_d, is computed and compared with a deformation iteration tolerance, $tol_d = 10^{-4}$. If

$$err_d = \|\mathbf{u} \cdot \mathbf{n}\|_2 \text{ on } \Gamma_b^0 > tol_d = 10^{-4}, \tag{4.30}$$

the mesh deformation proceed as described above and the three stages are repeated again using the updated initial guess for the variables (4.27c) and bubble rise velocity (4.28b). On the other hand, if $err_d < tol_d$, the numerical solution is terminated and the variable solutions (4.27b) and rise velocity (4.28b) are declared as the solutions for the given dimensionless parameters. Furthermore, the interface location around which the last solution to the variables is obtained is also declared as the steady state bubble shape. It is noteworthy that occasionally, there is the need to carry out remeshing. This is also done at this stage. Basically, we adapt the mesh around the interface to the curvature of the interface and the flow field around it while other boundaries of the domain are maintained at a fixed number of mesh points.

4.3 Steady state model validation

The model derived and the numerical solution strategies discussed in the previous sections were validated by simulating the experiment of [17] in which the velocity field around a Taylor bubble rising in stagnant olive oil in a pipe of diameter $19\,mm$ was measured using Particle

Image Velocimetry (PIV) at five different positions around the bubble. The fluid properties used in the experiment and the corresponding dimensionless parameters are given in Table 4.1.

Table 4.1: Dimensionless parameters corresponding to the properties of the fluid used for validation.

Fluid properties				parameters			
$\rho\,(kgm^{-3})$	$\mu\,(Nsm^{-2})$	$\gamma\,(Jm^{-2})$	$V_b\,(m^3)$	Nf	Eo	U_m	H_b
911	84 $\times 10^{-3}$	3.82 $\times 10^{-5}$	10 $\times 10^{-6}$	88.95	98.33	0	2.00

Here, H_b denotes the dimensionless height of a cylinder of the same diameter as the pipe used in the experiment that has the same volume as the gas phase. It can also be referred to as the aspect ratio for the bubble.

We solved the derived finite element models for the calculated dimensionless parameters using initial bubble shape shown in Figure 4.2. The mesh is boundary fitted and is structured such that regions around the bubble are finely resolved. Table 4.2 shows the dimensionless edge lengths of elements used for the labelled boundary regions around the domain (see Figure 4.2). For immediate regions around the bubble, $\Big($(2b), (2c), (2d), (4b) and (6a)$\Big)$, triangle with smaller edge lengths, leading to finer mesh, are used. At the interface, we maintained a fixed range of triangles $(700 - 800)$, while the distribution and range of triangle edge lengths are left for the automatic mesh adaptor to determine.

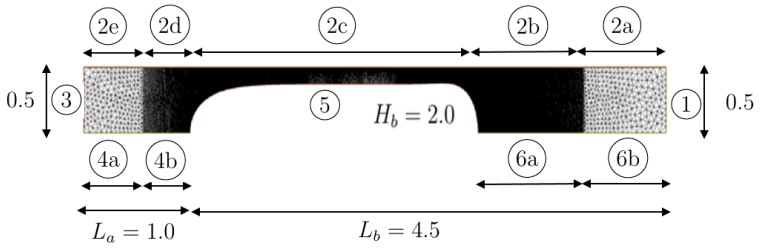


Figure 4.2: Mesh structure around Taylor bubble

To guide the distribution and triangles edge length range, we adapt the interface mesh to the curvature of the interface and flow field, and a maximum edge length of 0.06 was stipulated. It is noteworthy that in Table 4.2, the number of triangles on the boundary is calculated by dividing the boundary length by the boundary corresponding triangle edge length.

Table 4.2: Number and length of the edge of triangle elements at different sections of the domain boundary used in mesh generation.

Boundary region(s)	Triangle edge length	Boundary length	Number of triangles
(1) and (3)	0.042	0.5	12
(2a) and (6b)	0.042	varies	varies
(2b) and (6a)	0.004	1.0	250
(2c)	0.004	varies	varies
(2d) and (4b)	0.007	0.45	64
(2e) and (4a)	0.042	0.55	13
(5)	varies	varies	700-800

For the validation and the results to be presented, we maintained a fixed dimensionless distance of $L_a = 1.0$ and $L_b = 4.5$ ahead and below the bubble nose, respectively. These distances and mesh structure have been tested to ensure that the inlet and outlet boundaries as well as the mesh have insignificant influence on both the steady state and linear stability results. The converged steady shape and the flow patterns around it are shown in Figure 4.3. It should be noted that for domain length in which the inlet and outlet boundaries have no influence on the steady state results, in place of boundary conditions (3.8) and (3.9), periodic boundary condition can be imposed. This approach was used by [66] in their numerical study of Taylor bubble dynamics and can easily be implemented within FreeFem++.

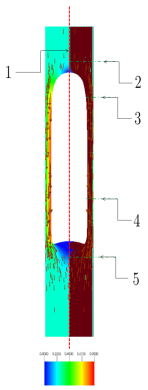
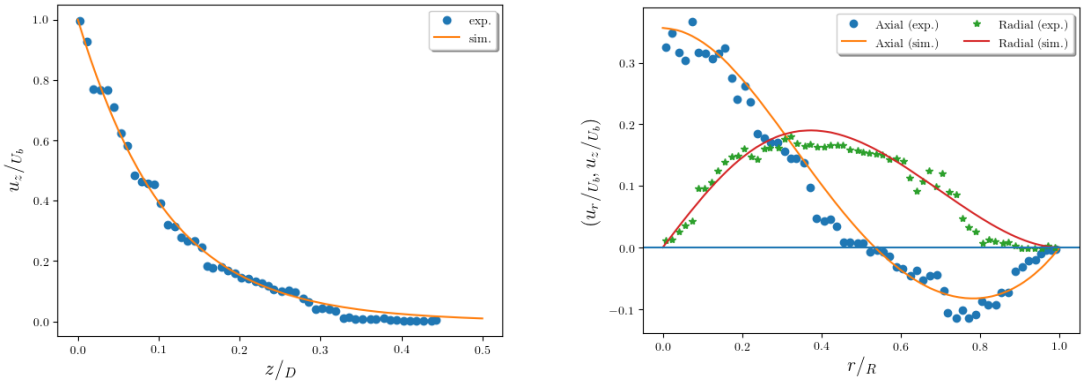


Figure 4.3: Flow structure around the steady state topology in a moving frame of reference showing the five different positions at which measurements were taken for validation.

The predicted dimensionless bubble rise velocity is 0.2928, correspond to a deviation of 3.3663% from the experimentally measured value of 0.303. Further comparisons with the experiment

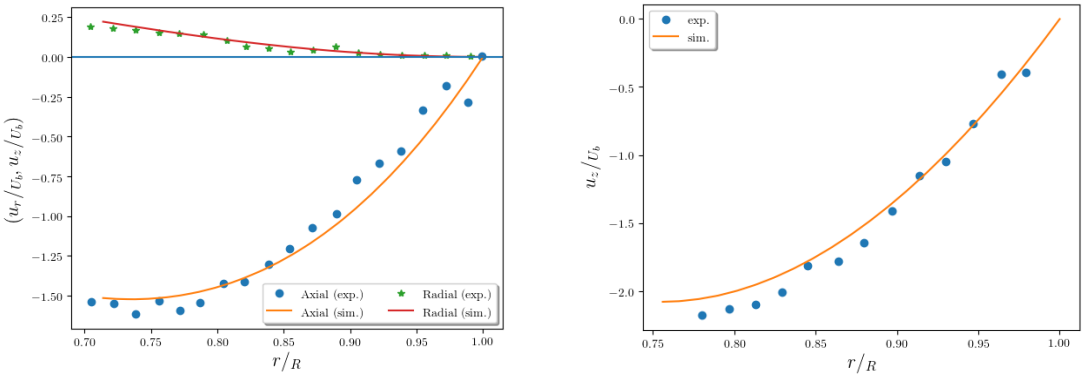
were carried out using the flow field results at the five measurement positions shown in Figure 4.3. Ahead of the bubble, velocity measurements were taken along the tube axis and in the radial direction at axial distance of $0.111D$. Figures 4.4a and 4.4b show the velocity profiles for these two locations and are well predicted by our simulation.



(a) (b)

Figure 4.4: Velocity profiles ahead of the bubble, (a) axial velocity component along the tube axis (position 1) and (b) axial and radial velocity components at $\frac{z}{D} = 0.111$ ahead of the bubble nose (position 2); Numerical results (solid lines) compared to experimental PIV measurements (symbols) of [17].

Figure 4.5a compared the velocity measurement taken at axial distance of $0.504D$ below the bubble nose. At this point, the film is still developing as seen in the magnitude of the radial velocity. When the film is fully developed, the magnitude of the radial velocity at all points in the radial direction are approximately zero.



(a) (b)

Figure 4.5: Velocity profiles in the film regions, (a) axial and radial velcity components in the developing film at $\frac{z}{D} = 0.504$ below the bubble nose (position 3) and (b) axial velocity component in the fully developed film (position 4); Numerical results (solid lines) compared to experimental PIV measurements (symbols) of Bugg and Saad [17].

By progressively plotting the radial velocity profile at various points below the bubble nose, a point is reached at which the radial velocity becomes zero. The axial velocity profile at this location is shown in Figure 4.5b and the dimensionless film thickness was measured to be 0.1235 . Although no experimental measurement of the film thickness was reported in [17], the deviation of the numerical simulation results from the theoretical estimated value of [15] using (2.13), which predicts the film thickness to be 0.1193, is 3.52%.

As the liquid emerges from the falling film region into the wake of the bubble, the radial component of its velocity reappear in order to redirect the liquid from the film back towards the center of the tube. Figure 4.6 shows the velocity profile in the wake of the Taylor bubble at axial distance of $\frac{1}{5}D$ below the bubble bottom.

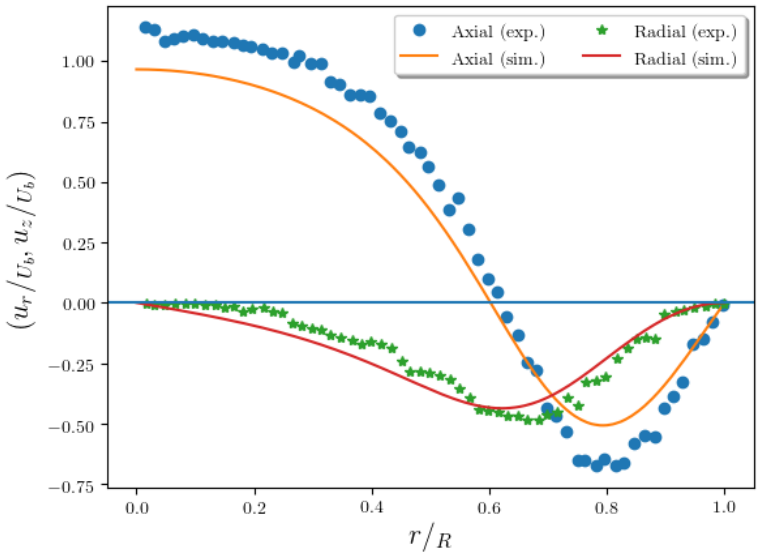


Figure 4.6: Axial and radial components of velocity at distance $\frac{z}{D} = 0.20$ below the bubble bottom (position 5); Numerical results (solid lines) compared to experimental PIV measurements (symbols) of Bugg and saad [17].

While the radial component of the experimental velocity profile is reasonably predicted by the numerical simulation, it is obvious that there is large deviation of the numerical axial velocity from the experiment data. We note that similar large deviation of the axial velocity was observed by [17, 66] in their numerical simulations of the same experiment. We therefore agree with [66] that it is very much possible that the experimental data for the wake region are slightly inaccurate.

4.4 Steady state characterisations in stagnant liquids

Previous sections have addressed the derivation, numerical solution and validation of steady state model. Here, the focus is on detailed presentation of the results of the steady state simulation carried out on a Taylor bubble of dimensionless volume $V_B = 0.3389\pi$, equivalent to aspect ratio, $H_B = 1.3556$, in stagnant liquid. The effects of dimensionless parameters Nf and Eo on the hydrodynamic features defining a steadily rising Taylor bubble, depicted in Figure 4.7 using notations that are define in Table 4.3, are addressed. The ranges of Nf and Eo covered are $[40, 300]$ and $[10, 300]$, respectively. We limited our analysis to these ranges because at higher Nf and Eo, our steady state solution began to depend on the choice of pseudo-time step-size, δt. Further details on this problem are given in section 4.6.

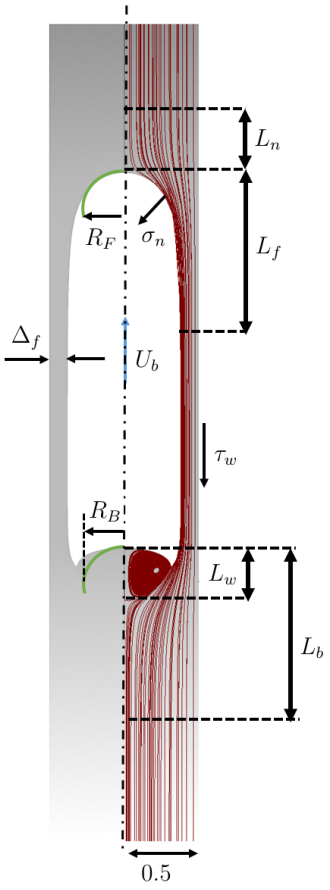


Figure 4.7: Schematic representation of the main hydrodynamic features of Taylor bubble discussed in the thesis. All features are dimensionless and are based on the characteristic scales stated in section 3.2

Table 4.3: Definition of notations depicted in Figure 4.7.

Region of domain	Notation	Definition
Nose region	U_b	Bubble rise velocity
	R_F	Average radius of curvature of bubble nose
	L_n	Flow stabilisation length ahead of bubble nose
Film region	L_f	Flow stabilisation length in the liquid film
	Δ_f	Equilibrium film thickness
Wall	τ_w	Shear stress at the wall
Interface	σ_n	Normal stress at the interface
Bottom region	R_B	Average radius of curvature of bubble bottom
	L_w	Length of wake below bubble bottom
	L_b	Flow stabilisation length below bubble bottom

4.4.1 Qualitative analysis of steady state shapes and flow field

It is insightful to qualitatively examine the influence of the two dimensionless parameters that define a steadily rising Taylor bubble in stagnant liquid on both the steady state Taylor bubble shape and the flow field around it before proceeding to a more detailed presentation of the quantitative results for all the hydrodynamic features highlighted. For each Taylor bubble, inspired by [58], the steady state shape is presented as a sectional plane through the center of its three-dimensional axisymmetric shape, coloured using the velocity magnitude, with streamline and vector field superimposed on the left and right side of the axis of symmetry, respectively.

Effect of inverse viscosity number

The inverse viscosity is a measure of the relative importance of the magnitude of the gravity to viscous force. At constant Eo and U_m, increase in Nf translates to decrease in the viscosity of the liquid, and its influence on the bubble shape and the surrounding flow field is shown in Figure 4.8 for $Eo = 220$ and $U_m = 0.00$. By increasing Nf, the resistance to the rise of Taylor bubble by the liquid phase is decreased, making it easier for the bubble to rise faster, which is reflected in the magnitude of the rise velocity in Figure 4.8. For the same increment in Nf, it can be seen that the corresponding increment in the rise velocity decreases as Nf is increased progressively. It is therefore expected, as already proven experimentally and theoretically, that

the rise velocity approaches a constant value as Nf is further increased.

It is discernible from the same figure that the thickness of the film between the interface and the tube wall decreases with Nf. This can be attributed to the decrease in the magnitude of the normal component of the traction force exerted on the interface, i.e the normal stress in the direction normal to the interface, as Nf is increased. The decrease in the normal stress magnitude with progressive increase in inverse viscosity number is manifested in the decrease in the value of pressure inside the bubble, also shown in Figure 4.8. The accompany effect of the decrease in film thickness with increase in Nf is the decrease in the length of the bubble in order to ensure that the volume of the bubble is conserved.

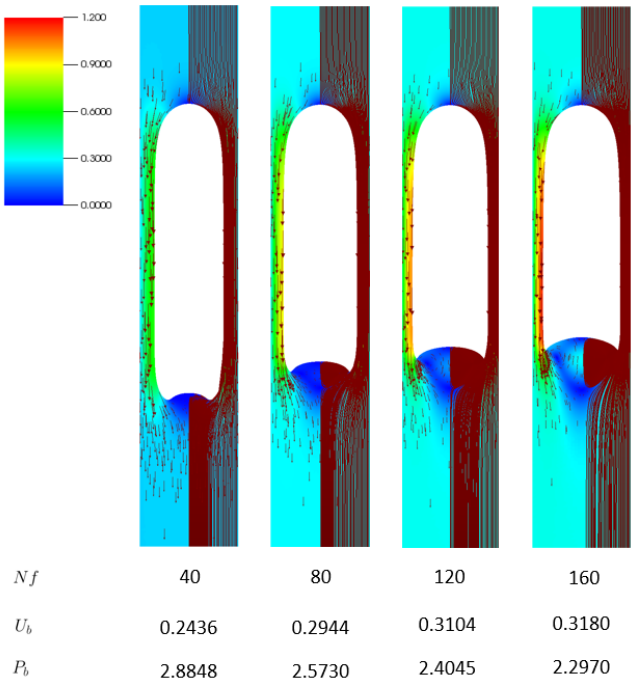


Figure 4.8: Effect of Nf on steady state bubble shape and the surrounding flow field for $Eo = 220$ and $U_m = 0$; showing streamlines and vector field superimposed on velocity magnitude pseudocolour plot on the right and left sides of the symmetry axis, respectively.

Another qualitative feature that is observable in Figure 4.8 is the increase in the intensity of the recirculation in the wake region as Nf is increased. The reason for this can be understood from the perspective of the origin of the recirculation which is a result of the adverse pressure drop that accompanies the jetting of the liquid in the film into the bottom of the bubble, leading to flow separation. The magnitude of the jetting velocity, depicted by the colouration of the

film region as represented on the colour map on the top left hand side of the figure, increases with increasing value of Nf, resulting in increased wake length and wake volume. Another effect of the increase in the intensity of the recirculatory flow in the wake region with Nf is the increase in indentation of the bubble bottom, which in turn, resulted in the Taylor bubble becoming more dimpled. We anticipate that as Nf is further increased, the bubble bottom will eventually form a skirted tail and then, finally culminate in the breakup of small bubbles from the tail. It is therefore expected that at very high Nf and Eo, as we approach topological transitions, having a converged steady state solution will become increasingly difficult.

Effect of Eötvös number

For a fixed value of Nf and U_m, changes in the Eötvös number indicate variation in the relative effect of the surface tension force to the buoyancy force. To describe the effect of Eo on steady state shape and flow field around a Taylor bubble, we show four simulation cases, with a fixed Nf of 100 in Figure 4.9.

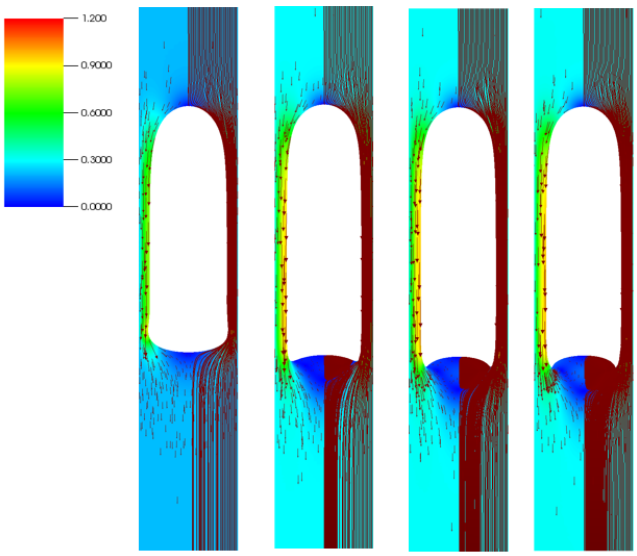


Figure 4.9: Effect of Eo on steady state bubble shape and the surrounding flow field at $Nf = 100$ and $U_m = 0$; showing streamlines and vector field superimposed on velocity magnitude pseudocolour plot on the right and left sides of the symmetry axis, respectively.

Under the influence of Eo, changes in concavity of the Taylor bubble bottom are most glaring. Progressively, as Eo increases, the bubble bottom becomes more deformed with the tails of the Taylor bubbles getting elongated, which, of course, is the result of the decrease in the tendency of the interface to resist deformation as Eo is increased. Unlike variation in inverse viscosity number, changes in Eötvös number have marginal influence on the rise velocity of the bubble, particularly beyond $Eo = 100$, Figure 4.9. Similarly, above $Eo = 100$, the influence of increase in Eo on the bubble pressure is negligible, the manifestation of which is seen in the bubble maintaining almost a constant length. It thus appears that the limit of the influence of Eo on the bubble rise velocity and film thickness is around $Eo = 100$. At $Eo = 20$, which falls within the regime where surface tension is significant as mapped out by [114], the bubble is quite different from those of other higher Eo in terms of its rise velocity, nose and bottom curvatures, film thickness and bubble length. To shed more light on the distinctive features of Taylor bubble in this regime, we show in Figure 4.10 the effect of Nf on the steady state shapes and flow fields at $Eo = 10$ and 20.

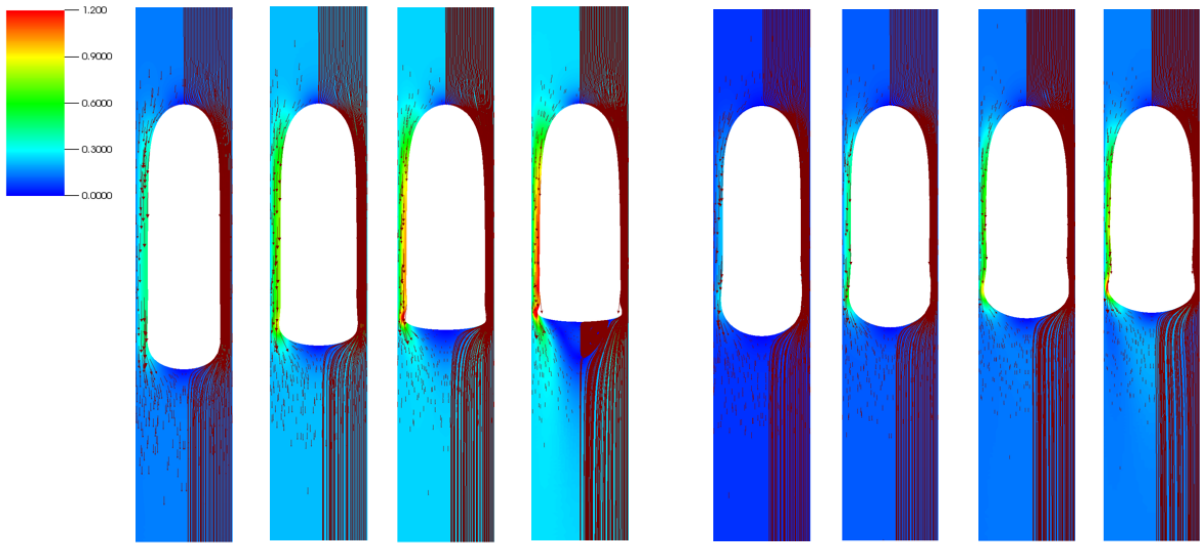


Figure 4.10: Effect of variation of Nf on steady state Taylor bubble shapes at low Eötvös numbers (a) $Eo = 20$ (b) $Eo = 10$; showing streamlines and vector field superimposed on velocity magnitude pseudocolour plot on the right and left sides of the symmetry axis, respectively.

In contrast to what was observed at higher value of Eo in Figure 4.8, increase in the value of Nf has little influence, which decreases with decrease in Eo, on the change in bubble length and deformation of the bubble bottom. Rather, what can be seen is the emergence of a bulge in the film region close to the bubble bottom which becomes more pronounced and appears to propagates towards the nose in the form of capillary wave as Nf and Eo are increased and decreased, respectively.

In Figure 4.11, we show the complete numerical results for a Taylor bubble rising in stagnant liquid to better visualize the effects of the two dimensionless parameters, over the entire parameters spaces examined, on the bubble shape and the surrounding flow field.

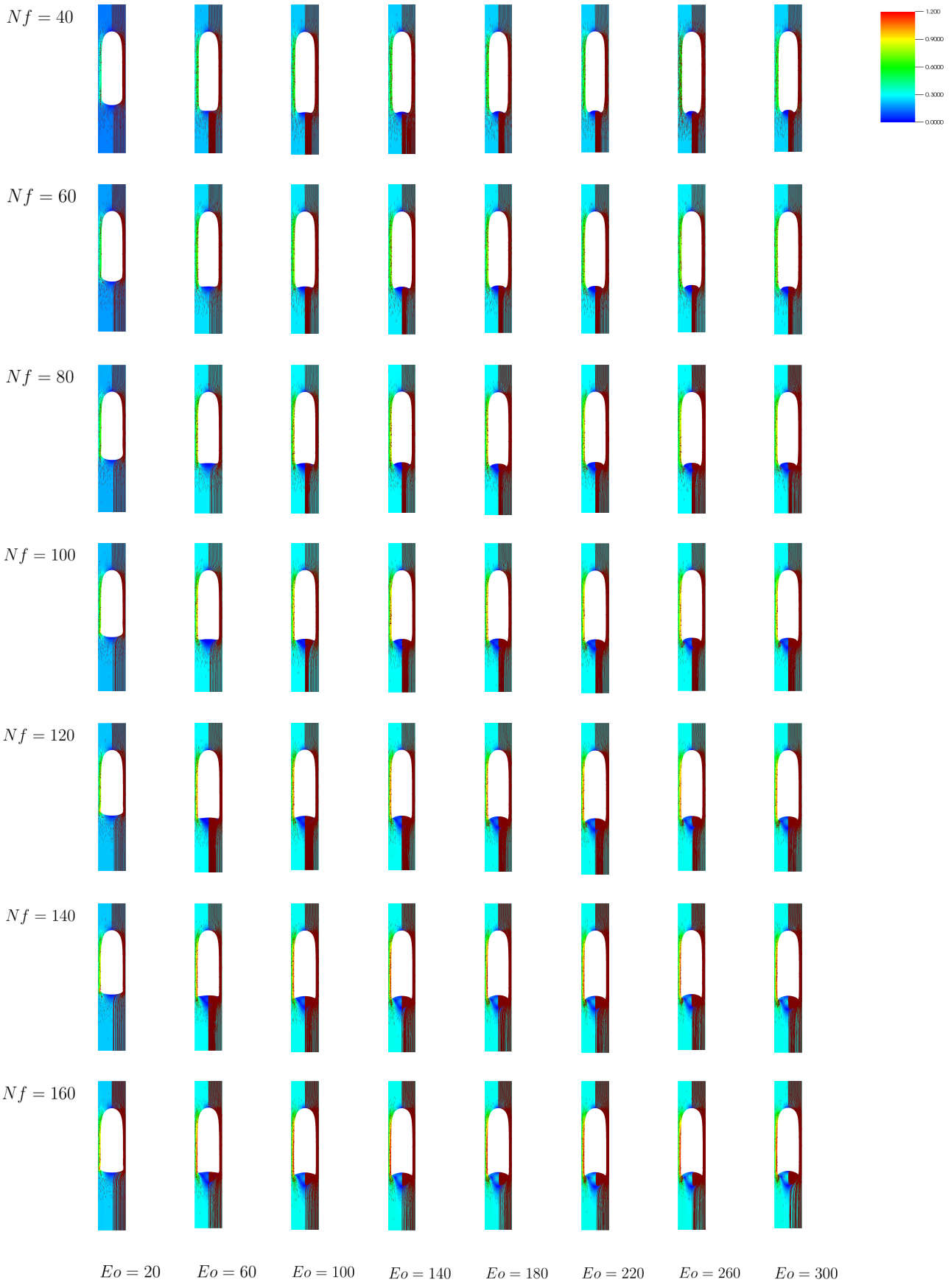


Figure 4.11: Steady state bubble shapes and surrounding flow fields; effect of inverse viscosity and Eötvös numbers.

4.4.2 Hydrodynamic features of the nose region

The hydrodynamics features around the nose region as highlighted in the introductory chapter of the thesis are the bubble rise velocity, the distance ahead of the bubble nose, in moving frame of reference, at which the flow becomes fully developed and the bubble nose curvature. Here, we present how the magnitude of these features are influenced by variation in the values of the model dimensionless parameters.

Taylor bubble rise velocity

The rise velocity is one of the key features in the hydrodynamics of Taylor bubbles because of its important in determining void fraction and developing predictive model for computing pressure drop in slug flow. We compare our numerical results with the existing empirical correlation of [111] for Taylor bubble rise velocity in stagnant liquids given as equation (2.8), shown in Figure 4.12.

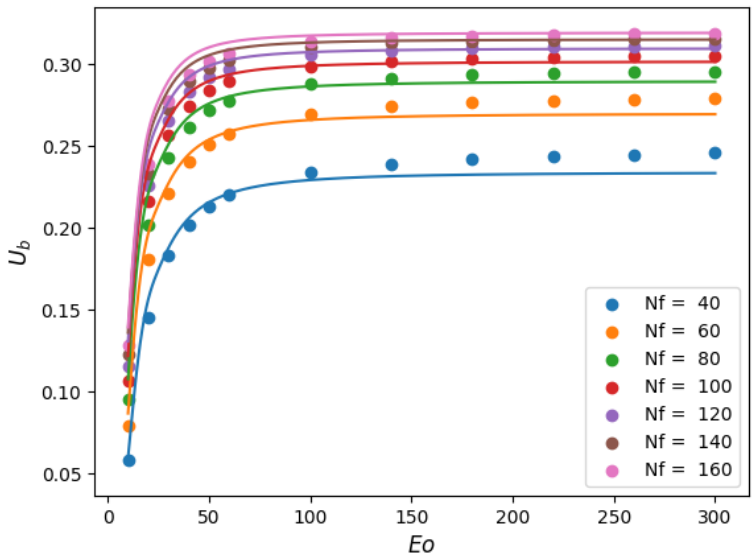


Figure 4.12: Effect of Nf and Eo on steady state bubble rise velocity in stagnant liquids. Comparison between numerical results (coloured marker symbols) and analytical prediction of equation (2.8) (coloured continuous line).

From Figure 4.12, it is clear that the bubble rise velocity and the separation distance between two consecutive sets of data, at constant Eo, are increasing and decreasing functions of the

inverse viscosity number across all Eötvös numbers, respectively. As aforementioned, the increase in the bubble rise velocity with Nf occurs due to the diminishing opposing viscous force, causing the Taylor bubble to experience less resistance and thus, rises faster. The decreasing function of the separating distance on the other hand reaffirm the existence of a maximum Nf across all Eo at which the rise velocity becomes independent of the viscous forces. For condition in which the rise velocity is independent of surface tension, which can be deduced from Figure 4.12 to be slightly above $Eo = 100$, the limiting value of Nf and the corresponding bubble rise velocity, as established by numerous previous studies [15, 30, 45, 58, 66, 111, 114, 116], are 300 and 0.35, respectively.

For comparison, a good agreement is demonstrated between the rise velocity from our numerical simulations and that predicted by (2.8) of [111]. The results show that the performance of the correlation in the prediction of bubble rise velocity is reasonably far better at higher Nf, as the agreement between the numerical results and the equation improves with increase in inverse viscosity number. This is because a large number of experiment data used in the development of the model are based on experiments conducted in the inertia regime.

Curvature radius of bubble nose

The shape of the nose region of a Taylor bubble determines the rise velocity of the bubble and is an important factor in the stability of the bubble.

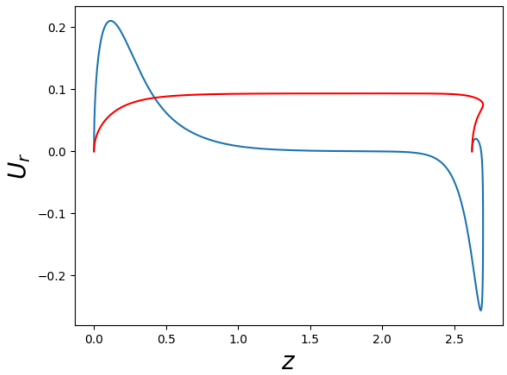


Figure 4.13: Typical radial velocity profile (coloured blue) along the interface (coloured red).

Figure 4.13 shows a typical profile of the radial component of the velocity along the interface of a Taylor bubble. Starting from the nose of the bubble, which is a stagnation point in a frame of reference that moves with bubble rise velocity, the general observation is that the radial velocity component increases until it peaked before gradually diminishing, approaching zero in the fully developed film. By nose region, we refer to the region starting from the nose and ending at the point at which the radial velocity on the interface attains its maximum value. For all points in this region, we compute the mean radius of curvature which is related to the total curvature by (4.31) and take the average. The average is reported as the mean radius of curvature of the nose region, which in the literature is referred to as the frontal radius, R_F.

$$\frac{2}{R_m} = 2\kappa_m = \kappa_a + \kappa_b = \kappa \tag{4.31}$$

Here, κ_m and R_m denote the mean curvature and the mean radius of curvature, respectively. κ, κ_a and κ_b remains the total curvature, principal curvature in the $r-z$ plane and principal curvature in the $r-\theta$ plane, respectively.

The effect of the two dimensionless parameters that define the rise of a Taylor bubble in stagnant liquid on the frontal radius is shown in Figure 4.14.

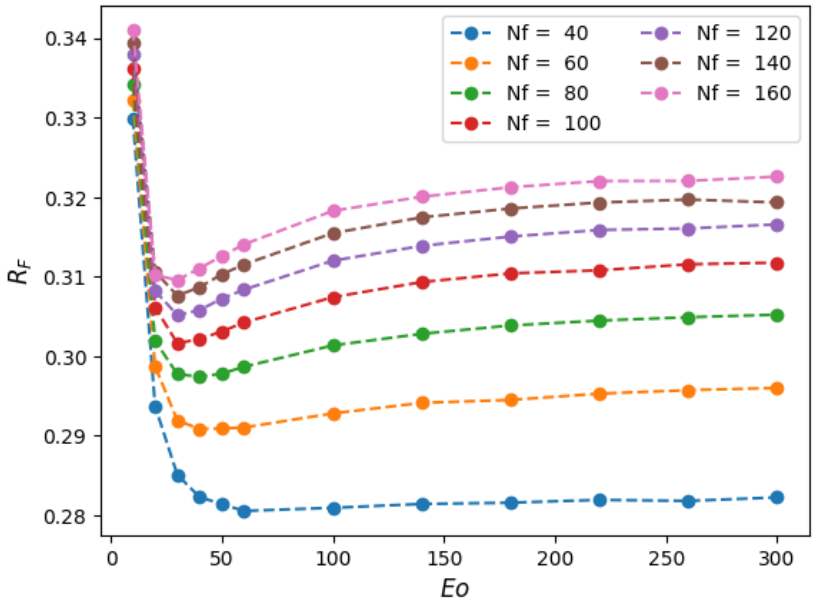


Figure 4.14: Frontal radius of Taylor bubble: influence of inverse viscosity and Eötvös numbers

From Figure 4.14, the results indicate that for $Eo > 100$, the frontal radius is weakly dependent on Eötvös number, increases with Nf and is tending towards becoming independent of inverse viscosity number at much higher value of Nf. The result is consistent with the effects that Nf and Eo have on the bubble rise velocity, confirming the fact that the bubble rise velocity is related to the curvature of the bubble nose. For $Eo < 100$, the frontal radius is a decreasing function of the Eötvös number until a particular Eo value is reached at which it began to increase. The critical value of Eo at the turning point decreases with increase in Nf, approaching a constant value that lies between $Eo = 30$ and $Eo = 20$, which is probably related to the emergence of bulge around the lower part of the film region.

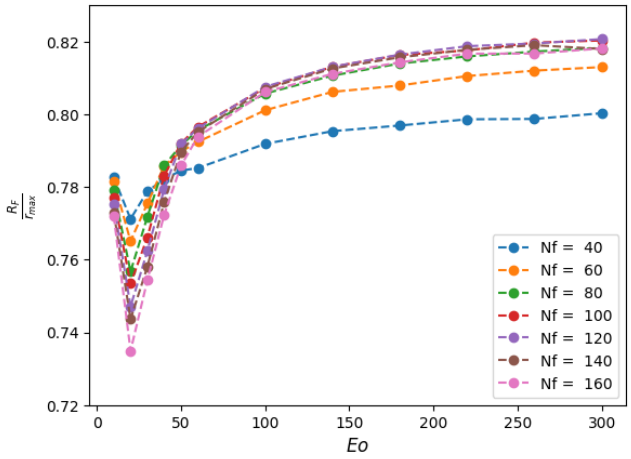
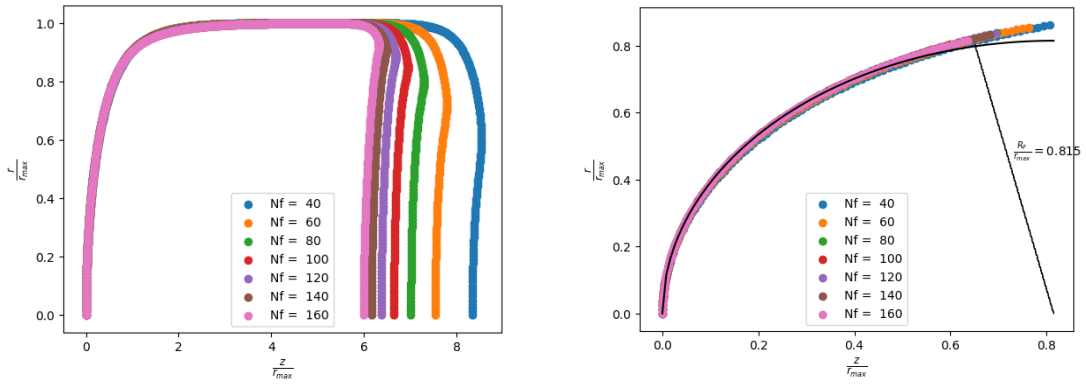


Figure 4.15: Normalised frontal radius; showing convergence towards a constant value of 0.815 when $Nf \geq 80$

For $Eo > 100$, the average frontal radius for $Nf = 40$, 60, 80, 100, 120, 140 and 160 are 0.2818, 0.2951, 0.3043, 0.3108, 0.3155, 0.3188 and 0.3216 respectively. These results are in agreement with previous studies [16, 35, 36, 41] which suggest that the bubble nose is prolate-like rather than spherical shape, in which $R_F \approx 0.4$. Under inertia condition, [15] demonstrated that the normalised frontal radius, using the maximum radius of the Taylor bubble interface, r_{max}, is the same for all liquids and takes a value of 0.75. We normalised the frontal radius using their corresponding r_{max}, the result, shown in Figure 4.15, indicates that the normalised R_F approaches a value of 0.815 at higher Nf and that the limit of Nf at which viscosity have a strong influence on the curvature of the nose is $Nf \leq 60$. The normalised bubble shape for $Eo = 220$, together with an enlarge view of the nose region showing a plot of the normalised

frontal radius limit, are shown in Figure 4.16.



(a) (b)

Figure 4.16: Normalised bubble showing (a) full bubble shape (b) nose region with a plot of normalised frontal radius limit (continuous black line): effect of Nf at $Eo = 220$

Developing length ahead of bubble nose

In a fixed frame of reference, a rising Taylor bubble in stagnant liquid displaces the liquid ahead of it, steering the flow towards its side into the annular place between the bubble and the wall. The influence of the rising bubble is strongly felt by the liquid closest to the bubble nose and it decreases as we move farther away from the nose until at some distance, the stagnant nature of the liquid into which the bubble is rising is attained. This distance ahead of the bubble nose in a fixed frame of reference at which the flow field far ahead of the bubble nose is attained is known as developing length, or more commonly in the Taylor bubble literature stabilisation length, ahead of the bubble nose.

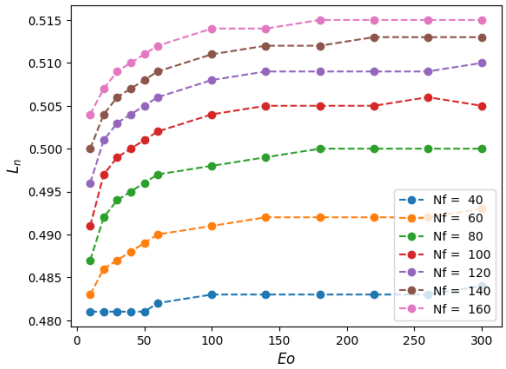


Figure 4.17: Developing length ahead of Taylor bubble nose: influence of inverse viscosity and Eötvös numbers

Considering a frame of reference moving with the bubble velocity in which our simulation is carried out, the stabilisation length ahead of the bubble is then the distance ahead of the bubble, along the line of symmetry, at which the magnitude of the axial velocity equals the magnitude of the axial velocity far ahead of the bubble nose, which, for stagnant liquid, equals the bubble rise velocity. Our analysis of the stabilisation length shows that there is high inherent sensitivity when determining the axial position at which the rise velocity is attained i.e. a marginal change in the value of the axial velocity has a proportionately much greater impact on the location of the axial position. For this reason, the stabilisation length is taken as the distance at which the axial velocity equals 99% of the magnitude of the axial velocity far ahead of the bubble nose, which in this case is the bubble rise velocity. The influence of the flow dimensionless parameters on the stabilisation length is shown in Figure 4.17. Just like the bubble rise velocity, the developing length initially increased with Eo before plateauing beyond $Eo = 100$ for all Nf, and at constant Eo, it increases with Nf, showing the tendency of the existence of upper limit to the value of Nf beyond which the influence of increase in Nf on stabilisation length becomes negligibly very small. The reason for this can be attributed to the increase in the momentum imparted on the liquid ahead of the bubble nose in a fixed frame of reference as the bubble rise velocity increases with Nf and some Eo ranges.

4.4.3 Hydrodynamic features of the film region

The features that define the hydrodynamics of the film region are the developing length in the film region, the equilibrium film thickness and the velocity profiles in the fully developed film. Both the stabilisation length and the equilibrium film thickness are crucial parameters to determine as one expects the flow pattern in the wake of a Taylor bubble to be independent of the bubble length for bubble of lengths greater than the stabilisation length and to be heavily dependent on the equilibrium film thickness [82]. The influence of inverse viscosity and Eötvös numbers on the quantitative values of these features are discussed.

Developing length below bubble nose

We noted earlier that starting from the bubble nose, the radial component of the velocity increases, peaking at the point where the nose region ends. Beyond this point, along the interface, the radial velocity begins to decrease, becoming zero in the fully developed film. The first point at which the radial velocity is zero and the axial velocity becomes fully developed, is known as the developing or stabilisation length for the film. For the same reason adduced for the stabilisation length ahead of the bubble nose, the stabilisation length in the film region is determined to be the point at which the radial velocity and the rate of change in axial velocity along the interface $\left(\frac{du_z}{ds}\right)$ are less than 1% of their maximum values along the interface. The results for the developing length is shown in Figure 4.18.

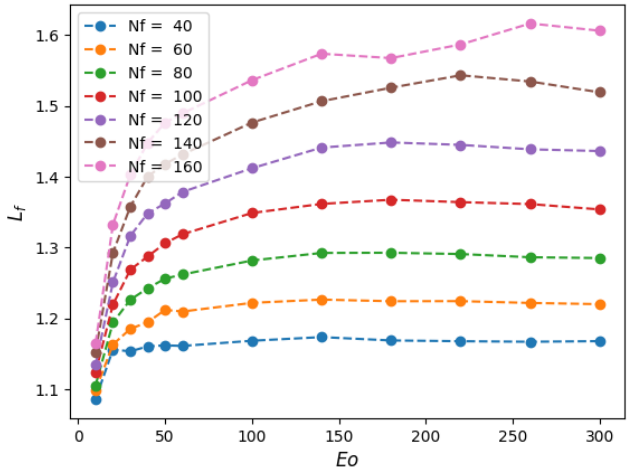


Figure 4.18: Developing length below the bubble nose: influence of inverse viscosity and Eötvös numbers

As expected, much like what happened with the features that characterised the nose region, the dependency of the stabilisation length in the film region on inverse viscosity shows an increasing function. With increase in rise velocity that is associated with increasing Nf, the film needs to travel a longer distance below the bubble nose before it becomes fully developed. However, unlike the rise velocity or nose stabilisation length, it appears there might not be upper limit to the Nf at which the stabilisation length remains unchanged even on further increase in Nf. The results, therefore indicate that as the inverse viscosity is increased it will become increasingly difficult to obtain a truly stabilised film around Taylor bubbles that are

not extremely long. We note that the seeming wavy nature of the results at higher Nf and Eo is most likely a numerical artefact. It could be associated with spurious velocity that sometimes appear on the interface for simulations carried out at higher Nf and Eo. Further details on the effect of spurious velocity on our numerical simulations are given in chapter 6.

Equilibrium film thickness

Below the developing length in the film region, the liquid film is deemed to have attained equilibrium and the thickness is from there onward constant until Taylor bubble tail region is approached. We measured the film thickness at the point where the equilibrium film thickness is first attained and the results are compared with the theoretical prediction of [15]. From (2.12), the equation that relates equilibrium film thickness to bubble rise velocity can be written as

$$\frac{4Nf}{3U_b}\Delta_f^3 + 2\Delta_f - 1 = 0 \tag{4.32}$$

Using the theoretical rise velocity computed from (2.8), we solve (4.32) iteratively for Δ_f for different Nf and the results are compared with our numerical prediction in Figure 4.19. In principle, the iterative solution obtained from (4.32) is the same as the application of the cubic brown model of [64] given as (2.14).

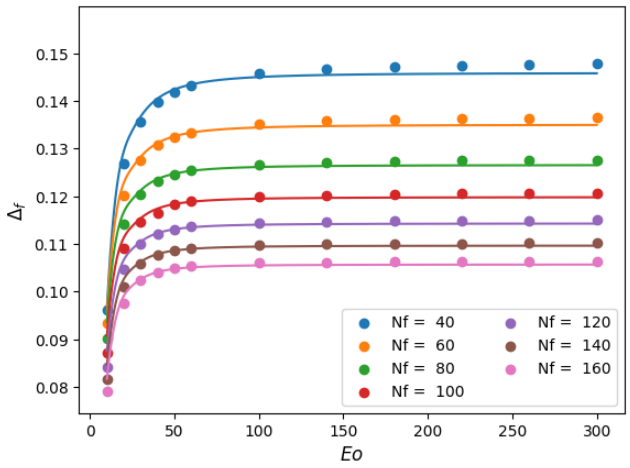


Figure 4.19: Equilibrium film thickness: Comparison between numerical simulations (coloured markers) and theoretical prediction using (4.32) and (2.8) (coloured continuous solid line) for different inverse viscosity and Eötvös numbers.

The agreement between the numerical and theoretical prediction is remarkably good, particularly at higher Nf. This is not surprising, as the thin liquid film assumption becomes more valid at higher inverse viscosity number. As aforementioned, the decrease in the equilibrium film thickness with Nf is due to the decrease in the magnitude of the normal stress exerted on the interface as the fluid viscosity is decreased. It is noteworthy that despite the seemingly dependency of the stabilisation length of the liquid film on the Eötvös number at higher Nf, the liquid film thickness remains almost constant beyond $Eo = 100$, supporting the claim that the dependency on Eo noticed in the stabilisation length of the film might not be real. However, even if on further investigations of higher Nf, it turns out that the stabilisation length for the film depends on Eo, it thus means that the equilibrium thickness might take a longer distance below the bubble nose to be attained, it magnitude would remain independent of Eo in as much as the Eötvös number is greater than 100.

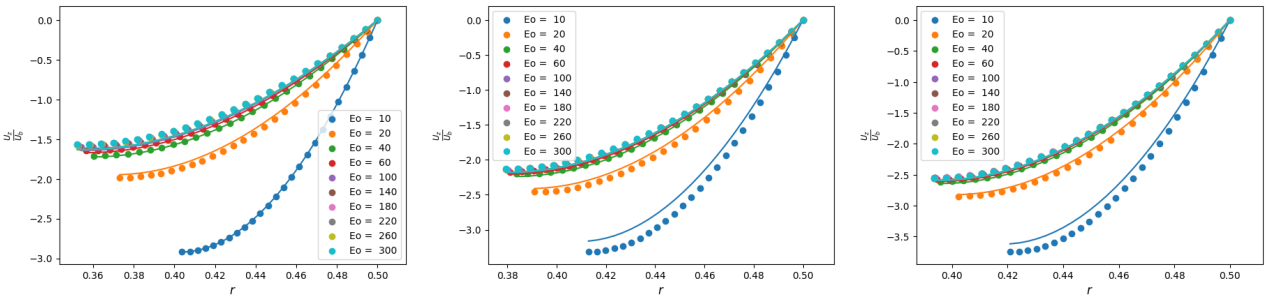
As soon as the liquid film becomes stabilised, the axial velocity profile in the film is also fully developed. The dimensionless form of the equation that governs the liquid flow in this region is given as [15]

$$\frac{1}{r}\frac{d}{dr}\left[r\frac{du_z}{dr}\right] = -Nf \tag{4.33}$$

Solving (4.33) gives

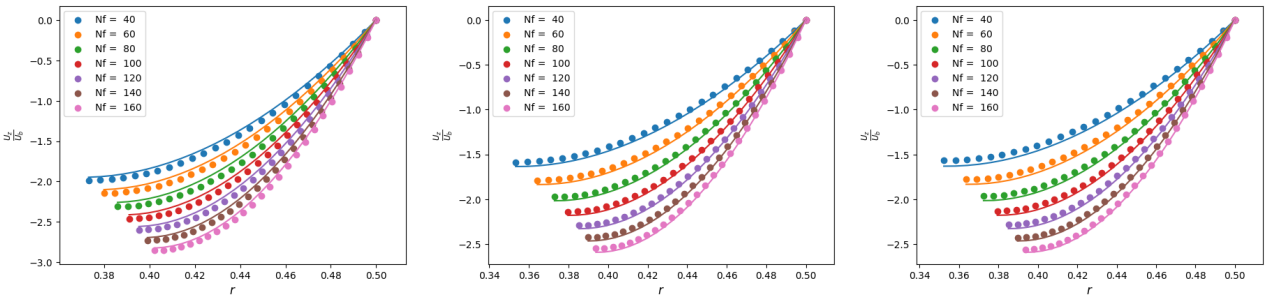
$$u_z = -Nf\left[\left(\frac{0.25 - r^2}{4}\right) - \frac{1}{2}\left(0.5 - \Delta_f\right)^2 \ln\left(\frac{0.5}{r}\right)\right] \tag{4.34}$$

The prediction from (4.34) scaled using bubble rise velocity compared to our numerical results are shown in Figures 4.20 and 4.21. Noticeably, is the improvement in the agreement between our numerical results and the theoretical predictions as the dimensionless parameters values approach inertia regime, which of course is expected.



(a) (b) (c)

Figure 4.20: Axial velocity profile in the fully developed film: effect of Eötvös number at (a) $Nf = 40$ (b) $Nf = 100$ (c) $Nf = 160$. Comparison between numerical simulations (coloured markers) and theoretical predictions of (4.34) (coloured solid lines)



(a) (b) (c)

Figure 4.21: Axial velocity profile in the fully developed film: effect of inverse viscosity number at (a) $Eo = 20$ (b) $Eo = 140$ (c) $Eo = 260$. Comparison between numerical simulations (coloured markers) and theoretical predictions of (4.34) (coloured solid lines)

4.4.4 Hydrodynamic features at the wall and interface

The liquid film is bounded on the right and left by the wall and the interface, and at these boundaries, the normal velocity and the shear stresses are zero, respectively. Here, we discuss the effect of dimensionless parameters on the shear and normal stresses at wall and interface boundaries, respectively.

Wall shear stress

Obtaining reliable information on the wall shear stress is important, especially if slug flow develops concurrently with heat or mass transfer. Practical applications involve processes like

membrane separations [106], where an optimized wall shear stress is highly desirable. Fundamentally, a low wall shear stress cannot generate a significant distortion to the concentration polarization layer at the membrane surface; however, a high wall shear stress may interfere with the membrane surface chemistry, causing subsequent damage with implications on the fiber life span [58].

From equation (3.24), the shear stress at any boundary is defined as

$$\boldsymbol{\tau} = \mathbf{n}.\mathbf{T} \times \mathbf{n} \tag{4.35}$$

which, on axisymetric boundary, the nonzero component simplifies to

$$\tau = Nf^{-1}\left[\mathbf{n} \cdot \frac{d\mathbf{u}}{ds} + \mathbf{t} \cdot \frac{d\mathbf{u}}{dn}\right] \tag{4.36}$$

and when evaluated at the wall, gives

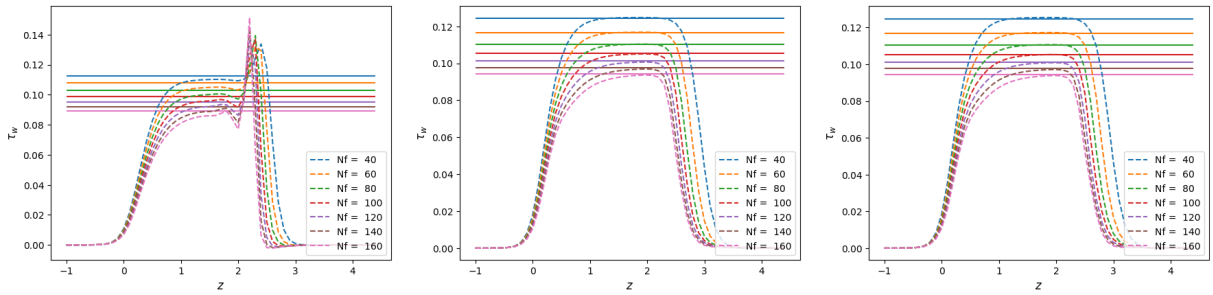
$$\tau_w = -Nf^{-1}\frac{du_z}{dr} \tag{4.37}$$

where τ_w denotes the dimensionless shear stress evaluated at the wall.
In the fully developed film, using (4.34), the wall shear stress becomes

$$\tau_w = 0.25 - (0.5 - \Delta_f)^2 \tag{4.38}$$

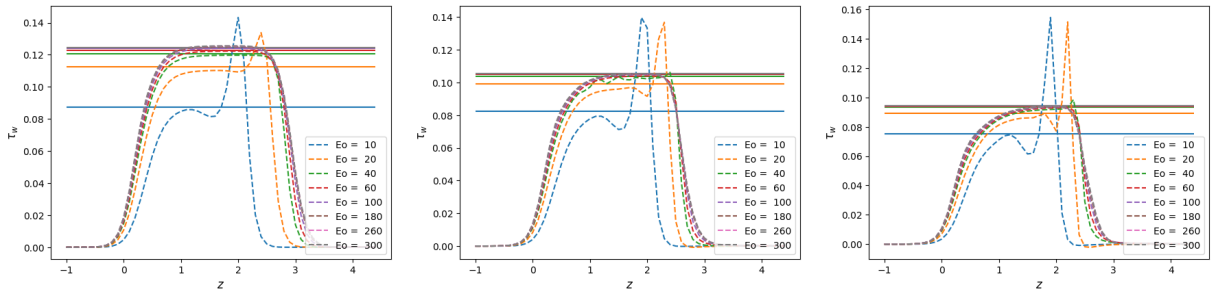
Since, in the fully developed film, the film thickness is a constant, (4.38), when evaluated, is a straight line for any given Nf and Eo combinations. We superimposed the results evaluated using (4.38) on our numerically computed results using (4.37), shown in Figures 4.22 and 4.23. Beyond the limit at which surface tension has strong influence on the dynamics of the bubble, equation (4.38) adequately predicts the effect of Nf and Eo on the wall shear stress in the developed film region. While increase in Nf leads to a reduction in the wall shear stress, Eo has no significant impact on it. Both effects can be related to the effect of the parameters on the equilibrium film thickness and its velocity profiles, shown in Figures 4.19, and 4.21 and

4.20, respectively. The apparent peaks observed in Figures 4.22a and 4.23 when surface tension effect is very strong can be related to the undulation that appears towards the end of the liquid film, with the influence becoming more pronounced as Nf is increased and Eo is decreased.



(a) (b) (c)

Figure 4.22: Shear stress at wall boundary: Numerical effects of inverse viscosity number at (a) $Eo = 20$ (b) $Eo = 140$ (c) $Eo = 260$ (broken lines) compared to theoretical prediction of (4.38) in the developed film (solid lines)



(a) (b) (c)

Figure 4.23: Shear stress at wall boundary: Numerical effects of Eötvös number at (a) $Nf = 40$ (b) $Nf = 100$ (c) $Nf = 160$ (broken lines) compared to theoretical prediction of (4.38) in the developed film (solid lines)

The maximum wall shear stress, τ_w^m, for the combined effect of Nf and Eo is plotted in Figure 4.24.

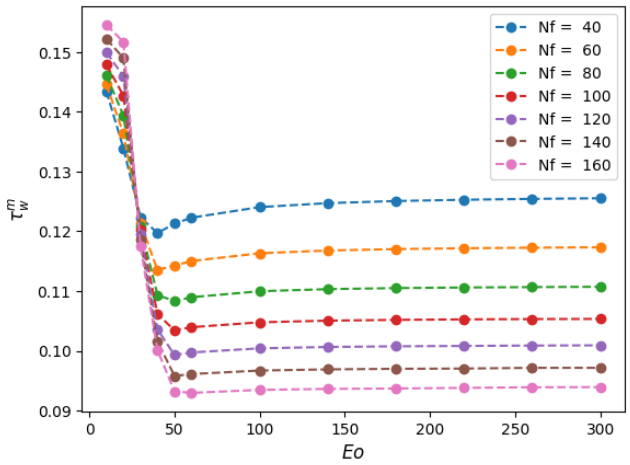


Figure 4.24: Maximum wall shear stress: effects of inverse viscosity and Eötvös numbers.

Interface normal stress

The normal stress is the quantity through which the flow field variables (liquid velocity and pressure) interact with the interface parameters (bubble pressure and curvature) via the normal stress boundary condition. It determines the deformation of the interface by the flow. From equation (3.24), the normal stress at the interface in the direction of unit normal to the interface is defined as

$$\sigma_n = -\mathbf{n}\cdot\mathbf{T}\cdot\mathbf{n} = -\left[-p + 2Nf^{-1}\mathbf{n}\cdot\frac{d\mathbf{u}}{dn}\right] \tag{4.39}$$

From the normal boundary condition (3.11), we can write

$$-\mathbf{n}\cdot\mathbf{T}\cdot\mathbf{n} + z = P_b - Eo^{-1}\kappa \tag{4.40}$$

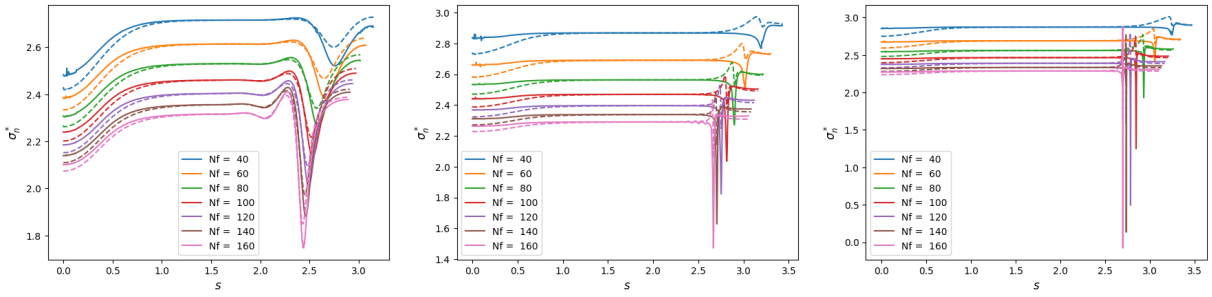
We find it more informative to express the normal stress in terms of the total pressure by adding the gravity term to the hydrodynamic pressure, so that

$$\sigma_n^* = -\left[-p_T + 2Nf^{-1}\mathbf{n}\cdot\frac{d\mathbf{u}}{dn}\right] = P_b - Eo^{-1}\kappa \tag{4.41}$$

where

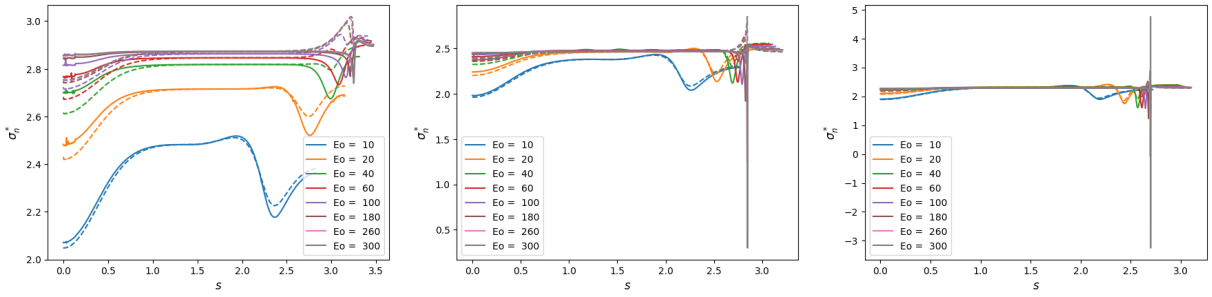
$$p_T = p + z$$

Figures 4.25 and 4.26 show the effect of inverse viscosity and Eötvös numbers on interface normal stress and total pressure.



(a) (b) (c)

Figure 4.25: Normal stress (solid lines) and total pressure (broken lines) at the interface: effect of inverse viscosity number at (a) $Eo = 20$ (b) $Eo = 140$ (c) $Eo = 260$

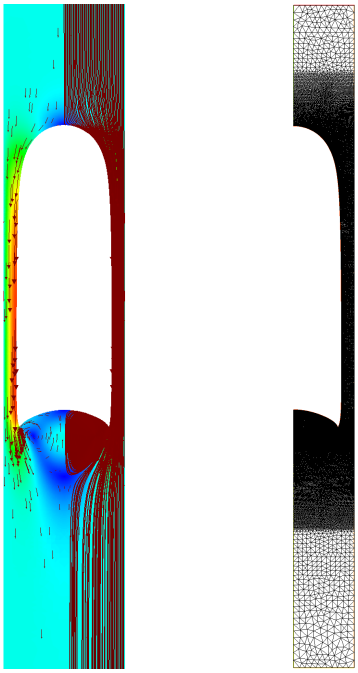


(a) (b) (c)

Figure 4.26: Normal stress (solid lines) and total pressure (broken lines) at the interface: effect of Eötvös number at (a) $Nf = 40$ (b) $Nf = 100$ (c) $Nf = 160$

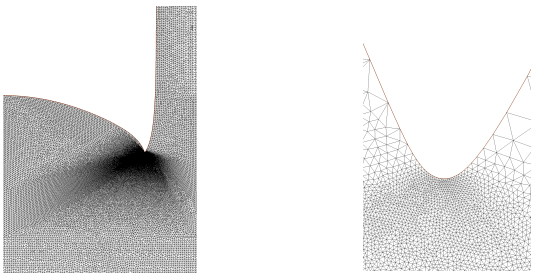
It is apparent that the effect of Nf is to decrease the normal stress exerted on the bubble as it is increased while on the other hand surface tension has no significant influence on normal stress if the flow condition is such that $Eo > 100$. Within the fully developed liquid film, we see that both the pressure and the normal stress matches in order to satisfy (4.41). This is because within this region, the interface is almost vertical, which makes $n_r \approx -1$, $n_z \approx 0$ and $\kappa \approx 0$, and developed film implies $u_r = \frac{du_r}{dn} = 0$, making the viscous and curvature stresses contribution zero. Thus, (4.41) reduces to $\sigma_n^* = p_T = P_b$. Since the bubble pressure is a constant, the implication of this is that the viscous and curvature forces are only important in the front and bottom regions and it is the interplay between them that determines the shape of the nose and bottom regions. To probe further the observed sharp peak in the interface stress

around the bubble bottom, particularly for higher Eo and Nf, Figures 4.25c, 4.26b and 4.26c, we examined the bubble shape and mesh for $Nf = 160$ and $Eo = 300$. It is clear from Figures 4.27 and 4.28b that the bubble bottom and the tail are well resolved. It is therefore not likely that the observed spikes are due to unresolved mesh and as such not physical. Should there be any error in the results, it is likely going to be due to errors in curvature computation as it is possible that the cubic spline technique implemented breaks down when two points under consideration are very close in their numerical values, as expected for points in the tail region.



(a) (b)

Figure 4.27: Taylor bubble (a) shape and (b) mesh structure for $Nf = 160$ and $Eo = 300$.



(a) (b)

Figure 4.28: Enlarged view of Taylor bubble (a) bottom and (b) tail tip mesh structures for $Nf = 160$ and $Eo = 300$.

Just as we did for the wall shear stress, we extract the maximum normal stress, σ_n^m exerted on

the interface to see the combined effect of Nf and Eo and the results are shown in Figure 4.29.

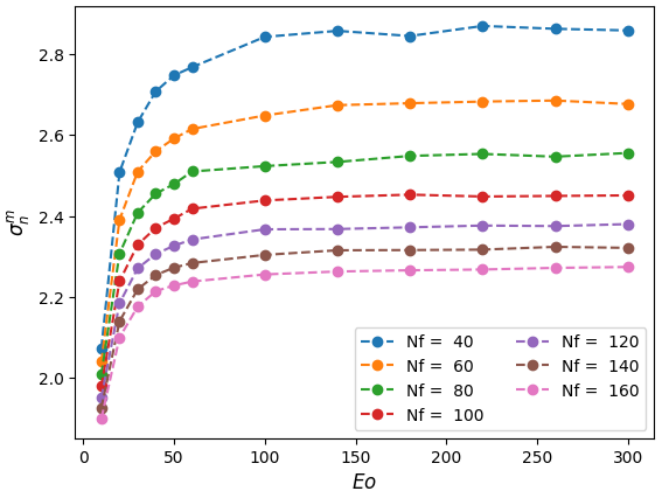


Figure 4.29: Maximum interface normal stress: effects of inverse viscosity and Eötvös numbers.

4.4.5 Hydrodynamic features of bottom region

The features discuss here encompass those that define the bottom of the bubble which are the shape of the bottom and the length of the developing length below the bottom, and those that defines the wake, if present, which are the length of the wake and the position vector of the vortex eye. These features play an important role in the coalescence of two consecutive rising bubbles and the stability of a trailing bubble.

Curvature radius of bubble bottom and shape

Herein, we quantitatively examine the effects of varying flow conditions on the Taylor bubble bottom shape using the sign of the radius of curvature. Because of the varying shapes that are associated with Taylor bubble bottom, we find it convenient and sufficient to define the shape of the bubble bottom base on the curvature evaluated at the bottom along the axis of symmetry. Essentially, a positive (resp. negative) radius of curvature signifies a convex (resp. concave) bottom shape with respect to the liquid phase. Figure 4.30 shows the mean radius of curvature for different Nf and varying Eo.

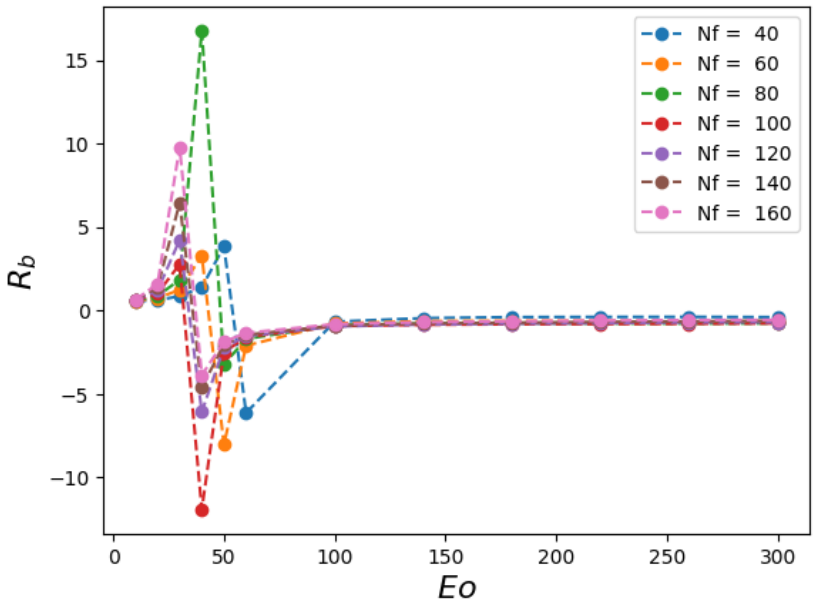


Figure 4.30: Taylor bubble bottom radius of curvature: influence of inverse viscosity and Eötvös numbers

Although, the critical value of Eo at which the curvature radius becomes independent of surface tension parameter remain the same, unlike the frontal radius, there is only subtle difference in the curvature of the bottom for different inverse viscosity numbers. However, as depicted in Figures 4.31 and 4.32, there is an increase in the emergence of tail structure which, as inverse viscosity and Eötvös numbers are increased, becomes more pointed and progressively migrate towards the wall. It therefore means that the effect of increased Nf and Eo is to drive the Taylor bubble bottom shape towards the formation of a skirted bubble, with the eventual breakup of the protruding tail structure as small bubbles.

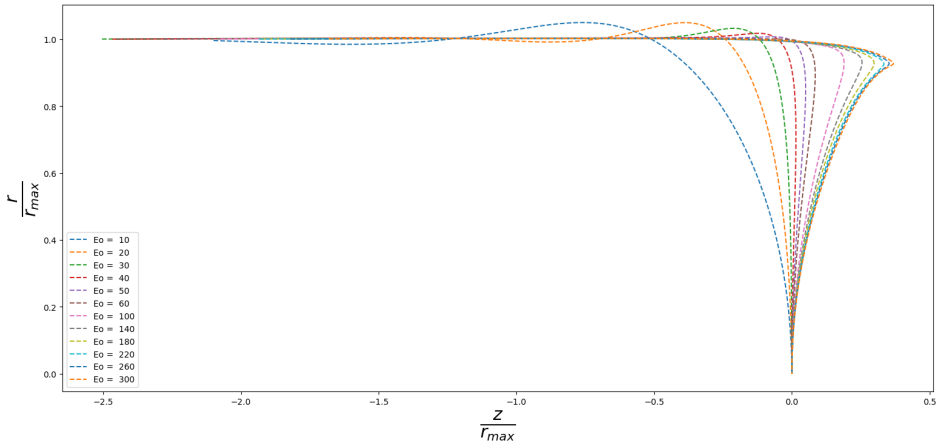


Figure 4.31: Bottom deformation: influence of Eötvös number for $Nf = 160$

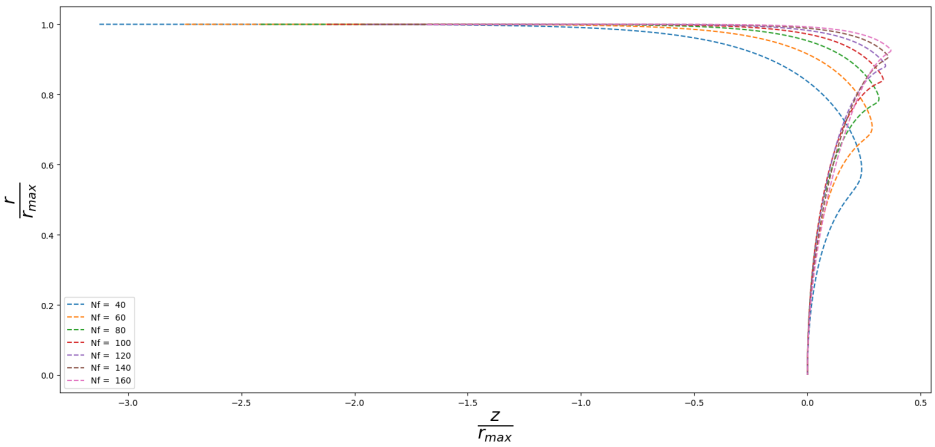


Figure 4.32: Bottom deformation: influence of inverse viscosity number for $Eo = 300$

Wake structure below bubble bottom

Where it is present, the wake is a region of recirculation behind a rising Taylor bubble. We characterise the structure using its length and the position vector of the eye of the vortex, with reference to the position vector of the bubble bottom along the axis of symmetry .

The wake length is defined as the distance between the bottom of the bubble, along the axis of symmetry of the tube and the stagnation point, which can also be defined as the point of flow separation, behind the bubble [82]. Thus, the wake length is calculated by taking the difference between the axial position of the bubble rear and the stagnation point, and the results are shown in Figure 4.33.

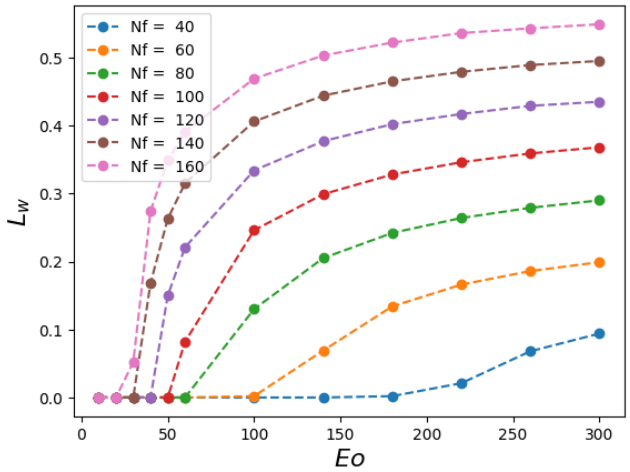
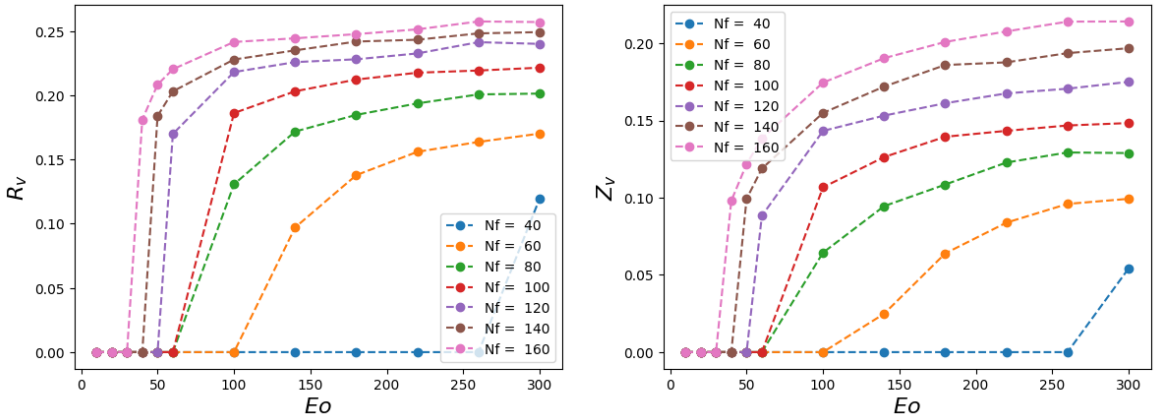


Figure 4.33: Wake length: influence of inverse viscosity and Eötvös numbers

As expected, the wake length shows an increasing dependency on the inverse viscosity number, which is as a result of increasing velocity of the liquid jet emanating from liquid film into the body of liquid behind the bubble, making the liquid to travel farther distance before flow separation occurs. It is also noticeable that the Eo at which the wake emerges depends on Nf, decreasing as Nf is increased. For all Nf, the trend is such that, the influence of Eo on wake length will eventually become negligible at some Eo and it is likely that the occurrence will take place at the same Eo for all Nf.

The location of the vortex centre was extracted from the streamline images, generated using open source visualisation tool, VisIt 2.10.3. For conditions where wake structure exist, the numerical results for the dimensionless radial, R_v, and axial, Z_v, coordinates of the vortex eye are plotted as a function of the Eötvös number in Figures 4.34a and 4.34b, respectively. The trend for all simulation sets is similar and may be closely described by a function in which the values for both R_v and Z_v eventually plateau. For a given Nf, these indicate that an increase in Eo shifts the overall vortex center to the tip of the tail, until no further axial or radial movement occurs. Overall, when juxtaposed with increasing length of the wake, shown in Figure 4.33 and deformation of the bubble bottom, shown in Figures 4.31 and 4.32, it appears the combined effect of increasing Nf and Eo is to stretch the wake structure in the axial direction about the vortex eye.



(a) (b)

Figure 4.34: Effect of inverse viscosity and Eötvös numbers on (a) radial (b) axial, location of the vortex eye with reference to bubble bottom.

Utilising the information from the results of Figures 4.30 and 4.34, we draw up a map that demarcates the boundaries where the bubble bottom shape is convex or concave and indicate whether or not the shape is associated with the presence of wake as a function of Nf and Eo, shown in Figure 4.35.

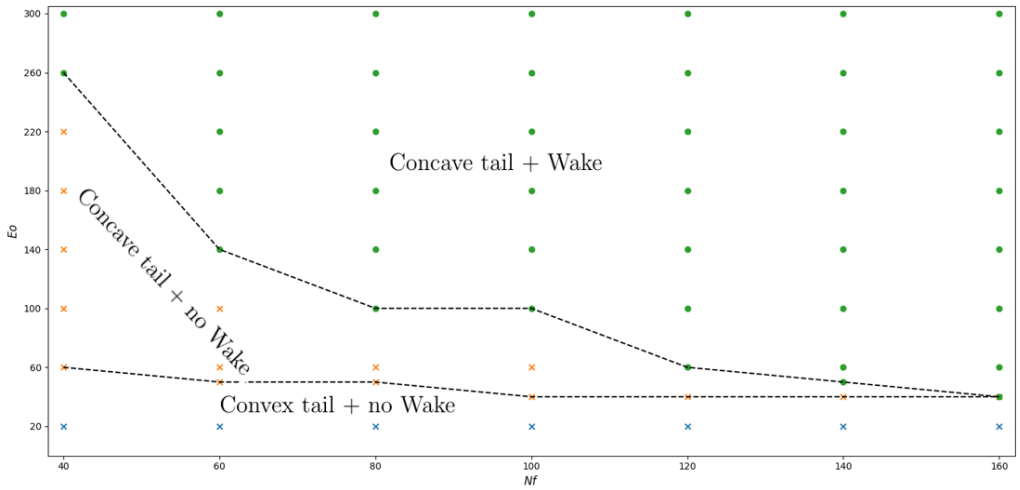


Figure 4.35: Taylor bubble bottom: influence of inverse viscosity and Eötvös numbers, showing region in the parameters space where bubble bottom takes concave or convex shape and whether or not the shape is associated with a wake.

Developing length below bubble bottom

The dimensionless stabilisation length below the bubble bottom, L_b, similar to the the stabilisation length ahead of the bubble, refers to the distance below the bottom of the bubble in a fixed frame of reference at which the flow field far behind the bubble bottom is attained. This length, in the context of two consecutive rising bubbles, is the minimum distance below the leading bubble bottom, above which there is no any form of interaction with the trailing bubble. Numerically, in a moving frame of reference, we determine this length as the difference between the axial location of the point where the magnitude of the axial velocity along the symmetry axis, starting from the far end of the bubble, is less than 99% of its magnitude at the far end and the axial location of the bubble bottom. The computed length as a function of the model dimensionless parameters are plotted in Figure 4.36, displaying similar trend as the wake length and for the same reason.

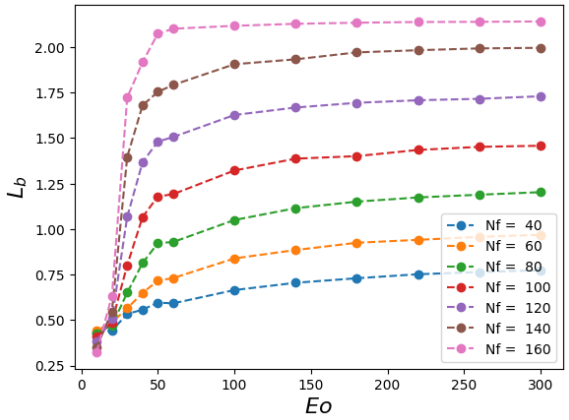


Figure 4.36: Bottom length: influence of inverse viscosity and Eötvös numbers

4.5 Steady state characterisations in flowing liquids

In the previous sections, we have examined the effects of two of the three dimensionless parameters that define the rise of a Taylor bubble in flowing liquids. This section focusses on the role of the liquid velocity profile into which the bubble is rising in a fixed frame of reference. We characterised the liquid using the dimensionless Froude number that is based on the liquid velocity at the tube center, i.e the maximum liquid velocity. Since our aim is to examine the transition of Taylor bubble from symmetric to asymmetric shapes in downward liquid, preference was given to downward liquid flow, with the space of U_m being $(-1.0) - (0.20)$. The few upward liquid flow simulations carried out were done for completeness. The focus of the literature regarding the dynamics of a steadily rising Taylor bubble in flowing liquid has largely been on upward liquid flow, with feature of primary concern been the bubble rise velocity. For this feature, a number of theoretical, experimental and numerical studies have been carried out. For downward liquid flow, on the other hand, studies are scarce even on the bubble rise velocity, of course, because of the transition associated with the flow. For this reason, we limit reporting quantitative measurements to three steady state features; the bubble rise velocity, nose curvature and film thickness, which we discuss simultaneously along with qualitative influence of U_m on Taylor bubble dynamics.

4.5.1 Bubble rise velocity in upward liquid flow

Before proceeding to discuss the results, we compared our numerical simulation for upward liquid flow with the theoretical prediction. We recall the correlation of [79] which has been theoretically and numerically confirmed to correctly predict the rise velocity in upward flowing liquids, given as (2.10) and reproduced here.

$$U_b = C_1 U_m + C_o \tag{4.42}$$

Theoretical expressions for C_0 and C_1 were given by [11] taking into consideration the effect of Eo as

$$C_0 = \frac{0.486}{\sqrt{2}} \sqrt{1 + 20\left(1 - \frac{6.8}{Eo}\right)} \left\{ \frac{1. - 0.96e^{-0.0165Eo}}{1. - 0.52e^{-0.0165Eo}} \right\} \tag{4.43}$$

$$C_1 = 1.145 \left[1 - \frac{20}{Eo}\left(1 - e^{-0.0125Eo}\right) \right] \tag{4.44}$$

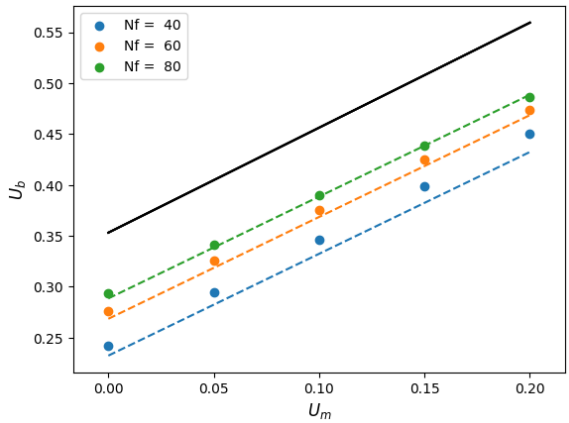
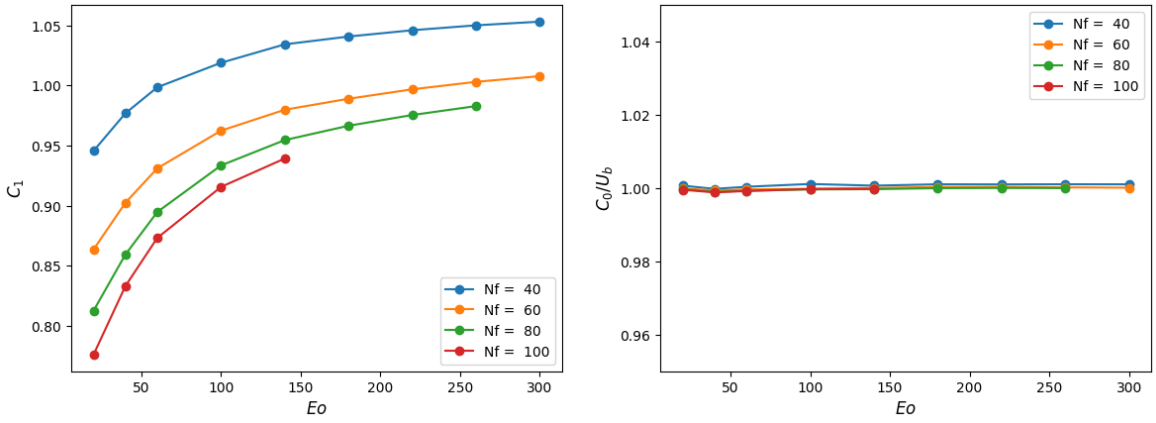


Figure 4.37: Effect of imposed upward liquid flow on bubble rise velocity for varying inverse viscosity numbers. Comparison between numerical result (coloured markers), theoretical prediction using (4.43) and (4.44) (black solid line) and theoretical prediction using (2.8) and (4.44) (coloured dashed line).

We show in figure 4.37 the comparison between prediction using (4.43) and (4.44) of [11], prediction using (4.44) of [11] complemented by (2.8) of [111] for the prediction of C_0, which is approximately equivalent to dimensionless rise velocity in stagnant liquid and our numerical results. It is evident that the theoretical expresions of [11] overpredicts the bubble rise velocity.

This is because the expressions were derived for cases in which flow due to the bubble motion can be considered as inviscid, which only holds in inertia regime. When the correlation of [111] which accounts for the effect of viscosity and surface was used in the computation of C_0, we noticed reasonable agreement, which improves as Nf is increased, between the theoretical prediction and our numerical results. Therefore, it is significant to incorporate the effect of both Nf and Eo in C_0 and C_1, particularly for bubbles rising under non-inertia condition.

We estimated the values of C_0 and C_1 for the few numerical simulations carried out for upward liquid flow and the results, accounting for the effect of Nf and Eo, are shown in Figure 4.38.

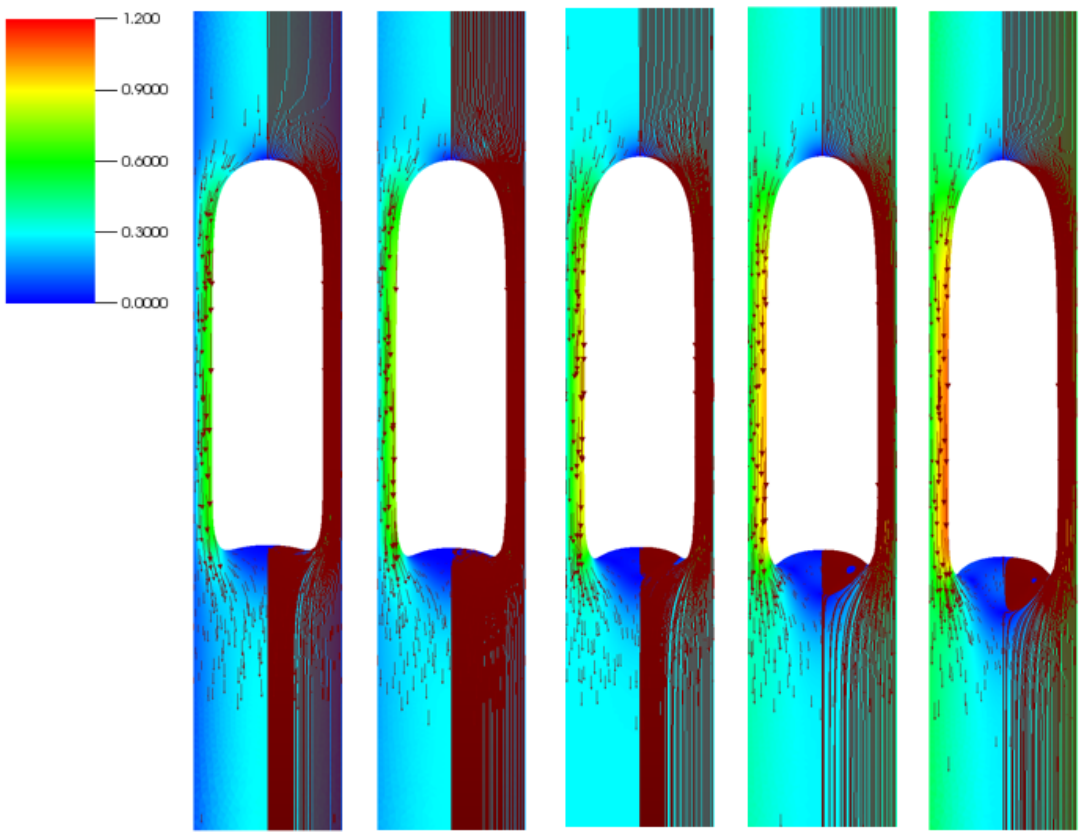


(a) (b)

Figure 4.38: Effect of inverse viscosity and Eötvös numbers on (a) C_1 (b) C_0.

4.5.2 Qualitative and quantitative analysis of steady state shapes and flow field in flowing liquids

The Froude number based on the maximum liquid velocity is a measure of the relative significance of inertia force due to the flowing liquid to buoyancy force due to gravity, which in downward (resp. upward) liquid flow is in opposite (resp. same) direction as the force of gravity, thereby opposing (resp. facilitating) the rise of the bubble. For a constant $Nf = 80$ and $Eo = 140$, the effect of imposed upward and downdward liquid flow is shown in Figure 4.39.



U_m	-0.20	-0.10	0.00	0.10	0.20
U_b	0.1022	0.1967	0.2915	0.3868	0.4823
P_b	2.6415	2.6121	2.5822	2.5509	2.5194

Figure 4.39: Effect of U_m on steady state bubble shape and the surrounding flow field at $Nf = 80$ and $Eo = 140$; showing streamlines and vector field superimposed on velocity magnitude pseudocolour plot on the right and left side of the symmetry axis.

The most obvious effect is the decrease (resp. increase) in the intensity of the wake flow, accompany by decrease (resp. increase) of the concavity of the bubble bottom, with increase in the magnitude of the downward (resp. upward) liquid flow. This, as earlier noted when discussing stagnant liquid case, can be linked to the decrease (resp. increase) in the magnitude of the liquid emerging from the film into the liquid slug, which is a manifestation of the decrease (resp. increase) in bubble rise velocity, as the downward (resp. upward) liquid velocity is increased. Quantitatively, the effect of liquid flow imposition on the rise velocity is shown in Figure 4.40

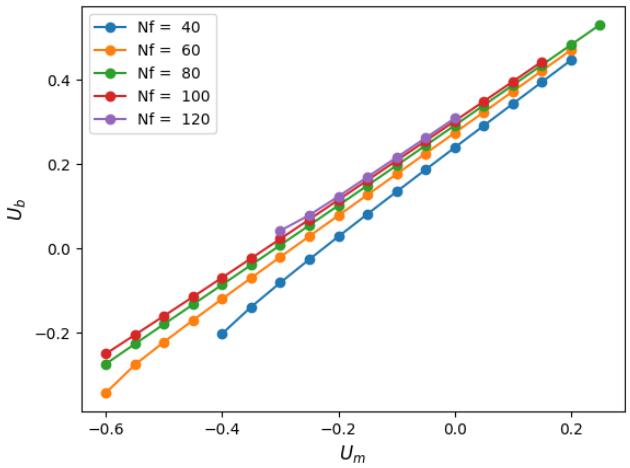


Figure 4.40: Effect of U_m on steady state bubble rise velocity at $Eo = 140$ and different Nf.

Noticeably also is the increase (resp. decrease) in the curvature radius of the bubble nose with increase in the magnitude of the downward (resp. upward) liquid flow. This flattening (resp. pointing) of the bubble nose can be attributed to the increase (resp. decrease) in the normal stress exerted on the bubble nose relative to that in stagnant liquid as a result of the increased opposing (resp. supportive) inertia force in downward (resp. upward) liquid flow (see Figure 4.41).

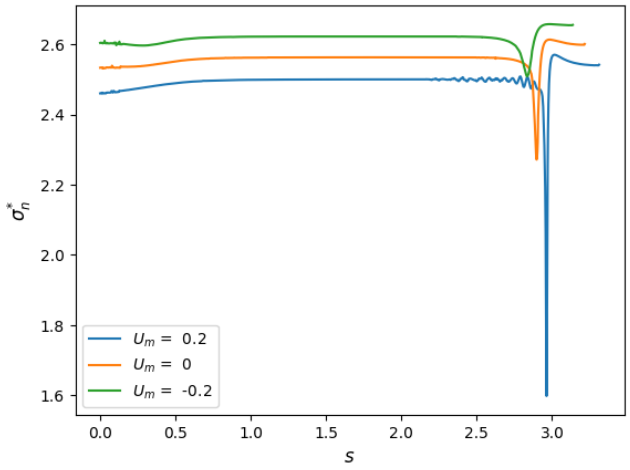


Figure 4.41: Effect of U_m on steady state modified interface normal stress (4.41) at $Nf = 80$ and $Eo = 140$.

It is clear from Figure 4.41 that interface normal stress is an increasing (resp. decreasing) function of increased liquid velocity in downward (resp. upward) liquid flow. As explained in previous section for stagnant liquid, within the equilibrium film, the normal stress, total

pressure and the bubble pressure are equal, which is responsible for the observed increased (resp. decreased) in bubble pressure with increasing downward (resp. upward) liquid flow (see Figure 4.39). Also, outside the equilibrium film region, i.e the nose, developing film and bottom regions, we stated that it is the interplay between the viscous stress and curvature that determines the shape of the regions. To buttress this claim, we once again modify the normal stress by choosing the reference pressure to be the bubble pressure such that

$$\sigma_n^{**} = -\left[-p_T * +2Nf^{-1}\mathbf{n}\cdot\frac{d\mathbf{u}}{dn}\right] = -Eo^{-1}\kappa \tag{4.45}$$

where

$$p_T* = p_T - P_b$$

Thereby making the equilibrium film region normal stress to be approximately zero. As we approach the nose region, the net effect of viscous stress on the normal stress in downward (resp. upward) liquid flow is to increase (resp. decrease) the normal stress relative to that in a stagnant liquid, which in order to satisfy the normal stress balance at the interface, the curvature stress has to decrease (resp. increase), leading to the observed increase (resp. decrease) in the radius of curvature of the nose.

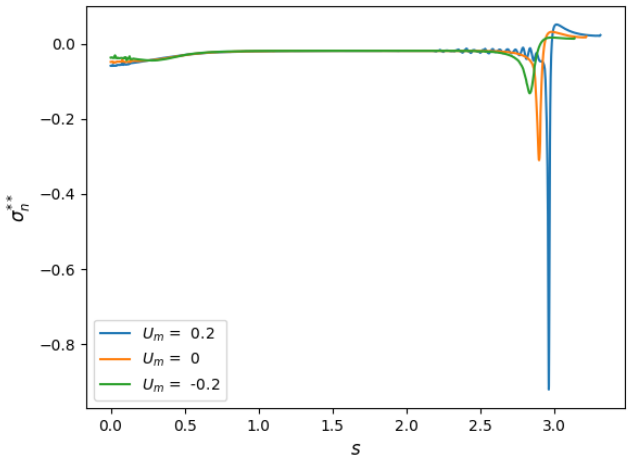


Figure 4.42: Effect of U_m on steady state modified interface normal stress at $Nf = 80$ and $Eo = 140$.

4.6 Steady state numerical simulations challenges

The focus is to compute a steady state solution and a fully implemented steady state model requires that both the time dependent part of the momentum equations (3.1) and kinematic boundary condition (3.13) be set to zero. In the steady state model implemented in this study, rather than enforcing a no penetration condition, $(\mathbf{u} \cdot \mathbf{n})$, at the interface as the true condition that determine the interface deformation, we incorporated a pseudo-time-step parameter, δt, in the condition, (3.48), that allows gradual satisfaction of the no penetration condition and a flexibility in controlling the size of the interface deformation, making the implemented condition to be similar to first order time discretisation of the unsteady kinematic condition. The concept has been used in the computation of steady state solution of free surface problems. However, in our study, the strategy becomes problematic as the dimensionless inverse viscosity and Eötvös numbers become very large. In fact it was the major limitation in computing the steady state solution in stagnant and flowing liquid for high Nf and Eo. As Nf and Eo are increased beyond the investigated parameter space in this study, there was the need to increase the pseudo-time-step size to ensure that the code remains stable. Although increasing the pseudo-time-step solved the stability problem, it led to the emergence of spurious velocity on the interface, causing the interface to become wavy. When smaller pseudo-time-step size was used for the same simulation, the waviness on the interface disappeared but the code became unstable before steady state solution was reached. Of course, the pseudo-time-step is not the only source of the spurious velocity observed, we observed also that as Nf is further increased, the used of continuous element for pressure approximation becomes unreliable. Studies have shown that to appropriately capture the discontinuity of normal stress at the interface, discontinuous element should be used in approximating pressure. Our preliminary investigation into this showed that by changing the continuous P_1 element used for approximation of pressure in standard Taylor-Hood element combination employed in this study to discontinuous P_0, the emergence of spurious velocity was significantly reduced. Thus, full implementation of the steady state model and corrections of the emergence of spurious velocity are left for future considerations.

4.7 Summary

In this chapter, we developed a steady state model using Galerkin finite element method. Our validation of the model using the experimental data of [17], shows a good agreement between the numerical results and the experiment. Utilising the model, we compute the steady state shapes and hydrodynamic features characterising the nose, film, interface and bottom regions around the bubble for different dimensionless inverse viscosity numbers, Eötvös numbers and Froude number based on liquid centreline velocity. For almost all the steady features analysed, our results show that from $Eo = 100$ and above, surface tension has insignificant influence on the magnitude of the features. From the normalised frontal radius, in the nose region, we contend that $Nf \leq 60$ can be considered as regime of strong viscous effect on the radius of curvature of the nose. Similarly, for the film region, we deduced that it is the interaction between the curvature and viscous stress that modifies the shape of the nose and bottom region. This is premised on the fact that in the equilibrium film region, the interface normal stress based on total pressure, total pressure and bubble pressure are equal and non-zero while the curvature and viscous stresses are zero. For the bottom region, we made use of our results for both the dependency of bubble bottom shape and existence of wake on inverse viscosity and Eötvös numbers to draw up a regime map depicting regions of dimensionless parameters space where wake can and cannot be observed together with the prevailing bubble bottom shape. We stress that the primary goal of this chapter is to generate steady state solution for linear stability and energy analyses in the following chapter. However, we note that the systematic nature of the analysis of the steady state features carried out in this chapter using the inverse viscosity and the Eötvös numbers as the base dimensionless parameters can be considered new. More importantly is the contribution to the understanding of the underlying physics of the features analysed.

Chapter 5

Linear stability and energy budget analyses

The steady state model for an axisymmetric Taylor bubble rising in a stagnant and moving liquid was developed and solved in the previous chapter. In this chapter we are examining the stability of a three-dimensional axisymmetric Taylor bubble generated from the steady state two-dimensional axisymmetric solution by revolving it around the axis of symmetry. The stability of a flow is determined by disturbing the steady state solution of the flow, known as the base flow, infinitesimally and then examining whether the disturbance will grow or die down with time [93, 102]. In doing that, the governing equations for the variables are written as a time-independent component (base flow) plus a time-dependent component (perturbation).

In section 5.1, the model governing the evolution of the perturbations added to the base flow is derived by linearising the perturbed governing equations written around the perturbed three-dimensional bubble. The numerical approach used in solving the stability model and the validation carried out on the model are discussed in sections 5.2 and 5.3, respectively. The results of the stability analysis of the base flow solutions for both the stagnant and flowing liquids are presented in section 5.4. In section 5.5, the equation for energy budget analysis is derived and the results of the analysis discussed. A summary for the chapter is written in section 5.6.

5.1 Linear stability model formulation

We imagine that the two-dimensional axisymetric steady state solution for the rising bubble is revolved in the azimuthal direction to form a three-dimensional bubble, just as shown in Figure 3.1. The governing equations and boundary conditions for this flow are as described in section 3.2. Thus, we begin the model development from the weak forms of the momentum and continuity equations derived in section 3.3.

$$\int_V \left\{ \frac{\partial \mathbf{u}}{\partial t} \cdot \mathbf{\Phi} + \left[(\mathbf{u} \cdot \nabla) \mathbf{u} \right] \cdot \mathbf{\Phi} + 2Nf^{-1} \mathbf{E}(\mathbf{u}) : \mathbf{E}(\mathbf{\Phi}) - p(\nabla . \mathbf{\Phi}) \right\} dV \\ - \int_{A_b} \left\{ \left[Eo^{-1} \kappa + \mathrm{z} - \mathrm{P_b} \right] \mathbf{n} \cdot \mathbf{\Phi} \right\} dA_b = 0 \tag{5.1}$$

$$\int_V \left\{ \varepsilon p \varphi + (\nabla . \mathbf{u}) \varphi \right\} dV = 0 \tag{5.2}$$

In addition, we have the weak form of kinematic boundary condition which is the unsteady form of the equation that governs the deformation of the interface (3.48) used in steady state calculation.

$$\int_{A_b} \left\{ \left[\frac{d\mathbf{r}_b}{dt} \cdot \mathbf{n} - \mathbf{u} \cdot \mathbf{n} \right] \xi \right\} dA_b = 0 \tag{5.3}$$

In a way similar to domain perturbation, we shall assume that the three-dimensional base flow domain is perturbed by the addition of infinitesimal deformation field $\tilde{\mathbf{x}}$ to its position vector and that equations (5.1), (5.2) and (5.3)) hold on the three-dimensional perturbed domain. This concept of writing the weak forms of the governing equations around the perturbed domain has been used in the examination of three-dimensional linear stability analysis of coating flow problems [21, 23]. The perturbed three-dimensional domain can then be linearised around the base state three-dimensional axisymmetric domain, the deformation field restricted to the interface, just as it is expected in the classical linear stability approach, and finally, the linearisation of the perturbed flow field variables about the base state solution is carried out. This approach to the derivation of the linear stability model can be seen as an extension of the total linearisation method used in solving two-dimensional viscous free boundary problems [27, 60] to three-dimensional linear stability analysis.

Let the position vector of the perturbed domain be written as

$$\mathbf{r} = \mathbf{r}^0 + \epsilon\tilde{\mathbf{x}} \tag{5.4}$$

Equation (5.4) is similar to (3.58), the difference being that $\mathbf{r}^0$ now represents the position vector of the unperturbed three-dimensional base flow domain and $\tilde{\mathbf{x}}$ is a deformation field that is defined in the entire base flow domain. The linearised elemental volume of the perturbed three-dimensional domain is given as [18, 21]

$$dV = |\mathbf{F}|\, dV^0 \tag{5.5}$$

where dV and dV^0 are elemental volume for the perturbed and base flow three-dimensional domains; $|\cdot|$ denotes the determinant operator and $\mathbf{F}$ is the deformation gradient define as

$$\mathbf{F} = \mathbf{I} + \nabla\tilde{\mathbf{x}} \tag{5.6}$$

which in cylindrical coordinates system is given as

$$\mathbf{F}(\tilde{\mathbf{x}}) = \begin{bmatrix} \left(1 + \frac{\partial \tilde{x}_r}{\partial r^0}\right) & \left(\frac{1}{r^0}\frac{\partial \tilde{x}_r}{\partial \theta^0} - \frac{\tilde{x}_\theta}{r^0}\right) & \frac{\partial \tilde{x}_r}{\partial z^0} \\ \frac{1}{r^0}\frac{\partial \tilde{x}_\theta^0}{\partial r^0} & \left(1 + \frac{\tilde{x}_r}{r^0} + \frac{1}{r^0}\frac{\partial \tilde{x}_\theta}{\partial \theta^0}\right) & \frac{\partial \tilde{x}_\theta}{\partial z^0} \\ \frac{\partial \tilde{x}_z}{\partial r^0} & \frac{1}{r^0}\frac{\partial \tilde{x}_z}{\partial \theta^0} & \left(1 + \frac{\partial \tilde{x}_z}{\partial z^0}\right) \end{bmatrix} \tag{5.7}$$

and (5.5) simplified to

$$dV = (1 + \nabla \cdot \tilde{\mathbf{x}})\, dV^0 \tag{5.8}$$

Thus, we can relate the elemental volume in the perturbed three-dimensional domain to the base flow two-dimensional axisymmetric domain, $d\Omega^0 = r^0 dr^0 dz^0$ as follow

$$dV = r dr d\theta dz = (1 + \nabla \cdot \tilde{\mathbf{x}})\, dV^0 = (1 + \nabla \cdot \tilde{\mathbf{x}})\, r^0 dr^0 d\theta^0 dz^0 \tag{5.9}$$

$$dV = (1 + \nabla \cdot \tilde{\mathbf{x}})\, d\Omega^0 d\theta^0 \tag{5.10}$$

Similarly, an elemental area on the perturbed interface in the three-dimensional domain, dA_b can be related to base flow length of arc, Γ_b^0 in the two-dimensional axisymmetric domain

$$dA_b = (1 + \nabla_s \cdot \tilde{\mathbf{x}})\, d\Gamma_b^0 d\theta^0 \tag{5.11}$$

and the interface terms can be linearised as follow

$$\mathbf{n} = \mathbf{n}^0 + \epsilon\tilde{\mathbf{n}} \tag{5.12a}$$

$$\kappa = \kappa^0 + \epsilon\tilde{\kappa} \tag{5.12b}$$

$$\mathbf{\Phi} = \mathbf{\Phi} + \epsilon\,(\tilde{\mathbf{x}} \cdot \nabla)\,\mathbf{\Phi} \tag{5.12c}$$

$$\mathbf{u} = \mathbf{u} + \epsilon\,(\tilde{\mathbf{x}} \cdot \nabla)\,\mathbf{u} \tag{5.12d}$$

where $\tilde{\mathbf{n}}$ is the additional term due linearisation of the unit normals on the perturbed interface and can be deduced from (3.62); $\tilde{\kappa}$ is the curvature perturbation given by (3.65).

If we substitute (5.4), (5.10), (5.11) and (5.12), together with the flow field perturbations

$$\mathbf{u} = \mathbf{u}^0 + \epsilon\tilde{\mathbf{u}} \tag{5.13a}$$

$$p = p^0 + \epsilon\tilde{p} \tag{5.13b}$$

into equations (5.1), (5.2) and (5.3), neglecting all terms of order ϵ^2, the equations gives

momentum equations

$$\begin{aligned}
&\int_0^{2\pi}\Bigg\{\int_{\Omega^0}\left\{\left[\left(\mathbf{u}^0\cdot\nabla\right)\mathbf{u}^0\right]\cdot\mathbf{\Phi}+2Nf^{-1}\mathbf{E}\left(\mathbf{u}^0\right):\mathbf{E}\left(\mathbf{\Phi}\right)-p^0\left(\nabla.\,\mathbf{\Phi}\right)\right\}d\Omega^0\\
&-\int_{\Gamma_b^0}\left\{\left[Eo^{-1}\kappa^0+z^0-P_b^0\right]\mathbf{n}^0\cdot\mathbf{\Phi}\right\}d\Gamma_b^0\Bigg\}d\theta^0\\
&+\epsilon\int_0^{2\pi}\int_{\Omega^0}\left\{\frac{\partial\tilde{\mathbf{u}}}{\partial t}\cdot\mathbf{\Phi}+\left[\left(\mathbf{u}^0\cdot\nabla\right)\tilde{\mathbf{u}}+\left(\tilde{\mathbf{u}}\cdot\nabla\right)\mathbf{u}^0\right]\cdot\mathbf{\Phi}+2Nf^{-1}\mathbf{E}\left(\tilde{\mathbf{u}}\right):\mathbf{E}\left(\mathbf{\Phi}\right)-\tilde{p}\left(\nabla.\,\mathbf{\Phi}\right)\right\}d\Omega^0d\theta^0\\
&-\epsilon\int_0^{2\pi}\int_{\Gamma_b^0}\left\{\left[Eo^{-1}\tilde{\kappa}+\tilde{z}\right]\mathbf{n}^0\cdot\mathbf{\Phi}\right\}d\Gamma_b^0d\theta^0\\
&+\epsilon\int_0^{2\pi}\int_{\Gamma_b^0}\tilde{\mathbf{x}}\cdot\mathbf{n}^0\left\{\left[\left(\mathbf{u}^0\cdot\nabla\right)\mathbf{u}^0\right]\cdot\mathbf{\Phi}+2Nf^{-1}\mathbf{E}\left(\mathbf{u}^0\right):\mathbf{E}\left(\mathbf{\Phi}\right)-p^0\left(\nabla.\,\mathbf{\Phi}\right)\right\}d\Gamma_b^0d\theta^0\\
&-\epsilon\int_0^{2\pi}\int_{\Gamma_b^0}\left\{\left[Eo^{-1}\kappa^0+z^0-P_b^0\right]\left[\tilde{\mathbf{n}}\cdot\mathbf{\Phi}+\left[\left(\tilde{\mathbf{x}}\cdot\nabla\right)\mathbf{\Phi}\right]\cdot\mathbf{n}^0+\left(\nabla_s\cdot\tilde{\mathbf{x}}\right)\mathbf{n}^0\cdot\mathbf{\Phi}\right]\right\}d\Gamma_b^0d\theta^0=0
\end{aligned}\tag{5.14}$$

continuity equation

$$\begin{aligned}
&\int_0^{2\pi}\int_{\Omega^0}\left\{\left\{\varepsilon p^0\varphi+\left(\nabla.\,\mathbf{u}^0\right)\varphi\right\}\left[1+\nabla\cdot\tilde{\mathbf{x}}\right]\right\}d\Omega^0d\theta^0\\
&+\epsilon\int_0^{2\pi}\int_{\Omega^0}\left\{\left\{\varepsilon\tilde{p}\varphi+\left(\nabla.\,\tilde{\mathbf{u}}\right)\varphi\right\}\right\}d\Omega^0d\theta^0=0
\end{aligned}\tag{5.15}$$

kinematic boundary condition

$$\begin{aligned}
&\int_0^{2\pi}\int_{\Gamma_b^0}\left\{\left\{\left[\frac{d\mathbf{r}_b^0}{dt}\cdot\mathbf{n}^0-\mathbf{u}^0\cdot\mathbf{n}^0\right]\xi\right\}\left[1+\nabla_s\cdot\tilde{\mathbf{x}}\right]\right\}d\Gamma_b^0d\theta^0\\
&+\epsilon\int_0^{2\pi}\int_{\Gamma_b^0}\left\{\left[\frac{d\tilde{\mathbf{x}}}{dt}\cdot\mathbf{n}^0-\tilde{\mathbf{u}}\cdot\mathbf{n}^0-\mathbf{u}^0\cdot\tilde{\mathbf{n}}-\left[\left(\tilde{\mathbf{x}}\cdot\nabla\right)\mathbf{u}^0\right]\cdot\mathbf{n}^0\right]\xi\right\}d\Gamma_b^0d\theta^0=0
\end{aligned}\tag{5.16}$$

Here $\mathbf{u}^0$, p^0 and P_b^0 represent the base flow solutions for the variables; $\tilde{\mathbf{u}}$ and $\tilde{p}$ denotes the perturbation to the flow field variables.

By virtue of the status of the axisymmetric base state equations at convergence, noted in equations (4.25) and (4.26), the first two lines of (5.14) and the first lines of (5.15) and (5.16) are zeros. The last two lines of (5.14) are the additional terms due to the linearisation of the domain and boundary terms of (5.1), respectively. We note that in arriving at the additional terms

in the line corresponding to the domain linearisation, we have used the Gauss's divergence theorem to restrict the deformation to the interface as in classical linear stability formulation.

Simplifying the remainder of equations (5.14), (5.15) and (5.16) further by substituting for $\tilde{\mathbf{n}}$ and $\tilde{\kappa}$ using (3.62) and (3.65), respectively, taking the deformation field to be of the form

$$\tilde{\mathbf{x}} = \tilde{h}\mathbf{n}^0, \tag{5.17}$$

since it has now been restricted to the interface and using the relations

$$\mathbf{u}^0 = \left(\mathbf{u}^0 \cdot \mathbf{n}^0\right)\mathbf{n}^0 + \left(\mathbf{u}^0 \cdot \mathbf{t}^0\right)\mathbf{t}^0 \tag{5.18a}$$

$$\nabla = \left(\mathbf{I} - \mathbf{n}^0 \otimes \mathbf{n}^0\right) \cdot \nabla + \left(\mathbf{n}^0 \otimes \mathbf{n}^0\right) \cdot \nabla \tag{5.18b}$$

to decompose the terms in the line corresponding to domain linearisation into their tangential and normal components, we have, after a little algebra, the following as the perturbation equations for the momentum equations, continuity equation and kinematic boundary condition, respectively

momentum equations

$$\begin{aligned}
&\int_0^{2\pi}\int_{\Omega^0}\left\{\frac{\partial\tilde{\mathbf{u}}}{\partial t}\cdot\mathbf{\Phi} + \left[\left(\mathbf{u}^0\cdot\nabla\right)\tilde{\mathbf{u}} + \left(\tilde{\mathbf{u}}\cdot\nabla\right)\mathbf{u}^0\right]\cdot\mathbf{\Phi} + 2Nf^{-1}\mathbf{E}\left(\tilde{\mathbf{u}}\right):\mathbf{E}\left(\mathbf{\Phi}\right) - \tilde{p}\left(\nabla.\,\mathbf{\Phi}\right)\right\}d\Omega^0 d\theta \\
&-\int_0^{2\pi}\int_{\Gamma_b^0} Eo^{-1}\left\{-\frac{d\tilde{h}}{ds}\left[\mathbf{n}\cdot\frac{d\mathbf{\Phi}}{ds} - \kappa_a\left(\mathbf{t}\cdot\mathbf{\Phi}\right)\right] + \left[\tilde{h}\left(\kappa_a^2+\kappa_b^2\right) + \frac{1}{r^2}\frac{\partial^2\tilde{h}}{\partial\theta^2}\right]\mathbf{n}\cdot\mathbf{\Phi}\right\}d\Gamma_b^0 d\theta \\
&-\int_0^{2\pi}\int_{\Gamma_b^0}\left\{\tilde{h}n_z\left(\mathbf{n}\cdot\mathbf{\Phi}\right)\right\}d\Gamma_b^0 d\theta \\
&+\int_0^{2\pi}\int_{\Gamma_b^0}\tilde{h}\left\{\left(\mathbf{u}^0\cdot\mathbf{t}\right)\left[\frac{d\mathbf{u}^0}{ds}\cdot\mathbf{\Phi}\right] + \left[-p^0 + 2Nf^{-1}\left(\mathbf{t}\cdot\frac{d\mathbf{u}^0}{ds}\right)\right]\left(\mathbf{t}\cdot\frac{d\mathbf{\Phi}}{ds}\right)\right. \\
&\left.+\left[-p^0 + 2Nf^{-1}\frac{u_r^0}{r}\right]\left(\frac{\Phi_r}{r} + \frac{1}{r}\frac{\partial\Phi_\theta}{\partial\theta}\right)\right\}d\Gamma_b^0 d\theta \\
&+\int_0^{2\pi}\int_{\Gamma_b^0}\left\{\left[Eo^{-1}\kappa + z - P_b^0\right]\left[\left(\mathbf{t}\cdot\mathbf{\Phi}\right)\frac{d\tilde{h}}{ds} + \frac{\Phi_\theta}{r}\frac{\partial\tilde{h}}{\partial\theta} + \tilde{h}\kappa\left(\mathbf{n}\cdot\mathbf{\Phi}\right)\right]\right\}d\Gamma_b^0 d\theta = 0
\end{aligned} \tag{5.19}$$

continuity equation

$$\int_0^{2\pi} \int_{\Omega^0} \left\{ \{ \varepsilon \tilde{p} \varphi + (\nabla . \, \tilde{\mathbf{u}}) \, \varphi \} \right\} d\Omega d\theta = 0 \tag{5.20}$$

kinematic boundary condition

$$\int_0^{2\pi} \int_{\Gamma_b^0} \left\{ \left[\frac{d\tilde{h}}{dt} - \tilde{\mathbf{u}} \cdot \mathbf{n} + \left(\mathbf{u}^0 \cdot \mathbf{t} \right) \frac{d\tilde{h}}{ds} - \tilde{h} \left(\frac{d\mathbf{u}^0}{dn} \cdot \mathbf{n} \right) \right] \xi \right\} d\Gamma_b^0 d\theta = 0 \tag{5.21}$$

Where $\frac{d}{dn} = (\mathbf{n} \cdot \nabla)$ is an operator that denotes derivative in the normal direction.
In equations (5.19)-(5.21), we have suppressed the use of the superscript $''0''$ to denote base state quantities for the unit tangent, unit normal, spatial coordinates r, θ, z and the curvature for brevity.

It is not practical to investigate the evolution of all possible types of perturbation on a given base flow. A way forward is to express a disturbance as a combination of linearly independent fundamental modes using normal modes, and then examining the evolution of each individual mode [93]. Let us take the following normal mode forms for the perturbations

$$\tilde{\mathbf{u}} \left(r, \theta, z, t \right) = \hat{\mathbf{u}} \left(r, z \right) e^{(\mathrm{i}m\theta + \beta t)} \tag{5.22a}$$

$$\tilde{p} \left(r, \theta, z, t \right) = \hat{p} \left(r, z \right) e^{(\mathrm{i}m\theta + \beta t)} \tag{5.22b}$$

$$\tilde{h} \left(s, \theta, t \right) = \hat{h} \left(s \right) e^{(\mathrm{i}m\theta + \beta t)} \tag{5.22c}$$

and their corresponding test functions as

$$\mathbf{\Phi} \left(r, \theta, z \right) = \bar{\mathbf{\Phi}} \left(r, z \right) e^{(-\mathrm{i}m\theta)} \tag{5.23a}$$

$$\varphi \left(r, \theta, z \right) = \bar{\varphi} \left(r, z \right) e^{(-\mathrm{i}m\theta)} \tag{5.23b}$$

$$\xi \left(s, \theta \right) = \bar{\xi} \left(s \right) e^{(-\mathrm{i}m\theta)} \tag{5.23c}$$

where $\hat{\mathbf{u}}$, $\hat{p}$ and $\hat{h}$ are complex functions of space representing the velocity, pressure and interface perturbations amplitude, respectively. i is the imaginary identity unit satisfying $\mathrm{i}^2 = -1$; m is a dimensionless wave number in the azimuthal direction θ, also known as eigenmode, and is a

whole number; β is a complex constant called the complex growth rate which can be decomposed into its real β_R and imaginary β_I parts denoting temporal growth rate and frequency, respectively: If β_R is positive, the disturbance grows exponentially in time and the base flow is linearly unstable; if β_R is negative, the disturbance decays and the normal mode is linearly stable; if β_R is zero, the disturbance is neutrally stable.

It should be noted that in choosing the form of test functions in (5.23), we have taken into consideration that the inner product of two complex functions, say, $\mathfrak{f}$ and $\mathfrak{g}$ defined in a domain Ω is given by

$$\langle \mathfrak{f}, \mathfrak{g} \rangle = \int_{\Omega} (\mathfrak{f}\mathfrak{g}^*)\, d\Omega \tag{5.24}$$

where $''*''$ is used to represent the complex conjugate of function g.

Substituting (5.22) and (5.23) into (5.19)-(5.21), separating the momentum equation into its components, we have the following equations governing the normal mode evolution of the perturbations as a function of dimensionless parameters, Nf, Eo, U_m and m.

momentum: radial component

$$\begin{aligned}
&\int_{\Omega^0} \left\{ \beta \hat{u}_r \bar{\Phi}_r + \left[\hat{u}_r \frac{\partial u_r^0}{\partial r} + \hat{u}_z \frac{\partial u_r^0}{\partial z} + u_r^0 \frac{\partial \hat{u}_r}{\partial r} + u_z^0 \frac{\partial \hat{u}_r}{\partial z} \right] \bar{\Phi}_r \right. \\
&+ Nf^{-1} \left[2 \frac{\partial \hat{u}_r}{\partial r} \frac{\partial \bar{\Phi}_r}{\partial r} + \left(2 + m^2\right) \frac{\hat{u}_r \bar{\Phi}_r}{r^2} + 3\mathfrak{i} m \frac{\hat{u}_\theta \bar{\Phi}_r}{r^2} \right. \\
&\left. \left. - \mathfrak{i} m \frac{\bar{\Phi}_r}{r} \frac{\partial \hat{u}_\theta}{\partial r} + \frac{\partial \bar{\Phi}_r}{\partial z} \left(\frac{\partial \hat{u}_r}{\partial z} + \frac{\partial \hat{u}_z}{\partial r} \right) \right] - \hat{p} \left(\frac{\partial \bar{\Phi}_r}{\partial r} + \frac{\bar{\Phi}_r}{r} \right) \right\} d\Omega^0 \\
&- \int_{\Gamma_b^0} Eo^{-1} \left\{ -\frac{d\hat{h}}{ds} \left[n_r \frac{d\bar{\Phi}_r}{ds} - \kappa_a \left(t_r \bar{\Phi}_r \right) \right] + \hat{h} \left[\kappa_a^2 + \kappa_b^2 - \frac{m^2}{r^2} \right] n_r \bar{\Phi}_r \right\} d\Gamma_b^0 \\
&- \int_{\Gamma_b^0} \left\{ \hat{h} n_z \left(n_r \bar{\Phi}_r \right) \right\} d\Gamma_b^0 + \int_{\Gamma_b^0} \hat{h} \left\{ \left(u_r^0 t_r \right) \left[\frac{du_r^0}{ds} \bar{\Phi}_r \right] \right. \\
&\left. + \left[-p^0 + 2Nf^{-1} \left(t_r \frac{du_r^0}{ds} \right) \right] \left(t_r \frac{d\bar{\Phi}_r}{ds} \right) + \left[-p^0 + 2Nf^{-1} \frac{u_r^0}{r} \right] \left(\frac{\bar{\Phi}_r}{r} \right) \right\} d\Gamma_b^0 \\
&+ \int_{\Gamma_b^0} \left\{ \left[Eo^{-1} \kappa + z - P_b^0 \right] \left[\left(t_r \bar{\Phi}_r \right) \frac{d\hat{h}}{ds} + \hat{h} \kappa \left(n_r \bar{\Phi}_r \right) \right] \right\} d\Gamma_b^0 = 0
\end{aligned} \tag{5.25}$$

momentum: azimuthal component

$$\begin{aligned}
&\int_{\Omega^0} \Bigg\{ \beta \hat{u}_\theta \bar{\Phi}_\theta + \left[u_r^0 \frac{\partial \hat{u}_\theta}{\partial r} + u_z^0 \frac{\partial \hat{u}_\theta}{\partial z} + \frac{u_r^0 \hat{u}_\theta}{r} \right] \bar{\Phi}_\theta + Nf^{-1} \Bigg[\left(1 + 2m^2\right) \frac{\hat{u}_\theta \bar{\Phi}_\theta}{r^2} + \frac{\partial \hat{u}_\theta}{\partial z} \frac{\partial \bar{\Phi}_\theta}{\partial z} \\
&+ \frac{\partial \hat{u}_\theta}{\partial r} \frac{\partial \bar{\Phi}_\theta}{\partial r} - \left(\frac{\hat{u}_\theta}{r} \frac{\partial \bar{\Phi}_\theta}{\partial r} + \frac{\bar{\Phi}_\theta}{r} \frac{\partial \hat{u}_\theta}{\partial r} \right) + \mathfrak{i} m \left(\frac{\hat{u}_r}{r} \frac{\partial \bar{\Phi}_\theta}{\partial r} + \frac{\hat{u}_z}{r} \frac{\partial \bar{\Phi}_\theta}{\partial z} \right) - 3\mathfrak{i} m \frac{\hat{u}_r \bar{\Phi}_\theta}{r^2} \Bigg] \\
&- p \left(-\mathfrak{i} m \frac{\bar{\Phi}_\theta}{r} \right) \Bigg\} d\Omega^0 + \int_{\Gamma_b^0} \hat{h} \left\{ \left[-p^0 + 2Nf^{-1} \frac{u_r^0}{r} \right] \left(-\mathfrak{i} m \frac{\bar{\Phi}_\theta}{r} \right) \right\} d\Gamma_b^0 \\
&+ \int_{\Gamma_b^0} \left\{ \hat{h} \left[Eo^{-1} \kappa + z - P_b^0 \right] \left[\mathfrak{i} m \frac{\bar{\Phi}_\theta}{r} \right] \right\} d\Gamma_b^0 = 0
\end{aligned} \tag{5.26}$$

momentum: axial component

$$\begin{aligned}
&\int_{\Omega^0} \Bigg\{ \beta \hat{u}_z \bar{\Phi}_z + \left[\hat{u}_r \frac{\partial u_z^0}{\partial r} + \hat{u}_z \frac{\partial u_z^0}{\partial z} + u_r^0 \frac{\partial \hat{u}_z}{\partial r} + u_z^0 \frac{\partial \hat{u}_z}{\partial z} \right] \bar{\Phi}_z \\
&+ Nf^{-1} \left[2 \frac{\partial \hat{u}_z}{\partial z} \frac{\partial \bar{\Phi}_z}{\partial z} + m^2 \frac{\hat{u}_z \bar{\Phi}_z}{r^2} - \mathfrak{i} m \frac{\bar{\Phi}_z}{r} \frac{\partial \hat{u}_\theta}{\partial z} + \frac{\partial \bar{\Phi}_z}{\partial r} \left(\frac{\partial \hat{u}_r}{\partial z} + \frac{\partial \hat{u}_z}{\partial r} \right) \right] \\
&- \hat{p} \left(\frac{\partial \bar{\Phi}_z}{\partial z} \right) \Bigg\} d\Omega^0 \\
&- \int_{\Gamma_b^0} Eo^{-1} \left\{ -\frac{d\hat{h}}{ds} \left[n_z \frac{d\bar{\Phi}_z}{ds} - \kappa_a \left(t_z \bar{\Phi}_z \right) \right] + \hat{h} \left[\kappa_a^2 + \kappa_b^2 - \frac{m^2}{r^2} \right] n_z \bar{\Phi}_z \right\} d\Gamma_b^0 \\
&- \int_{\Gamma_b^0} \left\{ \hat{h} n_z \left(n_z \bar{\Phi}_z \right) \right\} d\Gamma_b^0 \\
&+ \int_{\Gamma_b^0} \hat{h} \left\{ \left(u_z^0 t_z \right) \left[\frac{du_z^0}{ds} \bar{\Phi}_z \right] + \left[-p^0 + 2Nf^{-1} \left(t_z \frac{du_z^0}{ds} \right) \right] \left(t_z \frac{d\bar{\Phi}_z}{ds} \right) \right\} d\Gamma_b^0 \\
&+ \int_{\Gamma_b^0} \left\{ \left[Eo^{-1} \kappa + z - P_b^0 \right] \left[\left(t_z \bar{\Phi}_z \right) \frac{d\hat{h}}{ds} + \hat{h} \kappa \left(n_z \bar{\Phi}_z \right) \right] \right\} d\Gamma_b^0 = 0
\end{aligned} \tag{5.27}$$

continuity

$$\int_{\Omega^0} \left\{ \left[\varepsilon \hat{p} + \frac{\partial \hat{u}_r}{\partial r} + \frac{\hat{u}_r}{r} - \mathfrak{i} m \frac{\hat{u}_\theta}{r} + \frac{\partial \hat{u}_z}{\partial z} \right] \bar{\varphi} \right\} d\Omega^0 = 0 \tag{5.28}$$

kinematic boundary condition

$$\int_{\Gamma_b^0} \left\{ \left[\beta \hat{h} - \hat{\mathbf{u}} \cdot \mathbf{n} + \left(\mathbf{u}^0 \cdot \mathbf{t} \right) \frac{d\hat{h}}{ds} - \hat{h} \left(\frac{d\mathbf{u}^0}{dn} \cdot \mathbf{n} \right) \right] \bar{\xi} \right\} d\Gamma_b^0 = 0 \tag{5.29}$$

By introducing the normal modes, we have transferred the time dependence into the complex growth rate β and azimuthal dependency into the eigenmode m which now allows us to integrate

out the azimuthal dimension leading to the equations being written around the two-dimensional axisymetric base flow domain and boundaries with a multiplicative factor $2\pi e^{\beta t}$ which cancelled out.

Following the same procedures as done section 4.1 for steady state model, the combined finite element models for the perturbations equations (5.25)-(5.29) can be written as

$$\beta \mathbf{B}\mathbf{y} = \mathbf{J}\mathbf{y} \tag{5.30}$$

with

$$\begin{aligned}
\mathbf{B} &= \begin{bmatrix} \bar{\mathbf{B}}_{r,r} & 0 & 0 & 0 & 0 \\ 0 & \bar{\mathbf{B}}_{\theta,\theta} & 0 & 0 & 0 \\ 0 & 0 & \bar{\mathbf{B}}_{z,z} & 0 & 0 \\ 0 & 0 & 0 & 0 & 0 \\ 0 & 0 & 0 & 0 & \bar{\mathbf{B}}_{h} \end{bmatrix}, \quad \mathbf{y} = \begin{bmatrix} \hat{\mathbf{v}}_r \\ \hat{\mathbf{v}}_\theta \\ \hat{\mathbf{v}}_z \\ \hat{\mathbf{p}} \\ \hat{\mathbf{h}} \end{bmatrix} \quad \text{and} \\
\mathbf{J} &= - \begin{bmatrix} \left(\bar{\mathbf{C}}_{r,r} + \bar{\mathbf{K}}_{r,r}\right) & \bar{\mathbf{K}}_{r,\theta} & \left(\bar{\mathbf{C}}_{r,z} + \bar{\mathbf{K}}_{r,z}\right) & -\bar{\mathbf{Q}}_r^T & \bar{\mathbf{M}}_{r,h} \\ \bar{\mathbf{K}}_{r,\theta}^T & \left(\bar{\mathbf{C}}_{\theta,\theta} + \bar{\mathbf{K}}_{\theta,\theta}\right) & \bar{\mathbf{K}}_{z,\theta}^T & -\bar{\mathbf{Q}}_\theta^T & \bar{\mathbf{M}}_{\theta,h} \\ \left(\bar{\mathbf{C}}_{z,r} + \bar{\mathbf{K}}_{z,r}\right) & \bar{\mathbf{K}}_{z,\theta} & \left(\bar{\mathbf{C}}_{z,z} + \bar{\mathbf{K}}_{z,z}\right) & -\bar{\mathbf{Q}}_z^T & \bar{\mathbf{M}}_{z,h} \\ -\bar{\mathbf{Q}}_r & -\bar{\mathbf{Q}}_\theta & -\bar{\mathbf{Q}}_z & -\bar{\mathbf{Q}}_p & 0 \\ -\bar{\mathbf{X}}_r & 0 & -\bar{\mathbf{X}}_z & 0 & \bar{\mathbf{X}}_h \end{bmatrix}
\end{aligned} \tag{5.31}$$

where the operator $(\cdot)^T$ in this instant denotes the Hermitian transpose. The expression for the coefficient matrices for the radial and axial components of the velocity perturbations in the momentum and continuity equations are the same as those stated in section 4.1. The only difference is that in this case, the matrices are complex. Below are the remaining coefficient matrices that are either not stated before or different from the previously given ones

continuity equation

$$\bar{\mathbf{Q}}_\theta = \int_{\Omega^{0,e}} \left\{ \mathbf{i}m\bar{\mathbf{\Lambda}} \frac{\bar{\mathbf{\Psi}}^T}{r} \right\} d\Omega^{0,e}; \tag{5.32}$$

momentum equation: growth rate part

$$\bar{\mathbf{B}}_{i,i} = \int_{\Omega^{0,e}} \left\{ \bar{\mathbf{\Psi}} \bar{\mathbf{\Psi}}^T \right\} d\Omega^{0,e} \quad \forall\, i = r, \theta, z \tag{5.33}$$

momentum equation: convective part

$$\bar{\mathbf{C}}_{\theta,\theta} = \int_{\Omega^{0,e}} \left\{ \bar{\mathbf{\Psi}} \left[\left(\mathbf{u}^0 \cdot \nabla \right) \bar{\mathbf{\Psi}}^T + \frac{u_r^0 \bar{\mathbf{\Psi}}^T}{r} \right] \right\} d\Omega^{0,e} \tag{5.34}$$

momentum equation: viscous part

$$\bar{\mathbf{K}}_{i,i} = \int_{\Omega^{0,e}} Nf^{-1} \left\{ 2 \frac{\partial \bar{\mathbf{\Psi}}}{\partial i} \frac{\partial \bar{\mathbf{\Psi}}^T}{\partial i} + \left(2\delta_{r,i} + m^2 \right) \frac{\bar{\mathbf{\Psi}} \bar{\mathbf{\Psi}}^T}{r^2} + \delta_{r,i} \frac{\partial \bar{\mathbf{\Psi}}}{\partial z} \frac{\partial \bar{\mathbf{\Psi}}^T}{\partial z} + \delta_{z,i} \frac{\partial \bar{\mathbf{\Psi}}}{\partial r} \frac{\partial \bar{\mathbf{\Psi}}^T}{\partial r} \right\} d\Omega^0 \;\forall\, i = r, z \tag{5.35a}$$

$$\bar{\mathbf{K}}_{\theta,\theta} = \int_{\Omega^{0,e}} Nf^{-1} \left\{ \left(1 + 2m^2 \right) \frac{\bar{\mathbf{\Psi}} \bar{\mathbf{\Psi}}^T}{r^2} + \frac{\partial \bar{\mathbf{\Psi}}}{\partial z} \frac{\partial \bar{\mathbf{\Psi}}^T}{\partial z} + \frac{\partial \bar{\mathbf{\Psi}}}{\partial r} \frac{\partial \bar{\mathbf{\Psi}}^T}{\partial r} - \left(\frac{\bar{\mathbf{\Psi}}^T}{r} \frac{\partial \bar{\mathbf{\Psi}}}{\partial r} + \frac{\bar{\mathbf{\Psi}}}{r} \frac{\partial \bar{\mathbf{\Psi}}^T}{\partial r} \right) \right\} d\Omega^{0,e} \tag{5.35b}$$

$$\bar{\mathbf{K}}_{i,\theta} = \int_{\Omega^{0,e}} Nf^{-1} \left\{ \delta_{r,i} 3\mathfrak{i}m \frac{\bar{\mathbf{\Psi}} \bar{\mathbf{\Psi}}^T}{r^2} - \mathfrak{i}m \frac{\bar{\mathbf{\Psi}}}{r} \frac{\partial \bar{\mathbf{\Psi}}^T}{\partial i} \right\} d\Omega^{0,e} \;\forall\, i = r, z \tag{5.35c}$$

momentum equation: interface deformation part

$$\begin{aligned}
\bar{\mathbf{M}}_{i,h} = & - \int_{\Gamma_b^{0,e}} Eo^{-1} \left\{ - \left[n_i \frac{d\bar{\mathbf{\Psi}}}{ds} - \kappa_a \left(t_i \bar{\mathbf{\Psi}} \right) \right] \frac{d\bar{\boldsymbol{\eta}}^T}{ds} + n_i \left[\kappa_a^2 + \kappa_b^2 - \frac{m^2}{r^2} \right] \bar{\mathbf{\Psi}} \bar{\boldsymbol{\eta}}^T \right\} d\Gamma_b^{0,e} \\
& - \int_{\Gamma_b^0} \left\{ n_z n_i \bar{\mathbf{\Psi}} \bar{\boldsymbol{\eta}}^T \right\} d\Gamma_b^0 \\
& + \int_{\Gamma_b^0} \left\{ \left\{ \left(u_i^0 t_i \right) \left[\frac{du_i^0}{ds} \bar{\mathbf{\Psi}} \right] + \left[-p^0 + 2Nf^{-1} \left(t_i \frac{du_i^0}{ds} \right) \right] \left(t_i \frac{d\bar{\mathbf{\Psi}}}{ds} \right) \right\} \bar{\boldsymbol{\eta}}^T \right\} d\Gamma_b^0 \\
& + \int_{\Gamma_b^0} \left\{ \left[Eo^{-1} \kappa + z - P_b^0 \right] \left[\left(t_i \bar{\mathbf{\Psi}} \right) \frac{d\bar{\boldsymbol{\eta}}^T}{ds} + \kappa \left(n_i \bar{\mathbf{\Psi}} \bar{\boldsymbol{\eta}}^T \right) \right] \right\} d\Gamma_b^0 \quad \forall\, i = r, z
\end{aligned} \tag{5.36a}$$

$$\bar{\mathbf{M}}_{\theta,h} = \int_{\Gamma_b^0} \left\{ \left[\left(-p^0 + 2Nf^{-1} \frac{u_r^0}{r} \right) - \left(Eo^{-1} \kappa + z - P_b^0 \right) \right] \left(-\mathfrak{i}m \frac{\bar{\mathbf{\Psi}} \bar{\boldsymbol{\eta}}^T}{r} \right) \right\} d\Gamma_b^0 \tag{5.36b}$$

kinematic boundary condition

$$\bar{\mathbf{X}}_i = \int_{\Gamma_b^{0,e}} n_i \left\{ \bar{\boldsymbol{\eta}} \boldsymbol{\Psi}^T \right\} d\Gamma_b^{0,e} \quad \forall\, i = r, z \tag{5.37a}$$

$$\bar{\mathbf{X}}_h = \int_{\Gamma_b^{0,e}} \left\{ \left(\mathbf{u}^0 \cdot \mathbf{t} \right) \bar{\boldsymbol{\eta}} \frac{d\bar{\boldsymbol{\eta}}^T}{ds} - \left(\frac{d\mathbf{u}^0}{dn} \cdot \mathbf{n} \right) \bar{\boldsymbol{\eta}} \bar{\boldsymbol{\eta}}^T \right\} d\Gamma_b^{0,e} \tag{5.37b}$$

$$\bar{\mathbf{B}}_h = \int_{\Gamma_b^{0,e}} \left\{ \bar{\boldsymbol{\eta}} \bar{\boldsymbol{\eta}}^T \right\} d\Gamma_b^{0,e} \tag{5.37c}$$

The system of equations resulting from the perturbations evolution equations given by (5.30) is a classical problem known as generalised eigenvalue problem, with β being the eigenvalue, $\mathbf{B}$ the mass matrix, $\mathbf{J}$ the Jacobian matrix and $\mathbf{y}$ the eigenfunctions. In the next section, we discuss how the eigenvalue and eigenfunctions of the problem are computed using iterative Arnoldi method.

Before moving to next section, we note that, in addition to the governing equations and kinematic boundary, we imposed at the inlet, wall and outlet boundaries, the following conditions

$$\hat{\mathbf{u}} = \mathbf{0} \quad \text{on} \quad \Gamma_{in}^0 \text{ and } \Gamma_{wall}^0 \tag{5.38}$$

$$\mathbf{n} \cdot \hat{\mathbf{T}} \cdot \mathbf{n} = 0 \quad \text{and} \quad (\mathbf{I} - \mathbf{n} \otimes \mathbf{n}) \cdot \hat{\mathbf{u}} = 0 \quad \text{on} \quad \Gamma_{out}^0 \tag{5.39}$$

where

$$\hat{\mathbf{T}} = -\hat{p} + 2Nf^{-1}\mathbf{E}\left(\hat{\mathbf{u}}\right) \tag{5.40}$$

with

$$\mathbf{E}\left(\hat{\mathbf{u}}\right) = \frac{1}{2}\left[\nabla\hat{\mathbf{u}} + \nabla\hat{\mathbf{u}}^T\right] \tag{5.41}$$

We stress that while it is customary to impose regularity conditions along the axis of symmetry Γ_{sym}^0, we didn't apply any condition in this case because the model equations were written around the perturbed three-dimensional domain and then linearised before integrating out

the θ dimension. In fact, having additional regularity conditions imposed along the axis of symmetry leads to non-physical instability.

5.2 Linear stability model solution

The stability of the steady state solution to the addition of an infinitesimal perturbations of normal mode forms as the dimensionless parameters are varied is found by solving large, generalized, asymmetric matrix eigenvalue problem given by (5.30) for eigenvalues with largest real part. These eigenvalues, also known as the most dangerous or leading eigenvalues, are of greatest interest to the stability of the flow as they grow the fastest, thus dominating other eigenvalues [23]. The asymmetric nature of the problem, as can be seen by inspection of the Jacobian matrix, is due to the convective and interface deformation contributions to the matrix. In addition, it can also be seen that the mass matrix is singular, with several rows having identically zero entries, which can be attributed to the absence of time derivative terms in the continuity equation and though not obvious, due to the requirement that the perturbation vectors satisfy homogeneous essential boundary conditions [21, 77].

The implication of having singularity in the mass matrix is that the number of true eigenvalues of the problem is smaller than the dimension of the problem, with the number of missing eigenvalues equal to the number of algebraic equations having identically zero row in the matrix [21]. These missing eigenvalues, also referred to as *infinite eigenvalue*, appears as leading eigenvalues when the eigenvalue problem is solved. As such, it is essential when computing the true leading eigenvalues that dictate the stability of a problem that the infinite eigenvalues be removed from the system of equations. This can be achieved by carrying out spectral transformation, in which the original problem is transformed into a new one in which the all the eigenvalues of the original problem are mapped to a new position while their eigenvectors remain the same. One of such transformations that mapped the infinite eigenvalues to zero is the shift-and-invert transformation [23]. Another transformation that is mathematically equivalent to the shift-and-invert is the Cayley transformation [61, 74]. For our analysis, we used the

shift-and-invert transformation. In this transformation, the original problem is transformed to

$$(\mathbf{J} - \upsilon\mathbf{B})^{-1}\,\mathbf{B}\mathbf{y} = \tau\mathbf{y} \tag{5.42}$$

where υ is a complex constant known as the shift; τ is the eigenvalue of the new problem and is related to the eigenvalue of the original problem β by

$$\tau = \frac{1}{(\beta - \upsilon)}$$

Essentially, the shift-and-invert method transforms the generalised eigenvalue problem into a simple eigenvalue problem by mapping the infinite eigenvalues to zero and the eigenvalues of the original problem that are closest to the shift value to be the leading ones. We solve the simple eigenvalue problem given by (5.42) using iterative Arnoldi method available in ARPACK [62], which can be used within FreeFem++. The accuracy of the converged leading eigenvalue is confirmed by ensuring that the residual

$$|\mathbf{J}\mathbf{y} - \beta\mathbf{B}\mathbf{y}|\,, \tag{5.43}$$

is always less than 1×10^{-10}.

5.3 Linear stability model validation

We test the validity of our linear stability analysis model and solution method by examining the stability of a spherical bubble of fixed volume in a stagnant liquid under the assumptions that the effects of gravity and boundaries are negligible, Figure 5.1.



Figure 5.1: Spherical bubble in stagnant liquid.

The bubble is stable under these conditions and the analytical solution to the problem has been studied in the literature [75, 95]. We compare our numerical results for the eigenvalues with the solution given in [95] for a small amplitude normal mode perturbations. The characteristic scales used for the non-dimensionalisation of the governing equations are

$$\text{Length} \quad L \tag{5.44a}$$

$$\text{Velocity} \quad \sqrt{\frac{\sigma}{\rho L}} \tag{5.44b}$$

$$\text{Presure} \quad \frac{\sigma}{L} \tag{5.44c}$$

With these scales the only dimensionless group that characterise the stability of the problem for the stated assumptions is the Ohnesorge number (Oh)and the modifications required to be made to the existing models (5.25)-(5.29), after neglecting all the gravity related terms, are the dimensionless groups given as

$$Nf = Oh; \quad Eo = 1 \tag{5.45}$$

where Oh is the Ohnesorge number define as

$$Oh = \frac{\mu}{\sqrt{\rho L \gamma}}$$

Analytical solution

Based on the dimensionless scales stated above, we derived the dimensionless form of the characteristic equation given as equation (45) in [95] as

$$\begin{aligned}&\left[\mathcal{H}^{(1)}_{m-\frac{1}{2}}(X^*)\right]\beta^2 + Oh\left[4m(m+2)^2 - 2(m+2)(2m+1)(\mathcal{H}^{(1)}_{m-\frac{1}{2}}(X^*)+2)\right]\beta \\ &+ (m+1)(m-1)(m+2)(\mathcal{H}^{(1)}_{m-\frac{1}{2}}(X^*)+2) = 0\end{aligned} \tag{5.46}$$

where

$$X^* = \left[\frac{\beta}{Oh}\right]^{\frac{1}{2}}$$

$$\mathcal{H}_n^{(1)}(\omega) = \frac{\omega H_{n+1}^{(1)}(\omega)}{H_n^{(1)}(\omega)}$$

In equation (5.46), m remains the eigenmode in the azimuthal direction; ω is a constant that equals the value of X^*; $\mathcal{H}$ is the quotient of the Hankel's functions.

For a fixed value of Oh, we solve iteratively for β . The initial guess used for the iterative solution is the dimensionless equivalent of equation (49) in [95], which is

$$\beta^2 - 2Oh\left[(n+2)(2n+1)\right]\beta + (n+1)(n-1)(n+2) = 0 \tag{5.47}$$

Once the solution for the first eigenvalue is gotten, we continuously used the β for the previous Oh as the initial guess for the next value of Oh. We implemented the solution steps in MATLAB and generated the analytical solution for Oh ranging between 0 and 1 based on $L = R$, the radius of the bubble.

Base state solution

At steady state, in the absence of gravity and since the liquid surrounding the bubble is stagnant ($\mathbf{u} = 0$), the continuous forms of the governing equations reduced to

$$-\nabla p = 0 \tag{5.48}$$

and the normal stress boundary condition to

$$-p + P_b = \kappa \text{ on } \Gamma_b \tag{5.49}$$

From equation (5.48), it implies the pressure field in the liquid phase surrounding the bubble is a constant,

$$p = P_a \tag{5.50}$$

and the bubble pressure becomes

$$Pb = \kappa + P_a \text{ on } \Gamma_b \tag{5.51}$$

where P_a is a constant and has the physical meaning of the dimensionless ambient pressure. For the linear stability analysis, the value of P_a was set to zero.

Linear stability solution

We solve the modified forms of the perturbation equations (5.25)-(5.29) as explained above using the base state solutions computed in the previous subsection with characteristic length scale of $L = 12.5R$. For the purpose of comparison, we scaled back our results to $L = R$. Figures 5.2 and 5.3 compare the real and imaginary parts of the eigenvalues computed, respectively, as a function of the Ohnesorge number, with the analytical solution of (5.46) for four different azimuthal wavenumbers. The agreement is very good for the four eigenmodes over the entire range of Ohnesorge number.

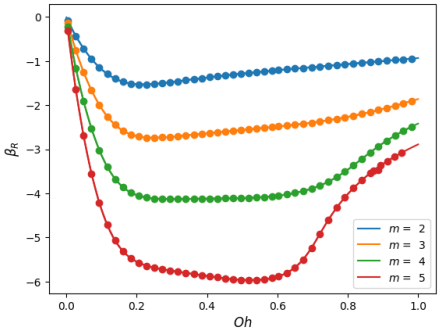


Figure 5.2: Comparison between amplification rate from analytical solution of equation (5.46) (coloured continuous solid line) and numerical global linear stability analysis (coloured markers), for modes m = 2, 3, 4 and 5.

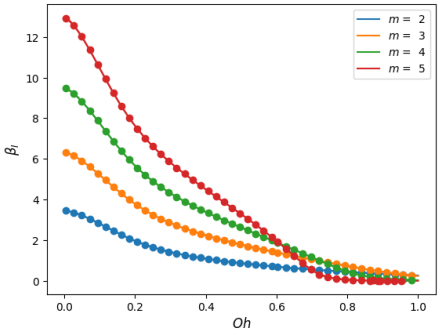
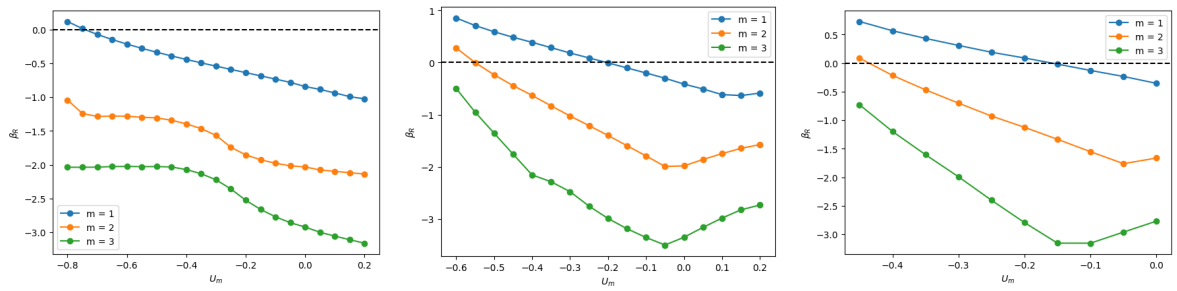


Figure 5.3: Comparison between oscillation frequency from analytical solution of equation (5.46) (coloured continuous solid line) and numerical global linear stability analysis (coloured markers), for modes m = 2, 3, 4 and 5.

5.4 Stability analysis of steady state solutions

5.4.1 Growth rate

The stability of Taylor bubble steady state solution for a given Nf, Eo and U_m to the addition of small perturbations is determined, as earlier noted, by the sign of the growth rate, the real part of the complex eigenvalue, β_R, when the generalised eigenvalue problem (5.30) is solved, as discussed in section 5.2. We considered five inverse viscosity numbers, $40, 60, 80, 100$ and 120 for which we have their steady state solutions computed under downwardly imposed flowing liquid, with emphasis placed on the first four Nf. Figure 5.4 shows the results for the growth rate when stability analysis was carried out on $Nf = 80$ for three different Eo as a function of U_m.

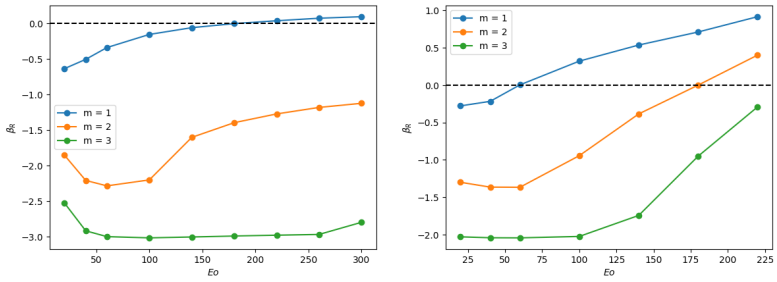


(a) (b) (c)

Figure 5.4: Largest growth rate for $Nf = 80$ as a function of tube center liquid velocity at (a) $Eo = 20$ (b) $Eo = 180$ (c) $Eo = 300$: showing results for $m = 1, 2$ and 3.

For the three Eötvös numbers, the most unstable mode is $m = 1$, which physically is the mode that deflects the bubble sideways, off from the axis of the symmetry. The mode becomes unstable at liquid velocity that is in the intervals $[-0.75, -0.70)$, $[-0.25, -0.20)$ and $[-0.20, -0.15)$ for $Eo = 20$, 180 and 300, respectively. The magnitude of U_m at which the bubble becomes unstable decreases with increased Eötvös number and the reason for this lies in the stabilisation effect of surface tension which decreases as Eo is increased. For the entire Eo investigated, Figure 5.5 shows the influence of Eo on the onset of instability at fixed U_m for the same Nf. It is noteworthy that in Figures 5.4 and 5.5, and the subsequent figures to be presented, the growth rate for mode $m = 0$ is not shown. For virtually all the conditions considered in the

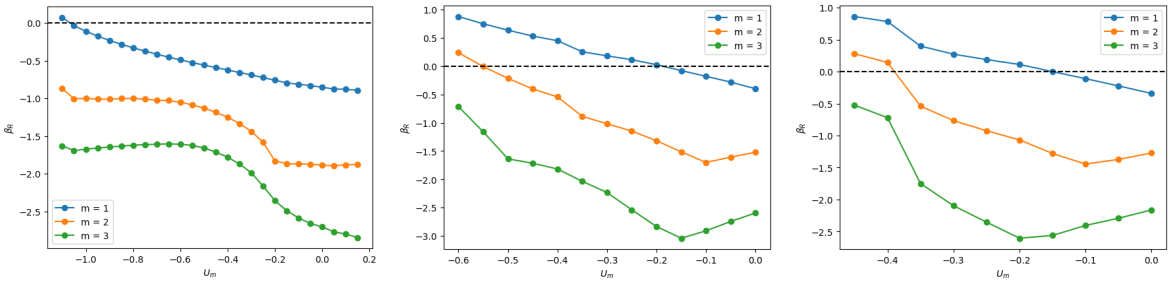
analysis, the growth rate for the mode is negative. Only a few cases, for which we assumed that it is due to numerical errors, we recorded positive growth rate of very small magnitude.



(a) (b)

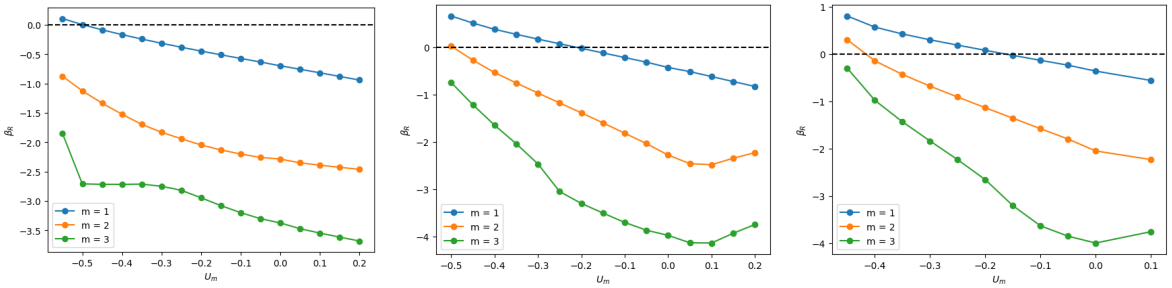
Figure 5.5: Largest growth rate for $Nf = 80$ as a function of Eötvös number at (a) $U_m = -0.20$ (b) $U_m = -0.55$: showing results for $m = 1, 2$ and 3.

To account for the effect of Nf, we show similar results to Figure 5.4 for $Nf = 100$ and $Nf = 60$ in Figures 5.6 and 5.7, respectively.



(a) (b) (c)

Figure 5.6: Largest growth rate for $Nf = 100$ as a function of tube center liquid velocity at (a) $Eo = 20$ (b) $Eo = 180$ (c) $Eo = 300$: showing results for $m = 1, 2$ and 3.



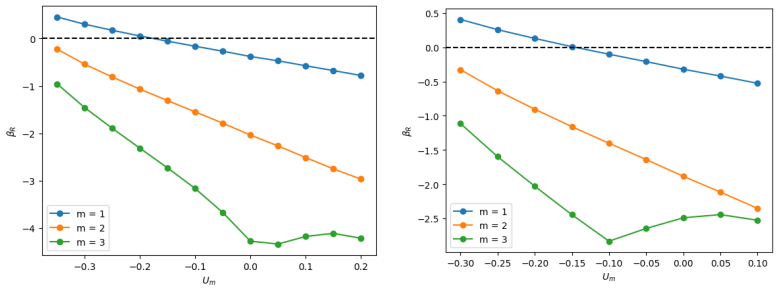
(a) (b) (c)

Figure 5.7: Largest growth rate for $Nf = 60$ as a function of tube center liquid velocity at (a) $Eo = 20$ (b) $Eo = 180$ (c) $Eo = 300$: showing results for $m = 1, 2$ and 3.

It is evident that the effect of Nf on the onset of instability for $Eo = 180$ and $Eo = 300$ is different from that of $Eo = 20$. For $Eo = 180$ and $Eo = 300$, the general trend is that as the inverse viscosity number is increased, the tendency of the bubble to become easily unstable increased, although the effect appears marginal. The U_m interval for the onset of instability for $Eo = 180$ are $[-0.25, -0.20)$, $[-0.25, -0.20)$ and $[-0.20, -0.15)$ and for $Eo = 300$ are $[-0.20, -0.15)$, $[-0.20, -0.15)$ and $[-0.20, -0.15)$, when $Nf = 60, 80$ and 100, respectively. Our result for $Nf = 120$ confirmed the decreasing trend of the magnitude of U_m at which the bubble becomes unstable for $Eo = 300$ as it showed that the interval decreased to $[-0.15, -0.10)$. It thus means that although the magnitude of U_m for the onset of instability decreases with Nf, the effect becomes negligibly small as Eo is increased.

In contrast to the effect of Nf at higher Eo, the trend for $Eo = 20$ is exactly the opposite; the tendency for the bubble to become unstable decreases as inverse viscosity number is increased. Taking into consideration all our results for $Nf \geq 60$ for all Eo ranging between 20 and 300, the limit of Eo at which the influence of increasing inverse viscosity number on the onset of instability have opposite effects is in interval $(60, 100)$. This limit is in agreement with our steady state numerical simulations where we observed that the limit of strong influence of surface tension on almost all steady state features examined was 100.

It is noteworthy that our analysis for $Nf \leq 60$, more specifically, $Nf = 40$ does not conform with the aforementioned trend for $Eo \geq 100$. We observed that the magnitude of U_m at which the bubble become unstable for $Nf = 40$ is lower relative to higher Nf. Our results for $Nf = 40$ for $Eo = 180$ and $Eo = 300$ are shown in Figure 5.8 in which the intervals for the onset of instability are $[-0.20, -0.15)$ and $[-0.15, -0.10)$, respectively. This may be related to the influence of Nf on the frontal radius of curvature as the lost in axisymmetric bubble shape, signified by mode $m = 1$, is more about the bubble nose than any other region around the bubble. We had earlier noted from our steady state results for normalised frontal radius of curvature in stagnant liquid, shown in Figure 4.15, that it appears the limit of strong influence of viscosity on bubble radius of curvature is $Nf \leq 60$.



(a) (b)

Figure 5.8: Largest growth rate for $Nf = 40$ as a function of tube center liquid velocity at (a) $Eo = 180$ (b) $Eo = 300$: showing results for $m = 1, 2$ and 3.

5.4.2 Asymmetric bubble shapes

For all the analysis carried out, the complex eigenvalues obtained are generally real, the magnitude of the imaginary part being of order 10^{-10}. From (5.4), (5.17) and (5.22c), for every points on the three-dimensional axisymmetric base state interface with position vector (r^0, θ^0, z^0) in cylindrical coordinates, the corresponding deformed interface points in Cartesian coordinates are constructed using the expressions:

$$x = r^0 cos\left(\theta^0\right) + \epsilon\left[h_R n_r cos\left(m\theta^0\right) - h_I n_r sin\left(m\theta^0\right)\right] cos\left(\theta^0\right) \quad \forall\, \theta^0 \in [0, 360] \tag{5.52a}$$

$$y = r^0 sin\left(\theta^0\right) + \epsilon\left[h_R n_r cos\left(m\theta^0\right) - h_I n_r sin\left(m\theta^0\right)\right] sin\left(\theta^0\right) \quad \forall\, \theta^0 \in [0, 360] \tag{5.52b}$$

$$z = z^0 + \epsilon\left[h_R n_z cos\left(m\theta^0\right) - h_I n_z sin\left(m\theta^0\right)\right] \quad \forall\, \theta^0 \in [0, 360] \tag{5.52c}$$

where h_R and h_I denote the real and imaginary parts of the magnitude of the interface deformation in the normal direction; n_r and n_z remain the radial and axial components of the unit normal to the base state interface, respectively; m, as earlier defined is the wavenumber in the azimuthal direction; ϵ is a small arbitrary constant that signifies the size of the perturbation.

In the following, we show the effects of tube center velocity, Eötvös number and inverse viscosity number on the deformed three-dimensional bubble shapes for mode $m = 1$ taking the value of $\epsilon = 0.05$. Where applicable, for the conditions shown, we show the corresponding deformed bubble shape when $m = 2$. In general, increased tube center velocity and Eötvös

number lead to increased deformation of the interface of the asymmetric Taylor bubble. For inverse viscosity number, we observed similar increased deformation when Nf is increased and decreased beyond $Nf = 80$.

Effect of tube center velocity

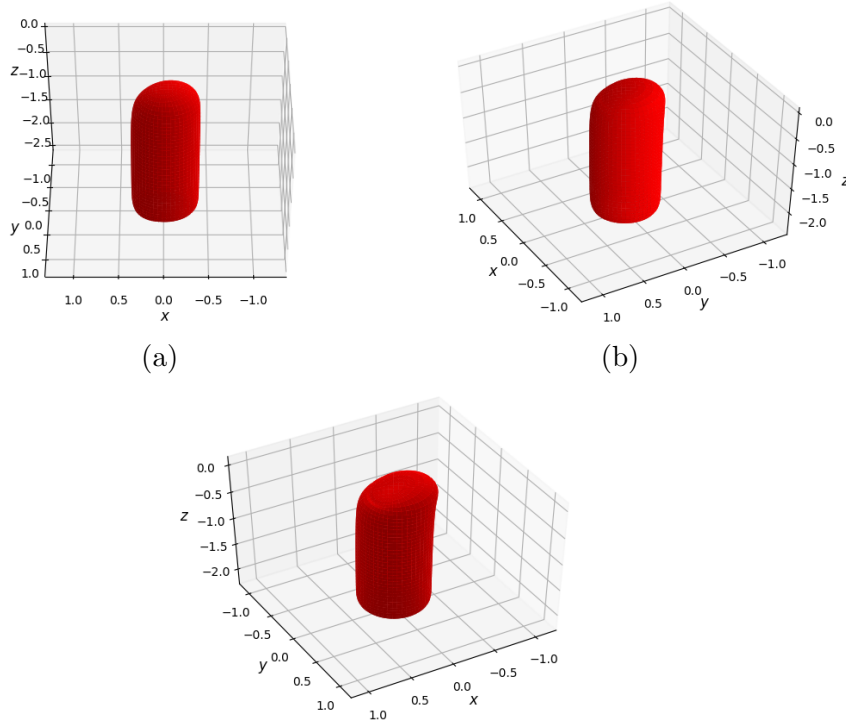


Figure 5.9: Deformed bubble shape for $Nf = 100$ and $Eo = 220$ at (a) $U_m = -0.25$ (b) $U_m = -0.40$ (c) $U_m = -0.55$ when $m = 1$.

The only condition shown in Figure 5.9 for which mode $m = 2$ is unstable is shown in Figure 5.10.

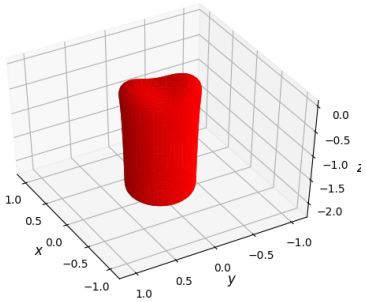


Figure 5.10: Deformed bubble shape for $Nf = 100$ and $Eo = 220$ at $U_m = -0.55$ when $m = 2$.

Effect of Eötvös number

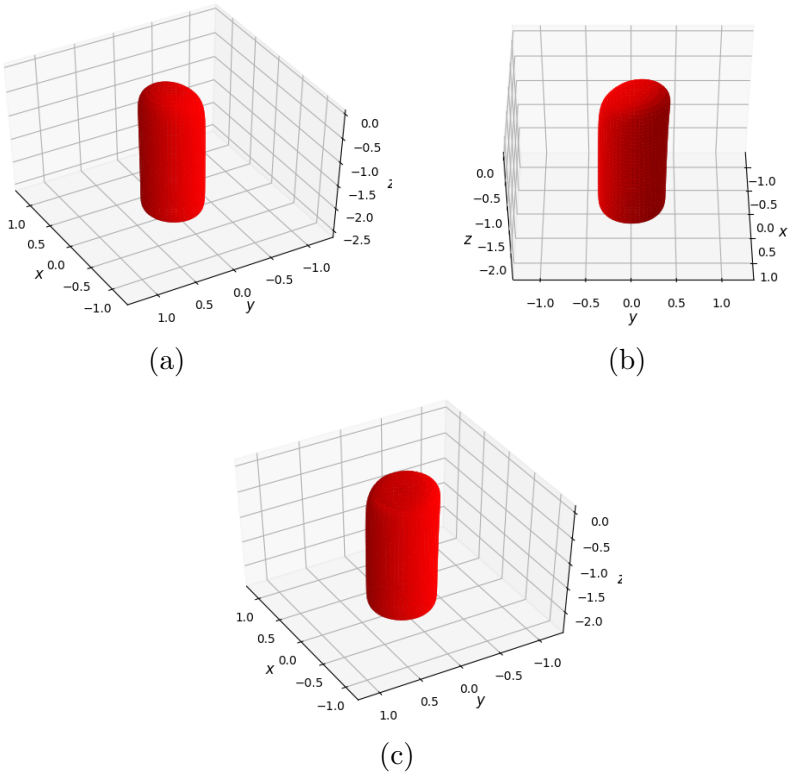


Figure 5.11: Deformed bubble shape for $Nf = 80$ and $U_m = -0.50$ at (a) $Eo = 100$ (b) $Eo = 180$ (c) $Eo = 260$ when $m = 1$.

The only condition shown in Figure 5.11 for which mode $m = 2$ is unstable is shown in Figure 5.10.

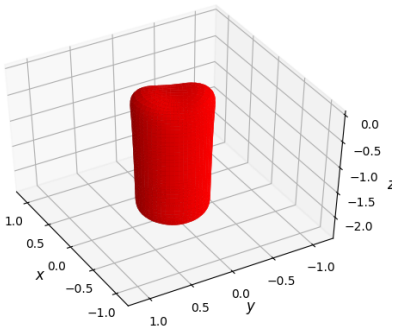
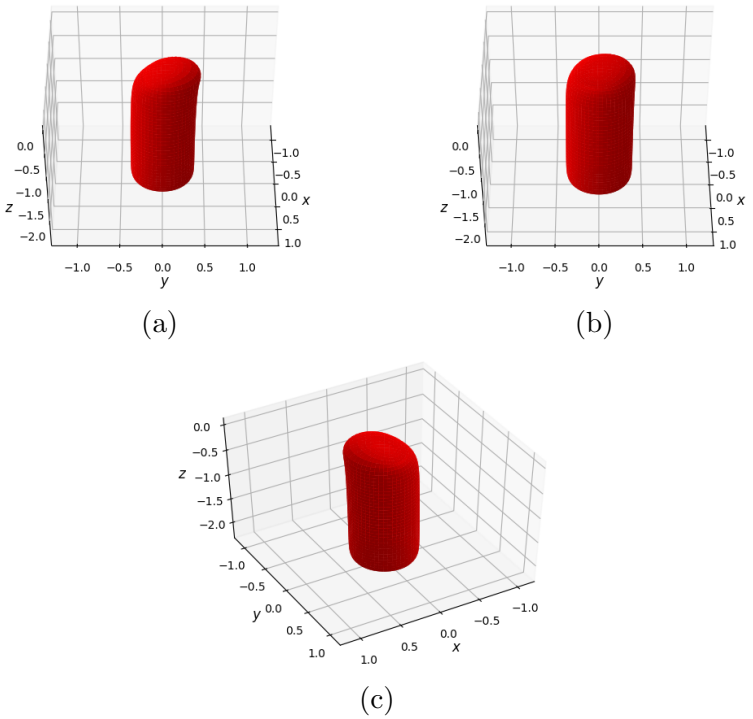


Figure 5.12: Deformed bubble shape for $Nf = 80$ and $U_m = -0.50$ at $Eo = 260$ when $m = 2$.

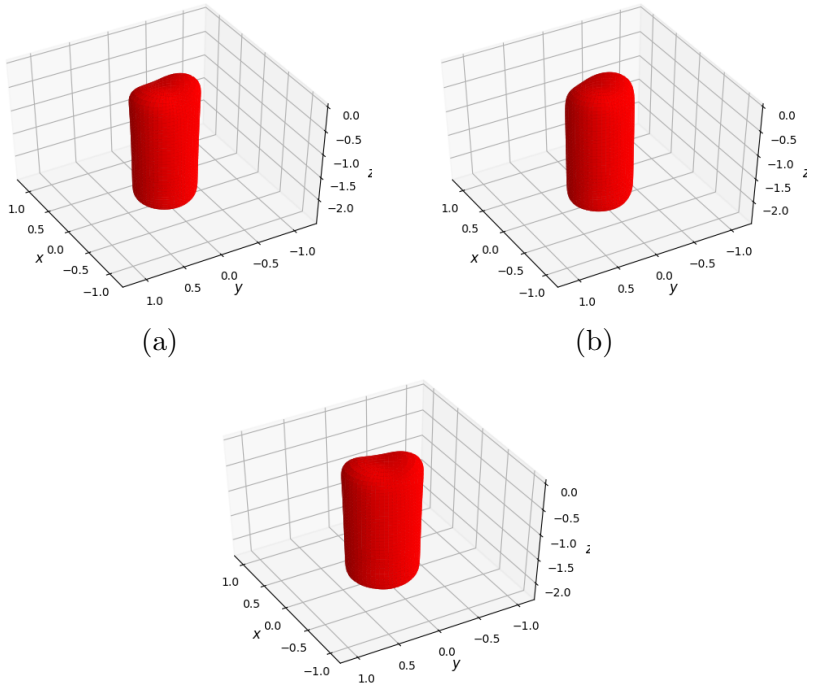
Effect of inverse viscosity number



(a) (b)

(c)

Figure 5.13: Deformed bubble shape for $Eo = 300$ and $U_m = -0.45$ at (a) $Nf = 60$ (b) $Nf = 80$ (c) $Nf = 100$ when $m = 1$.



(a) (b)

(c)

Figure 5.14: Deformed bubble shape for $Eo = 300$ and $U_m = -0.45$ at (a) $Nf = 60$ (b) $Nf = 80$ (c) $Nf = 100$ when $m = 2$.

5.4.3 Instability map

Using the results for the growth rate and the bubble shape discussed in sections 5.4.1 and 5.4.2, we draw up maps for the different Nf investigated, showing the boundary demarcating regions where symmetric and asymmetric Taylor bubbles can be observed for downward liquid flow condition, as a function of Eo. Figure 5.15 shows the instability regime maps for our linear analysis.

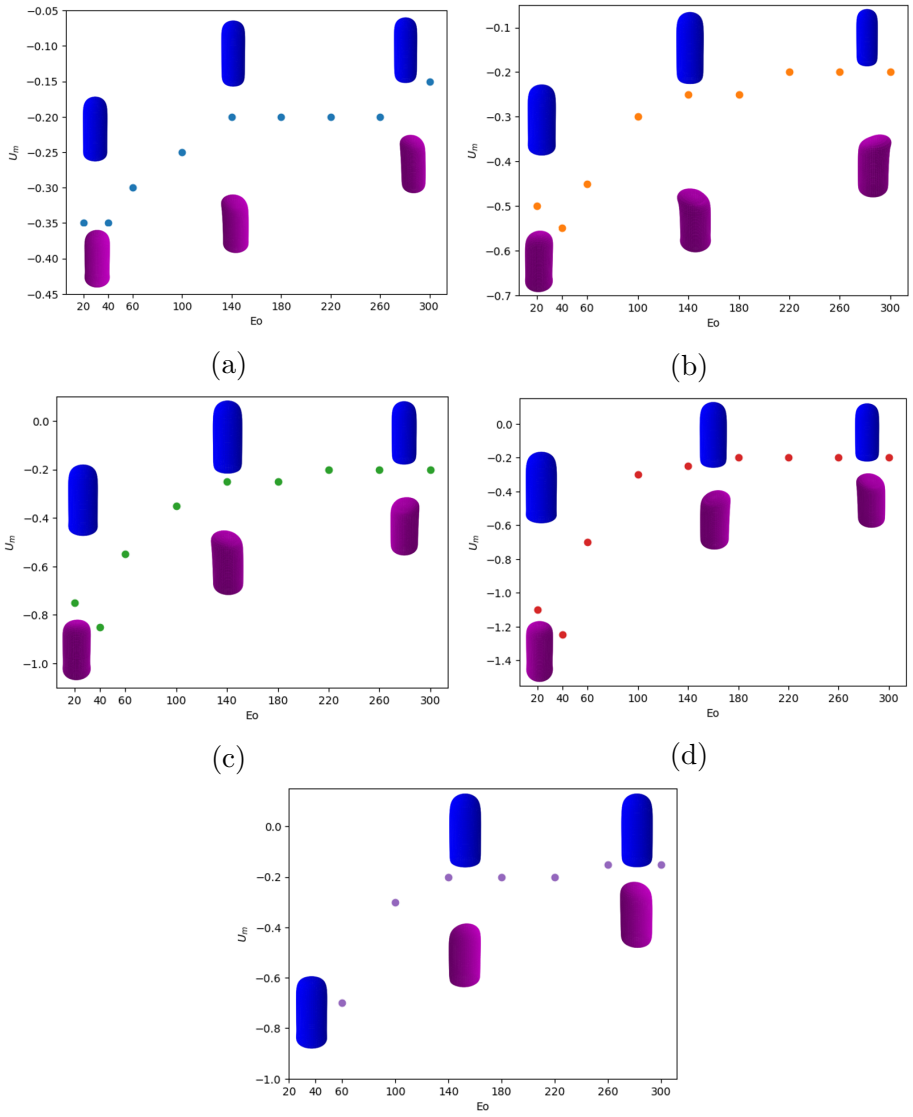


Figure 5.15: Instability showing the onset of transition to asymmetric bubble shape in downward liquid flow for (a) $Nf = 40$ (b) $Nf = 60$ (c) $Nf = 80$ (c) $Nf = 100$ (e) $Nf = 120$.

An interesting feature about the stability maps shown in Figure 5.15 is the striking resemblance

to the results of normalised frontal radius for stagnant liquid shown in Figure 4.15. The results therefore shows that the onset of instability may be related to the normalised radius of curvature of the nose.

We show in Table 5.1 the results for the bubble rise velocity at the onset of instability for the space of dimensionless parameters investigated. It is noticeable that for certain range of Eo, for any given Nf, the bubble has positive rise velocity at the onset of transition. This means that, physically, it is impossible to obtain an axisymmetric downward flowing Taylor bubble in vertical pipes under such conditions; i.e before the axisymmetric Taylor bubble begins to move downward, it would have transitioned to asymmetric bubble. Experimental investigations have shown that it is possible for a Taylor bubble to be held stationary in pipe. For the inverse viscosity numbers investigated, the critical conditions of Eo at which this can be observed lies in the interval $(100, 140]$ and $(60, 100]$ for $Nf \leq 80$ and $Nf > 80$, respectively. Below the lower bound of the critical condition, it is possible to observe both axisymmetric stationary and downward falling Taylor bubbles. For $Nf = 6087.38$ and $Eo = 33.06$, a stable axisymmetric Taylor bubble was shown to have being held stationary in downward liquid flow by [80], which falls within the range of our analysis results.

Table 5.1: Bubble rise velocity at the onset of transition to asymmetric Taylor bubble: effect of inverse viscosity and Eötvös numbers.

Nf		40		60		80		100		120	
		$-U_m^*$	U_b	$-U_m^*$	U_b	$-U_m^*$	U_b	$-U_m^*$	U_b	$-U_m^*$	U_b
Eo	20	0.35	−0.1946	0.50	−0.2621	0.75	−0.4172	1.10	−0.6479		
	40	0.35	−0.1445	0.55	−0.2509	0.85	−0.4422	1.25	−0.7033		
	60	0.30	−0.0823	0.45	−0.1537	0.55	−0.1938	0.65	−0.4393	0.70	−0.2613
	100	0.25	−0.0257	0.30	−0.0168	0.35	−0.0352	0.30	0.0300	0.30	0.0404
	140	0.20	0.0284	0.25	0.0292	0.25	0.0551	0.25	0.0690	0.20	0.1234
	180	0.20	0.0287	0.25	0.0274	0.25	0.0521	0.20	0.1128	0.20	0.1218
	220	0.20	0.0287	0.20	0.0767	0.20	0.0989	0.20	0.1109	0.20	0.1206
	260	0.20	0.0284	0.20	0.0760	0.20	0.0978	0.20	0.1094	0.15	0.1654
	300	0.15	0.0838	0.20	0.0754	0.20	0.0969	0.20	0.1082	0.15	0.1645

Where U_m^* is the value of U_m at the onset of instability.

5.5 Energy budget analysis

In section 5.4, we have examined the stability of the steady state solutions to the additional of small perturbations and determined the effect of the model dimensionless parameters on the onset of transition to asymmetric Taylor bubble. However, this analysis does not provide insight into the mechanism that drives the instability. A way to do this is to analyse how energy is being transferred from the base flow to the disturbed flow by studying the growth of the kinetic energy of the disturbances [54, 56]. This is based on the fact that an unstable disturbed flow implies that the kinetic energy of an initially small disturbance added to the flow grows with time. Thus, by investigating the contribution of mechanisms of different physical origins that account for the production of this energy, one can identify the most dominant one that drives the instability [12]. This concept has been well used in studying the mechanism governing the instabilities of parallel two-phase flows [83, 100, 101, 103] and in [12] it was used in classifying the instabilities in these flows into five different groups.

5.5.1 Energy balance model

To derive the equation that governs the growth of the disturbance kinetic energy, the classical approach is to multiply the continuous forms of the momentum perturbation equations for the velocity components with their corresponding complex conjugates of the perturbations velocities, integrate over the domain, add the three resulting equations and finally simplify the added equations. Considering that our perturbation equations for the velocity components were derived from the weak form of the continuous momentum equations written around the perturbed domain, the development of the weak form of the energy equation must follow the same strategy. In fact, we can derive the energy equation from the derived perturbation equations for the velocity components by setting the test functions for the velocity components in

the equations to equal the complex conjugate of the velocity perturbations

$$\bar{\Phi}_r = \hat{u}_r^* \tag{5.53a}$$

$$\bar{\Phi}_\theta = \hat{u}_\theta^* \tag{5.53b}$$

$$\bar{\Phi}_z = \hat{u}_z^* \tag{5.53c}$$

and then carry out necessary simplifications. This is because we have chosen the test functions to be of similar forms as the velocity components and in deriving the perturbation equations, we used the complex conjugates of the test functions in the inner product. Carrying out the substitutions, we have

$$\begin{aligned}
&\beta \int_{\Omega^0} \left\{ |\hat{u}_r|^2 + |\hat{u}_\theta|^2 + |\hat{u}_z|^2 \right\} d\Omega^0 \\
&+ \int_{\Omega^0} \left\{ |\hat{u}_r|^2 \frac{\partial u_r^0}{\partial r^0} + |\hat{u}_z|^2 \frac{\partial u_z^0}{\partial z} + \frac{|\hat{u}_\theta|^2 u_r^0}{r} + \left(\frac{\partial u_r^0}{\partial z} + \frac{\partial u_z^0}{\partial r^0} \right) \mathbb{R}\left\{ \hat{u}_r \hat{u}_z^* \right\} \right\} d\Omega^0 \\
&+ \int_{\Omega} Nf^{-1} \left\{ 2 \left| \frac{\partial \hat{u}_r}{\partial r} \right|^2 + 2 \left| \frac{\partial \hat{u}_z}{\partial z} \right|^2 + \frac{1}{r^2} \left[\left(2 + m^2\right) |\hat{u}_r|^2 + \left(1 + 2m^2\right) |\hat{u}_\theta|^2 + m^2 |\hat{u}_z|^2 \right] + \left| \frac{\partial \hat{u}_\theta}{\partial r} \right|^2 \right. \\
&\left. + \left| \frac{\partial \hat{u}_\theta}{\partial z} \right|^2 + \left| \frac{\partial \hat{u}_r}{\partial z} + \frac{\partial \hat{u}_z}{\partial r} \right|^2 - \frac{1}{r} \frac{\partial |\hat{u}_\theta|^2}{\partial r} + \frac{6m}{r^2} \mathbb{I}m\left\{ \hat{u}_r \hat{u}_\theta^* \right\} + \frac{2m}{r} \mathbb{I}m\left(\hat{u}_z^* \frac{\partial \hat{u}_\theta}{\partial z} + \hat{u}_r^* \frac{\partial \hat{u}_\theta}{\partial r} \right) \right\} d\Omega^0 \\
&- \int_{\Gamma_b^0} Eo^{-1} \left\{ -\frac{d\hat{h}}{ds} \left[\mathbf{n} \cdot \frac{d\hat{\mathbf{u}}^*}{ds} - \kappa_a \left(\mathbf{t} \cdot \hat{\mathbf{u}}^* \right) \right] + \hat{h} \left[\kappa_a^2 + \kappa_b^2 - \frac{m^2}{r^2} \right] \mathbf{n} \cdot \hat{\mathbf{u}}^* \right\} d\Gamma_b^0 \\
&- \int_{\Gamma_b^0} \left\{ \hat{h} n_z \left(\mathbf{n} \cdot \hat{\mathbf{u}}^* \right) \right\} d\Gamma_b^0 \\
&+ \int_{\Gamma_b^0} \hat{h} \left\{ \left(\mathbf{u}^0 \cdot \mathbf{t} \right) \left[\frac{d\mathbf{u}^0}{ds} \cdot \hat{\mathbf{u}}^* \right] + \left[-p^0 + 2Nf^{-1} \left(\mathbf{t} \cdot \frac{d\mathbf{u}^0}{ds} \right) \right] \left(\mathbf{t} \cdot \frac{d\hat{\mathbf{u}}^*}{ds} \right) \right. \\
&\left. + \left[-p^0 + 2Nf^{-1} \frac{u_r^0}{r} \right] \left(\frac{\hat{u}_r^*}{r} - \mathbf{i}m \frac{\hat{u}_\theta^*}{r} \right) \right\} d\Gamma_b^0 \\
&+ \int_{\Gamma_b^0} \left\{ \left[Eo^{-1} \kappa + z - P_b^0 \right] \left[\left(\mathbf{t} \cdot \hat{\mathbf{u}}^* \right) \frac{d\hat{h}}{ds} + \hat{h} \left(\mathbf{i}m \frac{\hat{u}_\theta^*}{r} \right) + \hat{h} \kappa \left(\mathbf{n} \cdot \hat{\mathbf{u}}^* \right) \right] \right\} d\Gamma_b^0 = 0
\end{aligned} \tag{5.54}$$

Here the symbol $|.|$ represents the magnitude of a complex function; $\mathbb{R}$ and $\mathbb{I}$ denote the real and imaginary part of a complex function, respectively. Equation (5.54) is the energy budget formulation that governs the evolution of the disturbance kinetic equation, as each term in the equation denotes some kind of energy.

Because the stability of the flow is govern by the real part of the eigenvalue, following [12], we separate the energy terms and write the energy balance equation as

$$\dot{E} = REY + DIS + INT \tag{5.55a}$$

$$INT = NOR + TAN \tag{5.55b}$$

$$NOR = TEN + HYD + BUB \tag{5.55c}$$

and the expressions for the terms are

$$\dot{E} = \beta_R \int_{\Omega^0} \left\{ |\hat{u}_r|^2 + |\hat{u}_\theta|^2 + |\hat{u}_z|^2 \right\} d\Omega^0 \tag{5.56}$$

$$REY = -\int_{\Omega^0} \left\{ |\hat{u}_r|^2 \frac{\partial u_r^0}{\partial r^0} + |\hat{u}_z|^2 \frac{\partial u_z^0}{\partial z} + \frac{|\hat{u}_\theta|^2 u_r^0}{r} + \left(\frac{\partial u_r^0}{\partial z} + \frac{\partial u_z^0}{\partial r^0} \right) \mathbb{R}\left\{ \hat{u}_r \hat{u}_z^* \right\} \right\} d\Omega^0 \tag{5.57}$$

$$\begin{aligned} DIS = -\int_{\Omega} Nf^{-1} \Bigg\{ & 2 \left| \frac{\partial \hat{u}_r}{\partial r} \right|^2 + 2 \left| \frac{\partial \hat{u}_z}{\partial z} \right|^2 + \frac{1}{r^2} \left[\left(2 + m^2\right) |\hat{u}_r|^2 + \left(1 + 2m^2\right) |\hat{u}_\theta|^2 + m^2 |\hat{u}_z|^2 \right] + \left| \frac{\partial \hat{u}_\theta}{\partial r} \right|^2 \\ & + \left| \frac{\partial \hat{u}_\theta}{\partial z} \right|^2 + \left| \frac{\partial \hat{u}_r}{\partial z} + \frac{\partial \hat{u}_z}{\partial r} \right|^2 - \frac{1}{r} \frac{\partial |\hat{u}_\theta|^2}{\partial r} + \frac{6m}{r^2} \mathbb{I}m\left\{ \hat{u}_r \hat{u}_\theta^* \right\} + \frac{2m}{r} \mathbb{I}m\left(\hat{u}_z^* \frac{\partial \hat{u}_\theta}{\partial z} + \hat{u}_r^* \frac{\partial \hat{u}_\theta}{\partial r} \right) \Bigg\} d\Omega \end{aligned} \tag{5.58}$$

$$\begin{aligned} TAN = & \mathbb{R} \Bigg\{ -\int_{\Gamma_b^0} \hat{h} \Bigg\{ \left(\mathbf{u}^0 \cdot \mathbf{t} \right) \left[\frac{d\mathbf{u}^0}{ds} \cdot \hat{\mathbf{u}}^* \right] + \left[-p^0 + 2Nf^{-1} \left(\mathbf{t} \cdot \frac{d\mathbf{u}^0}{ds} \right) \right] \left(\mathbf{t} \cdot \frac{d\hat{\mathbf{u}}^*}{ds} \right) \\ & + \left[-p^0 + 2Nf^{-1} \frac{u_r^0}{r} \right] \left(\frac{\hat{u}_r^*}{r} - \mathbb{i}m \frac{\hat{u}_\theta^*}{r} \right) \Bigg\} d\Gamma_b^0 \Bigg\} + \int_{\Gamma_b^0} Eo^{-1} \left\{ \frac{d\hat{h}}{ds} \left[\kappa_a \left(\mathbf{t} \cdot \hat{\mathbf{u}}^* \right) \right] \right\} d\Gamma_b^0 \\ & - \int_{\Gamma_b^0} \left\{ \left[Eo^{-1}\kappa + z - P_b^0 \right] \left[\left(\mathbf{t} \cdot \hat{\mathbf{u}}^* \right) \frac{d\hat{h}}{ds} + \hat{h} \left(\mathbb{i}m \frac{\hat{u}_\theta^*}{r} \right) \right] \right\} d\Gamma_b^0 \Bigg\} \end{aligned} \tag{5.59}$$

$$NOR = \mathbb{R}\left\{\int_{\Gamma_b^0} Eo^{-1}\left\{-\frac{d\hat{h}}{ds}\left[\mathbf{n}\cdot\frac{d\hat{\mathbf{u}}^*}{ds}\right]+\hat{h}\left[\kappa_a^2+\kappa_b^2-\frac{m^2}{r^2}\right]\mathbf{n}\cdot\hat{\mathbf{u}}^*\right\}d\Gamma_b^0+\int_{\Gamma_b^0}\left\{\hat{h}n_z\left(\mathbf{n}\cdot\hat{\mathbf{u}}^*\right)\right\}d\Gamma_b^0 - \int_{\Gamma_b^0}\left\{\left[Eo^{-1}\kappa+z-P_b^0\right]\left[\hat{h}\kappa\left(\mathbf{n}\cdot\hat{\mathbf{u}}^*\right)\right]\right\}d\Gamma_b^0\right\} \tag{5.60}$$

$$TEN = \mathbb{R}\left\{\int_{\Gamma_b^0} Eo^{-1}\left\{-\frac{d\hat{h}}{ds}\left[\mathbf{n}\cdot\frac{d\hat{\mathbf{u}}^*}{ds}\right]+\hat{h}\left[\kappa_a^2+\kappa_b^2-\kappa^2-\frac{m^2}{r^2}\right]\mathbf{n}\cdot\hat{\mathbf{u}}^*\right\}d\Gamma_b^0\right\} \tag{5.61}$$

$$HYD = \mathbb{R}\left\{\int_{\Gamma_b^0}\left\{\hat{h}\left(n_z-z\kappa\right)\left(\mathbf{n}\cdot\hat{\mathbf{u}}^*\right)\right\}d\Gamma_b^0\right\} \tag{5.62}$$

$$BUB = \mathbb{R}\left\{\int_{\Gamma_b^0}\left\{P_b^0\left[\hat{h}\kappa\left(\mathbf{n}\cdot\hat{\mathbf{u}}^*\right)\right]\right\}d\Gamma_b^0\right\} \tag{5.63}$$

Where KIN represents the time rate of change in the disturbance kinetic energy, with the time derivative captured in the factor β_R, which for an unstable flow is positive; REY denotes the rate of transfer of energy by the Reynolds stress from the base flow to the disturbed flow; DIS represents the rate of viscous dissipation of energy of disturbed flow; The rate of work done by the velocity and stress disturbances in deforming the interface is denoted by INT, and can be decomposed into its normal, NOR and tangential TAN components. The normal work done at the interface is further subdivided into TEN, HYD and BUB, representing work done at the interface against interface tension, gravity and bubble pressure, respectively.

We scaled all the energy terms using KIN, so that the energy balance equation becomes

$$\beta_R = REY^* + DIS^* + TEN^* + HYD^* + BUB^* + TAN^* \tag{5.64}$$

where $ff^* \quad \forall\ ff\ \in\ \{REY, DIS, TEN, HYD, BUB, TAN\}$ denote the scaled energy terms, given as

$$ff^* = \frac{ff}{KIN} \quad \forall\ ff\ \in\ \{REY, DIS, TEN, HYD, BUB, TAN\} \tag{5.65}$$

Thus, indicating that the growth rate must equal the sum of all the scaled energy terms on the right hand side. We confirm the validity of the derived relation by quantifying all the energy terms and examining whether the energy balances. Table 5.2 shows our result for $Nf = 80$

and $Eo = 140$ at three different downward liquid flow velocities. For brevity, we dropped the asterisk power on the energy terms.

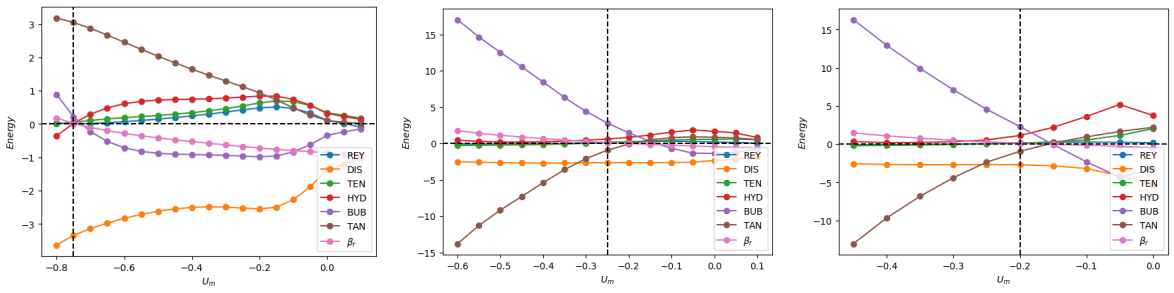
Table 5.2: Balance of energy distribution among the different energy terms in (5.64) for $Nf = 80$, $Eo = 140$ and mode, $m = 1$.

U_m	β_R	REY	DIS	TEN	HYD	BUB	TAN	SUM	DIF
-0.10	-0.2442	0.3260	-2.6008	0.5245	1.2070	-0.5126	0.8117	-0.2442	2.230×10^{-6}
0.00	-0.4474	0.2269	-2.1745	0.5412	1.1340	-0.9108	0.7358	-0.4473	1.398×10^{-5}
0.10	-0.6404	0.0413	-1.6299	0.4210	0.6429	-0.5639	0.4481	-0.6404	-7.672×10^{-6}

The difference between the growth rate, β_R computed from linear stability analysis and the sum of the energy terms on the right hand side of (5.64), SUM, denoted as DIF in Table 5.2 is reasonably small.

5.5.2 Energy analysis of linear stability results

From the linear analysis results presented in section 5.4, the most unstable mode in downward liquid flow is $m = 1$. Here, we examine the contribution of each of the energy terms in (5.64) in order to understand their roles in driving the bubble towards asymmetric shape and identify the most dominant of them. For ease of comparison, we show the energy results for similar conditions presented in section 5.4. In Figure 5.16, the energy results for $Nf = 80$ when $Eo = 20, 180$ and 300 are shown.



(a) (b) (c)

Figure 5.16: Energy analysis for $Nf = 80$ as a function of tube center liquid velocity at (a) $Eo = 20$ (b) $Eo = 180$ (c) $Eo = 300$ when $m = 1$. The point where β_R first become positive, marking the onset of asymmetric bubble is indicated by the black vertical dashed lines.

For Eo of 180 and 300, the most dominant energy term is the normal component of the interface energy due to bubble pressure. That the most dominant energy is supplied by bubble pressure indicates that the origin of the instability is in the gas phase. On the other hand, the largest energy term when $Eo = 20$ is that due to tangential component of the interface energy. To probe the tangential energy component further, we split the energy term, (5.59), into different components based on the base state group that supplies energy to the tangential perturbations.

$$TAN_{ut} = \mathbb{R}\left\{-\int_{\Gamma_b^0} \hat{h}\big(\mathbf{u}^0\cdot\mathbf{t}\big)\left[\frac{d\mathbf{u}^0}{ds}\cdot\hat{\mathbf{u}}^*\right]\right\} \tag{5.66a}$$

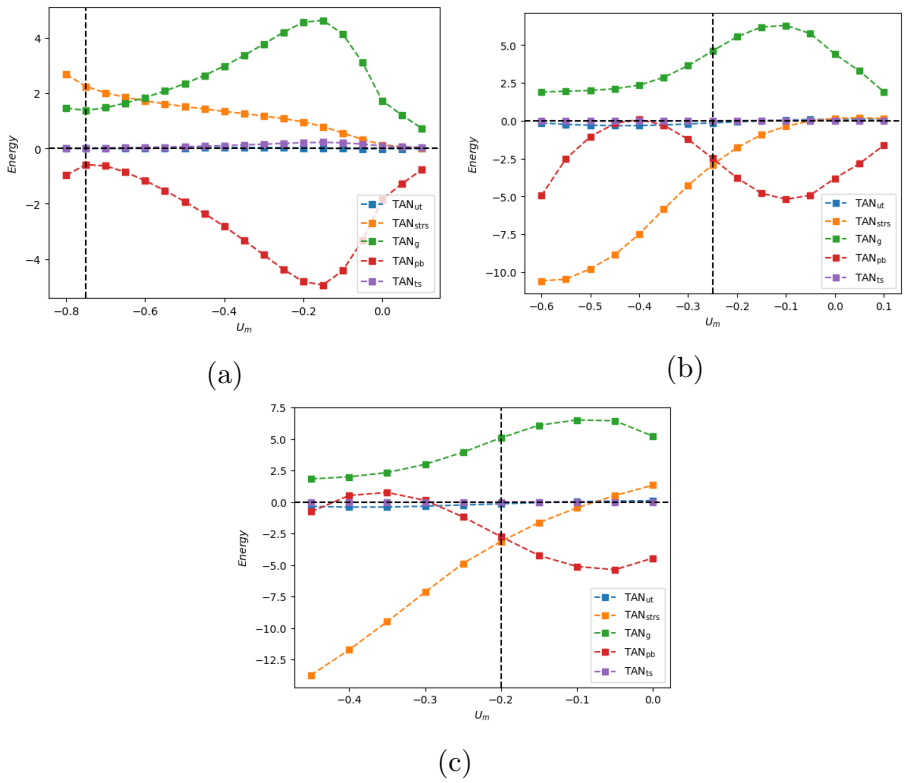
$$TAN_{strs} = \mathbb{R}\left\{-\int_{\Gamma_b^0} \hat{h}\left\{\left[-p^0 + 2Nf^{-1}\left(\mathbf{t}\cdot\frac{d\mathbf{u}^0}{ds}\right)\right]\left(\mathbf{t}\cdot\frac{d\hat{\mathbf{u}}^*}{ds}\right) + \left[-p^0 + 2Nf^{-1}\frac{u_r^0}{r}\right]\left(\frac{\hat{u}_r^*}{r} - \mathrm{i}m\frac{\hat{u}_\theta^*}{r}\right)\right\}\right\} \tag{5.66b}$$

$$TAN_{ts} = \mathbb{R}\left\{\int_{\Gamma_b^0} Eo^{-1}\left\{\frac{d\hat{h}}{ds}\left[\kappa_a\left(\mathbf{t}\cdot\hat{\mathbf{u}}^*\right)\right] - \kappa\left[\left(\mathbf{t}\cdot\hat{\mathbf{u}}^*\right)\frac{d\hat{h}}{ds} + \hat{h}\left(\mathrm{i}m\frac{\hat{u}_\theta^*}{r}\right)\right]\right\} d\Gamma_b^0\right\} \tag{5.66c}$$

$$TAN_g = \mathbb{R}\left\{\int_{\Gamma_b^0} -z\left[\left(\mathbf{t}\cdot\hat{\mathbf{u}}^*\right)\frac{d\hat{h}}{ds} + \hat{h}\left(\mathrm{i}m\frac{\hat{u}_\theta^*}{r}\right)\right] d\Gamma_b^0\right\} \tag{5.66d}$$

$$TAN_{pb} = \mathbb{R}\left\{\int_{\Gamma_b^0} P_b\left[\left(\mathbf{t}\cdot\hat{\mathbf{u}}^*\right)\frac{d\hat{h}}{ds} + \hat{h}\left(\mathrm{i}m\frac{\hat{u}_\theta^*}{r}\right)\right] d\Gamma_b^0\right\} \tag{5.66e}$$

The terms TAN_{ut}, TAN_{strs}, TAN_{ts}, TAN_g and TAN_{pb} denote the tangential energy contribution due to, streaming tangential velocity, tangential stress, surface tension, gravity and bubble pressure on the interface as captured by the base state terms $\mathbf{u}\cdot\mathbf{t}$, $\left[-p^0 + 2Nf^{-1}\left(\mathbf{t}\cdot\frac{d\mathbf{u}^0}{ds}\right)\right] + \left[-p^0 + 2Nf^{-1}\frac{u_r^0}{r}\right]$, Eo, z and P_b in the expressions, respectively. The base state term in TAN_{strs} is considered as tangential stress because it can obtained by taking the double dot product of the stress tensor and the tangential projection operator, $(\mathbf{I} - \mathbf{n}\otimes\mathbf{n})$. For the conditions shown in Figure 5.16, we generated the plots for the tangential energy components, shown in Figure 5.17.



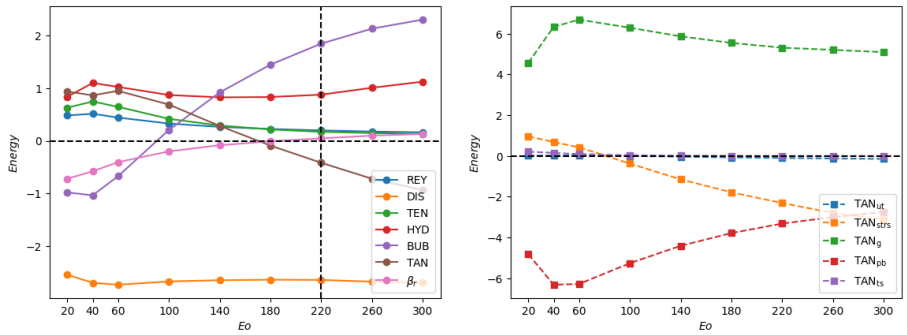
(a) (b)

(c)

Figure 5.17: Distribution of tangential energy for $Nf = 80$ as a function of tube center liquid velocity at (a) $Eo = 20$ (b) $Eo = 180$ (c) $Eo = 300$ when $m = 1$. The point where β_R first become positive, marking the onset of asymmetric bubble is indicated by the black vertical dashed lines.

It is seen that the major contributor to the tangential energy term for $Eo = 20$ is the tangential stress. For the fact that the largest source of energy to TAN, that drives the instability, is tangential stress, which is of liquid phase, the instability can be said to originate from the liquid phase. While tangential stress portion of TAN is stabilising at higher Eötvös number, it is destabilising in region where surface tension effect is strong. It is for this reason that the magnitude of U_m at which transition to asymmetric bubble increases and decreases in the high and negligible surface tension effect regions as inverse viscosity number is increased, respectively, because it is expected, just like the base state normal stress shown in Figure 4.25, that the base state tangential stress on the interface will decrease as the inverse viscosity number is increased. As earlier noted, interval $(60, 100)$ appears to be the limit of surface tension at which the effect of increasing Nf beyond $Nf = 60$ have opposing effect on the magnitude of U_m at which the bubble become unstable. This limit is reflected in the role of tangential stress component of the tangential energy term, see Figure 5.18b, as it shows that this component switch from being a

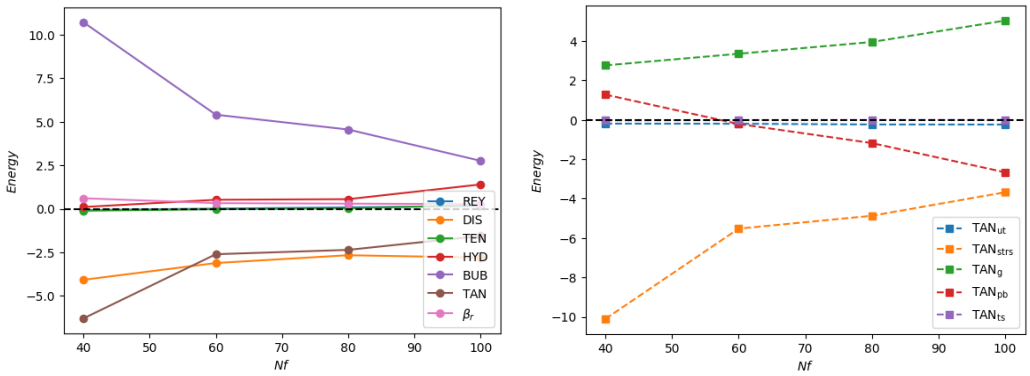
destabilising to a stabilising quantity in the same interval $(60, 100)$.



(a) (b)

Figure 5.18: Energy distribution of component energy terms in equation (a) (5.64) (b) (5.66) for $Nf = 80$, $U_m = -0.20$ and $m = 1$ as a function of Eötvös number, showing a switch in the role of TAN_{strs} from destabilising to stabilising energy term in open interval $(60, 100)$.

To understand the force that makes the magnitude of the downward liquid velocity at onset of instability decreases as Nf is decreased in the low surface tension effect region, Figure 5.19b shows the effect of Nf on the perturbation energy at $Eo = 300$ and $U_m = -0.25$.



(a) (b)

Figure 5.19: Energy distribution of component energy terms in equation (a) (5.64) (b) (5.66) for $Eo = 300$, $U_m = -0.25$ and $m = 1$ as a function of inverse viscosity number, showing a trend in the role of TAN_{pb} from stabilising to destabilising energy term as Nf is decreased.

Although, for all Nf, BUB remains the dominant destabilising energy term and TAN_{strs} also retains its stabilising influence as noted earlier for this region of Eo, what is noticeable is emergence of TAN_{pb} as a destabilising quantity as Nf is decreased. This reduces the total increment in the stabilisation effect of TAN relative to the increment associated with destabilisation energy term BUB as Nf is decreased. Consequently, leading to the decrease in the magnitude

of U_m requires for the bubble to transition from symmetric to asymmetric bubble shape.

From the general analysis carried out for Nf and Eo parameter spaces investigated, it is evident that it is the need for the bubble to continue to satisfy the interface stress conditions that drives the bubble towards asymmetric shape in downward liquid flow. Therefore, in contrast to the conclusion of [65] that it is the normal component of gravity on the interface that drives the transition to asymmetric Taylor bubble shape, our analysis shows that the dominant source of energy driving the instability depends on the effect of surface tension. When surface tension has negligible and strong influence on the steady state dynamics, the dominat energy terms driving the transition to asymetric shape are the normal bubble pressure of the gas phase and tangential stress in the liquid phase, respectively. We note that the analysis of [65] was carried out locally around the nose region under the assumptions that the effects of viscosity and surface tension are negligible. A look at Figures 5.18a and 5.19a shows that the energy term due to normal component of gravity on the interface is an increasing function of Nf and Eo. It is plausible that at very high inverse viscosity and Eötvös numbers, which correspond to negligible viscosity and surface tension influence regions, that the energy term due to gravity, HYD may overtake BUB as the most dominant destabilising energy term. It is therefore very likely that the mechanism governing the instability in region of extreme negligible surface tension and viscosity effect is different from that encountered in this investigation.

5.6 Summary

The focus of this chapters was on linear stability and energy budget analyses. Finite element linear stability model was derived using the concept of total linearisation method of [60]. The model was validated by comparing the numerical results from the model with theoretical prediction of the growth rate and oscillation frequency for the normal mode small-amplitude oscillation of spherical bubble in a stagnant liquid in an unbounded domain under the assumption of negligible effect of gravity. The model was then used to examine the influence of inverse viscosity and Eötvös numbers on the magnitude of liquid tube center velocity at the onset

of transition to asymmetric Taylor bubble shapes. To understand the mechanism governing the transition to instability, an energy budget finite element model was derived, validated and utilised to analyse the contribution of energy of different physical origins in driving the bubble towards instability. The analysis showed that the instability is interfacial in nature and the major contribution to energy production that drives the instability comes from the bubble pressure and the tangential stress when surface tension effect on the steady state dynamics are negligible and significant, respectively.

Chapter 6

Conclusions and future work

6.1 Conclusions

The study in this dissertation is concerned with the numerical simulations of a rising Taylor bubble in circular tubes, focussing on computation of steady state solution, linear stability analysis of the steady state solution and energy analysis of the linear stability analysis results. Linear stability analysis of a rising Taylor bubble is an area that has received less attention when compared to the numerous numerical, theoretical and experimental studies that have been carried on steady state solution of a rising Taylor bubble. Existing previous theoretical studies examining stability of Taylor bubble are the work of [10] and [65] which focussed on the breakup of Taylor bubble when it encounters turbulent eddies and the transition of Taylor bubble from symmetric to asymmetric bubble shape, respectively. Although more practical, assumptions such as negligible viscosity and surface tension effects make it easier to carry out analysis that are based on potential solution around Taylor bubble nose, which, though, have been successful in predicting steady state solutions but have not been able to correctly predict some of the recent experimental studies concerning stability. This study made no such assumptions, rather we solved the full governing equations of motion around a full Taylor bubble.

The investigation, which began in chapter 3, hinged on three key areas: steady state computa-

tion and analysis, linear stability analysis and energy budget analysis, and it focused primarily on the study of transition of Taylor bubble from symmetric to asymmetric shape. For each of the key areas, mathematical model needed for the analysis was developed and the model numerically solved using Galerkin finite element method implemented within FreeFem++, an open source finite element package.

In chapter 3, we derived Galerkin weak form of the equations governing the rise of three-dimensional Taylor bubble of constant volume in liquid contained in vertical circular tubes, characterised by dimensionless inverse viscosity number, Eötvös number and Froude number based on centreline liquid velocity. Direct computation of interface curvature using cubic spline techniques and its approximation based on Laplace-Beltrami operator were discussed. In addition, equations that allow determination of interface deformation and bubble pressure were derived.

Starting from the Galerkin weak form of the governing equations and constitutive relations derived in chapter 3, we developed a steady state model for a two-dimensional axisymmetric rising Taylor bubble in chapter 4. The model was validated against experimental data of [17] and afterwards, it was employed to compute the steady state solutions of the rising bubble for ranges of Nf, Eo and U_m parameters values. Steady state features defining the nose, film, interface and bubble bottom regions in addition to the wall were computed and where applicable were compared with theoretical predictions. For all comparisons made, our numerical results reasonably agree with the theoretical results. From the analysis of our results, we deduced that the value of Eo and Nf that demarcates region where surface tension and viscosity have strong influence on the dynamics of a rising Taylor bubble from where they do not, lies in the interval $[60, 100)$ and $[60, 80)$, respectively.

Extending the total linearisation method of [60] to linear stability analysis, in chapter 5, linear stability model describing the evolutions of perturbations imposed on the steady state solutions was derived. As a form of validation, the numerical prediction from the model was compared

with the theoretical results of [95] for small-amplitude shape oscillation of spherical bubble in stagnant liquid with the effect of gravity and boundary neglected. Our numerical solution agrees well with the analytical solution. Using the model, the stability of the steady state solutions were examined for both stagnant and flowing liquids. The analysis showed that the leading unstable mode is $m = 1$, which is the mode that correspond to the deflection of the bubble nose away from the axis of symmetry, and the magnitude of U_m at the onset of instability is dependent on both inverse viscosity and Eötvös numbers. For the unstable mode, the three-dimensional deformed bubble shapes showing the influence of the three dimensionless parameters were presented for mode $m = 1$ and $m = 2$ and stability maps indicating region where symmetric and asymmetric bubbles can be observed for the Nf investigated as a function of Eo were shown.

From the linear stability model, model equation describing the evolution of kinetic energy of the perturbations imposed on the base state was derived in the same chapter 5. Our confirmation showed that the derived energy equation satisfy the law of conservation of energy for the perturbations. To understand the leading mechanism that drives the instability observed, we analysed the distribution of energy among the different energy production and dissipation terms. From the analysis, for $Eo \geq 100$, the leading energy production term driving the instability is the normal component of energy on the interface due to bubble pressure while for $Eo < 60$ the leading energy production term driving the instability is the tangential component of energy on the interface due to tangential stress. Energy analysis showed that the aforementioned steady state intervals $[60, 100)$ and $[60, 80)$ for Eo and Nf separates the region of the parameter space where the tangential energy term due to base state tangential stress TAN_{strs} and bubble pressure, TAN_{pb} can be destabilising and stabilising, respectively.

Although the study focussed on not-too-high Nf and Eo parameter spaces which made it difficult to compare our results directly with experiment studies, it provides insight into the roles viscosity and surface tension play in the transition to asymmetric Taylor bubble in downward liquid flow, which has not been investigated before. The analysis carried out here is

considered as a first step in our investigations towards understanding the possibly different mechanisms that govern the various instabilities encountered in the dynamics of Taylor bubble and the analysis has given us clues as to the steps to be followed to address the other problems.

6.2 Future work

6.2.1 Wake instability and breakup of bubble

We have only investigated one of the three stability problems highlighted in section 1.3. The other two instabilities are only encountered in very high Nf and Eo regime. Even the investigated instability problem in the study requires extension into high Nf, since, as noted in section 5.5.2, it is very likely that it is a different mechanism that control the instability in that space. Once issues surrounding the steady state model and spurious velocity are resolved, the next phase is the use of the existing model for the computation of the steady state solution needed for the analysis of wake instability and extension of the current study into inertia regime. As Nf is further increased, the flow at some point will eventually becomes turbulent, which is the regime we anticipate that instability associated with complete Taylor bubble breakup will occur. Thus, requiring a modification to both the steady state and linear stability models. For the former, some progress, though not included in this report, have been made at the inception of my PhD towards deriving a turbulent model for the problem. As for the latter, we foresee no difficulty in direct extension of the current stability model to turbulent regime once the steady state model for the turbulent regime is finally resolved.

6.2.2 Three-dimensional numerical simulations of Taylor bubble

Ultimately, after the linear stability analyses for the various problems mentioned in this report are addressed and the parameter spaces within which the instability can be observed established, it would be interesting to visualised how the instability would emerge by carrying out fully unsteady three-dimensional numerical simulation of one of the conditions that falls within

the unstable region. As physical experiment are quite very expensive when compared with numerical experiment, numerical solution seems a much easier means of visualising the instability. In this regard, as part of my PhD work which is also not reported here, we have validated a three-dimensional numerical simulation code that is based on diffuse interface method for the simulation of Taylor bubble rise. Figure 6.1 shows one of the validation carried out on the code, displaying the shape of Taylor bubble at various simulation time step during its rise in water. The rise velocity of the bubble became steady at time step of $220,000$ and the shape of the bubble at this time-step is compared with the experiment. The computed rise velocity was $0.14859\,ms^{-1}$, which is less than 2% deviation from the experimental measured value of $0.151\,ms^{-1}$. It is part of the future goal to make use of the same code for the numerical simulation of the instability observed in this report and other future study to be investigated.

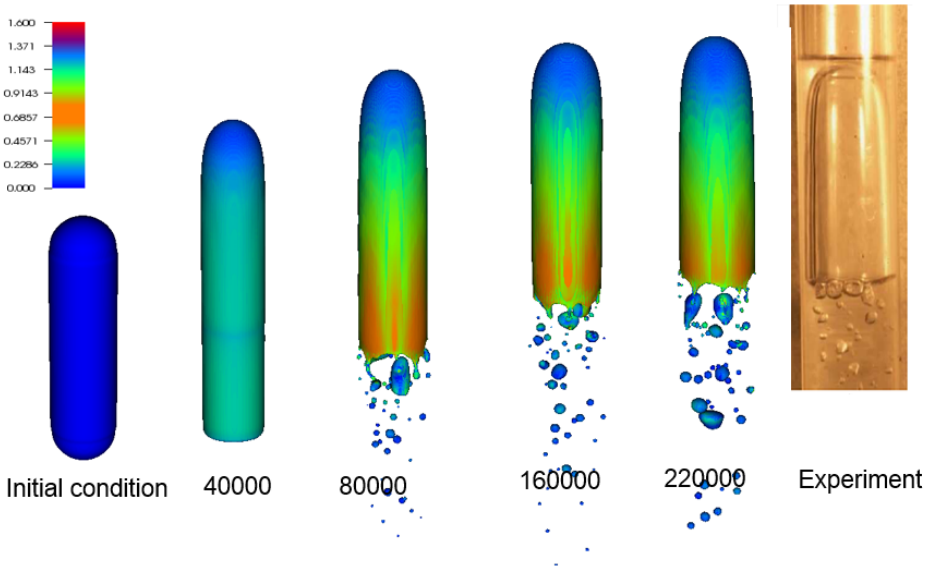


Figure 6.1: Isosurface of Taylor bubble coloured with the magnitude of the velocity at different computational time steps compared with the experimental steady shape of Rana *et al* [98] .

References

[1] Ali, S. F. and Yeung, H. (2014). Two-phase flow patterns in large diameter vertical pipes. *Asia-Pac. J. Chem. Eng.*, 9:105–116.

[2] Ambrose, S. (2015). *The rise of Taylor bubbles in vertical pipes*. PhD thesis, University of Nottingham.

[3] Anjos, G., Mangiavacchi, N., Borhani, N., and Thome, J. R. (2014). 3D ALE finite-element method for two-phase flows with phase change. *Heat Transfer Engineering*, 35(5):537–547.

[4] Araújo, J. D. P., Miranda, J. M., Pinto, A. M. F. R., and Campos, J. B. L. M. (2012). Wide-ranging survey on the laminar flow of individual Taylor bubbles rising through stagnant Newtonian liquids. *Int. J. Multiph. Flow*, 43:131–148.

[5] Arnold, D., Brezzi, F., and Fortin, M. (1984). A stable finite element for the Stokes equations. *Calcolo*, 21:337–344.

[6] Bae, S. and Kim, D. (2007). Computational study of the axial instability of rimming flow using Arnoldi method. *Int. J. Numer. Meth. Fluids*, 53:691–711.

[7] Baïsch, E. (2001). Finite element discretization of the Navier-Stokes equations with a free capillary surface. *Numerische Mathematik*, 88(2):203–235.

[8] Barrett, J., Garcke, H., and Nürnberg, R. (2013). Eliminating spurious velocities with a stable approximation of viscous incompressible two-phase Stokes flow. *Comput. Methods Appl. Mech. Eng.*, 267:511–530.

[9] Batchelor, G. (1967). *An introduction to fluid dynamics*. Cambridge University Press, UK.

[10] Batchelor, G. (1987). The stability of a large gas bubble rising through liquid. *J. Fluid Mech.*, 184:399–422.

[11] Bendiksen, K. (1985). On the motion of long bubbles in vertical tubes. *Int. J. Multiphase Flow*, 11:797–812.

[12] Boomkamp, P. and Miesen, R. (1996). Classification of instabilities in parallel two-phase flow. *Int. J. Multiphase Flow*, 22:67–88.

[13] Brackbill, J., Kothe, D., and Zemach, C. (1992). A continuum method for modeling surface tension. *J. Comput. Phys.*, 100:335–354.

[14] Brezzi, F. and Falk, R. (1991). Stability of higher-order Hood-Taylor methods. *SIAM J NUMER. ANAL*, 28(3):581–590.

[15] Brown, R. (1965). The mechanics of large gas bubbles in tubes I. Bubble velocities in stagnant liquids. *Can. J. Chem. Eng*, 43:217–223.

[16] Bugg, J., Mack, K., and Rezkallah, K. (1998). A numerical model of Taylor bubbles rising through stagnant liquids in vertical tubes. *Int. J. Multiphase Flow*, 24:271–281.

[17] Bugg, J. D. and Saad, G. A. (2002). The velocity field around a Taylor bubble rising in a stagnant viscous fluid: Numerical and experimental results. *Int. J. Multiphase Flow*, 28:791–803.

[18] Cairncross, R., Schunk, P., Baer, T., Rao, R., and Sackinger, P. (2000). A finite element method for free surface flows of incompressible fluids in three dimensions. Part I. Boundary fitted mesh motion. *Int. J. Numer. Meth. Fluids*, 33:375–403.

[19] Campos, J. and Guedes de Carvalho, J. (1988). An experimental study of the wake of gas slugs rising in liquids. *J. Fluid Mech.*, 196:27–37.

[20] Capponi, A., James, M., and Lane, S. (2016). Gas slug ascent in a stratified magma: Implications of flow organisation and instability for Strombolian eruption dynamics. *Earth Planet. Sci. Lett.*, 435:159–170.

[21] Carvalho, M. and Scriven, L. (1999). Three-dimensional stability analysis of free surface flows: application to forward deformable roll coating. *J. Comput. Phys.*, 151:534–562.

[22] Chireux, V., Fabre, D., Risso, F., and Tordjeman, P. (2015). Oscillations of a liquid bridge resulting from the coalescence of two droplets. *Physics of Fluids*, 27:062103.

[23] Christodoulou, C. and Scriven, L. (1988). Finding leading modes of a viscous free surface flow: An asymmetric generalized eigenproblem. *J. Sci. Comput.*, 3(4):355–406.

[24] Clift, R., Grace, J., and Weber, M. (1978). *Bubbles, drops and particles*. Academic Press, NY.

[25] Collins, R., De Moraes, F., Davidson, J., and Harrison, D. (1978). The motion of a large gas bubble rising through liquid flowing in a tube. *J. Fluid Mech*, 89:497–514.

[26] Constantinides, A. and Mostoufi, N. (1999). *Numerical methods for chemical engineers with MATLAB applications*. Prentice Hall PTR, NY.

[27] Cuvelier, C. and Schulkes, R. (1990). Some numerical methods for the computation of capillary free boundaries governed by the Navier-Stokes equations. *SIAM Rev.*, 32(3):355–423.

[28] Davies, R. and Taylor, G. (1950). The mechanics of large bubbles rising through extended liquids and through liquids in tubes. *Proc. R. Soc. Lond. A*, 200:375–390.

[29] Dhanjal, A. and Saravan-Butler, M. (2014). Simulating the effect of pipe diameter on Taylor bubble stability in vertical riser systems. Undergraduate report, Department of Chemical Engineering, Imperial College London.

[30] Dumitrescu, D. (1943). Strömung an einer Luftblase im senkrechten Rohr. *Z. Angew. Math. Mech*, 23(3):139–149.

[31] Dziuk, G. (1991). An algorithm for evolutionary surfaces. *ZNumer. Math.*, 58(1):603–612.

[32] Elgeti, S. and Sauerland, H. (2016). Deforming fluid domains within the finite element method: five mesh-based tracking methods in comparison. *Archives of Computational Methods in Engineering*, 23:323–361.

[33] Fabre, J. (2016). A long bubble rising in still liquid in a vertical channel: a plane inviscid solution. *J. Fluid Mech.*, 794:R4.

[34] Fabre, J. and Figueroa-Espinoza, B. (2014). Taylor bubble rising in a vertical pipe against laminar or turbulent downward flow: symmetric to asymmetric shape transition. *J. Fluid Mech.*, 755:485–502.

[35] Fabre, J. and Liné, A. (1992). Modeling of two-phase slug flow. *Annu. Rev. Fluid Mech.*, 24:21–46.

[36] Feng, J. (2008). Buoyancy-driven motion of a gas bubble through viscous liquid in a round tube. *J. Fluid Mech.*, 609:377–410.

[37] Feng, J. (2009). A long gas bubble moving in a tube with flowing liquid. *Int. J. Multiphase Flow*, 35:738–746.

[38] Fershtman, A., Babin, V., Barnea, D., and Shemer, L. (2017). On shapes and motion of an elongated bubble in downward liquid pipe flow. *Physics of Fluids*, 29:112103.

[39] Figueroa-Espinoza, B. and Fabre, J. (2011). Taylor bubble moving in a flowing liquid in vertical channel: transition from symmetric to asymmetric shape. *J. Fluid Mech.*, 679:432–454.

[40] Fraggedakis, D., Pavlidis, M., Dimakopoulos, Y., and Tsamopoulos, J. (2016). On the velocity discontinuity at critical volume of a bubble rising in a viscoelastic fluid. *J. Fluid Mech.*, 789:310–346.

[41] Funada, T., Joseph, D., Maehara, T., and Yamashita, S. (2005). Ellipsoidal model of the rise of a Taylor bubble in a round tube. *Int. J. Multiph. Flow*, 31:473–491.

[42] Ganesan, S. and Tobiska, L. (2008). An accurate finite element scheme with moving meshes for computing 3D-axisymmetric interface flows. *Int. J. Multiph. Flow*, 57:119–138.

[43] Goldsmith, H. and Mason, S. (1962). The movement of single large bubbles in closed vertical tubes. *J. Fluid Mech.*, 14:42–58.

[44] Grace, J., Wairegi, T., and Brophy, J. (1978). Break-up of drops and bubbles in stagnant media. *Can. J. of Chem. Engng*, 65:3–8.

[45] Griffith, P. and Wallis, G. B. (1961). Two phase slug flow. *ASME: J. Heat Transfer*, 83:07–320.

[46] Griffiths, D. and Smith, I. (2006). *Numerical methods for engineers.* Chapman and Hall, NY.

[47] Gross, S. and Reusken, A. (2010). *Numerical methods for two-phase incompressible flows.* pringer Heidelberg Dordrecht, London.

[48] Ha Ngoc, H. and Fabre, J. (2006). A boundary element method for calculating the shape and velocity of two-dimensional long bubble in stagnant and flowing liquid. *Engng Anal. Bound. Elem.*, 30:539–552.

[49] Havre, K., Stornes, K., and Stray, H. (2000). Taming slug flow in pipelines. Technical Report no. 4, ABB Review.

[50] Hecht, F. (2012). New development in FreeFem++. *J. Numer. Math.*, 20(3-4):251–265.

[51] Heinrich, J. and Pepper, D. (1999). *Intermediate finite element method : fluid flow and heat transfer applications.* Taylor & Francis Group.

[52] Hewitt, G. (1982). Flow regimes. In Hestroni, G., editor, *Handbook of multiphase systems*, chapter 2, pages 3–94. Hemisphere Publishing Corporation.

[53] Hirt, C. and Nichols, B. (1981). Volume of fluid (VOF) method for the dynamics of free boundaries. *J. Comput. Phys.*, 39:201–225.

[54] Hooper, A. and Boyd, W. (1983). Shear-flow instability at the interface between two viscous fluids. *J. Fluid Mech.*, 128:507–528.

[55] Hsu, Y. and Simon, F. (1969). Stability of cylindrical bubbles in a vertical pipe. ASME-AIChE Heat Transfer Conference, Minneapolis, Minn.

[56] Hu, H. and Joseph, D. (1989). Lubricated pipelining: stability of core-annular flow. Part 2. *J. Fluid Mech.*, 205:359–396.

[57] Johnson, A. and Tezduyar, T. (1994). Mesh update strategies in parallel finite element computations of flow problems with moving boundaries and interfaces. *Comp. Methods Appl. Mech. Eng.*, 119:73–94.

[58] Kang, C., Quan, S., and Lou, J. (2010). Numerical study of a Taylor bubble rising in stagnant liquids. *Phys. Rev. E.*, 81:1539–3755.

[59] Karapantsios, T., Paras, S., and Karabelas, A. (1989). Statistical characteristics of free falling films at high reynolds numbers. *Int. J. Multiphase Flow*, 15:1–21.

[60] Kruyt, N., Cuvelier, C., Segal, A., and Van Der Zanden, J. (1988). A total linearization method for solving viscous free boundary flow problems by the finite-element method. *Int. J. Numer. Methods Fluids*, 8:351–363.

[61] Lehoucq, R. and Salinger, A. (2001). Large-scale eigenvalue calculations for stability analysis of steady flows on massively parallel computers. *Int. J. Numer. Methods Fluids*, 36:309–327.

[62] Lehoucq, R., Sorensen, D., and Yang, C. (1997). ARPACK user's guide: solution of large scale eigenvalue problems with implicitly restarted Arnoldi methods. *SIAM*.

[63] Lizarraga-Garcia, E., Buongiorno, J., Al-Safran, E., and Lakehal, D. (2017). A broadly applicable unified closure relation for Taylor bubble rise velocity in pipes with stagnant liquid. *Int. J. Multiph. Flow*, 89:345–358.

[64] Llewellin, E., Del Bello, E., Taddeucci, J., Scarlato, P., and Lane, S. (2012). The thickness of the falling film of liquid around a Taylor bubble. *Proc. R. Soc. A*, 468:1041–1064.

[65] Lu, X. and Prosperetti, A. (2006). Axial stability of Taylor bubbles. *J. Fluid Mech.*, 568:173–192.

[66] Lu, X. and Prosperetti, A. (2009). A numerical study of Taylor bubbles. *Ind. Eng. Chem. Res.*, 48:242–252.

[67] M., C. and Raviart, P. (1973). Conforming and nonconforming finite element methods for solving the stationary Stokes equations I. *RAIRO Anal. Numér.*, 7(R-3):33–76.

[68] Magnini, M., Pulvirenti, B., and Thome, J. (2013). Numerical investigation of hydrodynamics and heat transfer of elongated bubbles during flow boiling in a microchannel. *Int. J. Heat Mass Tran.*, 59:451–471.

[69] Mao, Z. and Dukler, A. (1989). An experimental study of gas-liquid slug flow. *Experiments in Fluids*, 8:169–1821.

[70] Mao, Z. and Dukler, A. (1990). The motion of Taylor bubbles in vertical tubes I. A numerical simulation for the shape and rise velocity of Taylor bubbles in stagnant and flowing liquids. *J. Comput. Phys.*, 91:2055–2064.

[71] Mao, Z. and Dukler, A. (1991). The motion of Taylor bubbles in vertical tubes II. Experimental data and simulations for laminar and turbulent flow. *Chem. Eng. Sci.*, 46:132–160.

[72] Martin, C. (1976). Vertically downward two-phase slug flow. *Trans. ASME J. Fluids Engng*, 98:715–722.

[73] Maxworthy, T. (1967). A note on the existence of wakes behind large, rising bubbles. *J. Fluid Mech.*, 27:367–368.

[74] Meerbergen, K., Spence, A., and Roose, D. (1994). Shift-invert and Cayley transforms for the detection of rightmost eigenvalue of nonsysmmetric matrices. *BIT*, 34:409–423.

[75] Miller, C. and Scriven, L. (1968). The oscillations of a fluid droplet immersed in another fluid. *J . Fluid Mech.*, 32:417–435.

[76] Moissis, R. and Griffith, P. (1962). Entrance effect in a two-phase slug flow. *J. Heat Transf.*, 84:29–38.

[77] Natarajan, R. (1992). An Arnoldi-based iterative scheme for nonsymmetric matrix pencils arising in finite element stability problems. *J. Comput. Phys.*, 100:128–142.

[78] Nickens, H. and Yannitel, D. (1987). The effect of surface tension and viscosity on the rise velocity of a large gas bubble in a closed vertical liquid-filled tube. *Int. J. Multiphase Flow*, 13:57–69.

[79] Nicklin, D., Wilkes, J., and Davidson, J. (1962). Two-phase flow in vertical tubes. *Trans. Inst. Chem. Engrs*, 40:61–68.

[80] Nigmatulin, T. (2001). Surface of a Taylor bubble in vertical cylindrical flows. *Dokl. Phys.*, 46:803–805.

[81] Nogueira, S., Riethmuller, M., Campos, J., and Pinto, A. (2006a). Flow in the nose region and annular film around a Taylor bubble rising through vertical columns of stagnant and flowing Newtonian liquids. *Chem. Eng. Sci.*, 61:845–857.

[82] Nogueira, S., Riethmuller, M., Campos, J., and Pinto, A. (2006b). Flow patterns in the wake of a Taylor bubble rising through vertical columns of stagnant and flowing Newtonian liquids: an experimental study. *Chem. Eng. Sci.*, 61:7199–7212.

[83] Ó Náraigh, L., Spelt, P., Matar, O. K., and Zaki, T. (2011). Interfacial instability in turbulent flow over a liquid film in a channel. *Int. J. Multiphase Flow*, 37:812–830.

[84] Ohnuki, A. and Akimoto, H. (2000). Experimental study on transition of flow pattern and phase distribution in upward air-water two-phase flow along a large vertical pipe. *Int. J. Multiphase Flow*, 26:267–286.

[85] Omebere-Iyari, N., Azzopardi, B., and Ladam, Y. (2007). The identification of two-phase flow patterns and their transitions in large diameter vertical pipes at elevated pressures. *AIChE J.*, 53:2493–2504.

[86] Omebere-Iyari, N., Azzopardi, B., Lucas, D., Beyer, M., and Prasser, H. (2008). The characteristics of gas/liquid flow in large risers at high pressures. *Int. J. Multiphase Flow*, 34:461–476.

[87] Osher, S. and Sethian, J. (1988). Fronts propagating with curvature dependent speed: Algorithms based on Hamilton Jacobi formulations. *J. Comput. Phys.*, 79:12–49.

[88] Pepper, D. and Heinrich, J. (2017). *The finite element method: basic concepts and applications with MATLAB, MAPLE, and COMSOL*. Taylor & Francis Group.

[89] Pering, T. and McGonigle, A. (2018). Combining spherical-cap and Taylor bubble fluid dynamics with plume measurements to characterize basaltic degassing. *Geosciences*, 8(2):42.

[90] Pinto, A. and Campos, J. (1996). Coalescence of two gas slugs rising in a vertical column of liquid. *Chem. Eng. Sci.*, 51(1):45–54.

[91] Pinto, A., Coelho Pinheiro, M., and Campos, J. (1998). Coalescence of two gas slugs rising in a co-current flowing liquid in vertical tubes. *Chem. Eng. Sci.*, 53(16):2973–2983.

[92] Polonsky, S., Shemer, L., and Barnea, D. (1999). The relation between the Taylor bubble motion and the velocity field ahead of it. *Int. J. Multiphase Flow*, 25:957–975.

[93] Pozrikidis, C. (2011). *Introduction to theoretical and computational fluid dynamics*. Taylor & Francis Group.

[94] Pringle, C., Ambrose, S., Azzopardi, B., and Rust, A. (2015). The existence and behaviour of large diameter Taylor bubbles. *Int. J. Multiphase Flow*, 72:318–323.

[95] Prosperetti, A. (1980). Normal-mode analysis for the oscillations of a viscous liquid drop in an immiscible liquid. *Journal de Mécanique*, 19(1):149–181.

[96] Prothero, J. and Burton, A. (1961). The physics of blood flow in capillaries: I. The nature of the motion. *Biophysical J.*, 1:565–575.

[97] Ramanan, N. and Engelman, M. (1996). An algorithm for simulation of steady free surface flows. *Int. J. Numer. Methods Fluids*, 22:103–120.

[98] Rana, B., Das, A., and Das, P. (2015). Mechanism of bursting Taylor bubbles at free surfaces. *Langmuir*, 31:9870–9881.

[99] Reddy, J. and Gartling, D. (2010). *The finite element method in heat transfer and fluid dynamics*. Taylor & Francis Group.

[100] Sahu, K., Ding, H., Valluri, P., and Matar, O. (2009). Linear stability analysis and numerical simulation of miscible two-layer channel flow. *Physics of Fluids*, 21:042104.

[101] Sahu, K., Valluri, P., Spelt, P., and Matar, O. (2007). Linear instability of pressure-driven channel flow of a newtonian and Herschel-Bulkley fluid. *Physics of Fluids*, 19:122101.

[102] Schmid, P. and Henningson, D. (2001). *Stability and transition in shear flows*. Springer.

[103] Selvam, B., Merk, S., Govindarajan, R., and Meiburg, E. (2007). Stability of miscible core-annular flows with viscosity stratification. *J. Fluid Mech.*, 592:23–49.

[104] Slikkeveer, P. and Van Loohuizen, E. (1996). An implicit surface tension algorithm for Picard solvers of surface-tension-dominated free and moving boundary problems. *Int. J. Numer. Methods Fluids*, 22:851–865.

[105] Sussman, M., Smereka, P., and Osher, S. (1994). A level set approach for computing solutions to incompressible two-phase flow. *J. Comp. Phys.*, 114:146–159.

[106] Taha, T. and Cui, Z. (2002). Hydrodynamic analysis of upward slug flow in tubular membranes. *Desalination*, 145:179–182.

[107] Taha, T. and Cui, Z. (2006). CFD modeling of slug flow in vertical tubes. *Chem. Eng. Sci.*, 61:676–687.

[108] Taylor, C. and Hood, P. (1973). A numerical solution of the Navier-Stokes equations using the finite element technique. *Comp. and Fluids*, 1:73–100.

[109] Temperley, H. and Chambers, L. (1945). Large volumes of gas in water. reproduced in. *Underwater Explosions Research*, 2.

[110] Tsamopoulos, J., Dimakopoulos, Y., Chatzidai, N., Karapetsas, G., and Pavlidis, M. (2008). Steady bubble rise and deformation in Newtonian and viscoplastic fluids and conditions of bubble entrapment. *J. Fluid Mech.*, 601:123–164.

[111] Viana, F., Pardo, R., Yánez, R., Trallero, J., and Joseph, D. (2003). Universal correlation for the rise velocity of long gas bubbles in round pipes. *J. Fluid Mech.*, 494:379–398.

[112] Wallis, G. (1969). *One-dimensional two-phase flow*. McGraw-Hill, New York.

[113] Weatherburn, C. (1927). *Differential geometry of three dimensions*. Cambridge University press, UK. part 127, pp 251.

[114] White, E. and Beardmore, R. (1962). The velocity of rise of single cylindrical air bubbles through liquids contained in vertical tubes. *Chem. Eng. Sci.*, 17:351–361.

[115] Zhou, W. and Dusek, J. (2017). Marginal stability curve of a deformable bubble. *Int. J. Multiphase Flow*, 89:218–227.

[116] Zukoski, E. (1966). Influence of viscosity, surface tension, and inclination angle on motion of long bubbles in closed tubes. *J. Fluid Mech.*, 25:821–837.

Appendix A

Computational development operators

A.1 Axisymmetric surface tensor products and operators

surface normal tensor product

$$\begin{aligned}\mathbf{n}\otimes\mathbf{n} &= \begin{bmatrix} n_r \\ 0 \\ n_z \end{bmatrix} \begin{bmatrix} n_r & 0 & n_z \end{bmatrix} \\ &= \begin{bmatrix} n_r^2 & 0 & n_r n_z \\ 0 & 0 & 0 \\ n_r n_z & 0 & n_z^2 \end{bmatrix} \\ &= n_r^2 \mathbf{i}_r \mathbf{i}_r + n_r n_z \mathbf{i}_r \mathbf{i}_z + n_r n_z \mathbf{i}_z \mathbf{i}_r + n_z^2 \mathbf{i}_z \mathbf{i}_z \end{aligned} \tag{A.1}$$

surface tangent tensor product

$$(\mathbf{I}-\mathbf{n}\otimes\mathbf{n}) = \begin{bmatrix} t_r^2 & 0 & t_r t_z \\ 0 & 1 & 0 \\ t_r t_z & 0 & t_z^2 \end{bmatrix} = t_r^2\mathbf{i}_r\mathbf{i}_r + t_r t_z\mathbf{i}_r\mathbf{i}_z + t_r t_z\mathbf{i}_z\mathbf{i}_r + t_z^2\mathbf{i}_z\mathbf{i}_z + 1\mathbf{i}_\theta\mathbf{i}_\theta \tag{A.2}$$

gradient operator

$$\nabla = \begin{bmatrix} \frac{\partial}{\partial r} \\ \frac{1}{r}\frac{\partial}{\partial\theta} \\ \frac{\partial}{\partial z} \end{bmatrix} = \frac{\partial}{\partial r}\mathbf{i}_r + \frac{1}{r}\frac{\partial}{\partial\theta}\mathbf{i}_\theta + \frac{\partial}{\partial z}\mathbf{i}_z \tag{A.3}$$

surface normal component of gradient operator

$$\begin{aligned}\nabla_n = [\mathbf{n}\otimes\mathbf{n}]\cdot\nabla &= \left[n_r^2\mathbf{i}_r\mathbf{i}_r + n_r n_z\mathbf{i}_r\mathbf{i}_z + n_r n_z\mathbf{i}_z\mathbf{i}_r + n_z^2\mathbf{i}_z\mathbf{i}_z\right]\cdot\left[\frac{\partial}{\partial r}\mathbf{i}_r + \frac{1}{r}\frac{\partial}{\partial\theta}\mathbf{i}_\theta + \frac{\partial}{\partial z}\mathbf{i}_z\right] \\ &= \left(n_r^2\frac{\partial}{\partial r} + n_r n_z\frac{\partial}{\partial z}\right)\mathbf{i}_r + \left(n_z^2\frac{\partial}{\partial z} + n_r n_z\frac{\partial}{\partial r}\right)\mathbf{i}_z \\ &= n_r\frac{d}{dn}\mathbf{i}_r + n_z\frac{d}{dn}\mathbf{i}_z\end{aligned}$$

surface tangent component of gradient operator

$$\begin{aligned}\nabla_s = [\mathbf{I}-\mathbf{n}\otimes\mathbf{n}]\cdot\nabla &= \left[t_r^2\mathbf{i}_r\mathbf{i}_r + t_r t_z\mathbf{i}_r\mathbf{i}_z + t_r t_z\mathbf{i}_z\mathbf{i}_r + t_z^2\mathbf{i}_z\mathbf{i}_z + 1\mathbf{i}_\theta\mathbf{i}_\theta\right]\cdot\left[\frac{\partial}{\partial r}\mathbf{i}_r + \frac{1}{r}\frac{\partial}{\partial\theta}\mathbf{i}_\theta + \frac{\partial}{\partial z}\mathbf{i}_z\right] \\ &= \left(t_r^2\frac{\partial}{\partial r} + t_r t_z\frac{\partial}{\partial z}\right)\mathbf{i}_r + \frac{1}{r}\frac{\partial}{\partial\theta}\mathbf{i}_\theta + \left(t_z^2\frac{\partial}{\partial z} + t_r t_z\frac{\partial}{\partial r}\right)\mathbf{i}_z \\ &= t_r\frac{d}{ds}\mathbf{i}_r + \frac{1}{r}\frac{\partial}{\partial\theta}\mathbf{i}_\theta + t_z\frac{d}{ds}\mathbf{i}_z\end{aligned}$$

gradient as sum of surface normal and tangent components

$$\begin{aligned}\nabla &= [\mathbf{n}\otimes\mathbf{n}]\cdot\nabla + [\mathbf{I}-\mathbf{n}\otimes\mathbf{n}]\cdot\nabla = \nabla_n + \nabla_s \\ &= \left(n_r\frac{d}{dn} + t_r\frac{d}{ds}\right)\mathbf{i}_r + \frac{1}{r}\frac{\partial}{\partial\theta}\mathbf{i}_\theta + \left(n_z\frac{d}{dn} + t_z\frac{d}{ds}\right)\mathbf{i}_z\end{aligned}$$

curvature as surface divergence of unit normal vector

$$\begin{aligned}\kappa = -\nabla_s \cdot \mathbf{n} &= -\left[t_r \frac{d}{ds}\mathbf{i}_r + \frac{1}{r}\frac{\partial}{\partial\theta}\mathbf{i}_\theta + t_z \frac{d}{ds}\mathbf{i}_z\right] \cdot [n_r \mathbf{i}_r + 0\mathbf{i}_\theta + n_z \mathbf{i}_z] \\ &= -\left(t_r \frac{dn_r}{ds} + \frac{n_r}{r} + t_z \frac{dn_z}{ds}\right) \\ &= -\left(\mathbf{t} \cdot \frac{d\mathbf{n}}{ds} + \frac{n_r}{r}\right)\end{aligned}$$

Appendix B

Steady state simulations results in flowing liquid

B.1 Additional bubble shapes in stagnant liquids

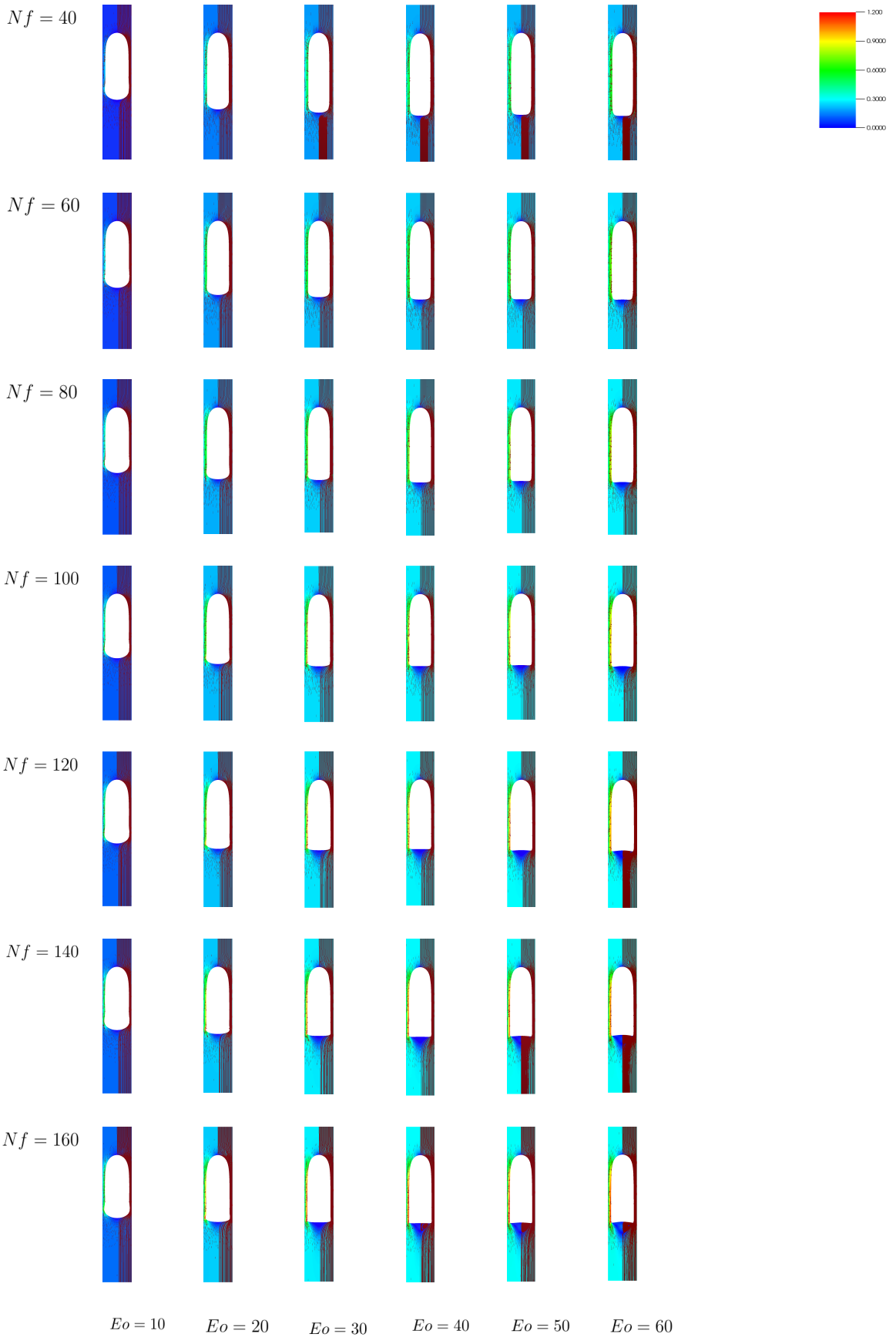


Figure B.1: Steady state bubble shapes and surrounding flow fields; effect of inverse viscosity and Eötvös numbers.

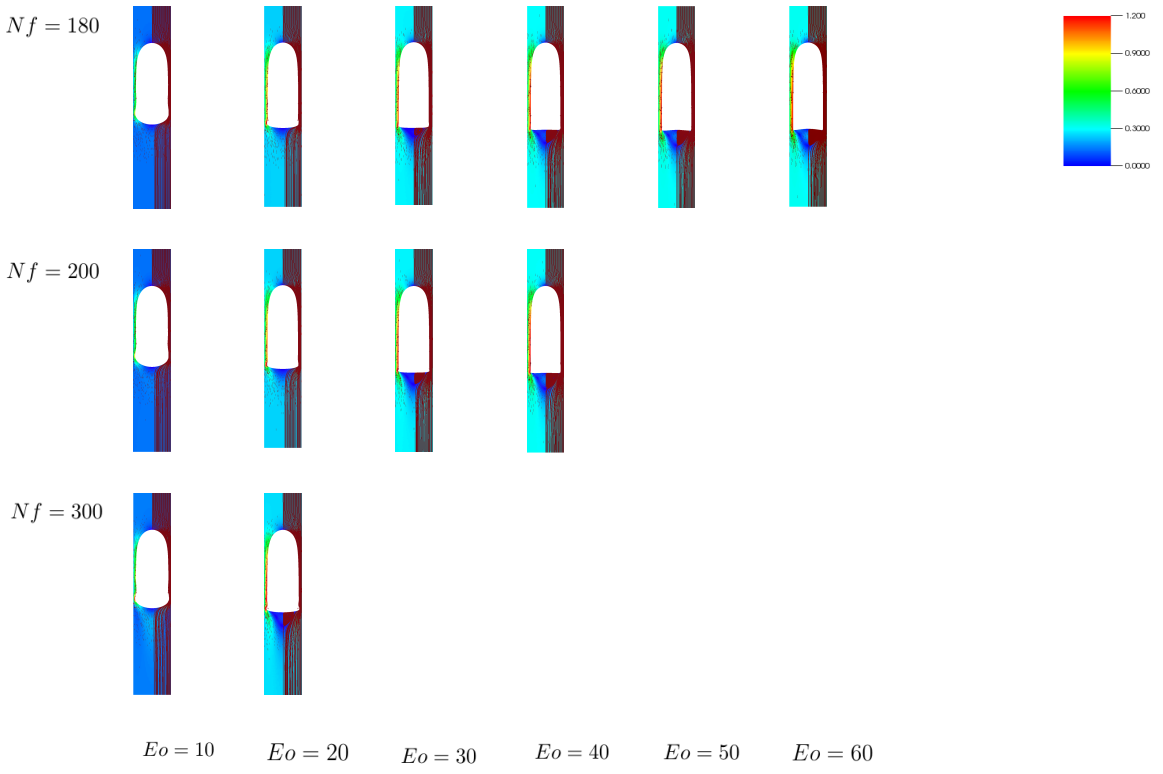


Figure B.2: Steady state bubble shapes and surrounding flow fields; effect of inverse viscosity and Eötvös numbers.

B.2 Steady state mean curvature

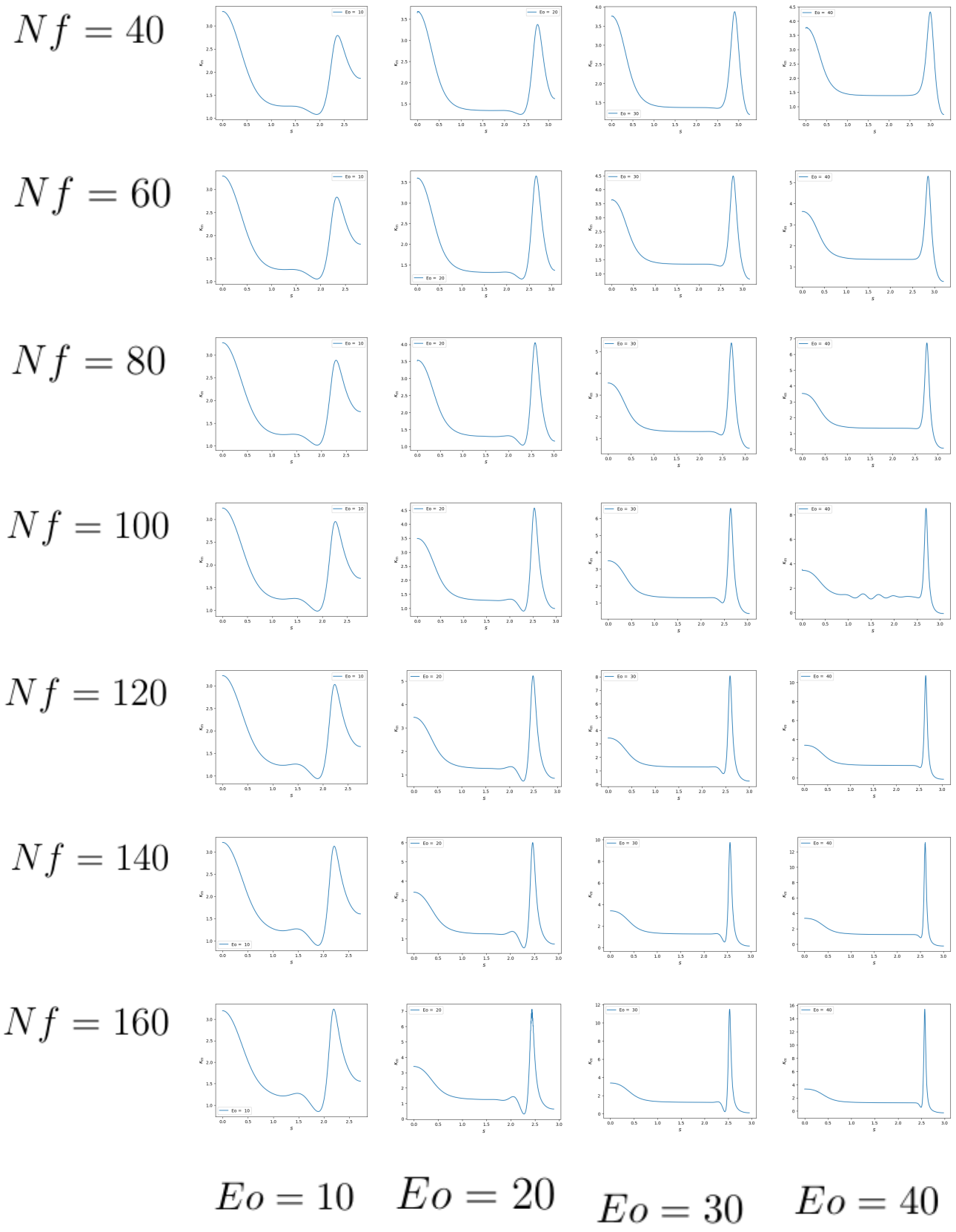


Figure B.3: Mean curvature of the bubble interface as a functions of Nf and Eo, $Eo = 10 - 40$.

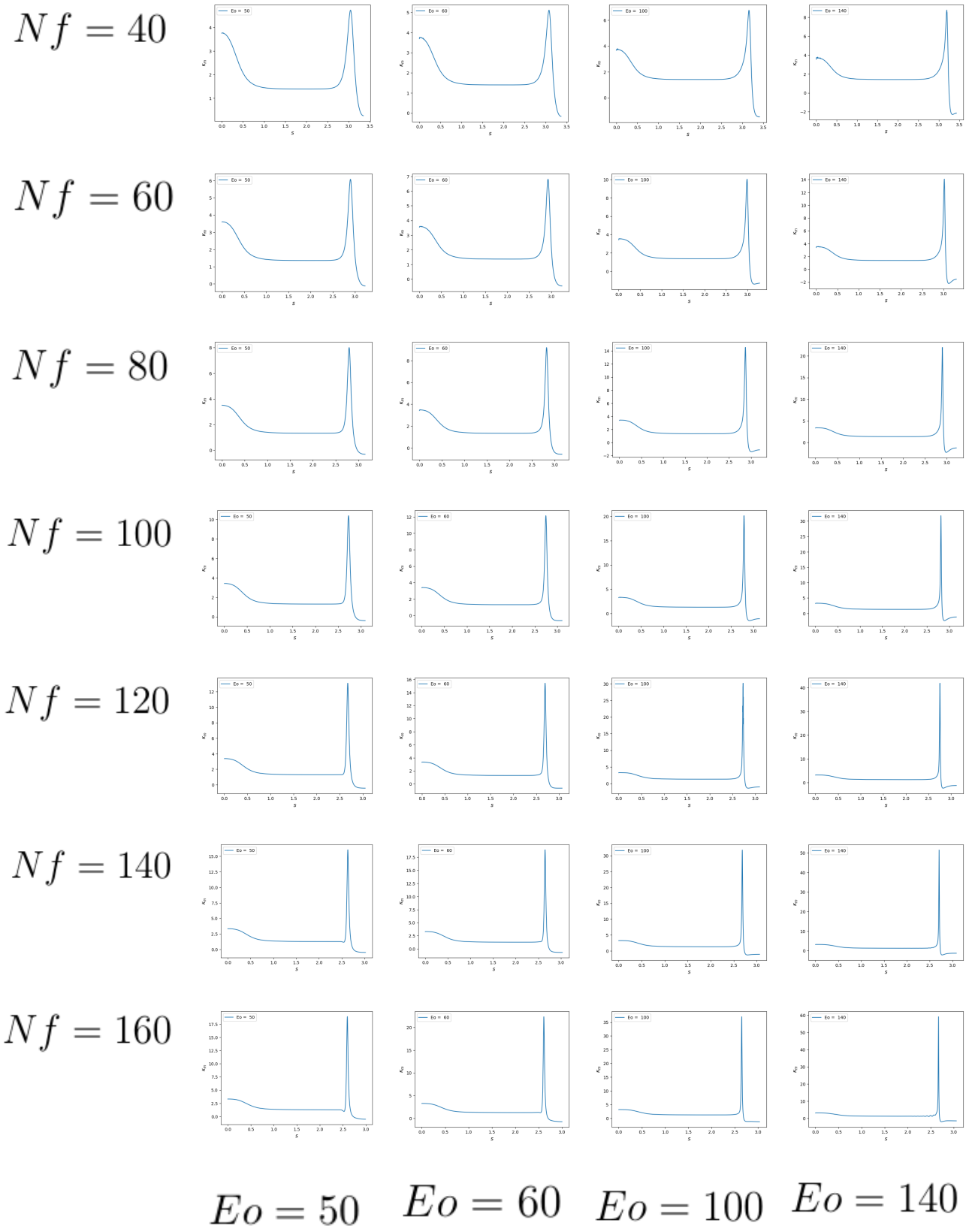


Figure B.4: Mean curvature of the bubble interface as a functions of Nf and Eo, $Eo = 50-140$.

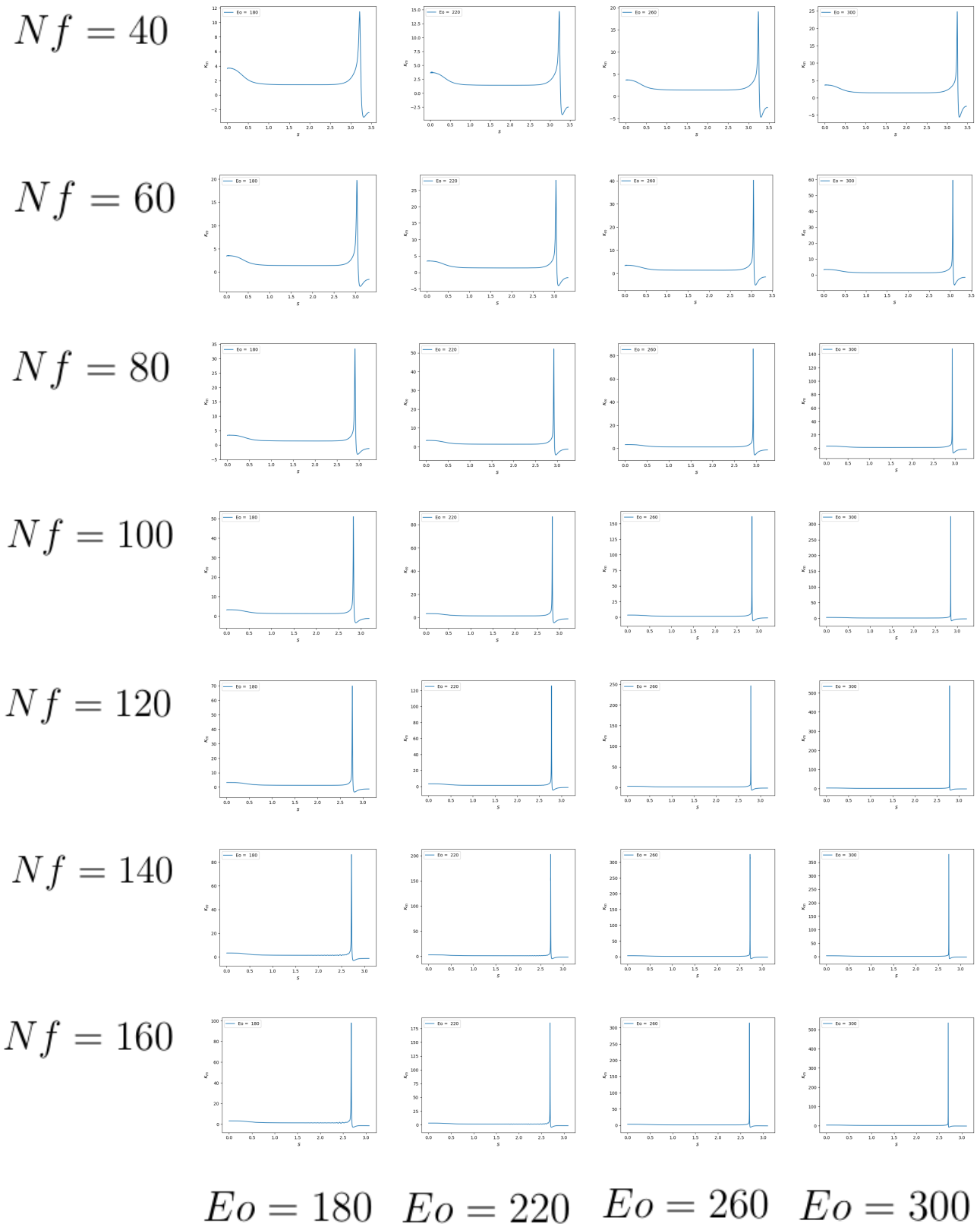


Figure B.5: Mean curvature of the bubble interface as a functions of Nf and Eo, $Eo = 180-300$.

B.3 Bubble shapes in flowing liquids

Bubble shape and flow field for $Nf = 100$

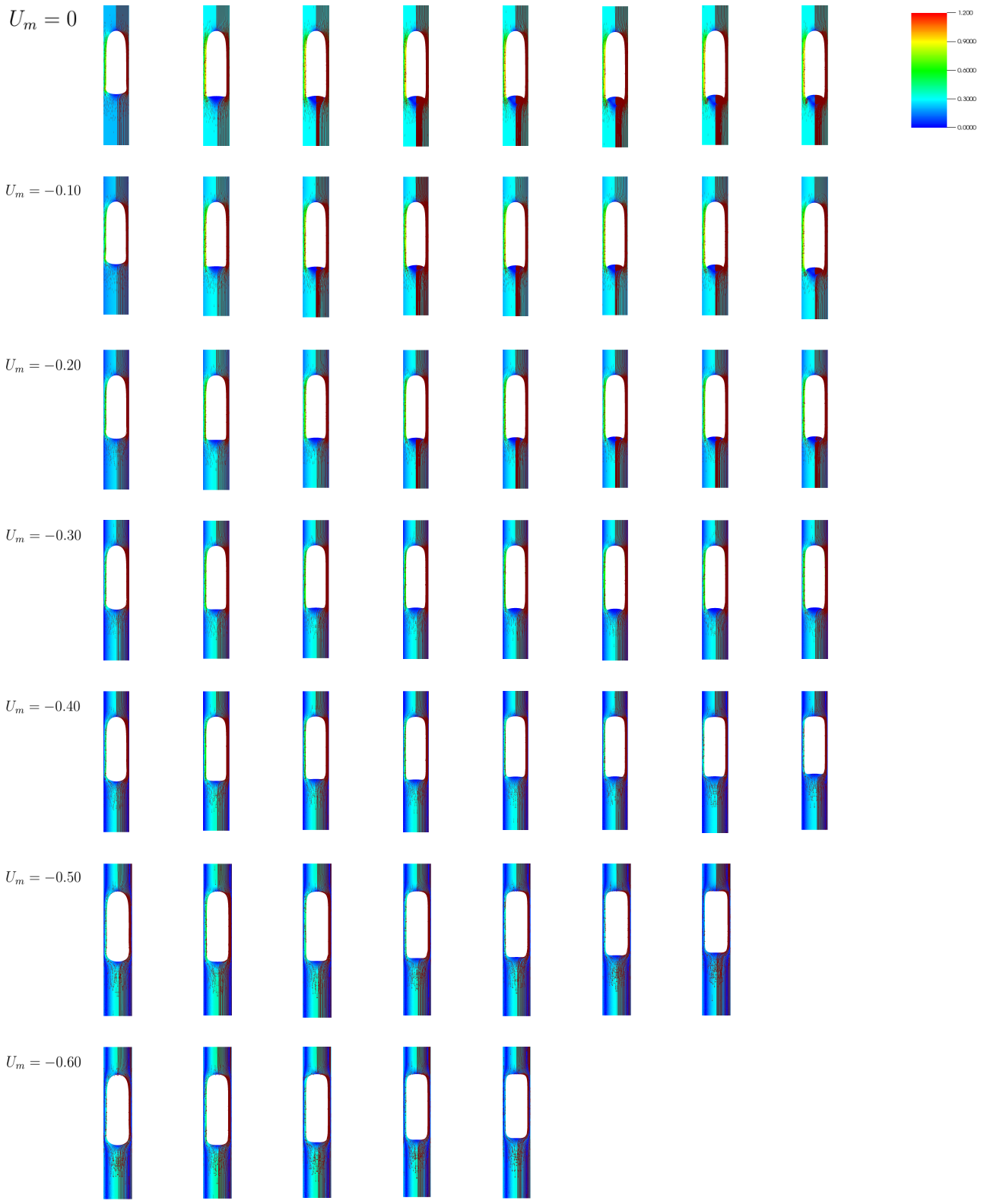


Figure B.6: Steady state bubble shapes and flow field; effect of centreline liquid velocity Froude number and Eötvös number for $Nf = 100$.

Bubble shape and flow field for $Nf = 80$

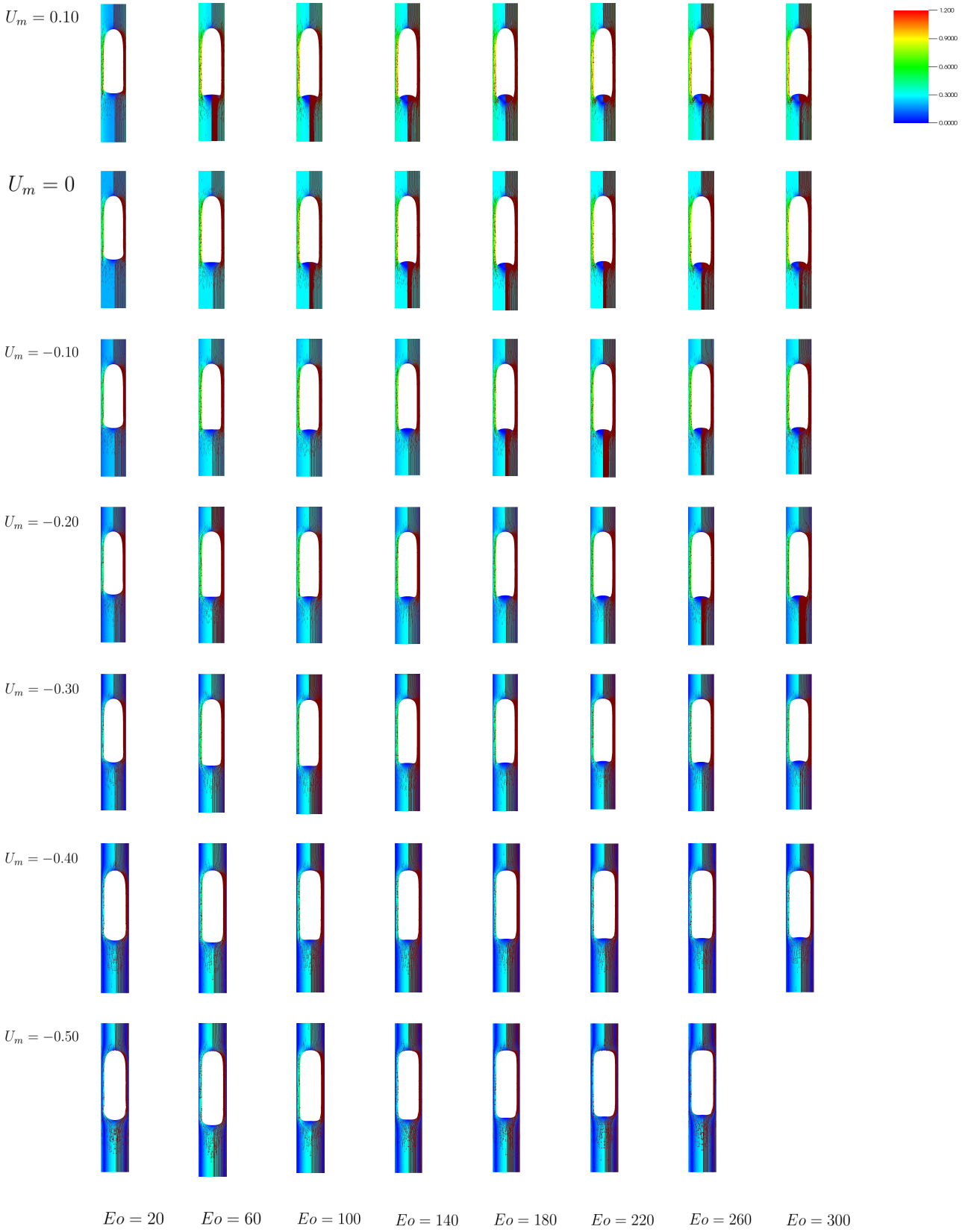


Figure B.7: Steady state bubble shapes and flow field; effect of centreline liquid velocity Froude number and Eötvös number for $Nf = 80$.

Bubble shape and flow field for $Nf = 60$

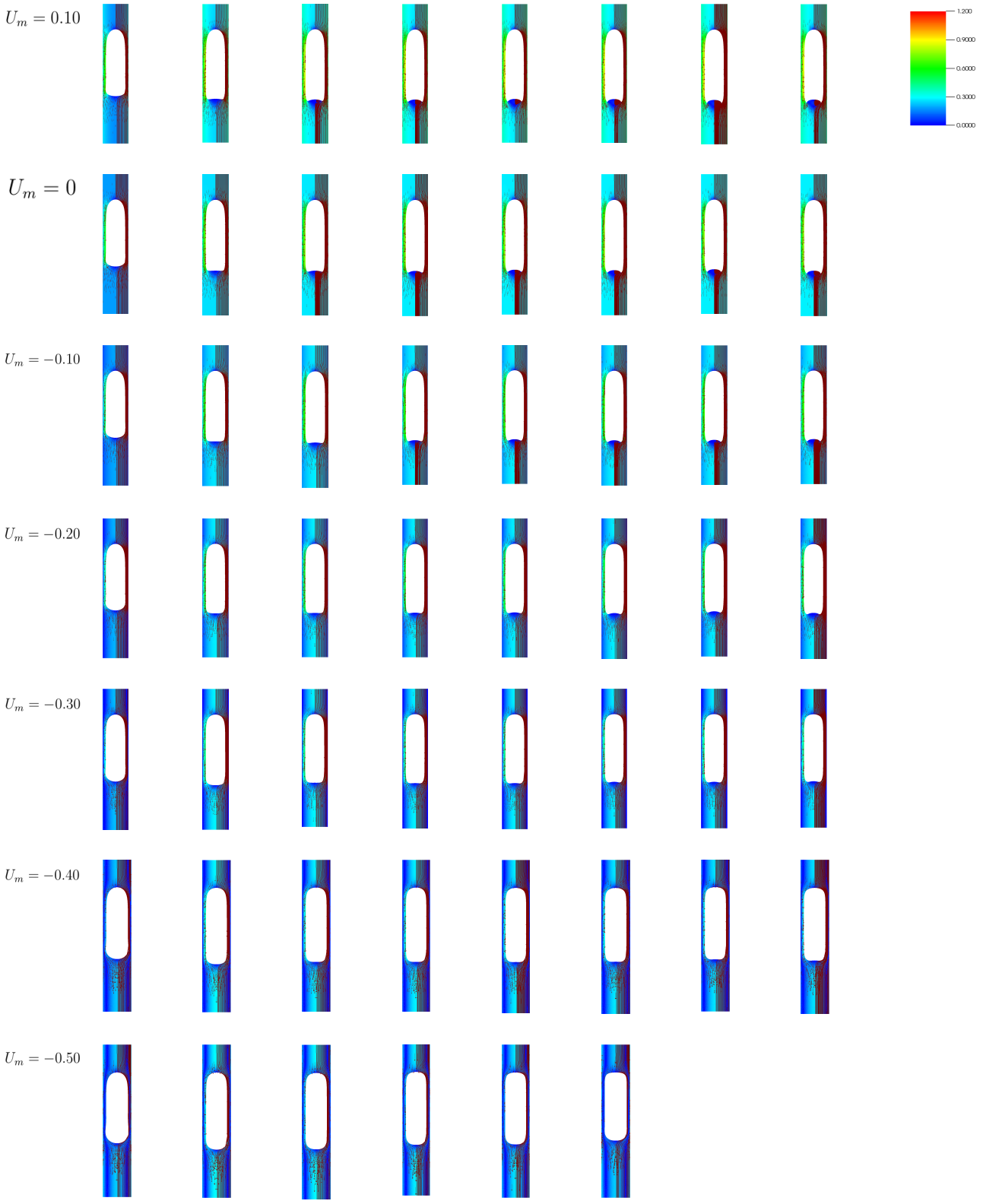


Figure B.8: Steady state bubble shapes and flow field; effect of centreline liquid velocity Froude number and Eötvös number for $Nf = 60$.

Bubble shape and flow field for $Nf = 40$

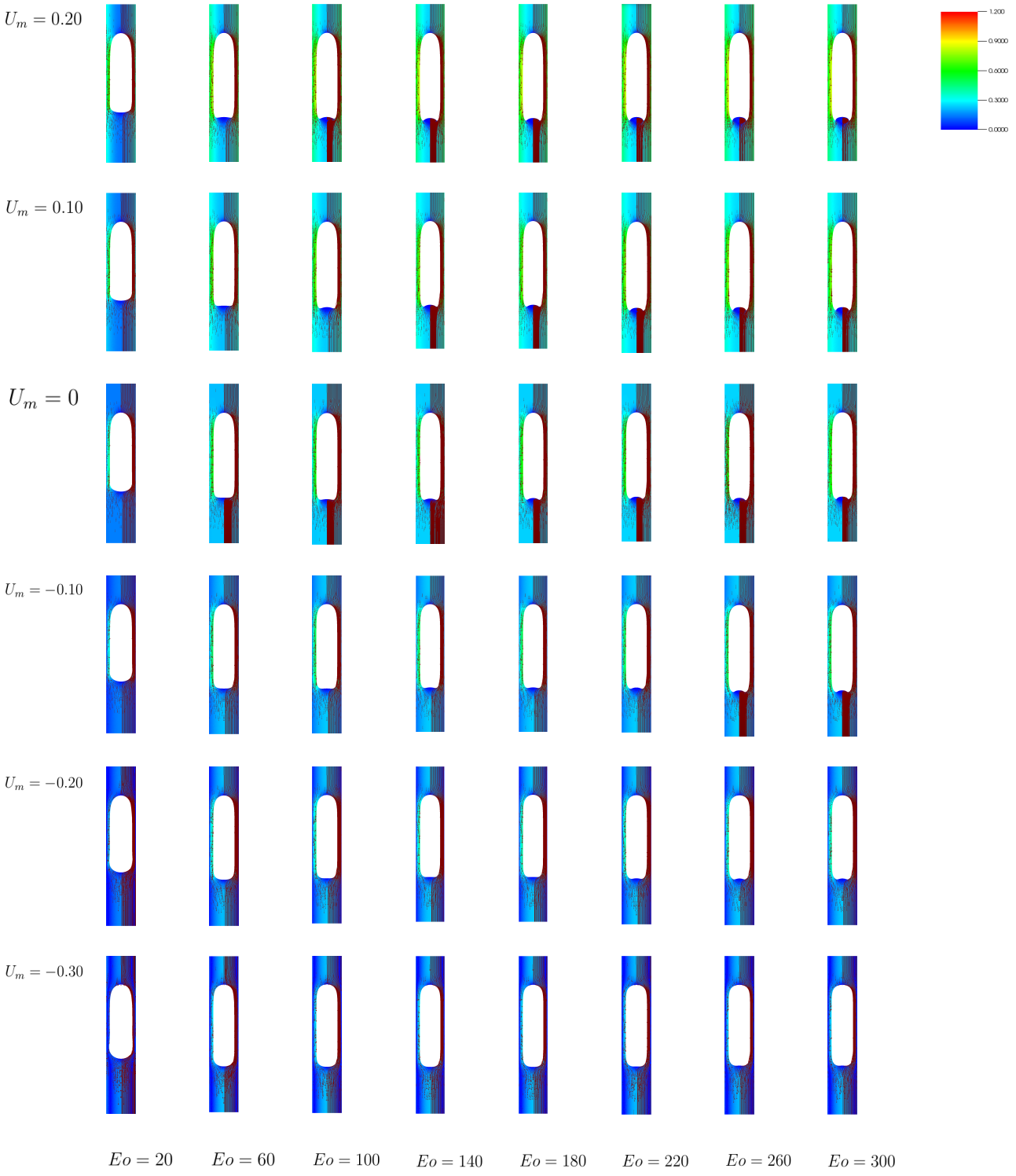


Figure B.9: Steady state bubble shapes and flow field; effect of centreline liquid velocity Froude number and Eötvös number for $Nf = 40$.

Appendix C

Stability analysis model and results

C.1 Model development

Interface stress : normal stress

The base state normal stress is given as

$$\sigma_n = \mathbf{T} : \mathbf{n} \otimes \mathbf{n} = \mathbf{n} \cdot \mathbf{T} \cdot \mathbf{n} \tag{C.1}$$

From (3.4) and (3.5), we have

$$\begin{aligned}\mathbf{T} = &\left[-p + 2Nf^{-1}\frac{\partial u_r}{\partial r}\right]\mathbf{i}_r\mathbf{i}_r + Nf^{-1}\left[\frac{1}{r}\frac{\partial u_r}{\partial \theta} - \frac{u_\theta}{r} + \frac{\partial u_\theta}{\partial r}\right]\mathbf{i}_r\mathbf{i}_\theta + Nf^{-1}\left[\frac{\partial u_r}{\partial z} + \frac{\partial u_z}{\partial r}\right]\mathbf{i}_r\mathbf{i}_z \\ &+Nf^{-1}\left[\frac{1}{r}\frac{\partial u_r}{\partial \theta} - \frac{u_\theta}{r} + \frac{\partial u_\theta}{\partial r}\right]\mathbf{i}_\theta\mathbf{i}_r + \left[-p + 2Nf^{-1}\left(\frac{u_r}{r} + \frac{1}{r}\frac{\partial u_\theta}{\partial \theta}\right)\right]\mathbf{i}_\theta\mathbf{i}_\theta + Nf^{-1}\left[\frac{\partial u_\theta}{\partial z} + \frac{1}{r}\frac{\partial u_z}{\partial \theta}\right]\mathbf{i}_\theta\mathbf{i}_z \\ &+Nf^{-1}\left[\frac{\partial u_r}{\partial z} + \frac{\partial u_z}{\partial r}\right]\mathbf{i}_z\mathbf{i}_r + Nf^{-1}\left[\frac{\partial u_\theta}{\partial z} + \frac{1}{r}\frac{\partial u_z}{\partial \theta}\right]\mathbf{i}_z\mathbf{i}_\theta + \left[-p + 2Nf^{-1}\frac{\partial u_z}{\partial z}\right]\mathbf{i}_z\mathbf{i}_z\end{aligned} \tag{C.2}$$

with $\mathbf{n} = \begin{bmatrix} n_r & 0 & n_z \end{bmatrix}$ and $\mathbf{u} = \begin{bmatrix} u_r & 0 & u_z \end{bmatrix}$ for base state, we have

$$\sigma_n = n_r^2 \left\{ -p + 2Nf^{-1} \frac{\partial u_r}{\partial r} \right\} + n_z^2 \left\{ -p + 2Nf^{-1} \frac{\partial u_z}{\partial z} \right\} + 2n_r n_z \left\{ \frac{\partial u_r}{\partial z} + \frac{\partial u_z}{\partial r} \right\} \tag{C.3}$$

which on simplification gives

$$\sigma_n = -p + 2Nf^{-1} \mathbf{n} \cdot \frac{d\mathbf{u}}{dn} \tag{C.4}$$

Interface stress : shear stress

On axisymmetric surface

$$\sigma_s = \mathbf{n} \cdot \mathbf{T} \times \mathbf{n} = \mathbf{T} : \mathbf{n} \otimes \mathbf{t} = \mathbf{n} \cdot \mathbf{T} \cdot \mathbf{t} \tag{C.5}$$

which when expanded, we have

$$\sigma_s = n_r t_r \left\{ -p + 2Nf^{-1} \frac{\partial u_r}{\partial r} \right\} + n_z t_z \left\{ -p + 2Nf^{-1} \frac{\partial u_z}{\partial z} \right\} + n_r t_z \left\{ \frac{\partial u_r}{\partial z} + \frac{\partial u_z}{\partial r} \right\} + n_z t_r \left\{ \frac{\partial u_r}{\partial z} + \frac{\partial u_z}{\partial r} \right\} \tag{C.6}$$

and on simplification as done for normal stress, gives

$$\sigma_s = Nf^{-1} \left[\mathbf{n} \cdot \frac{d\mathbf{u}}{ds} + \mathbf{t} \cdot \frac{d\mathbf{u}}{dn} \right] \tag{C.7}$$

At gas-liquid interface, $\sigma_s = 0$.

Interface stress : tangential stress

$$\sigma_t = \mathbf{T} : [\mathbf{I} - \mathbf{n} \otimes \mathbf{n}] \tag{C.8}$$

Using (A.2) and (C.2), we have

$$\sigma_t = t_r^2 \left\{ -p + 2Nf^{-1}\frac{\partial u_r}{\partial r} \right\} + t_z^2 \left\{ -p + 2Nf^{-1}\frac{\partial u_z}{\partial z} \right\} + 2t_r t_z \left\{ \frac{\partial u_r}{\partial z} + \frac{\partial u_z}{\partial r} \right\} + \left\{ -p + 2Nf^{-1}\frac{u_r}{r} \right\} \tag{C.9}$$

which on simplification gives

$$\sigma_t = -p + 2Nf^{-1}\mathbf{t} \cdot \frac{d\mathbf{u}}{ds} + \left\{ -p + 2Nf^{-1}\frac{u_r}{r} \right\} \tag{C.10}$$

Domain linearisation : interface rate of strain part

The rate of strain of a vector, say $\mathbf{u}$, $\mathbf{E}(\mathbf{u})$, defined in (3.5), can be expressed in terms of interface normal and tangent vector as follow:

Using the relation given in (C.1), the gradient of a vector $\mathbf{u}$ becomes

$$\nabla(\mathbf{u}) = \nabla_n(\mathbf{u}) + \nabla_s(\mathbf{u}) \tag{C.11}$$

which give

$$\begin{aligned}
\nabla(\mathbf{u}) = &\left(t_r\frac{du_r}{ds} + n_r\frac{du_r}{dn} \right)\mathbf{i}_r\mathbf{i}_r + \left(t_r\frac{du_\theta}{ds} + n_r\frac{du_\theta}{dn} \right)\mathbf{i}_r\mathbf{i}_\theta + \left(t_r\frac{du_z}{ds} + n_r\frac{du_z}{dn} \right)\mathbf{i}_r\mathbf{i}_z \\
&+ \left(\frac{1}{r}\frac{\partial u_r}{\partial\theta} - \frac{u_\theta}{r} \right)\mathbf{i}_\theta\mathbf{i}_r + \left(\frac{1}{r}\frac{\partial u_\theta}{\partial\theta} + \frac{u_r}{r} \right)\mathbf{i}_\theta\mathbf{i}_\theta + \left(\frac{1}{r}\frac{\partial u_z}{\partial\theta} \right)\mathbf{i}_\theta\mathbf{i}_z \\
&+ \left(t_z\frac{du_r}{ds} + n_z\frac{du_r}{dn} \right)\mathbf{i}_z\mathbf{i}_r + \left(t_z\frac{du_\theta}{ds} + n_z\frac{du_\theta}{dn} \right)\mathbf{i}_z\mathbf{i}_\theta + \left(t_z\frac{du_z}{ds} + n_z\frac{du_z}{dn} \right)\mathbf{i}_z\mathbf{i}_z
\end{aligned} \tag{C.12}$$

so that

$$\begin{aligned}
\mathbf{E}(\mathbf{u}) = &\left(t_r\frac{du_r}{ds} + n_r\frac{du_r}{dn} \right)\mathbf{i}_r\mathbf{i}_r + \frac{1}{2}\left(t_r\frac{du_\theta}{ds} + n_r\frac{du_\theta}{dn} + \frac{1}{r}\frac{\partial u_r}{\partial\theta} - \frac{u_\theta}{r} \right)\mathbf{i}_r\mathbf{i}_\theta \\
&+ \frac{1}{2}\left(t_r\frac{du_z}{ds} + n_r\frac{du_z}{dn} + t_z\frac{du_r}{ds} + n_z\frac{du_r}{dn} \right)\mathbf{i}_r\mathbf{i}_z + \frac{1}{2}\left(\frac{1}{r}\frac{\partial u_r}{\partial\theta} - \frac{u_\theta}{r} + t_r\frac{du_\theta}{ds} + n_r\frac{du_\theta}{dn} \right)\mathbf{i}_\theta\mathbf{i}_r \\
&+ \left(\frac{1}{r}\frac{\partial u_\theta}{\partial\theta} + \frac{u_r}{r} \right)\mathbf{i}_\theta\mathbf{i}_\theta + \frac{1}{2}\left(\frac{1}{r}\frac{\partial u_z}{\partial\theta} + t_z\frac{du_\theta}{ds} + n_z\frac{du_\theta}{dn} \right)\mathbf{i}_\theta\mathbf{i}_z + \frac{1}{2}\left(t_z\frac{du_r}{ds} + n_z\frac{du_r}{dn} + t_r\frac{du_z}{ds} + n_r\frac{du_z}{dn} \right)\mathbf{i}_z\mathbf{i}_r \\
&+ \frac{1}{2}\left(t_z\frac{du_\theta}{ds} + n_z\frac{du_\theta}{dn} + \frac{1}{r}\frac{\partial u_z}{\partial\theta} \right)\mathbf{i}_z\mathbf{i}_\theta + \left(t_z\frac{du_z}{ds} + n_z\frac{du_z}{dn} \right)\mathbf{i}_z\mathbf{i}_z
\end{aligned} \tag{C.13}$$

Domain linearisation : interface divergence part

Using (C.1), the divergence of a vector say $\mathbf{u}$, evaluated on a surface can also be expressed in terms of interface normal and tangent vector as follow,

$$\nabla \cdot \mathbf{u} = \nabla_n \cdot \mathbf{u} + \nabla_s \cdot \mathbf{u} \tag{C.14}$$

which gives

$$\nabla \cdot \mathbf{u} = \mathbf{t} \cdot \frac{d\mathbf{u}}{ds} + \mathbf{n} \cdot \frac{d\mathbf{u}}{dn} + \left\{ \frac{1}{r} \frac{\partial u_\theta}{\partial \theta} + \frac{u_r}{r} \right\} \tag{C.15}$$

With $u_\theta = 0$ for the base flow, using (C.13) and (C.15),

$$\mathbf{E}(\mathbf{u}) : \mathbf{E}(\mathbf{\Phi}) + p \nabla \cdot \mathbf{\Phi}$$

gives

$$\begin{aligned} \left[-p^0 + 2Nf^{-1} \left(\mathbf{n} \cdot \frac{d\mathbf{u}^0}{dn} \right) \right] \left(\mathbf{n} \cdot \frac{d\mathbf{\Phi}}{dn} \right) + \left[-p^0 + 2Nf^{-1} \left(\mathbf{t} \cdot \frac{d\mathbf{u}^0}{ds} \right) \right] \left(\mathbf{t} \cdot \frac{d\mathbf{\Phi}}{ds} \right) \\ + \left[-p^0 + 2Nf^{-1} \frac{u_r^0}{r} \right] \left(\frac{\Phi_r}{r} + \frac{1}{r} \frac{\partial \Phi_\theta}{\partial \theta} \right) \end{aligned} \tag{C.16}$$

Where we have used, $\sigma_s = 0$.

C.2 Maximum growth rate results

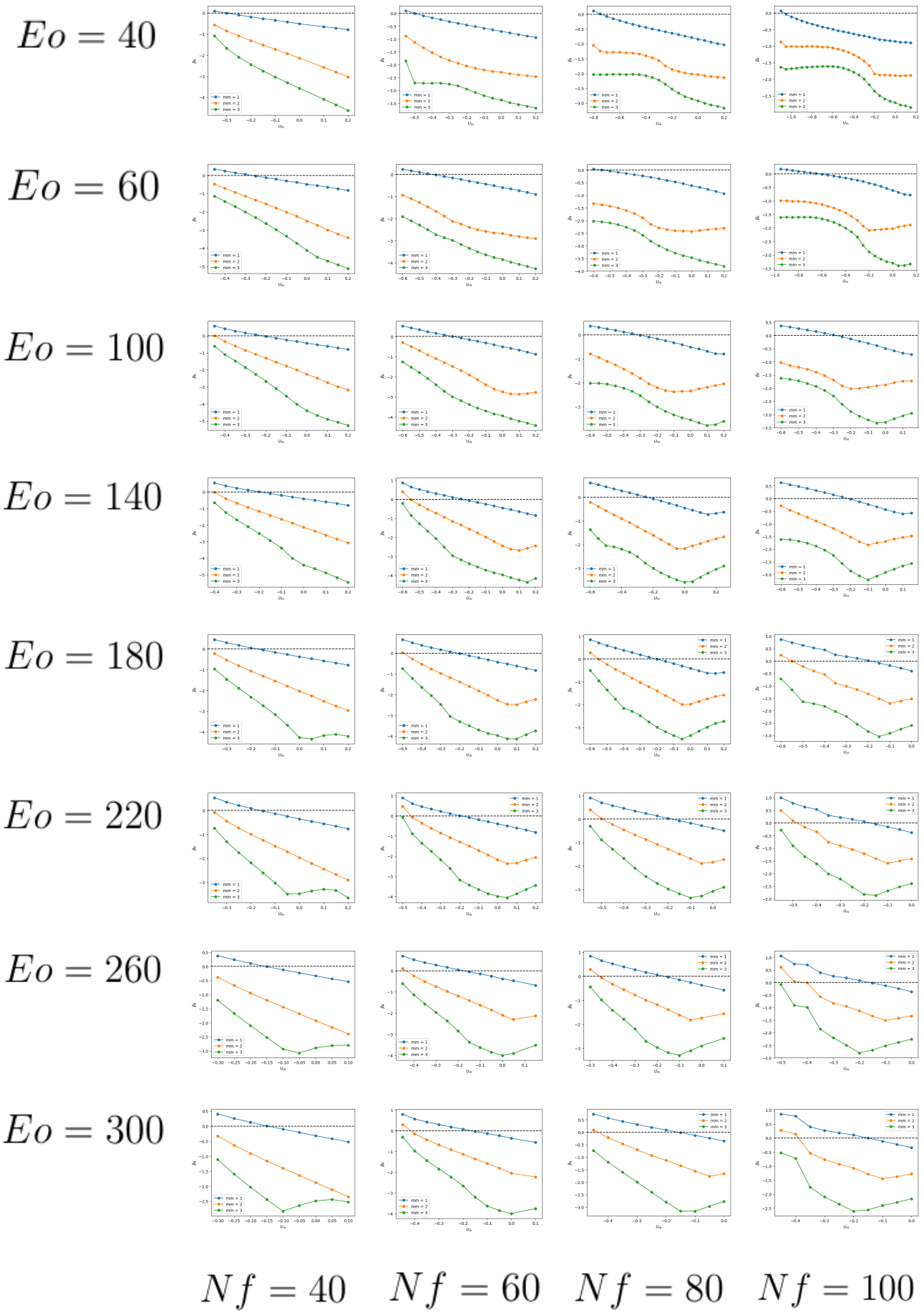


Figure C.1: Maximum growth rate as a function of liquid centreline Froude number; effect of Nf and Eo, showing modes, $m = 1, 2$ and 3.

C.3 Energy analysis

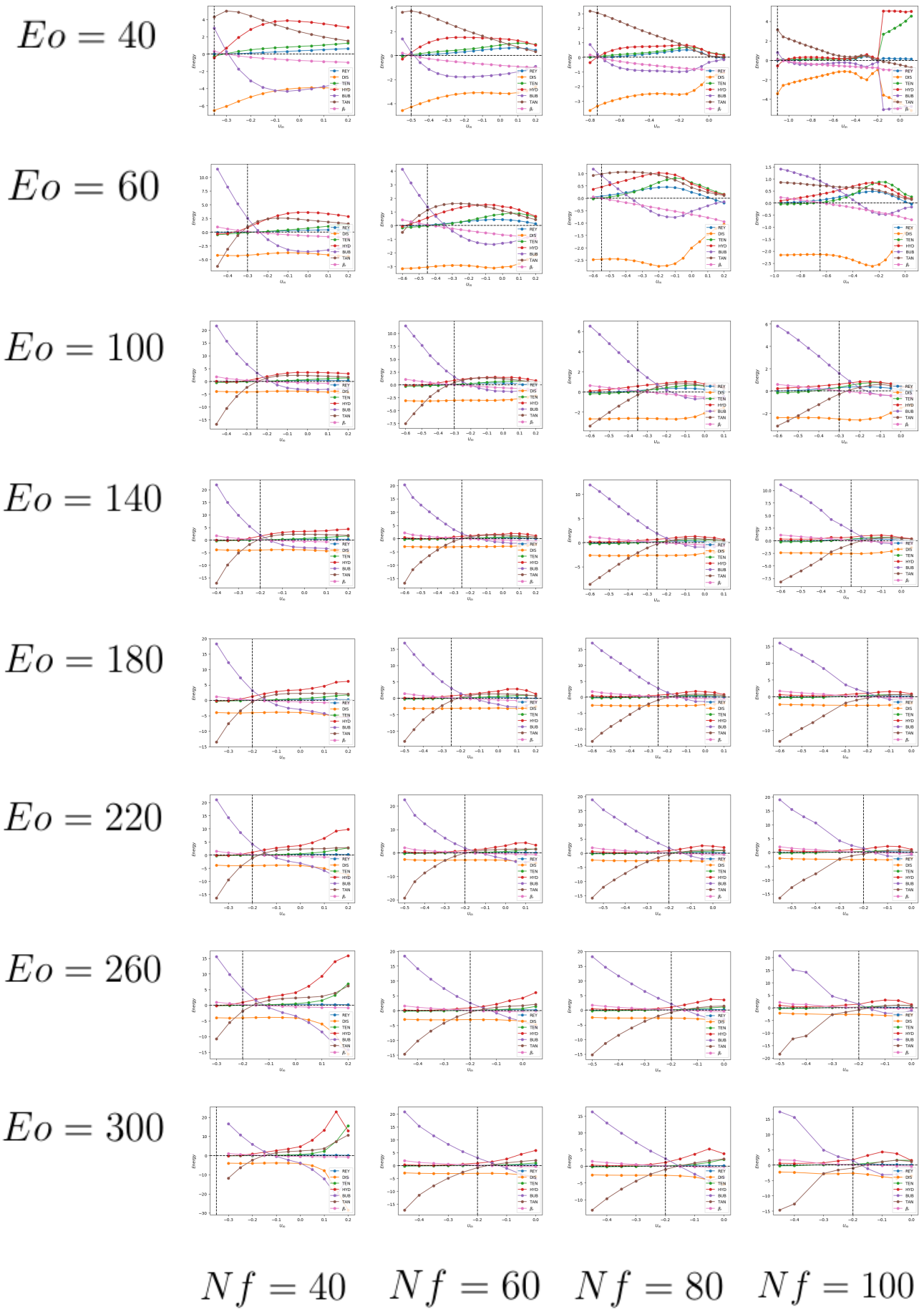


Figure C.2: Energy contribution of the different energy terms in (5.64) for mode, $m = 1$; effect of inverse viscosity and Eötvös numbers.

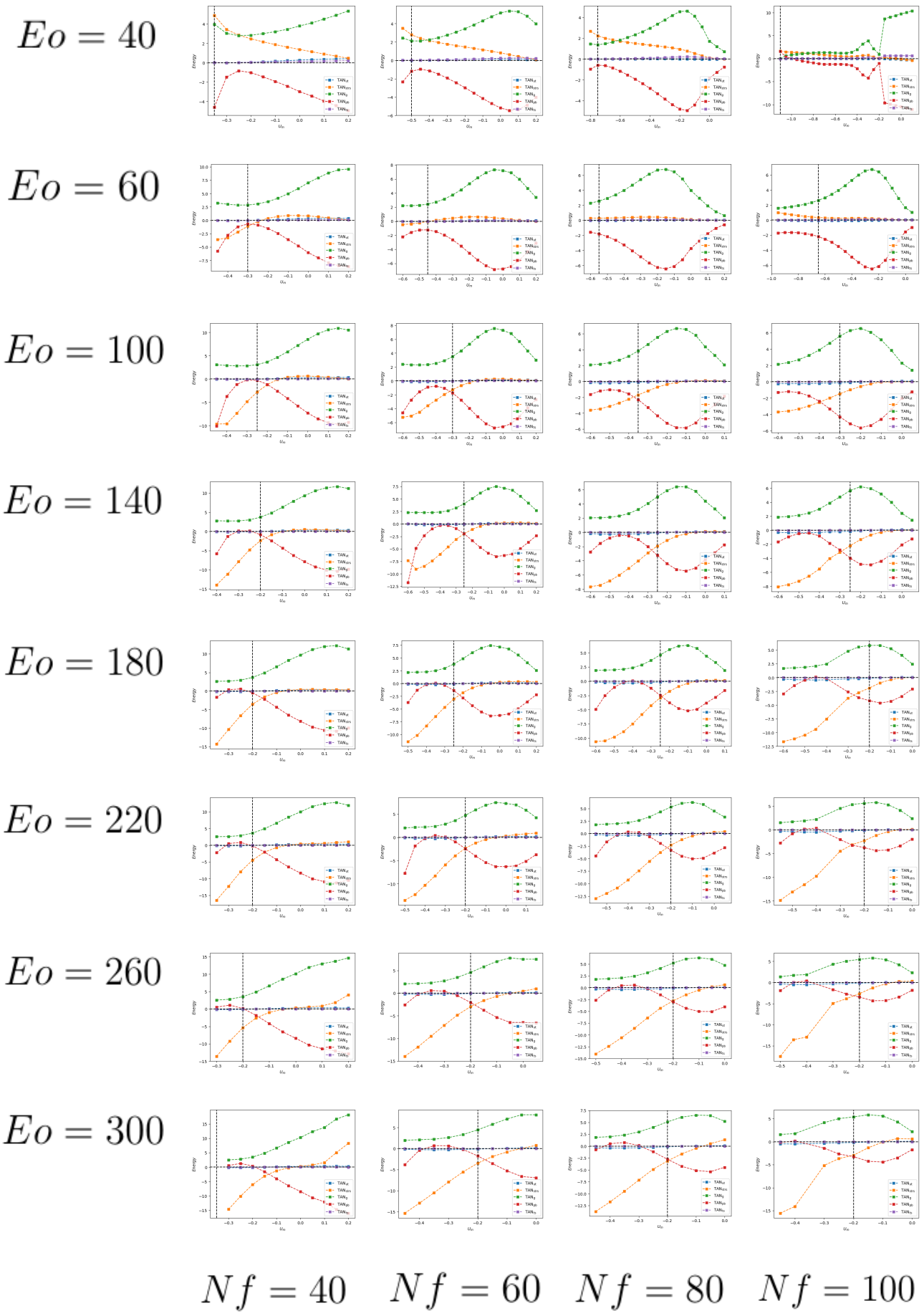


Figure C.3: Energy contribution of the different energy terms in (5.66) for mode, $m = 1$; effect of inverse viscosity and Eötvös numbers.